NANOSYSTEMS:

PHYSICS, CHEMISTRY, MATHEMATICS

NANOSYSTEMS:
PHYSICS, CHEMISTRY, MATHEMATICS

AIM AND SCOPE

The scope of the journal includes all areas of nano-sciences. Papers devoted to basic problems of physics, chemistry, material science and mathematics inspired by nanosystems investigations are welcomed. Both theoretical and experimental works concerning the properties and behavior of nanosystems, problems of its creation and application, mathematical methods of nanosystem studies are considered.

The journal publishes scientific reviews (up to 30 journal pages), research papers (up to 15 pages) and letters (up to 5 pages). All manuscripts are peer-reviewed. Authors are informed about the referee opinion and the Editorial decision.

CONTENT

CHEMISTRY AND MATERIAL SCIENCE

Approximation of eigenvalues of Schrödinger operators

J. F. Brasche[1], R. Fulsche[2]

[1]Institut für Mathematik, Technische Universität Clausthal,
Erzstraße 1, 30867 Clausthal-Zellerfeld, Germany
[2]Institut für Analysis, Leibniz Universität Hannover,
Welfengarten 1, 30167 Hannover, Germany

johannes.brasche@tu-clausthal.de, fulsche@math.uni-hannover.de

It is known that convergence of l. s. b. closed symmetric sesquilinear forms implies norm resolvent convergence of the associated self-adjoint operators and thus, in turn, convergence of discrete spectra. In this paper, in both cases, sharp estimates for the rate of convergence are derived. An algorithm for the numerical computation of eigenvalues of generalized Schrödinger operators in $L^2(\mathbb{R})$ is presented and illustrated by explicit examples; the mentioned general results on the rate of convergence are applied in order to obtain error estimates for these computations. An extension of the results to Schrödinger operators on metric graphs is sketched.

1. Introduction

Often, things become easier by passing to the limit. A striking example is provided by the one-dimensional Kronig–Penney model. Here, the Hamiltonian is the self-adjoint operator $H_b = -\Delta + b \sum_{n \in \mathbb{Z}} a_n \delta_n$ in $L^2(\mathbb{R})$.

If all coefficients a_n are positive, then, by Kato's monotone convergence theorem, the operators H_b converge in the strong resolvent sense to the Laplacian with Dirichlet boundary conditions at every point of $\mathbb{Z}$, as the coupling parameter b tends to infinity. If the family $(a_n)_{n \in \mathbb{Z}}$ is lower bounded by a positive constant, then the operators H_b converge in the norm resolvent sense with convergence rate $O(1/b)$ [1, Example 3.8]. Moreover, if the family $(1/a_n)_{n \in \mathbb{Z}}$ is summable, then the resolvents even converge w.r.t. the trace norm with convergence rate $O(1/b)$ [2, Theorem 3.1]. While it is difficult to investigate the operator H_b, it is trivial to determine the spectral properties of the limit operator and results on the rate of convergence may be used for a discussion of the Hamiltonian H_b. We refer to [1–8] for a detailed analysis of large coupling convergence of regular and generalized Schrödinger operators as well as other kinds of operators.

Another important class of examples is provided by Schrödinger operators with singular potentials. If the potential V vanishes outside a very small vicinity of the closed null set N, then one expects that a replacement of the Hamiltonian $-\Delta + V$ by a suitably chosen self-adjoint operator H that coincides with $-\Delta$ on the space $C_0^\infty(\mathbb{R}^d \setminus N)$ only leads to a negligible error. Due to the fact that H is equal to the free Hamiltonian outside the null set N, it is often easier to investigate the operator H than the regular Schrödinger operator $-\Delta + V$. The idea that the mentioned replacement only leads to small errors is supported by a large variety of convergence results. The most famous ones are results on point interactions; if the set N is finite and $d = 2, 3$, then for every self-adjoint operator H in $L^2(\mathbb{R}^d)$ that coincides with $-\Delta$ on the space $C_0^\infty(\mathbb{R}^d \setminus N)$, one can give potentials V_n such that the operators $-\Delta + V_n$ converge in the norm resolvent sense to H and the supports of the potentials V_n shrink to the set N [9].

Originally, point interaction Hamiltonians were introduced as an idealization of certain Schrödinger operators with short range potentials. In [10], one had the idea to use such operators for other purposes, too. One has shown that a large class of operators H can be approximated by point interaction Hamiltonians H_n. Since it is easy to compute the eigenvalues of the operators H_n, this fact may be used in order to compute the eigenvalues of H approximately. Later, a modification of the methods of [10] has led to an efficient algorithm for the numerical computation of eigenvalues of regular and generalized Schrödinger operators in $L^2(\mathbb{R}^d)$, $d = 2, 3$ [11]. In the subsequent article [12], these results have been extended to Schrödinger operators with magnetic potentials.

In the present paper, we shall concentrate on the one-dimensional case, where it is possible to obtain faster convergence with simpler algorithms. It was shown in [10] that weak convergence of measures implies norm resolvent convergence of the Schrödinger operators having these measures as potentials (cf. Theorem 1 below).

Based on this convergence result, we give a general construction for approximating finite signed measures μ by pure point measures μ_n such that the operators $-\Delta + \mu_n$ converge to $-\Delta + \mu$. Since norm resolvent convergence implies convergence of the isolated eigenvalues and the eigenvalues of $-\Delta + \mu_n$ can be computed efficiently, we end up with a general method for approximating the negative eigenvalues of Schrödinger operators with integrable potential on $\mathbb{R}$. We provide error estimates for each step of the construction and proof.

This paper is organized as follows: In section 2 we recall some notation and preliminary results. Section 3 and 4 provide very general results: As it is well known convergence of l.s.b. closed symmetric sesquilinear forms implies convergence of the associated self-adjoint operators in the norm resolvent sense. In section 3, we derive an asymptotically sharp estimate on the rate of convergence. Norm resolvent convergence of self-adjoint operators implies convergence of the points in the discrete spectra. In section 4, we quantify this result. Section 5 gives results on the convergence of the sesquilinear forms for our concrete problem. In section 6, we discuss the actual construction of the approximating measures, including error estimates in terms of the Fourier transform. Section 7 shows an efficient way to compute negative eigenvalues of Schrödinger operators with pure point potentials. In section 8, we added a short discussion about existence results of negative eigenvalues for Schrödinger operators. Section 9 demonstrates our algorithm by two examples. In one of the two examples, we deal with a singularly continuous measure potential, which cannot be treated by the classical approximation methods. Finally, in section 10, we discuss how our method may be extended to Schrödinger operators on other 1-dimensional domains and explicitly show this for operators on $[0, \infty)$.

2. Preliminaries

We will always denote by $\mathcal{H}$ a Hilbert space with inner product $\langle \cdot, \cdot \rangle$, which is linear in the first and antilinear in the second component. For a sesquilinear form a on $\mathcal{H}$ with domain $D(a)$ and for $c \in \mathbb{R}$, we denote by a_c the form

$$D(a_c) = D(a),$$
$$a_c(f, g) = a(f, g) + c\langle f, g \rangle.$$

If c is a lower bound of a, then a_{1-c} is an inner product on $D(a)$. Further, for $f \in D(a)$, we sometimes denote

$$a[f] := a(f, f).$$

The well-known Sobolev inequality for the Sobolev space $H^1(\mathbb{R})$ states that for each $\varepsilon > 0$ and each $f \in H^1(\mathbb{R})$

$$\|f\|_\infty^2 \leq \varepsilon \|f'\|_{L^2}^2 + \frac{4}{\varepsilon} \|f\|_{L^2}^2. \tag{1}$$

Let μ be a finite Radon measure on $\mathbb{R}$, i.e. a finite signed measure on the Borel-σ-algebra of $\mathbb{R}$, $\mathcal{B}(\mathbb{R})$. Then, we define the sesquilinear form a_μ by

$$D(a_\mu) = H^1(\mathbb{R}),$$
$$a_\mu(f, g) = \int_\mathbb{R} f'(x)\overline{g'(x)}dx + \int_\mathbb{R} f\overline{g}d\mu,$$

which is well known to be symmetric, lower-semibounded and closed. By $-\Delta + \mu$, we denote the self-adjoint operator associated with the form in the sense of Kato's first representation theorem (cf. [13, Theorem 2.6], [14, Theorem VIII.15]), i.e. $-\Delta + \mu$ is the self-adjoint operator in $L^2(\mathbb{R})$ with

$$D(-\Delta + \mu) \subseteq D(a_\mu),$$
$$\langle (-\Delta + \mu)f, g \rangle = a_\mu(f, g) \quad \forall f \in D(-\Delta + \mu), g \in D(a_\mu).$$

We say that a sequence (μ_n) of finite Radon measures on $\mathbb{R}$ converges weakly to the finite Radon measure μ if

$$\int_\mathbb{R} f(x)d\mu_n(x) \to \int_\mathbb{R} f(x)d\mu(x), \quad n \to \infty,$$

for each $f \in C_b(\mathbb{R})$, where $C_b(\mathbb{R})$ is the space of bounded continuous functions on $\mathbb{R}$. In particular, the corresponding Fourier transforms, which are defined as

$$\hat{\nu}(t) := \int_\mathbb{R} e^{itx}d\nu(x),$$

for a finite Radon measure ν on $\mathbb{R}$, converge pointwise. For a finite Radon measure μ, we let $\mu = \mu_+ - \mu_-$ be the Hahn–Jordan decomposition and set $|\mu| = \mu_+ + \mu_-$. If f is a measurable function, we define the measure $f\mu$ by

$$f\mu(B) = \int_B f d\mu, \quad B \in \mathcal{B}(\mathbb{R}).$$

χ_B denotes the indicator function of $B \in \mathcal{B}(\mathbb{R})$. The following theorem plays a key role in this paper:

Theorem 1 ([10, Theorem 3]). *Let μ_n, $n \in \mathbb{N}$, and μ be finite Radon measures on $\mathbb{R}$ such that $\mu_n \to \mu$ weakly. Then, the operators $-\Delta + \mu_n$ converge to $-\Delta + \mu$ in norm resolvent sense.*

One goal of the next sections will be to quantify this theorem.

3. Form convergence and norm resolvent convergence

The fact that the convergence of sesquilinear forms with common domain implies norm resolvent convergence of the associated operators is well known, cf. [14, Theorem VIII.25]. The following theorem gives a quantitative result for this statement.

Theorem 2. *Let A and B be self-adjoint and lower semi-bounded linear operators in $\mathcal{H}$ such that $A \geq 1$ and $B \geq 1$. Let a and b be the closed sesquilinear form associated with A and B, respectively. Assume that $D(a) = D(b) =: D$. If*

$$s := \sup_{g \in D, \ a(g,g)=1} |a(g,g) - b(g,g)| < 1,$$

then

$$\|B^{-1} - A^{-1}\| \leq \frac{s}{\sqrt{1-s}}.$$

Proof. For the whole proof, let f always be arbitrary in $\mathcal{H}$, such that $\|f\| = 1$. Since $B \geq 1$,

$$\|B^{-1}f\| \leq 1. \tag{2}$$

We set

$$g = \frac{B^{-1}f}{\sqrt{a(B^{-1}f, B^{-1}f)}}.$$

Then, $a(g,g) = 1$ and therefore

$$|a(g,g) - b(g,g)| \leq s.$$

Further,

$$b(g,g) = \frac{\langle f, B^{-1}f \rangle}{a(B^{-1}f, B^{-1}f)} \leq \frac{\|f\|\|B^{-1}f\|}{a(B^{-1}f, B^{-1}f)} \leq \frac{1}{a(B^{-1}f, B^{-1}f)}$$

by inequality (2). Since $s \geq 1 - b(g,g)$, we can conclude

$$s \geq 1 - \frac{1}{a(B^{-1}f, B^{-1}f)},$$

and therefore

$$a(B^{-1}f, B^{-1}f) \leq \frac{1}{1-s}. \tag{3}$$

Using $A \geq 1$ (and therefore $a \geq 1$ as well), we get

$$\|B^{-1}f - A^{-1}f\| \leq \sqrt{a(B^{-1}f - A^{-1}f, B^{-1}f - A^{-1}f)}.$$

Denoting $d = B^{-1}f - A^{-1}f$, we have

$$
\begin{aligned}
\|B^{-1}f - A^{-1}f\| \leq \sqrt{a(d,d)} &= \sup_{a(h,h)=1} |a(d,h)| \\
&= \sup_{a(h,h)=1} |a(B^{-1}f,h) - \langle f,h\rangle| \\
&= \sup_{a(h,h)=1} |a(B^{-1}f,h) - b(B^{-1}f,h)| \\
&= \sup_{a(h,h)=1} \left| a\left(\frac{B^{-1}f}{a[B^{-1}f]^{1/2}},h\right) - b\left(\frac{B^{-1}f}{a[B^{-1}f]^{1/2}},h\right) \right| a[B^{-1}f]^{1/2} \\
&\leq \sup_{a(c,c)=1=a(h,h)} |a(c,h) - b(c,h)| \frac{1}{\sqrt{1-s}}.
\end{aligned}
$$

The well-known identity

$$
\sup_{a(c,c)=1=a(h,h)} |a(c,h) - b(c,h)| = \sup_{a(h,h)=1} |a(h,h) - b(h,h)|,
$$

completes the proof. $\qquad\square$

Remark 3. Observe that the above estimate is good in the sense that it is asymptotically sharp: In the trivial case $a = \langle\cdot,\cdot\rangle$ and $b = (1+s)a$ we have

$$
\|B^{-1} - A^{-1}\| = \frac{s}{1+s},
$$

and the quotient of $\|B^{-1} - A^{-1}\|$ and the upper bound for $\|B^{-1} - A^{-1}\|$ in the above estimate tends to 1, as s tends to zero.

4. Convergence of isolated eigenvalues

A well-known consequence of norm convergence and norm resolvent convergence for self-adjoint operators is that it implies convergence of the discrete spectrum. The aim of the next two results is to quantify this result.

Lemma 4. *Let S and T be bounded and self-adjoint operators in $\mathcal{H}$ satisfying $\|S - T\| < \delta$ for some $\delta > 0$. If*

$$
(E - 2\delta, E + 2\delta) \cap \sigma(S) = \{E\},
$$

and E is an eigenvalue of S of multiplicity $n \in \mathbb{N}$, then

$$
(E - \delta, E + \delta) \cap \sigma(T) \subset \sigma_d(T),
$$

and the number, counting multiplicities, of eigenvalues of T in $(E - \delta, E + \delta)$ is equal to n.

Proof. For each $f \in \mathcal{H}$ and $B \in \mathcal{B}(\mathbb{R})$ we use the notation $\mu_{f,A}(B) = \|\chi_B(A)f\|^2$ for each self-adjoint operator A on $\mathcal{H}$. It is well-known that $\mu_{f,A}$ is a measure satisfying $\mu_{f,A}(\mathbb{R}) = \|f\|^2$ and $\|(A-c)f\|^2 = \int |\lambda - c|^2 d\mu_{f,A}(\lambda)$ for $c \in \mathbb{R}$. Further, $\mathcal{H}$ decomposes into $\mathcal{H} = \operatorname{ran} 1_B(A) \oplus \operatorname{ran} 1_{\mathbb{R}\setminus B}(A)$ for each $B \in \mathcal{B}(\mathbb{R})$.

Now, let $J = (E - \delta, E + \delta)$ and $\widetilde{J} = (E - 2\delta, E + 2\delta)$. The statement we want to prove is equivalent to $\dim \operatorname{ran} 1_J(T) = n$. We will prove this by contradiction.

Case 1: Assume $\dim \operatorname{ran} 1_J(T) < n$. Since $\dim \ker(S - E) = n > \dim \operatorname{ran} 1_J(T)$, there is some $f \in \ker(S - E)$ with $\|f\| = 1$ and $f \perp \operatorname{ran} 1_J(T)$. Hence

$$
\mu_{f,T}(J) = \|1_J(T)f\|^2 = \langle 1_J(T)^2 f, f\rangle = 0
$$

and thus,

$$
\|(T - E)f\|^2 = \int |\lambda - E|^2 d\mu_{f,T}(\lambda) \geq \int \delta^2 \mu_{f,T}(\lambda) = \delta^2 \|f\|^2.
$$

This is a contradiction, since it would imply

$$
\|(T - S)f\| = \|(T - E)f - (S - E)f\| = \|(T - E)f\| \geq \delta.
$$

Case 2: $\dim \operatorname{ran} 1_J(T) > n$. In this case, we can choose $f \in \operatorname{ran} 1_J(T)$ with $\|f\| = 1$ and $f \perp \ker(S - E)$. For this f, it holds $f \perp \operatorname{ran}_{\mathbb{R}\setminus J}(T)$ and hence

$$
\mu_{f,T}(\mathbb{R} \setminus J) = \langle (1_{\mathbb{R}\setminus J}(T))^2 f, f\rangle = 0.
$$

Thus,

$$\|(T - E)f\|^2 = \int |\lambda - E|^2 d\mu_{f,T}(\lambda) \leq \int \delta^2 d\mu_{f,T}(\lambda) = \delta^2 \|f\|^2.$$

It is $\operatorname{ran} 1_{\widetilde{J}}(S) = \ker(S - E)$, since E is the only point in $\sigma(S) \cap \widetilde{J}$. This implies

$$\mu_{f,S}(\widetilde{J}) = \langle (1_{\widetilde{J}}(S))^2 f, f \rangle = 0,$$

and hence

$$\|(S - E)f\|^2 = \int |\lambda - E|^2 d\mu_{f,S}(\lambda) \geq \int (2\delta)^2 d\mu_{f,S}(\lambda) = (2\delta)^2 \|f\|^2.$$

However, this is impossible, since it would imply

$$\|(S - T)f\| = \|(S - E)f - (T - E)f\| \geq \|(S - E)f\| - \|(T - E)f\| \geq \delta. \qquad \square$$

Recall the following result:

Theorem 5 ([15, Remark 2.1 and Theorem 3.1]). *For every finite Radon measure μ on $\mathbb{R}$, it holds:*

$$\sigma_{ess}(-\Delta + \mu) = [0, \infty).$$

From the previous lemma, one can derive the following result, which is applicable to our setting:

Theorem 6. *Let $A, \widetilde{A}$ be self-adjoint operators in $\mathcal{H}$ such that $\sigma_{ess}(A) = \sigma_{ess}(\widetilde{A}) = [0, \infty)$ and assume $A, \widetilde{A} \geq c$ for some $c \leq 0$. Denote $\alpha = 1 - c$ and let δ be such that $0 < \delta < \dfrac{1}{2\alpha}$. Further, assume that*

$$\|(A + \alpha)^{-1} - (\widetilde{A} + \alpha)^{-1}\| < \delta,$$

and

$$\left(\frac{E - 2\delta\alpha(E + \alpha)}{1 + 2\delta(E + \alpha)}, \frac{E + 2\delta\alpha(E + \alpha)}{1 - 2\delta(E + \alpha)} \right) \cap \sigma(A) = \{E\},$$

where E is an eigenvalue of A with multiplicity $n \in \mathbb{N}$. Then,

$$\left(\frac{E - \alpha\delta(E + \alpha)}{1 + \delta(E + \alpha)}, \frac{E + \alpha\delta(E + \alpha)}{1 - \delta(E + \alpha)} \right) \cap \sigma(\widetilde{A}) \subset \sigma_d(\widetilde{A}),$$

consists of finitely many eigenvalues of $\widetilde{A}$ and the number, counting multiplicities, of these eigenvalues is equal to n.

Proof. Apply the previous lemma to the resolvents $(A + \alpha)^{-1}$ and $(\widetilde{A} - \alpha)^{-1}$ and use the spectral mapping theorem. $\qquad \square$

In many applications, the minimum of the spectrum of A is an isolated eigenvalue with multiplicity one. Hence, it follows that the minimum of the spectrum of A_n is an isolated eigenvalue with multiplicity one for eventually every n, if the sequence (A_n) converges to A in the norm resolvent sense. Via the min-max principle, the rate of convergence of the lowest eigenvalue can be estimated directly with the aid of the associated sesquilinear forms:

Theorem 7. *Let A and B be self-adjoint and lower semibounded linear operators in $\mathcal{H}$ such that $A \geq 1 - c$ and $B \geq 1 - c$ with $c > 0$. Let a and b be the closed sesquilinear forms associated with A and B, respectively. Assume that $D(a) = D(b) =: D$ and*

$$s := \sup_{g \in D, \ a_c(g,g)=1} |a(g,g) - b(g,g)| < 1.$$

Further assume that $E_1(A) := \min \sigma(A)$ is a negative eigenvalue of A and $E_1(B) := \min \sigma(B)$ is a negative eigenvalue of B. Then

$$E_1(B) \leq E_1(A) + (E_1(A) + c)s. \tag{4}$$

Proof. Let f be a normalized eigenvector of A corresponding to the eigenvalue $E_1(A)$. Then $a_c(f, f) = (E_1(A) + c)$. Put

$$g := \frac{f}{\sqrt{E_1(A) + c}}.$$

Then, $a_c(g, g) = 1$. By the min-max-principle,

$$
\begin{aligned}
\min \sigma(B + cI) &= \min_{h \in D, \|h\| = 1} b_c(h, h) \\
&\leq b_c(f, f) = (E_1(A) + c) b_c(g, g) \\
&\leq (E_1(A) + c)(a_c(g, g) + s) = (E_1(A) + c)(1 + s),
\end{aligned}
$$

and hence, $E_1(B) = \min \sigma(B) \leq E_1(A) + (E_1(A) + c)s \leq E_1(A) + cs$. $\qquad \square$

Remark 8. a) Of course, changing the roles of A and B, we also get a lower bound for $E_1(B)$.
b) The smaller c is, the better estimate (4) is. In general, the smallest c is not known. However, if one knows (approximately) $E_1(A)$ and any constant c satisfying the hypothesis of the previous theorem and cs is sufficiently small, then one may use (4) repeatedly in order to obtain smaller and smaller constants c in the estimate (4) and hence better estimates for $E_1(B)$.

5. Convergence of the sesquilinear forms

The aim of this section is to present a quantitative version of the result presented in Theorem 1 above.

Lemma 9 ([10, Proof of Theorem 3]). *Let μ and μ_n, $n \in \mathbb{N}$, be finite Radon measures on $\mathbb{R}$ such that the sequence (μ_n) converges weakly to μ. Then there exists a common lower bound c for a_μ and all a_{μ_n} and*

$$\sup_{g \in H^1(\mathbb{R}), (a_\mu)_{1-c}(g, g) = 1} |(a_\mu - a_{\mu_n})(g, g)| \leq 2 \sup_{g \in H^1(\mathbb{R}), \|g\|_{H^1(\mathbb{R})} \leq 1} |(a_\mu - a_{\mu_n})(g, g)|.$$

Proposition 10 ([10, Lemma 2]). *Let ν and μ be finite Radon measures on $\mathbb{R}$. Then, for each $g \in H^1(\mathbb{R})$*

$$|a_\mu(g, g) - a_\nu(g, g)| = \left| \int_\mathbb{R} |g|^2 d(\mu - \nu) \right| \leq \|g\|_{H^1}^2 \frac{2}{\sqrt{\pi}} \left(\int_\mathbb{R} \frac{1}{1 + t^2} |\hat{\mu}(t) - \hat{\nu}(t)|^2 dt \right)^{1/2}.$$

In particular, if the finite Radon measures μ_n on $\mathbb{R}$ converge weakly to μ and the forms a_{μ_n} have a common lower bound c, then the forms a_{μ_n} converge to the form a_μ, and

$$\sup_{g \in H^1(\mathbb{R}), (a_\mu)_{1-c}(g, g) = 1} |a_\mu(g, g) - a_{\mu_n}(g, g)| \leq \frac{4}{\sqrt{\pi}} \left(\int_\mathbb{R} \frac{1}{1 + t^2} |\hat{\mu}(t) - \hat{\mu}_n(t)|^2 dt \right)^{1/2} \to 0$$

for $n \to \infty$.

The proposition provides an upper bound for the error one makes by truncating the potential.

Corollary 11. *Let μ be a finite Radon measure on $\mathbb{R}$ and $B \subset \mathbb{R}$ be a Borel set. Then*

$$|a_\mu(g, g) - a_{\chi_B \mu}(g, g)| \leq 2\|g\|_{H^1}^2 |\mu|(\mathbb{R} \setminus B) \tag{5}$$

for every $g \in H^1(\mathbb{R})$.

Proof. For every $t \in \mathbb{R}$

$$|\hat{\mu}(t) - \widehat{\chi_B \mu}(t)| = \left| \int_\mathbb{R} e^{itx} 1_{\mathbb{R} \setminus B}(x) d\mu(x) \right| \leq |\mu|(\mathbb{R} \setminus B),$$

and hence, the corollary follows from the previous theorem with $\nu = 1_B \mu$. $\qquad \square$

6. Weak approximation of measures by pure point measures

Given a finite Radon measure μ on $\mathcal{B}(\mathbb{R})$, we want to give a constructive way to approximate it by pure point measures. For this, it is justified by Corollary 11 to assume that μ has compact support. One can of course decompose μ into a continuous and a discrete part,

$$\mu = \mu_c + \mu_d,$$

where $\mu_d = \sum_{j=1}^{\infty} \alpha_j \delta_{x_j}$ for pairwise different $x_j \in \mathbb{R}$, $(\alpha_j) \in \ell^1(\mathbb{N}, \mathbb{R})$ and μ_c has a continuous cumulative distribution function $F_{\mu_c}(x) = \mu_c((-\infty, x])$. Both parts will be approximated separately. First, observe that using $\mu_d^n = \sum_{j=1}^{n} \alpha_j \delta_{x_j}$, one easily sees that μ_d^n converges weakly to μ_d and the following error estimate for the Fourier transforms of the measures follows directly:

$$|\hat{\mu}_d(t) - \hat{\mu}_d^n(t)| \leq \sum_{j=n+1}^{\infty} |\alpha_j|.$$

Now, let us assume that the measure μ is purely continuous. Further, assume that μ is supported inside the interval $[-K, K]$ for some sufficiently large $K > 0$. For convenience, we may assume that $K \in \mathbb{N}$. For $N \in \mathbb{N}$, we set

$$x_j^N := -K + \frac{j}{N}, \quad j = 0, \dots, 2NK,$$
$$a_j^N(\mu) := F_\mu(x_j) - F_\mu(x_{j-1}) = \mu(x_{j-1}, x_j), \quad j = 1, \dots, 2NK$$

and

$$\mu_N := \sum_{j=1}^{2NK} a_j^N(\mu) \delta_{x_j^N}.$$

It is easy to verify that F_{μ_N} converges pointwise to F_μ and hence μ_N converges weakly to μ. The following proposition gives an error estimate in terms of the Fourier transforms:

Proposition 12. *Let μ be a finite Radon measure on $\mathbb{R}$ with $\mathrm{supp}(\mu) \subset [-K, K]$ and continuous cumulative distribution function and let μ_N be constructed as above. Let $t \in \mathbb{R} \setminus \{0\}$ and $\varepsilon > 0$. Choose $N \in \mathbb{N}$ such that $\frac{1}{N} < \frac{\pi}{2|t|} \min\{1, \frac{\varepsilon^2}{2}\}$. Then*

$$|\widehat{\mu}(t) - \widehat{\mu}_N(t)| \leq \varepsilon |\mu|(\mathbb{R}).$$

Proof. First, observe that for given $t \neq 0$, $\delta_\varepsilon(t) = \frac{\pi}{2|t|} \min\{1, \frac{\varepsilon^2}{2}\}$ is a possible choice of δ for the uniform continuity of the function $x \mapsto e^{itx}$ and given $\varepsilon > 0$. The result follows from the following computations:

$$|\widehat{\mu}(t) - \widehat{\mu}_N(t)| = \left| \int_{\mathbb{R}} e^{itx} d\mu(x) - \int_{\mathbb{R}} e^{itx} d\mu_N(x) \right|$$

$$= \left| \int_{\mathbb{R}} e^{itx} d\mu(x) - \sum_{j=1}^{2NK} \mu((x_{j-1}, x_j)) e^{itx_j} \right|$$

$$= \left| \sum_{j=1}^{2NK} \int_{(x_{j-1}, x_j)} e^{itx} - e^{itx_j} d\mu(x) \right|$$

$$\leq \sum_{j=1}^{2NK} \int_{(x_{j-1}, x_j)} \underbrace{|e^{itx} - e^{itx_j}|}_{\leq \varepsilon} d|\mu|(x)$$

$$\leq \varepsilon |\mu|(\mathbb{R}).$$

$\square$

Given any $\widetilde{K} > 0$ and any $\delta > 0$, one can choose N such that $|\hat{\mu}(t) - \hat{\mu}_N(t)| < \delta$ for every $t \in [-\widetilde{K}, \widetilde{K}]$. In fact, in the preceding proposition, one simply has to choose $\varepsilon > 0$ sufficiently small and then N sufficiently large. For the final error estimate, we need not to give bounds for $|\hat{\mu}(t) - \hat{\mu}_N(t)|$, but for the integral occuring in Proposition 10. This bound is discussed now. Observe that the assumption $|\mu_N|(\mathbb{R}) \le |\mu|(\mathbb{R})$ is always fulfilled for our construction.

Proposition 13. *Let μ and ν be finite Radon measures on $\mathbb{R}$ with $|\nu|(\mathbb{R}) \le |\mu|(\mathbb{R})$. Let $\widetilde{K}$ and ε be any positive real numbers and suppose, in addition, that $|\hat{\mu}(t) - \hat{\nu}(t)| < \varepsilon$ for every t in the interval $[-\widetilde{K}, \widetilde{K}]$. Then*

$$\int_{\mathbb{R}} \frac{1}{1+t^2} |\hat{\mu}(t) - \hat{\nu}(t)|^2 dt \le \varepsilon^2 \pi + 8|\mu|(\mathbb{R})^2 \operatorname{atan}\left(\frac{1}{\widetilde{K}}\right).$$

Proof. We use

$$\int_{\mathbb{R}} \frac{1}{1+t^2} |\hat{\mu}(t) - \hat{\nu}(t)|^2 dt = \int_{-\infty}^{-\widetilde{K}} \frac{1}{1+t^2} |\hat{\mu}(t) - \hat{\nu}(t)|^2 dt + \int_{-\widetilde{K}}^{\widetilde{K}} \frac{1}{1+t^2} |\hat{\mu}(t) - \hat{\nu}(t)|^2 dt + \int_{\widetilde{K}}^{\infty} \frac{1}{1+t^2} |\hat{\mu}(t) - \hat{\nu}(t)|^2 dt,$$

and estimate the three integrals separately, where the estimates for the first and the third integral are identical. For the first integral

$$\int_{-\infty}^{-\widetilde{K}} \frac{1}{1+t^2} |\hat{\mu}(t) - \hat{\nu}(t)|^2 dt \le (2|\mu|(\mathbb{R}))^2 \int_{-\infty}^{-\widetilde{K}} \frac{1}{1+t^2} dt = 4|\mu|(\mathbb{R})^2 \left(\operatorname{atan}(-\widetilde{K}) + \frac{\pi}{2}\right) = 4|\mu|(\mathbb{R})^2 \operatorname{atan}\left(\frac{1}{\widetilde{K}}\right),$$

and for the second integral

$$\int_{-\widetilde{K}}^{\widetilde{K}} \frac{1}{1+t^2} |\hat{\mu}(t) - \hat{\nu}(t)|^2 dt \le \varepsilon^2 \int_{-\widetilde{K}}^{\widetilde{K}} \frac{1}{1+t^2} dt \le \varepsilon^2 \pi.$$

$\square$

7. Eigenvalues of $-\Delta + \sum_j \alpha_j \delta_{x_j}$

Let $x_1 < x_2 < \ldots < x_k$ and $\alpha_j \in \mathbb{R}$ for $j = 1, 2, \ldots, k$. As it is well known, the domain of the operator $-\Delta + \sum_{j=1}^{k} \alpha_j \delta_{x_j}$ (using the notation $x_0 = -\infty$ and $x_{k+1} = \infty$) is given by

$$D\left(-\Delta + \sum_{j=1}^{k} \alpha_j \delta_{x_j}\right) = \left\{f \in H^1(\mathbb{R}) \cap \bigoplus_{j=0}^{k} H^2((x_j, x_{j+1})); f'(x_j+) - f'(x_j-) = \alpha_j f(x_j) \text{ for } j = 1, \ldots, k\right\},$$

and the operator is just acting as $f \mapsto -f''$. As it can easily be seen, such operators can only have negative eigenvalues. For the readers convenience, we will now repeat an algorithm to find the eigenvalues of such an operator (cf. [9, proof of Theorem II 2.1.3]). Each eigenfunction f_λ for an eigenvalue $\lambda < 0$ of the operators needs to be of the form

$$f_\lambda(x) = a_j e^{\sqrt{-\lambda} x} + b_j e^{-\sqrt{-\lambda} x}, \quad x_j < x < x_{j+1}$$

for some constants $a_j, b_j \in \mathbb{R}$. Since the function needs to be in $L^2(\mathbb{R})$, it is necessary that $b_0 = 0$. By linearity, we may also assume $a_0 = 1$ (since $a_0 = 0$ would imply $f_\lambda = 0$). Such a function is in the domain of the operator (and hence an eigenfunction) if and only if it satisfies all the continuity and δ-boundary conditions, i.e.

$$f_\lambda(x_j+) = f_\lambda(x_j-),$$
$$f'_\lambda(x_j+) - f'_\lambda(x_j-) = \alpha_j f_\lambda(x_j),$$

for $j = 1, \ldots, k$ (and $a_k = 0$, which we will ignore for a short moment). Starting with $a_0 = 1, b_0 = 0$, these two conditions give a 2×2 system of linear equations at x_1 for a_1, b_1, which one can easily solve. Continuing with the conditions at x_2, one gets equations for a_2, b_2, and so on. In the end, one computes all the a_j and b_j such that the continuity and boundary-conditions are automatically fulfilled. However, in general, one will obtain $a_k \ne 0$. One can easily see that λ is an eigenvalue if and only if the a_k obtained by this method is equal to 0 (only then we have $f_\lambda \in L^2(\mathbb{R})$). Hence, we consider the a_k computed in the above manner as a function of λ. This $a_k(\lambda)$

depends continuously on $\lambda < 0$. The problem of finding a negative eigenvalue of $-\Delta + \sum \alpha_j \delta_{x_j}$ reduces to finding the zero of the continuous real-valued function $a_k(\lambda)$, which may be solved numerically. Observe that the runtime of the evaluation of $a_k(\lambda)$ depends only linearly on k (at each x_j we need to solve a 2×2 system of linear equations).

8. Existence of negative eigenvalues

It is crucial for our approximation method that there exist negative eigenvalues of the approximating operator. Hence, we will add a short discussion about the existence of negative eigenvalues for operators $-\Delta + \mu$. Recall (Theorem 5 above) that $\sigma_{ess}(-\Delta + \mu) = [0, \infty)$ for each finite Radon measure μ. In light of this result, for the existence of a negative eigenvalue of $-\Delta + \mu$, it suffices to show that there is a function $f \in H^1(\mathbb{R})$ with $a_\mu(f, f) < 0$. This directly gives the following well known result, which we quickly prove for completeness.

Proposition 14. *If the finite Radon measure μ satisfies $\mu(\mathbb{R}) < 0$, then $-\Delta + \mu$ has at least one negative eigenvalue.*

Proof. For $N \in \mathbb{N}$, consider the function f_N as pictured in Fig. 1. For N large enough,

$$a_\mu(f_N, f_N) = \int_{\mathbb{R}} |f_N'(x)|^2 dx + \int_{\mathbb{R}} |f_N|^2 d\mu < 0.$$
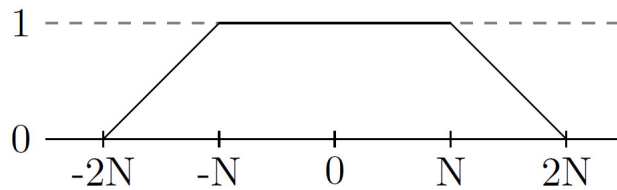
FIG. 1. The function f_N

□

Remark 15. If μ is a finite Radon measure with $\mu(\mathbb{R}) < 0$ and (μ_n) is a sequence of such measures converging weakly to μ, then it is easy to see that $\mu_n(\mathbb{R}) < 0$ for large n. In particular, if the approximation is good enough, then there exists a negative approximating eigenvalue of the Schrödinger operator $-\Delta + \mu_n$ approximating $-\Delta + \mu$. Therefore, under the assumption $\mu(\mathbb{R}) < 0$ our approximation scheme described above always works.

We will discuss some other results concerning the existence of negative eigenvalues here. First, we will recall some well known results extending the above Proposition 14 in some sense.

Theorem 16 ([16, Lemma 8]). *If $V \in C(\mathbb{R})$ with $V(x) \to 0$ as $|x| \to \infty$, $V \not\equiv 0$ and $\int_{\mathbb{R}} V(x)dx \leq 0$, then $-\Delta + V$ has at least one negative eigenvalue.*

Theorem 17 ([17, Theorem 2.5]). *Let $V(x)$ be a measurable function such that $\int_{\mathbb{R}} (1 + |x|^2)|V(x)|dx < \infty$, $V \not\equiv 0$ and $\int_{\mathbb{R}} V(x)dx \leq 0$. Then $-\Delta + V$ has at least one negative eigenvalue.*

It is unknown to the authors whether the above two results extend to one-dimensional Schrödinger operators with measure potentials. If similar results for Schrödinger operators with point interaction potentials hold, this would increase the applicability of our method.

It is easy to construct a continuous function $V \in L^1(\mathbb{R})$ such that $\int_{\mathbb{R}} V(x)dx = 0$ but $\int_{[-c,c]} V(x)dx > 0$ for all $c > 0$ and the assumptions for one of the above two theorems are fulfilled. Then, $-\Delta + V$ has a negative eigenvalue, but Proposition 14 is no longer sufficient to guarantee the existence of negative eigenvalues of the approximating Schrödinger operators. Hence, we will now discuss some other existence criteria for negative eigenvalues of operators $-\Delta + \sum_j \alpha_j \delta_{x_j}$ which are not covered by the above results. Although we are particularly

interested in the case of finitely many point interactions, the same results hold in case for infinitely many point interactions by the same proofs, i.e if we assume $\alpha_j, x_j \in \mathbb{R}$ for all $j \in \mathbb{Z}$, $\sum\limits_{j=-\infty}^{\infty} |\alpha_j| < \infty$ and the sequence $(x_j)_j$ is increasingly ordered. Nevertheless, we only formulate the results for finitely many point interactions.

Proposition 18. *Let $\alpha_j, x_j \in \mathbb{R}$ for $j = 1, \ldots, n$ and assume $x_1 < x_2 < \ldots < x_n$. Further, assume $a_k < 0$ for some $k \in \{1, \ldots, n\}$ and denote $d_k^- = x_k - x_{k-1}$ and $d_k^+ = x_{k+1} - x_k$ (with $d_k^- = \infty$ for $k = 1$ and $d_k^+ = \infty$ for $k = n$). If*

$$\frac{1}{d_k^-} + \frac{1}{d_k^+} < -\alpha_k,$$

then $-\Delta + \sum\limits_{j=1}^{n} \alpha_j \delta_{x_j}$ has at least one negative eigenvalue.
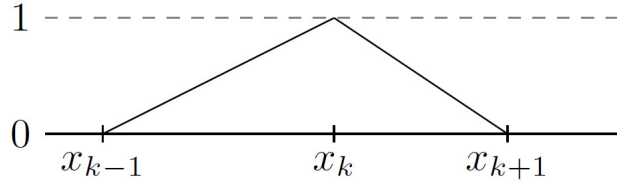
FIG. 2. The function f_{x_k}

Proof. For $d_k^-, d_k^+ < \infty$ consider f_{x_k} as pictured in Fig. 2. Then

$$a_{\sum_j \alpha_j \delta_{x_j}}(f_{x_k}, f_{x_k}) = \int\limits_{\mathbb{R}} |f_{x_k}'(x)|^2 dx + \sum\limits_{j=1}^{n} \alpha_j |f_{x_k}(x_j)|^2 = \frac{1}{d_k^-} + \frac{1}{d_k^+} + \alpha_k < 0.$$

The cases $d_k^- = \infty$ or $d_k^+ = \infty$ work similarly. $\square$

Proposition 19. *Let $\alpha_j, x_j \in \mathbb{R}$ for $j = 1, \ldots, n$ and assume $x_1 < \ldots < x_n$. Further, assume $a_k < 0$ for some $k \in \{1, \ldots, n\}$. If*

$$\frac{\alpha_k}{2} e^{-\alpha_k x_k} + \sum\limits_{x_j < x_k} \alpha_j e^{-\alpha_k x_j} + e^{-2\alpha_k x_k} \sum\limits_{x_j > x_k} \alpha_j e^{\alpha_k x_j} < 0,$$

then $-\Delta + \sum\limits_{j} \alpha_j \delta_{x_j}$ has at least one negative eigenvalue.

Proof. The function

$$f(x) = \begin{cases} e^{-\frac{\alpha_k}{2} x}, & x < x_k, \\ e^{-\alpha_k x_k} e^{\frac{\alpha_k}{2} x}, & x > x_k, \end{cases}$$

is an eigenfunction of $-\Delta + \alpha_k \delta_{x_k}$ to the eigenvalue $-\frac{\alpha_k^2}{4}$. Hence,

$$
\begin{aligned}
a_{\sum_j \alpha_j \delta_{x_j}}(f, f) &= \int\limits_{\mathbb{R}} |f'(x)|^2 dx + \alpha_k |f(x_k)|^2 + \sum\limits_{x_j < x_k} \alpha_j |f(x_j)|^2 + \sum\limits_{x_j > x_k} \alpha_j |f(x_j)|^2 \\
&= \langle (-\Delta + \alpha_k \delta_{x_k}) f, f \rangle + \sum\limits_{x_j < x_k} \alpha_j |f(x_j)|^2 + \sum\limits_{x_j > x_k} \alpha_j |f(x_j)|^2 \\
&= -\frac{\alpha_k^2}{4} \|f\|^2 + \sum\limits_{x_j < x_k} \alpha_j |f(x_j)|^2 + \sum\limits_{x_j > x_k} \alpha_j |f(x_j)|^2 \\
&= \frac{\alpha_k}{2} e^{-\alpha_k x_k} + \sum\limits_{x_j < x_k} \alpha_j e^{-\alpha_k x_j} + e^{-2\alpha_k x_k} \sum\limits_{x_j > x_k} \alpha_j e^{\alpha_k x_j} < 0.
\end{aligned}
$$

$\square$

9. Numerical examples

We want to continue with the presentation of two numerical examples. The following result will be useful to understand the examples, where $N_0(-\Delta + \mu)$ denotes the number of negative eigenvalues of the operator $-\Delta + \mu$ (counting multiplicities).

Theorem 20 ([15, Theorem 3.5]). *Let $\mu = \mu_+ - \mu_-$ be a finite Radon measure on $\mathbb{R}$ with corresponding Hahn–Jordan decomposition. Then*

$$N_0(-\Delta + \mu) \leq 1 + \frac{1}{2} \frac{\int_{\mathbb{R}} \int_{\mathbb{R}} |x - y| d\mu_-(x) d\mu_-(y)}{\mu_-(\mathbb{R})}.$$

9.1. Square well potential

The first example is well known, since it is essentially solvable. Hence, it will play the role of a test scenario. Consider the operator $-\Delta - \chi_{[-1,1]}$, i.e. the Schrödinger operator with a square well potential. By Proposition 14 and Theorem 20,

$$1 \leq N_0(-\Delta - \chi_{[-1,1]}) \leq 1 + \frac{2}{3}.$$

Further, the only negative eigenvalue λ satisfies $-1 < \lambda < 0$ and the equation

$$\tan \lambda = \frac{\sqrt{1 - \lambda^2}}{\lambda},$$

(see e.g. [18, Chapter 7.4]). By solving this equation numerically, one obtains

$$\lambda \approx -0.453753165860328.$$

For $N \in \mathbb{N}$ we get the Nth approximating operator $-\Delta + \sum_{j=1}^{2N} \alpha_j^N \delta_{x_j^N}$ given by

$$x_j^N = -1 + \frac{j}{N}, \quad j = 1, \ldots, 2N;$$

$$\alpha_j^N = -\frac{1}{N}, \quad j = 1, \ldots, 2N.$$

The negative eigenvalue for the Nth approximating operator, found by the procedure described in section 7 implemented in Matlab, can be seen in Table 1.

9.2. Cantor measure potential

The second example is supposed to show that our methods also work with respect to rather exotic potentials. Let μ_C be the Cantor measure, i.e. the measure which has the Cantor function as its cumulative distribution function. We want to find eigenvalues of the operator $-\Delta - \mu_C$. Using again Proposition 14 and Theorem 20 one gets

$$1 \leq N_0(-\Delta - \mu_C) \leq 1 + \frac{1}{2},$$

i.e. the operator has exactly one negative eigenvalue. While it is possible to approximate this eigenvalue of $-\Delta - \mu_C$ by the method described in section 6, we modify the approach here to obtain better results for this particular case. As it is well known, the Cantor set can be obtained as the limit set of a procedure of removing middle third intervals. Inspired by this, one can construct the Cantor measure easily as the limit of a sequence of pure point measures as follows: Let μ_N be the measures defined by (cf. Fig. 3)

$$\Lambda_0 = \left\{ \frac{1}{2} \right\},$$

$$\Lambda_N = \left\{ \frac{x}{3}; x \in \Lambda_{N-1} \right\} \cup \left\{ 1 - \frac{x}{3}; x \in \Lambda_{N-1} \right\}, \quad N \in \mathbb{N}$$

$$\mu_N = \frac{1}{2^N} \sum_{x \in \Lambda_N} \delta_x, \quad N \in \mathbb{N}.$$

It is easy to show that the μ_N converge to μ_C weakly for $N \to \infty$, e.g. by proving that the cumulative distribution functions converge pointwise. Hence, the negative eigenvalues of the operators $-\Delta - \mu_N$ converge to the eigenvalue of $-\Delta - \mu_C$. The numerically computed eigenvalues of $-\Delta - \mu_N$ can be seen, for some N, in Table 2. We will not give a full discussion of the error estimate of this modified method here, but we will compute

TABLE 1. Approximation of eigenvalue of $-\Delta - \chi_{[-1,1]}$

N	Eigenvalue
1	-0.545877203227244
2	-0.474617739449437
3	-0.462861650386081
4	-0.458844821756164
5	-0.457002447176188
10	-0.454562375073084
25	-0.453882500447814
50	-0.453785494551346
75	-0.453767533759611
100	-0.453761247723386
1000	-0.453753246677936
10000	-0.453753166668506
100000	-0.453753165868416
1000000	-0.453753165860430
λ	-0.453753165860328
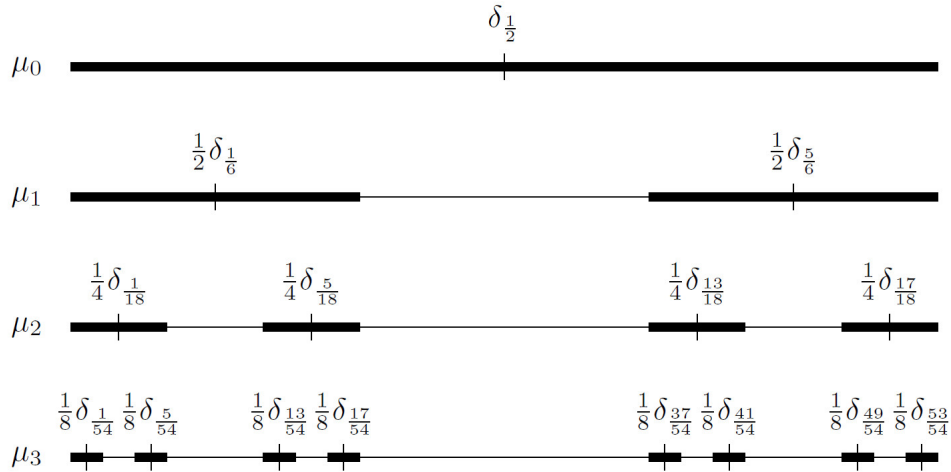
FIG. 3. Construction of the measures μ_N for $N = 0, 1, 2, 3$. The thick black bars are the intervals in the Nth step of the construction of the Cantor set.

$\hat{\mu}_C(t) - \hat{\mu}_N(t)$ in the appendix, which is the crucial step needed for deriving an error estimate (beside the general theory developed above).

10. Extension to other 1-dimensional domains

In this section, we will discuss how to extend Theorem 1 and our approximation method to Schrödinger operators on $L^2([0,\infty))$. Essentially the same ideas work for operators on $L^2(0,1)$ or to some extend even on finite metric graphs (cf. [19] for an introduction to this topic), but we will only discuss the case $[0,\infty)$ in detail. As it is well known, the self-adjoint realizations of the Laplacian on $L^2([0,\infty))$ can be parametrized by $\alpha \in [0, \pi)$

TABLE 2. Approximation of eigenvalue of $-\Delta - \mu_C$

N	Eigenvalue of $-\Delta - \mu_N$
1	-0.25
2	-0.190826516988754
3	-0.182601523317952
4	-0.181236785438422
5	-0.181005430450725
10	-0.180958390783868
15	-0.180958384580303
20	-0.180958384579497

through the boundary conditions

$$D(-\Delta_\alpha) = \{f \in H^2([0,\infty)); \; \cos(\alpha)f(0) + \sin(\alpha)f'(0) = 0\},$$
$$-\Delta_\alpha f = -f''.$$

The sesquilinear form a_α^0 associated to $-\Delta_\alpha$ is given by

$$D(a_\alpha^0) = H^1([0,\infty)),$$
$$a_\alpha^0(f,g) = \int\limits_{[0,\infty)} f'(x)\overline{g'(x)}dx - \cot(\alpha)f(0)\overline{g(0)}$$

for $\alpha \neq 0$ and

$$D(a_0^0) = H_0^1([0,\infty)),$$
$$a_0^0(f,g) = \int\limits_{[0,\infty)} f'(x)\overline{g'(x)}dx.$$

Throughout this section, we assume that all occuring measures are finite Radon measures on $[0,\infty)$, i.e. finite signed measures on $\mathcal{B}([0,\infty))$. Without loss of generality, we may assume that the measures have no point mass at 0 (this would only change the boundary condition and not the action of the resulting Schrödinger operator). For such a measure μ we define the Schrödinger operator with boundary conditions corresponding to $\alpha \in [0,\pi)$ and potential μ, $-\Delta_\alpha + \mu$, as the operator associated to the form a_α^μ

$$D(a_\alpha^\mu) = D(a_\alpha^0),$$
$$a_\alpha^\mu(f,g) = a_\alpha^0(f,g) + \int\limits_{[0,\infty)} f\bar{g}d\mu,$$

in the sense of Kato's first representation theorem, where it can easily be seen that a_α^μ is a small form perturbation of $a_{\pi/2}^0$ (or of a_0^0 if $\alpha = 0$) using the Sobolev inequality

$$\forall f \in H^1([0,\infty)) \; \forall \varepsilon > 0 : \|f\|_\infty^2 \le \varepsilon\|f'\|_{L^2}^2 + \frac{4}{\varepsilon}\|f\|_{L^2}^2. \tag{6}$$

Of course the term *boundary conditions* should not be taken too seriously in this setting – e.g. if μ has a singular continuous part in the vicinity of 0, it is completely unclear if the functions in the domain actually fulfill the boundary condition. In what follows we say, in natural analogy to the case of measures on $\mathbb{R}$, that measures μ_n on $[0,\infty)$ converge weakly to the measure μ on $[0,\infty)$ if

$$\int\limits_{[0,\infty)} fd\mu_n \to \int\limits_{[0,\infty)} fd\mu,$$

for all bounded and continuous functions f on $[0,\infty)$.

Theorem 21. *Let μ_n, $n \in \mathbb{N}$ and μ be finite Radon measures on $[0, \infty)$ without point mass at 0. If the μ_n converge weakly to μ, then $-\Delta_\alpha + \mu_n$ converge to $-\Delta_\alpha + \mu$ in the norm resolvent sense.*

Proof. Using the general theory, it suffices again to prove that the corresponding sesquilinear forms converge. Further, it can be shown in the same manner as on $\mathbb{R}$ (cf. Lemma 9 above and the proof in [10]) that we only need to show that

$$\sup_{f \in D(a_\alpha), \|f\|_{H^1([0,\infty))} \le 1} \left| \int_{[0,\infty)} |f|^2 d(\mu - \mu_n) \right| \to 0$$

for $n \to \infty$. Now observe that each function $f \in H^1([0, \infty))$ with $\|f\|_{H^1([0,\infty))} \le 1$ can be continued to a function $\widetilde{f} \in H^1(\mathbb{R})$ such that $\|\widetilde{f}\|_{H^1(\mathbb{R})} \le c$, where c is a constant independend of f. One way of achieving this is by setting

$$\widetilde{f}(x) = \begin{cases} f(x), & x \ge 0, \\ f(0)x + f(0), & -1 \le x < 0, \\ 0, & x < -1 \end{cases}$$

and $c = \sqrt{\dfrac{11}{3}}$,

$$\|\widetilde{f}\|^2_{H^1(\mathbb{R})} = \|f\|^2_{H^1([0,\infty))} + \int_{-1}^0 |f(0)x + f(0)|^2 dx + \int_{-1}^0 |f(0)|^2 dx$$

$$\le 1 + \frac{4}{3}|f(0)|^2 \le 1 + \frac{4}{3}\|f\|^2_\infty$$

$$\le 1 + \frac{8}{3}\|f\|^2_{H^1([0,\infty))} = \frac{11}{3}.$$

For a measure ν on $[0, \infty)$, we denote by ν^* the measure extended to $\mathbb{R}$ by setting it to 0 on $(-\infty, 0)$. Then

$$\sup_{f \in D(a_\alpha), \|f\|_{H^1([0,\infty))} \le 1} \left| \int_{[0,\infty)} |f|^2 d(\mu - \mu_n) \right| = \sup_{f \in D(a_\alpha), \|f\|_{H^1([0,\infty))} \le 1} \left| \int_{\mathbb{R}} |\widetilde{f}|^2 d(\mu^* - \mu_n^*) \right|$$

$$\le \frac{1}{c^2} \sup_{g \in H^1(\mathbb{R}), \|g\|_{H^1(\mathbb{R})} \le 1} \left| \int_{[0,\infty)} |g|^2 d(\mu^* - \mu_n^*) \right|.$$

As $\mu_n^* \to \mu^*$ weakly, this finishes the proof since the last quantity is known to converge to 0 by the results on $\mathbb{R}$. $\qquad\square$

Remark 22. a) Using the same idea, i.e. extending functions from $H^1([0, 1])$ uniformly to functions in $H^1(\mathbb{R})$, one can prove the corresponding theorem for Schrödinger operators on $L^2([0, 1])$. Even further, by the same method one gets the same result for Schrödinger operators on arbitrary finite metric graphs.
b) Using a construction analogous to the one on $\mathbb{R}$, one can easily construct pure point measures μ_N on $[0, \infty)$ approximating a given finite Radon measure μ on $[0, \infty)$ weakly.

It remains to discuss the method of computing the eigenvalues of $-\Delta_\alpha + \sum_{j=1}^n \beta_j \delta_{x_j}$ analogous to the method discussed in section 7. We may assume that the x_j are ordered increasingly, $0 < x_1 < \ldots < x_n$, and $\beta_j \in \mathbb{R}$. One can check that the operator $-\Delta_\alpha + \sum_j \beta_j \delta_{x_j}$ acts as $f \mapsto -f''$ a.e. and that the functions in its domain fulfill the boundary conditions $\cos(\alpha)f(0) + \sin(\alpha)f'(0) = 0$ and the usual continuity and δ boundary conditions at all x_j. Then, each eigenfunction f_λ for an eigenvalue $\lambda < 0$ has the form

$$f_\lambda(x) = a_j e^{\sqrt{-\lambda} x} + b_j e^{-\sqrt{-\lambda} x}, \quad x_{j-1} < x < x_j,$$

(with $x_0 = 0$ and $x_{n+1} = \infty$) for coefficients $a_j, b_j \in \mathbb{R}$, $j = 0, \ldots, n$. As in the case on the whole line, such a function is an eigenfunction (and hence λ an eigenvalue) if and only if $a_n = 0$ and it fulfills all boundary conditions. Therefore, let us consider the case $a_0 \ne 0$, from which we may assume $a_0 = 1$. Then, the boundary conditions at 0 uniquely determine b_0. We may now continue as we know it from section 7, computing iteratively the values of a_j and b_j from the values of a_{j-1}, b_{j-1} and the boundary and continuity conditions at x_j. At the

end, we get $a_n = a_n(\lambda)$ as a continuous function of λ and only need to find zeroes of this continuous real-valued function.

We still need to deal with the case $a_0 = 0$. It is easy to verify that for $\alpha = 0, \frac{\pi}{2}$ this never leads to a valid eigenfunction (and hence not to an eigenvalue). Further, if $n = 1$, one can also check that this never results in an eigenvalue. It is unknown to the authors if this case may lead to a negative eigenvalue of $-\Delta_\alpha + \sum_j \beta_j \delta_{x_j}$ for any choice of β_j and x_j. Anyway, this is not a problem: If $\alpha \neq 0, \frac{\pi}{2}$, then we just consider the case $a_0 = 0, b_0 = 1$ separately. From the boundary conditions, one imediately gets $\lambda = -(\cot(\alpha))^2$, hence we only need to check one more value of λ. Iterating now over all x_j, one can quickly check if this λ is an eigenvalue (again, by checking if $a_n(\lambda) = 0$).

Remark 23. a) With the same concept, it is possible to find eigenvalues of $-\Delta + \sum_j \alpha_j \delta_{x_j}$ on $L^2([0,1])$ (with suitable boundary conditions). Of course one can (and will) in this case also get eigenvalues ≥ 0. Here, one also has to use a suitable Ansatz for the eigenfunctions of non-negative eigenvalues.

b) This approach to find eigenvalues of $-\Delta + \sum_j \alpha_j \delta_{x_j}$ will not directly work on most metric graphs. But on certain classes of metric graphs, there are substitutional methods available for computing eigenvalues of Laplacians (and eigenvalues of $-\Delta + \sum_j \alpha \delta_{x_j}$ are just eigenvalues of a Laplacian on a metric graph with a few more vertices).

If such a method exists, our method for approximating eigenvalues of $-\Delta + \mu$ and the error estimates also work.

Appendix: Cantor measure and Fourier transform

Let μ_C be the Cantor measure and

$$\mu_N = \frac{1}{2^N} \sum_{x \in \Lambda_N} \delta_x$$

be the Nth approximating measure, as described above. We want to compute $\hat{\mu}_C(t) - \hat{\mu}_N(t)$. Denoting

$$S_N = \left\{ \frac{1}{2} + \sum_{j=1}^{N} \sigma_j \frac{1}{3^j}; \sigma \in \{-1,1\}^N \right\}$$

we are first going to show that $\Lambda_N = S_N$ for $N = 1, 2, 3, \ldots$. This will follow by induction. For $N = 1$ the relation is obvious. Hence, assume that $S_N = \Lambda_N$. It suffices to prove $\Lambda_{N+1} \subset S_{N+1}$, since clearly $|\Lambda_{N+1}| = 2^{N+1} = |S_{N+1}|$. Let $x \in \Lambda_{N+1}$. Then either

$$x = \frac{y}{3} \quad \text{or } x = 1 - \frac{y}{3}$$

for some $y \in \Lambda_N$. Assume the first case is true (the other case can be dealt with in the same way). Then, since $\Lambda_N = S_N$, for some $\sigma \in \{-1,1\}^N$

$$x = \frac{\frac{1}{2} + \sum_{j=1}^{N} \sigma_j \frac{1}{3^j}}{3} = \frac{1}{6} + \sum_{j=1}^{N} \sigma_j \frac{1}{3^{j+1}} = \frac{1}{2} - \frac{1}{3} + \sum_{j=1}^{N} \sigma_j \frac{1}{3^{j+1}} = \frac{1}{2} + \sum_{j=1}^{N+1} \tilde{\sigma}_j \frac{1}{3^j} \in S_{N+1}$$

with

$$\tilde{\sigma} = (-1, \sigma_1, \sigma_2, \ldots, \sigma_N) \in \{-1,1\}^{N+1}$$

and therefore $x \in S_{N+1}$.

In what follows, we will need the following trigonometric identity:

$$\prod_{j=1}^{N} \cos(\varphi_j) = \frac{1}{2^N} \sum_{\sigma \in \{-1,1\}^N} \cos(\sigma_1 \varphi_1 + \cdots + \sigma_N \varphi_N), \quad \text{for } \varphi_j \in \mathbb{R}, \ j = 1, \ldots, N. \tag{7}$$

The case $N = 2$ of this identity is a direct consequence of the angle sum identity for cosine, the general case follows easily by induction.

Now, we will compute the Fourier transform of μ_N:

$$\hat{\mu}_N(t) = \frac{1}{2^N} \sum_{x \in S_N} \hat{\delta}_x(t) = \frac{1}{2^N} \sum_{x \in S_N} e^{itx}$$

$$= \frac{1}{2^N} e^{\frac{1}{2}it} \sum_{\sigma \in \{-1,1\}^N} e^{it(\sigma_1 \frac{1}{3} + \sigma_2 \frac{1}{3^2} + \cdots + \sigma_N \frac{1}{3^N})}$$

$$= \frac{1}{2^N} e^{\frac{1}{2}it} \sum_{\sigma \in \{-1,1\}^N, \sigma_N = 1} e^{it(\sigma_1 \frac{1}{3} + \sigma_2 \frac{1}{3^2} + \cdots + \sigma_N \frac{1}{3^N})} + e^{-it(\sigma_1 \frac{1}{3} + \sigma_2 \frac{1}{3^2} + \cdots + \sigma_N \frac{1}{3^N})}$$

$$= \frac{1}{2^{N-1}} e^{\frac{1}{2}it} \sum_{\sigma \in \{-1,1\}^N, \sigma_N = 1} \cos\left(t(\sigma_1 \frac{1}{3} + \sigma_2 \frac{1}{3^2} + \cdots + \sigma_{N-1} \frac{1}{3^{N-1}} + \sigma_N \frac{1}{3^N})\right)$$

$$= \frac{1}{2^{N-1}} e^{\frac{1}{2}it} \sum_{\sigma \in \{-1,1\}^N, \sigma_N = 1} \frac{1}{2}\Big(\cos\left(t(\sigma_1 \frac{1}{3} + \sigma_2 \frac{1}{3^2} + \cdots + \sigma_{N-1} \frac{1}{3^{N-1}} + \sigma_N \frac{1}{3^N})\right)$$

$$+ \cos\left(-t(\sigma_1 \frac{1}{3} + \sigma_2 \frac{1}{3^2} + \cdots + \sigma_{N-1} \frac{1}{3^{N-1}} + \sigma_N \frac{1}{3^N})\right)\Big)$$

$$= \frac{1}{2^N} e^{\frac{1}{2}it} \sum_{\sigma \in \{-1,1\}^N} \cos\left(\sigma_1 \frac{t}{3} + \sigma_2 \frac{t}{3^2} + \cdots + \sigma_N \frac{t}{3^N}\right)$$

$$= e^{\frac{1}{2}it} \prod_{j=1}^{N} \cos\left(\frac{t}{3^j}\right).$$

Here, we used formula (7) in the last step. Summarizing, we get

$$\hat{\mu}_N(t) = e^{\frac{1}{2}it} \prod_{j=1}^{N} \cos\left(\frac{t}{3^j}\right).$$

Since the μ_N converge weakly to μ_C, the Fourier transforms converge pointwise. We get the well-known result

$$\hat{\mu}_C(t) = e^{\frac{1}{2}it} \prod_{j=1}^{\infty} \cos\left(\frac{t}{3^j}\right).$$

Observe that it seems, in light of the form of the Fourier transforms, that the most natural way to construct the Cantor measure actually may be as the limit of the measures μ_N. For the difference $\hat{\mu}_C(t) - \hat{\mu}_N(t)$ we get

$$\hat{\mu}_C(t) - \hat{\mu}_N(t) = e^{\frac{1}{2}it} \prod_{j=1}^{N} \cos\left(\frac{t}{3^j}\right)\Big(\prod_{j=N+1}^{\infty} \cos\left(\frac{t}{3^j}\right) - 1\Big),$$

which converges fast to 0 uniformly on compact intervals.

Acknowledgements

References

[1] BelHadjAli H., BenAmor A., Brasche J. Large Coupling Convergence: Overview and New Results. In *Partial Differential Equations and Spectral Theory* (Demuth M., Schulze B.-W., Witt I., editors), volume 211 of *Operator Theory: Advances and Applications*, pp. 73–117. Springer Basel, Basel, 2011.

[2] Brasche J. On large coupling convergence within trace ideals. *Methods Funct. Anal. Topology*, 2014, **20**, P. 3–9.

[3] Belgacem F., BelHadjAli H., BenAmor A., Thabet A. The Robin Laplacian in the large coupling limit: Convergence and spectral asymptotic. available on arXiv: 1511.06086.

[4] BelHadjAli H., BenAmor A., Brasche J. On trace and Hilbert-Schmidt norm estimates. *Bull. London Math. Soc.*, 2012, **44**, P. 661–674.

[5] BelHadjAli H., BenAmor A., Brasche J. Large coupling convergence with negative perturbations. *J. Math. Anal. Appl.*, 2014, **409**, P. 582–597.

[6] Ben Amor A., Brasche J. Sharp estimates for large coupling convergence with applications to Dirichlet operators. *J. Funct. Anal.*, 2008, **254**, P. 454–475.

[7] Brasche J., Demuth M. Dynkin's formula and large coupling convergence. *J. Funct. Anal.*, 2005, **219**, P. 34–69.

[8] Grubišić L. Relative Convergence Estimates for the Spectral Asymptotic in the Large Coupling Limit. *Integral Equations Operator Theory*, 2009, **65**, P. 51–81.

[9] Albeverio S., Gesztesy F., Høegh-Krohn R., Holden H. *Solvable Models in Quantum Mechanics*. AMS Chelsea Publishing, 2nd edition, 2005.

[10] Brasche J., Figari R., Teta A. Singular Schrödinger Operators as Limits Point Interaction Hamiltonians. *Potential Anal.*, 1998, **8**, P. 163–178.

[11] Brasche J., Ožanová K. Convergence of Schrödinger Operators. *SIAM J. Math. Anal.*, 2007, **39**, P. 281–297.

[12] Ožanová K. Approximation by point potentials in a magnetic field. *J. Phys. A: Math. Gen.*, 2006, **39**, P. 3071–3083.

[13] Kato T. *Perturbation Theory for Linear Operators*. Springer, 2nd edition, 1976.

[14] Reed M., Simon B. *Methods of Modern Mathematical Physics 1: Functional Analysis*. Academic Press, 1972.

[15] Brasche J., Exner P., Kuperin Y., Šeba P. Schrödinger Operators with Singular Interactions. *J. Math. Anal. Appl.*, 1994, **184**, P. 112–139.

[16] Schmincke U.-W. On Schrödinger's factorization method for Sturm-Liouville operators. *Proc. Roy. Soc. Edinburgh Sect. A*, 1978, **80**, P. 67–84.

[17] Simon B. The Bound State of Weakly Coupled Schrödinger Operators in One and Two Dimensions. *Ann. Phys.*, 1976, **97**, P. 279–288.

[18] Gustafson S., Sigal I. *Mathematical Concepts of Quantum Mechanics*. Springer, 2nd edition, 2011.

[19] Berkolaiko G., Kuchment P. *Introduction to Quantum Graphs*, volume 186 of *Mathematical Surveys and Monographs*. American Mathematical Society, 2013.

Solvable models of quantum beating

R. Carlone[1], R. Figari[2], C. Negulescu[3], L. Tentarelli[4]

[1]Università "Federico II" di Napoli, Dipartimento di Matematica e Applicazioni "R. Caccioppoli",
MSA, via Cinthia, I-80126, Napoli, Italy

[2]Università "Federico II" di Napoli, Dipartimento di Fisica e INFN Sezione di Napoli,
MSA, via Cinthia, I-80126, Napoli, Italy

[3]Université de Toulouse & CNRS, UPS, Institut de Mathématiques de Toulouse UMR 5219
F-31062 Toulouse, France

[4]Sapienza Università di Roma, Dipartimento di Matematica, Piazzale Aldo Moro, 5, 00185, Roma, Italy

raffaele.carlone@unina.it, rodolfo.figari@na.infn.it,
claudia.negulescu@math.univ-toulouse.fr, tentarelli@mat.uniroma1.it

We review some results about the suppression of quantum beating in a one dimensional nonlinear double well potential. We implement a single particle double well potential model, making use of nonlinear point interactions. We show that there is complete suppression of the typical beating phenomenon characterizing the linear quantum case.

1. Introduction

In the last decades, the quantum beating phenomenon has become a subject of great interest in different areas of quantum physics, ranging from quantum electrodynamics to particle physics, from solid state physics to molecular structure and dynamics.

Quantum beating was first experimentally observed in 1935 as a periodic inversion of the nitrogen atom with respect to the hydrogen atoms plane in the ammonia molecule. The phenomenon was then theoretically investigated examining the one dimensional dynamics of a quantum particle in a double well potential, the simplest example of a bistable potential. In Fig. 1, the two minima correspond to the average positions of the nitrogen atom in the two symmetric states.
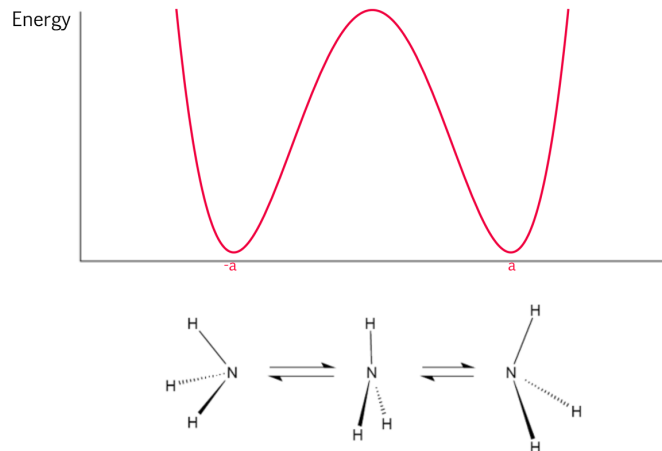
FIG. 1. Schematical representation of Ammonia molecule.

The ammonia molecule is pyramidally shaped. Three hydrogen atoms form the base and the nitrogen atom is located in one of the two distinguishable states (enantiomers) on one side or the other with respect to the base (chirality). The experiments on liquid ammonia showed that microwave radiation could induce a periodic transition

from one state to the other (quantum beating). It was also observed that the periodic nitrogen inversion was absent whenever the molecule was part of a large organic structure or the pressure was too high.

Many authors used an effective nonlinear potential, superimposed on the double well, to model the interaction of the single molecule with the outside structure (see [1–4]).

The beating phenomenon for a particle in a double well potential is expected to be visible when the ground state and the first excited state have very close energies, forming an almost single, degenerate, energy level. A superposition of these two states will evolve, concentrating periodically inside one well or the other, with a frequency proportional to the energy difference (see section 2.2 below).

When a nonlinear effective potential is assumed to model the interaction with the environment the dynamics to be investigated is the nonlinear Schrödinger equation:

$$\imath\hbar\frac{\partial\psi}{\partial t} = -\frac{\hbar^2}{2\,m}\frac{\partial^2\psi}{\partial\,x^2} + V(x) + \varepsilon|\psi|^\sigma\psi,$$

where $V(x)$ is a double well potential.

In order to comprehend the beating suppression induced by the environment one needs to prove that the nonlinear interaction destroys the periodic dynamics for all initial conditions, which in turn implies that the particle will be eventually confined to one of the wells (in which well the particle will finally collapse will depend on the specific chosen nonlinearity and/or on the initial conditions).

In a completely symmetric nonlinear double well, Sacchetti proved (see [5]) that for $\sigma = 2$, the result holds true, in the semiclassical approximation (i.e., "$\hbar \to 0$"). Related results were obtained in [6–9] in any dimension assuming a symmetry breaking nonlinear perturbation of the double well potential.

In [10], the beating phenomenon in the case of a linear and nonlinear "point well interactions" (for more, refer to [11]) is analyzed. The main advantage in using point interactions is that explicit solutions for the linear dynamics are available. Moreover, the analysis of the Schrödinger equation in the case of a nonlinear point interaction Hamiltonian can be reduced to the search of the solutions to a system of nonlinear Volterra integral equations for a complex function depending only on time. At least at the level of numerical computation this reduction turns out to be a remarkable simplification.

In this review, we recall first definition and properties of linear and nonlinear point interaction Hamiltonians. In the successive section, we consider a one dimensional Hamiltonian with two attractive point potentials. We examine its spectral properties and characterize the dependence of the energy difference between the ground state and the first exited state on the kinematical and dynamical parameters of the interaction. In this way, we will then be able to write down explicitly the beating solution for any range of parameters and successively to investigate the semiclassical limit.

We then investigate the Cauchy problem for the Schrödinger equation with two nonlinear point well potentials. As already mentioned, the description of the dynamics will be reduced to the analysis of a system of two Volterra integral equations. Based mainly on numerical analysis results, we will discuss the beating suppression.

2. The mathematical model – concentrated nonlinearities

First, we briefly recall the definition of point interaction Hamiltonians in $L^2(\mathbb{R})$ (see [11] for further details). For two point scatterers placed in $Y = \{y_1, y_2\}$ of strength $\underline{\gamma} = \{\gamma_1, \gamma_2\}$, $y_i, \gamma_i \in \mathbb{R}$, the formal Hamiltonian reads:

$$H_{\underline{\gamma},Y}\,\psi := ``-\frac{d^2}{dx^2}\,\psi + \gamma_1\delta_{y_1}\psi + \gamma_2\delta_{y_2}\psi\,", \tag{1}$$

where the (reduced) Planck constant $\hbar$ has been taken equal to one and the particle mass m equal to $1/2$. We will also assume that the two points are placed symmetrically with respect to the origin and that $|y_i| = a$.

The following result holds true (see [11]):

$$D(H_{\underline{\gamma},Y}) := \left\{\psi \in L^2(\mathbb{R}) \mid \psi = \phi^\lambda - \sum_{i,j=1}^{2}\left(\Gamma_{\underline{\gamma}}^\lambda\right)_{ij}^{-1}\phi^\lambda(y_j)G^\lambda(\cdot - y_i),\ \phi^\lambda \in H^2(\mathbb{R})\right\}, \tag{2}$$

$$\left(H_{\underline{\gamma},Y} + \lambda\right)\psi = \left(-\frac{d^2}{dx^2} + \lambda\right)\phi^\lambda, \tag{3}$$

are domain and action of a selfadjoint operator in $L^2(\mathbb{R})$ which acts as the free Laplacian on functions supported outside the two points $y_i = \pm a$. In (2) $G^\lambda(\cdot)$ is the free Laplacian Green function:

$$G^\lambda(x) := \frac{e^{-\sqrt{\lambda}|x|}}{2\sqrt{\lambda}},$$

and the matrix $\Gamma^\lambda_{\underline{\gamma}}$ is defined as:

$$\left(\Gamma^\lambda_{\underline{\gamma}}\right)_{ij} := \frac{1}{\gamma_i}\delta_{ij} + G^\lambda(y_i - y_j),$$

where the positive real number λ is chosen large enough to make the matrix $\Gamma^\lambda_{\underline{\gamma}}$ invertible.

One can immediately verify that the derivative of $G^\lambda(x)$ has a jump in the origin, equal to -1. This in turn implies that every function ψ in the domain satisfies the boundary conditions:

$$\frac{d\psi}{dx}\left(y_j^+\right) - \frac{d\psi}{dx}\left(y_j^-\right) = \gamma_j\,\psi(y_j), \quad j = 1, 2\,. \tag{4}$$

The dynamics generated by $H_{\underline{\gamma},Y}$ is then characterized as the free dynamics outside the two scatterers, satisfying at any time the boundary conditions (4).

Our aim is to investigate the behavior of the solutions of the nonlinear evolution problem:

$$\begin{cases} i\,\dfrac{\partial\psi}{\partial t} = H_{\underline{\gamma}(t),Y}\,\psi\,, & \forall(t,x) \in \mathbb{R}^+ \times \mathbb{R}\,, \\[2mm] \psi(0,x) = \psi_0(x) \in D(H_{\underline{\gamma}(0),Y}), & \forall x \in \mathbb{R}\,, \\[2mm] \gamma_j(t) := \gamma|\psi(t,y_j)|^{2\sigma}, \ \gamma < 0, \ \sigma \geq 0\,. \end{cases} \tag{5}$$

where the time dependence of $\underline{\gamma}$ is nonlinearly determined by the values in $\pm a$ of the solution itself.

There is an alternative way to represent the solutions of the Cauchy problem (5). Let us consider the following ansatz, suggested by the Duhamel's formula applied to the evolution equation (5) using the formal definition (1) for the Hamiltonian,

$$\psi(t,x) = (\mathcal{U}(t)\psi_0)(x) - i\,\gamma\sum_{j=1}^{2}\int_0^t U(t-s;x-y_j)|\psi(s,y_j)|^{2\sigma}\psi(s,y_j)\,ds\,. \tag{6}$$

where $U(\tau,y)$ is the integral kernel of the unitary group $e^{it\Delta}$, i.e.

$$U(\tau,y) := \frac{e^{i\frac{|y|^2}{4\tau}}}{\sqrt{4i\,\pi\,\tau}}\,, \qquad (\mathcal{U}(t)\xi)(x) = \int_{-\infty}^{\infty} U(t;x-y)\,\xi(y)\,dy, \quad \forall\xi \in L^2(\mathbb{R}).$$

From ansatz (6) one obtains for $i = 1, 2$:

$$\psi(t,y_i) = (\mathcal{U}(t)\psi_0)(y_i) - i\,\gamma\sum_{j=1}^{2}\int_0^t U(t-s;y_i-y_j)|\psi(s,y_j)|^{2\sigma}\psi(s,y_j)\,ds.$$

Explicitly

$$
\begin{cases}
\psi(t,-a) + \dfrac{\gamma}{2}\sqrt{\dfrac{\imath}{\pi}}\displaystyle\int_0^t \dfrac{\psi(s,-a)\,|\psi(s,-a)|^{2\sigma}}{\sqrt{t-s}}\,ds + \\[4mm]
\qquad\qquad + \dfrac{\gamma}{2}\sqrt{\dfrac{\imath}{\pi}}\displaystyle\int_0^t \dfrac{\psi(s,a)\,|\psi(s,a)|^{2\sigma}}{\sqrt{t-s}}\,e^{\imath\frac{a2}{(t-s)}}\,ds = (\mathcal{U}(t)\,\psi_0)(-a)\,, \\[8mm]
\psi(t,a) + \dfrac{\gamma}{2}\sqrt{\dfrac{\imath}{\pi}}\displaystyle\int_0^t \dfrac{\psi(s,a)\,|\psi(s,a)|^{2\sigma}}{\sqrt{t-s}}\,ds + \\[4mm]
\qquad\qquad \dfrac{\gamma}{2}\sqrt{\dfrac{\imath}{\pi}}\displaystyle\int_0^t \dfrac{\psi(s,-a)\,|\psi(s,-a)|^{2\sigma}}{\sqrt{t-s}}\,e^{\imath\frac{a2}{(t-s)}}\,ds = (\mathcal{U}(t)\,\psi_0)(a)\,.
\end{cases}
\tag{7}
$$

The problem was extensively discussed in [12], where it was proved that, if $\psi(t,\pm a)$ are solutions of (7), then the function (6) is the unique solution of (5) (see [13–15] and [16,17] for $d=2$ and $d=3$).

Remark 2.1. *It is worth pointing out that the solution of* (5) *mentioned before is guaranteed to be* global-in-time *only if $\sigma < 1$. On the other hand, whenever $\sigma \geq 1$ there exist initial data for which blow-up phoenomena may arise.*

Remark 2.2. *Throughout, we use the notation $q_1(t) \equiv \psi(t,-a)$, $q_2(t) \equiv \psi(t,a)$ and refer to (7) as the "charge equations".*

In the following subsection we examine the linear case analysing the necessary conditions to have quantum beating states.

2.1. Linear point interactions

Let us consider the linear case, corresponding to $\sigma = 0$ and $\gamma_j < 0$, for $j = 1, 2$, independent of t in (5). From the definition (3) the resolvent of the operator $H_{\gamma,Y}$ has integral kernel:

$$
(H_{\gamma,Y} + \lambda)^{-1}(x,x') = G^\lambda(x-x') - \sum_{i,j=1}^{2} \left(\Gamma_{\underline{\gamma}}^\lambda\right)^{-1}_{ij} G^\lambda(x-y_i)G^\lambda(x'-y_j).
\tag{8}
$$

As it is clear from (8), $H_{\gamma,Y}$ is a finite rank perturbation of the free Laplacian resolvent operator. This in turn implies that the essential spectrum of $H_{\gamma,Y}$ is $[0,\infty)$ and that $-\lambda$ is a negative eigenvalue if and only if the matrix $\Gamma_{\underline{\gamma}}^\lambda$ is not invertible:

$$
\det \Gamma_{(\gamma_1,\gamma_2)}^\lambda = \det \begin{pmatrix} \dfrac{1}{\gamma_1} + \dfrac{1}{2\sqrt{\lambda}} & G^\lambda(2a) \\[3mm] G^\lambda(2a) & \dfrac{1}{\gamma_2} + \dfrac{1}{2\sqrt{\lambda}} \end{pmatrix} = 0\,,
$$

or

$$
\left(\dfrac{1}{\gamma_1} + \dfrac{1}{2\sqrt{\lambda}}\right)\left(\dfrac{1}{\gamma_2} + \dfrac{1}{2\sqrt{\lambda}}\right) - \left(\dfrac{1}{2\sqrt{\lambda}}\right)^2 e^{-4\sqrt{\lambda}\,a} = 0\,.
\tag{9}
$$

All the relevant results concerning the point spectrum of $H_{\gamma,Y}$ are collected in the following lemma.

Lemma 2.3 ([10]). *Let $\gamma_1 \leq \gamma_2$ and let us define the ratio $\alpha := \dfrac{\gamma_2}{\gamma_1}$. Then, one has:*

  a): *There are two real solutions $\lambda_0 > \lambda_1 > 0$ to equation (9) if and only if $\gamma_i < 0$ for $i = 1, 2$ and*

$$
\dfrac{1}{|\gamma_1|} + \dfrac{1}{|\gamma_2|} < 2a\,.
\tag{10}
$$

  b): *For $\gamma_i = \gamma < 0$, $i = 1, 2$, satisfying (10) $(1/\gamma < a)$, one has*

$$
\Delta\lambda := \lambda_0 - \lambda_1 \simeq \gamma^2 e^{-|\gamma|\alpha}\,.
$$

In particular $\Delta\lambda \to 0$ exponentially as $|\gamma|\alpha \to \infty$.

c): *For $\gamma_i < 0$, $i = 1, 2$, satisfying (10) and $\alpha < 1$, one has*

$$\Delta\lambda := \lambda_0 - \lambda_1 \geq \gamma_1^2(1 - \alpha^2).$$

In particular $\Delta\lambda \to \infty$ as $|\gamma_1| \to \infty$.

d): *For $\gamma_i < 0$, $i = 1, 2$, satisfying (10) and $\alpha \leq 1$, one has:*

$$\lim_{|\gamma_1|\to\infty} 2\sqrt{\lambda_0}/\gamma_1 = -1, \quad \lim_{|\gamma_1|\to\infty} 2\sqrt{\lambda_1}/\gamma_2 = -1.$$

e): *For $\gamma_i < 0$, $i = 1, 2$, satisfying (10), the eigenfunctions associated with the two negative eigenvalues are (see [11])*

$$\phi_0(x) = c_0 G^{\lambda_0}(x - y_1) + c_1\,G^{\lambda_0}(x - y_2)\,, \tag{11}$$

$$\phi_1(x) = c_2 G^{\lambda_1}(x - y_1) + c_3 G^{\lambda_1}(x - y_2)\,, \tag{12}$$

where the coefficients c_0, c_1 and c_2, c_3 are solutions of:

$$\begin{pmatrix} \dfrac{1}{\gamma_1} + \dfrac{1}{2\sqrt{\lambda_0}} & \dfrac{1}{2\sqrt{\lambda_0}}e^{-2\sqrt{\lambda_0}\,a} \\[2ex] \dfrac{1}{2\sqrt{\lambda_0}}e^{-2\sqrt{\lambda_0}\,a} & \dfrac{1}{\gamma_2} + \dfrac{1}{2\sqrt{\lambda_0}} \end{pmatrix} \begin{pmatrix} c_0 \\[1ex] c_1 \end{pmatrix} = \begin{pmatrix} 0 \\[1ex] 0 \end{pmatrix},$$

and

$$\begin{pmatrix} \dfrac{1}{\gamma_1} + \dfrac{1}{2\sqrt{\lambda_1}} & \dfrac{1}{2\sqrt{\lambda_1}}e^{-2\sqrt{\lambda_1}\,a} \\[2ex] \dfrac{1}{2\sqrt{\lambda_1}}e^{-2\sqrt{\lambda_1}\,a} & \dfrac{1}{\gamma_2} + \dfrac{1}{2\sqrt{\lambda_1}} \end{pmatrix} \begin{pmatrix} c_2 \\[1ex] c_3 \end{pmatrix} = \begin{pmatrix} 0 \\[1ex] 0 \end{pmatrix}.$$

Solving explicitly the last equations at point **e)** of Lemma 2.3, we obtain:

$$\left|\frac{c_1}{c_0}\right| = \sqrt{\frac{(2\sqrt{\lambda_0}/\gamma_1) + 1}{(2\sqrt{\lambda_0}/\gamma_2) + 1}}\,,$$

$$\left|\frac{c_2}{c_3}\right| = \sqrt{\frac{(2\sqrt{\lambda_1}/\gamma_2) + 1}{(2\sqrt{\lambda_1}/\gamma_1) + 1}}\,.$$

The normalization condition finally gives:

$$c_0 = \frac{2|\gamma_1|\lambda_0^{3/4}}{\sqrt{\gamma_1\gamma_2\frac{(\gamma_1 + 2\sqrt{\lambda_0})}{(\gamma_2 + 2\sqrt{\lambda_0})} + \gamma_1\left(\gamma_1 + 4\sqrt{\lambda_0} + 2\sqrt{\lambda_0}\,a\left(\gamma_1 + 2\sqrt{\lambda_0}\right)\right)}}\,, \tag{13}$$

$$c_3 = \frac{2|\gamma_2|\lambda_1^{3/4}}{\sqrt{\gamma_1\gamma_2\frac{(\gamma_2 + 2\sqrt{\lambda_1})}{(\gamma_1 + 2\sqrt{\lambda_1})} - \gamma_2\left(\gamma_2 + 4\sqrt{\lambda_1} + 2\sqrt{\lambda_1}\,a\left(\gamma_2 + 2\sqrt{\lambda_1}\right)\right)}}\,. \tag{14}$$

A few remarks are worth noting:

Remark 2.4. *In our units the condition characterizing the semi-classical limit is $\delta := |\gamma|\alpha \gg 1$. In standard units the condition would be $\bar\delta := \dfrac{2m|\gamma|a}{\hbar^2} \gg 1$ and the energy difference:*

$$\triangle E \simeq \frac{2\,m\,\gamma^2}{\hbar^2}e^{-\bar\delta}\,.$$

Remark 2.5. *Notice the extreme instability of the energy difference with respect to the ratio α when it is close to the value one. While in the symmetric case ($\alpha = 1$) the energy difference is decreasing exponentially in the semiclassical limit the same quantity is going to infinity in the same limit for $\alpha < 1$. This fact will appear to be the main reason in the quantum beating suppression in the asymmetric and in the nonlinear case.*

Remark 2.6. *In the semi-classical limit, the coefficient ratios (13) and (14) tend to 1 in the symmetric case ($\alpha = 1$), whereas they tend to 0 for any $\alpha < 1$. In turn, this means that, in the same limit, the eigenfunctions (11) and (12) tend to be equally distributed on the two wells if $\alpha = 1$ whereas they are strongly confined in one of the well for any $\alpha < 1$.*

2.2. The beating phenomenon

Now, let us consider the linear case when the condition $\dfrac{1}{|\gamma_1|} + \dfrac{1}{|\gamma_2|} < 2a$ for the existence of two eigenvalues is fulfilled. Following standard notation, we will use in this subsection subscripts "f, e" instead of $0, 1$ to mean "<u>f</u>undamental" and "first <u>e</u>xcited state" (respectively). The corresponding eigenfunctions are:

$$\phi_f(x) = c_0 G^{\lambda_f}(x + a) + c_1 G^{\lambda_f}(x - a),$$
$$\phi_e(x) = c_2 G^{\lambda_e}(x + a) - c_3 G^{\lambda_e}(x - a).$$

The superposition of the two eigenfunctions:

$$\psi_{beat,0}^L(x) := \frac{1}{\sqrt{2}} \left(\phi_f(x) + \phi_e(x) \right)$$

will evolve in time as follows:

$$\psi_{beat}^L(t, x) = \frac{1}{\sqrt{2}} \left(e^{\imath \lambda_f t} \phi_f(x) + e^{\imath \lambda_e t} \phi_e(x) \right), \tag{15}$$

with a probability density given by:

$$\mathcal{P}(t, x) = \frac{1}{2} \left[|\phi_f(x)|^2 + |\phi_e(x)|^2 + 2\,\phi_f(x)\phi_e(x) \cos\left((\lambda_f - \lambda_e)t\right) \right].$$

Let us consider first the symmetric case. The two eigenfunctions ϕ_f and ϕ_e are correspondingly symmetric and antisymmetric with respect to the origin and have similar absolute value everywhere (see Fig. 2).
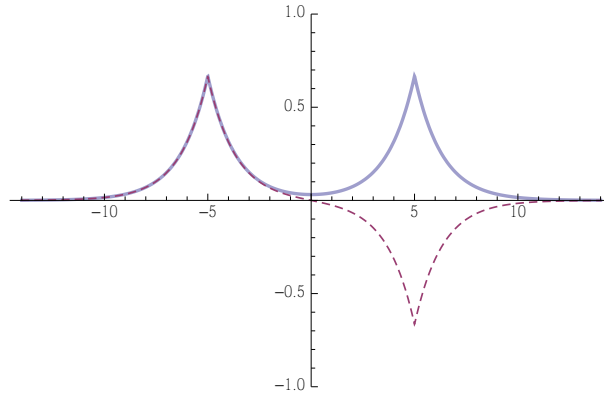
FIG. 2. Plot of the functions $\phi_f(x)$ with a thicked blue line and $\phi_e(x)$ with a dashed line.

It is clear that ψ_{beat}^L is initially supported around the point $-a$ and is an oscillating function with period $T_B = \dfrac{2\pi}{|\lambda_f - \lambda_e|}$ concentrated periodically on the left and on the right well, justifying the definition of (15) as a beating state.

The values assumed by the function $\psi_{beat}^L(t, x)$ in the centers of the two wells evolve as follows:

$$q_1^L(t) \equiv \psi_{beat}^L(t, -a) = \frac{1}{\sqrt{2}} \left(e^{\imath \lambda_f t} \phi_f(-a) + e^{\imath \lambda_e t} \phi_e(-a) \right),$$
$$q_2^L(t) \equiv \psi_{beat}^L(t, a) = \frac{1}{\sqrt{2}} \left(e^{\imath \lambda_f t} \phi_f(a) + e^{\imath \lambda_e t} \phi_e(a) \right).$$

and are plotted in Fig. 3.

The situation is remarkably different when $\alpha < 1$. In this case, as we pointed out in Remark 2.6, the two eigenstates are strongly confined in different wells for large γ_1. In particular, their product is going to be zero almost everywhere. Any initial superposition of the two eigenstate:

$$\psi_{asy,0}(x) := \alpha\,\phi_0(x) + \beta\,\phi_1(x), \quad \alpha, \beta \in \mathbb{C}, \quad |\alpha|^2 + |\beta|^2 = 1,$$

will evolve at time t into the state:

$$\psi_{asy}(t, x) := \alpha\,e^{\imath \lambda_0 t}\phi_0(x) + \beta\,e^{\imath \lambda_1 t}\phi_1(x).$$
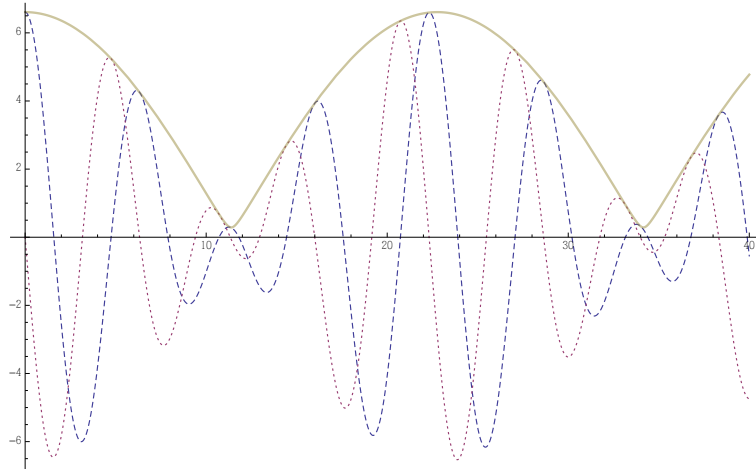
FIG. 3. Plot of the time-evolution of the functions $\mathrm{Re}\,q_1^L(t)$ as a dashed line, $\mathrm{Im}\,q_1^L(t)$ as a dotted line and $|q_1^L|(t)$ as a thick line

but the time dependent term in the square modulus will be negligible and no beating phenomenon will take place.

One expects that the asymmetry due to the nonlinearity will produce a similar suppression on time scales depending on the initial condition and on the strength of the nonlinearity.

2.3. Nonlinear point interactions

A detailed analytical study of the nonlinear case $\sigma > 0$ can be found in [12, 18] where the authors prove general results about existence of solutions, either local or global in time, and prove existence of blow-up solutions for $\sigma \geq 1$.

In the following, we analyze results about the evolution of a beating state obtained via numerical computation. A complete analytical analysis of equation (7) is still lacking. The problem is to quantify the amount of asymmetry necessary to suppress quantum beating induced by the nonlinearity and the time elapsed before that level is reached.

Let us consider an initial state which would evolve in a quantum beating state in the linear case:

$$\psi_0(x) := \alpha\,\phi_f(x) + \beta\,\phi_e(x)\,, \quad \alpha, \beta \in \mathbb{C} \quad |\alpha|^2 + |\beta|^2 = 1$$

In the following we investigate the Cauchy problem (5) with initial conditions

$$\psi(0, x) = \psi_0(x)$$

using its integral form (7). From [12, Theorem 6], we know that, under the assumptions $\sigma < 1$ and $\psi_0 \in H^1(\mathbb{R})$, the Cauchy problem has a unique solution which is global in time. Moreover in [12, Theorem 23], it is proved that if $\gamma < 0$ and $\sigma \geqslant 1$ then there exist initial data such that the solutions of the Cauchy problem blow-up in finite time.

Let us assume now that $\gamma < 0$ and $\sigma < 1$. We list the solutions to (7) obtained by numerical computation in [10]. In particular, we will compare the solution in the linear case with solutions to (7) with increasing powers of the non linearity. Our results show how the asymmetry generated by the nonlinear interactions produce the complete suppression of the beating phenomenon.

For the symmetric linear case we set $\sigma = 0$ and consider the linear Volterra-system associated with the initial condition given by:

$$\psi_{beat,0}^L(x) := \alpha\,\phi_f(x) + \beta\,\phi_e(x)\,, \quad \alpha, \beta \in \mathbb{R}\,, \tag{16}$$

which can be exactly solved:

$$\begin{cases} q_1(t) = \alpha\,\phi_f(-a)\,e^{\imath\,\lambda_f\,t} + \beta\,\phi_e(-a)\,e^{\imath\,\lambda_e\,t}\,, \\[2mm] q_2(t) = \alpha\,\phi_f(a)\,e^{\imath\,\lambda_f\,t} + \beta\,\phi_e(a)\,e^{\imath\,\lambda_e\,t}\,, \end{cases} \quad \forall t \in \mathbb{R}^+\,.$$

Figure 4 presents on the left the time-evolution of the numerical solutions of the Volterra-system associated to the parameters indicated in the figure caption.
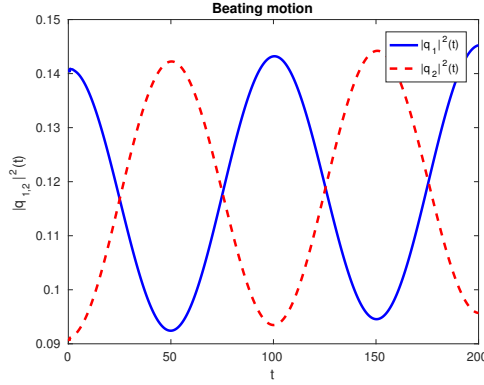
FIG. 4. The beating effect. Evolution in time of the numerical solutions $|q_1|^2(t)$ resp. $|q_2|^2(t)$ for $a = 3$, $\alpha = \sqrt{0.01}$, $\beta = \sqrt{0.99}$, $\gamma = -0.5$

Let us consider the nonlinear case. We assume the same initial condition and the same parameters as in the symmetric linear case (16). Increasing the power of the nonlinearity (we consider $\sigma = 0.3$, $\sigma = 0.7$, $\sigma = 0.9$) we observe that the time elapsed till the suppression of the beating effect is getting shorter and shorter. Here the time dependent point interaction strength is:

$$\gamma_\pm(t) = \gamma \, |\psi(t, \pm a)|^{2\sigma} \, .$$

In order to have at time $t = 0$ the same strength of the linear case $\gamma_\pm(0) = -0.5$, we assume

$$\gamma := 2 \, \gamma_\pm(0)/[|\psi_0(a)|^{2\sigma} + |\psi_0(-a)|^{2\sigma}] \, .$$

In Fig. 5, we plot the numerical solutions of the Volterra-system, *i.e.* $|q_1^{num}|^2(t)$ resp. $|q_2^{num}|^2(t)$ (in blue resp. red) as functions of time, and for the different nonlinearity exponents. As a reference, we plot also the exact solutions of the symmetric linear system, *i.e.* $|q_{beat,1}|^2(t)$ resp. $|q_{beat,2}|^2(t)$ (in cyan resp. magenta). Figures show clearly how the nonlinearity suppresses the beating-effect.
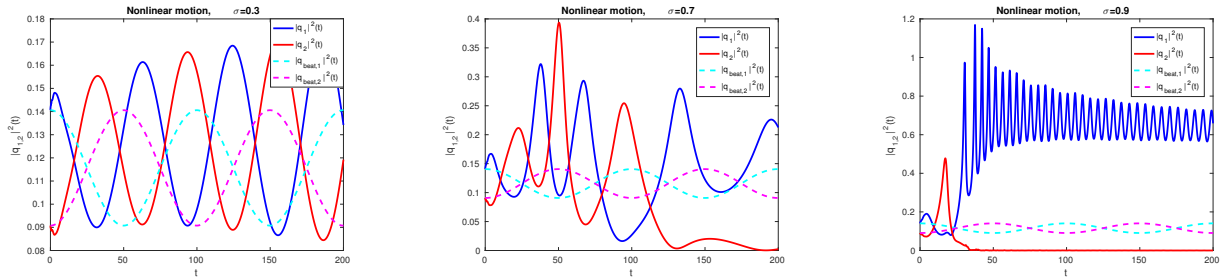
FIG. 5. The nonlinear time-evolution of the numerical solutions $|q_1^{num}|^2(t)$ resp. $|q_2^{num}|^2(t)$ (in blue/red full line) and corresponding linear beating solutions $|q_{beat,1}|^2(t)$ resp. $|q_{beat,2}|^2(t)$ (in cyan/magenta dashed line), for $\sigma = 0.3$ (left), $\sigma = 0.7$ (center) and $\sigma = 0.9$ (right)

3. Conclusion

In our numerical simulation, we showed that in a zero range nonlinear double well potential, the quantum beating mechanism is highly unstable under perturbations breaking the inversion symmetry of the problem.

The results shown in this review require further developments and extensions. In particular, it is necessary to examine analytically the solutions of the system of Volterra integral equations (7) to clarify the dependence on initial conditions of the time needed for the beating suppression. A generalization of the results to higher dimensions is in progress.

Acknowledgments

References

[1] Davies E.B. Symmetry breaking for a nonlinear Schrödinger equation. *Comm. Math. Phys.*, 1979, **64**(3), P. 191–210.

[2] Davies E.B. Nonlinear Schrödinger operators and molecular structure. *J. Phys. A*, 1995, **28**(14), P. 4025–4041.

[3] Herbauts I.M., Dunstan D.J. Quantum molecular dynamics study of the pressure dependence of the ammonia inversion transition. *Physical Review A*, 2007, **76**(6), article number 062506.

[4] Jona-Lasinio G., Presilla C. and Toninelli C. Environment induced localization and superselection rules in a gas of pyramidal molecules. *Mathematical physics in mathematics and physics (Siena, 2000)*, P. 207–217, Fields Inst. Commun. 30, Amer. Math. Soc., Providence, RI, 2001.

[5] Sacchetti A. Nonlinear time-dependent one-dimensional Schrödinger equation with double-well potential. *SIAM J. Math. Anal.*, 2004, **35**(5), P. 1160–1176.

[6] Grecchi V., Martinez A. and Sacchetti A. Splitting instability: the unstable double wells. *J. Phys. A*, 1996, **29**(15), P. 4561–4587.

[7] Grecchi V., Martinez A. and Sacchetti A. Destruction of the beating effect for a nonlinear Schrödinger equation. *Comm. Math. Phys.*, 2002, **227**(1), P. 191–209.

[8] Sacchetti A. Nonlinear time-dependent Schrödinger equations: the Gross-Pitaevskii equation with double-well potential. *J. Evol. Equ.*, 2004, **4**(3), P. 345–369.

[9] Sacchetti A. Nonlinear time-dependent one-dimensional Schrödinger equation with double-well potential. *SIAM J. Math. Anal.*, 2004, **35**(5), P. 1160–1176.

[10] Carlone R., Figari R. and Negulescu C. The quantum beating and its numerical simulation. *J. Math. Anal. Appl.*, 2017, **450**(2), P. 1294–1316.

[11] Albeverio S., Gesztesy F., Høegh-Krohn R. and Holden H. *Solvable models in quantum mechanics*. AMS Chelsea Publishing, Providence, RI, 2005.

[12] Adami R. and Teta A. A class of nonlinear Schrödinger equations with concentrated nonlinearity. *J. Funct. Anal.*, 2001, **180**(1), P. 148–175.

[13] Carlone R.,Correggi M. and Figari R. Two-dimensional time-dependent point interactions. *Functional analysis and operator theory for quantum physics*. P. 189–211, EMS Ser. Congr. Rep., Eur. Math. Soc., Zürich, 2017.

[14] Carlone R., Correggi M. and Tentarelli L. Well-posedness of the two-dimensional nonlinear Schrödinger equation with concentrated nonlinearity. *preprint* arXiv:1702.03651 [math-ph], 2017.

[15] Carlone R., Fiorenza A. and Tentarelli L. The action of Volterra integral operators with highly singular kernels on Hölder continuous, Lebesgue and Sobolev functions. *J. Funct. Anal.*, 2017, **273**(3), P. 1258–1294.

[16] Adami R., Dell'Antonio G., Figari R. and Teta A. The Cauchy problem for the Schrödinger equation in dimension three with concentrated nonlinearity. *Ann. Inst. H. Poincar Anal. Non Linéaire*, 2003, **20**(3), P. 477–500.

[17] Adami R., Dell'Antonio G., Figari R. and Teta A. Blow-up solutions for the Schrödinger equation in dimension three with a concentrated nonlinearity. *Ann. Inst. H. Poincar Anal. Non Linéaire*, 2004, **21**(1), P. 121–137.

[18] Adami R. and Teta A. A simple model of concentrated nonlinearity. *Mathematical results in quantum mechanics (Prague, 1998)*, P. 183–189, Oper. Theory Adv. Appl. 108, Birkhuser, Basel, 1999.

A model of electron transport through a boson cavity

A. A. Boitsev[1], J. Brasche[2], H. Neidhardt[3], I. Y. Popov[1]

[1]ITMO University, Kronverkskiy, 49, St. Petersburg, 197101, Russia

[2]Institut für Mathematik, TU Clausthal, Erzstr. 1, D-38678 Clausthal-Zellerfeld, Germany

[3]Weierstrass Institute, Mohrenstr. 39, D-10117 Berlin, Germany

boitsevanton@gmail.com, johannes.brasche@tu-clausthal.de,
hagen.neidhardt@wias-berlin.de, popov1955@gmail.com

We propose a model describing electronic transport through a boson cavity. We use the Jaynes–Cummings model dealing with a two-level quantum dot coupled to a quantized electro-magnetic field and two semi-infinite wires. The mathematical background of our model is given by the theory of self-adjoint extensions of symmetric operators. Using the boundary triplets approach, the gamma-field and the Weyl function were calculated. In addition, we obtained the scattering matrix for the model system.

Keywords: boundary triplets, extensions, scattering, solvable model.

Received: 21 February 2018

Revised: 1 March 2018

1. Introduction

To study the steady state current flowing through a quantum device in the framework of Landauer–Büttiker approach, it is necessary to consider a quantum system as an inner system (quantum dot) with left and right leads attached to it, i.e. free-fermion reservoirs with two different electro-chemical potentials. The goal was to calculate the steady electron current going from one lead through the dot the other one. This current is directly related to the transmission coefficients of some natural scattering system related to this particle transport problem. This, approach was justified a few years ago [1–3]. It, effectively, reduces the problem to investigation of a one-particle Hamiltonian.

In the present paper we consider the Jaynes–Cummings model [4, 5]. The Jaynes–Cummings model serves to determine how quantization of the radiation field affects the predictions for the evolution of the state of a two-level system in comparison with semi-classical theory of light-atom interaction. It is often applied to description of the interaction between an atom and a laser field [6]. We used a version suggested in [7,8]. More precisely, the authors of [7,8] use the discrete Hamiltonian. In contrast, we use the continuous Hamiltonian. Namely, we have a two-level quantum dot coupled, from one side, to the standard Jaynes–Cummings one-mode photon resonator, and from the other side to two semi-infinite leads. To construct the model, we use the operator extensions theory approach (see, e.g., [9–11] and references in [12]) in the framework of boundary triplet approach (see, e.g., [13–16]). Detailed mathematical background of the model is developed in [17].

2. Preliminaries

2.1. Linear relations

A linear relation Θ in $\mathcal{H}$ is a closed linear subspace of $\mathcal{H} \oplus \mathcal{H}$. The set of all linear relations in $\mathcal{H}$ is denoted by $\widetilde{\mathcal{C}}(\mathcal{H})$. We denote also by $\mathcal{C}(\mathcal{H})$ the set of all closed linear (not necessarily densely defined) operators in $\mathcal{H}$. Identifying each operator $T \in \mathcal{C}(\mathcal{H})$ with its graph $\mathrm{gr}\,(T)$, we regard $\mathcal{C}(\mathcal{H})$ as a subset of $\widetilde{\mathcal{C}}(\mathcal{H})$.

The role of the set $\widetilde{\mathcal{C}}(\mathcal{H})$ in extension theory becomes clear from Proposition 2.3. However, it's role in the operator theory is substantially motivated by the following circumstances: in contrast to $\mathcal{C}(\mathcal{H})$, the set $\widetilde{\mathcal{C}}(\mathcal{H})$ is closed with respect to taking inverse and adjoint relations Θ^{-1} and Θ^*. The latter is given by: $\Theta^{-1} = \{\{g, f\} : \{f, g\} \in \Theta\}$ and:

$$\Theta^* = \left\{ \begin{pmatrix} k \\ k' \end{pmatrix} : (h', k) = (h, k') \text{ for all } \begin{pmatrix} h \\ h' \end{pmatrix} \in \Theta \right\}.$$

A linear relation Θ is called symmetric if $\Theta \subset \Theta^*$ and self-adjoint if $\Theta = \Theta^*$.

2.2. Boundary triplets and proper extensions

Let us briefly recall some basic facts on boundary triplets. Let S be a densely defined closed symmetric operator with equal deficiency indices $n_\pm(S) := \dim(\mathfrak{N}_{\pm i})$, $\mathfrak{N}_z := \ker(S^* - z)$, $z \in \mathbb{C}_\pm$, acting on some separable Hilbert space $\mathfrak{H}$.

Definition 2.1.
(i) *A closed extension $\widetilde{S}$ of S is called proper if $\operatorname{dom}(S) \subset \operatorname{dom}(\widetilde{S}) \subset \operatorname{dom}(S^*)$.*
(ii) *Two proper extensions $\widetilde{S}'$, $\widetilde{S}$ are called disjoint if $\operatorname{dom}(\widetilde{S}') \cap \operatorname{dom}(\widetilde{S}) = \operatorname{dom}(S)$ and transversal if in addition $\operatorname{dom}(\widetilde{S}') + \operatorname{dom}(\widetilde{S}) = \operatorname{dom}(S^*)$.*

we denote by Ext_S the set of all proper extensions of S completed by the non-proper extensions S and S^* is denoted. For instance, any self-adjoint or maximal dissipative (accumulative) extension is proper.

Definition 2.2 ([18]). A triplet $\Pi = \{\mathcal{H}, \Gamma_0, \Gamma_1\}$, where $\mathcal{H}$ is an auxiliary Hilbert space and $\Gamma_0, \Gamma_1 : \operatorname{dom}(S^*) \to \mathcal{H}$ are linear mappings, is called a boundary triplet for S^* if the "abstract Green's identity":

$$(S^* f, g) - (f, S^* g) = (\Gamma_1 f, \Gamma_0 g) - (\Gamma_0 f, \Gamma_1 g), \quad f, g \in \operatorname{dom}(S^*). \tag{1}$$

is satisfied and the mapping $\Gamma := (\Gamma_0, \Gamma_1)^\top : \operatorname{dom}(S^*) \to \mathcal{H} \oplus \mathcal{H}$ is surjective, i.e. $\operatorname{ran}(\Gamma) = \mathcal{H} \oplus \mathcal{H}$.

A boundary triplet $\Pi = \{\mathcal{H}, \Gamma_0, \Gamma_1\}$ for S^* always exists whenever $n_+(S) = n_-(S)$. Note also that $n_\pm(S) = \dim(\mathcal{H})$ and $\ker(\Gamma_0) \cap \ker(\Gamma_1) = \operatorname{dom}(S)$.

With any boundary triplet Π one associates two canonical self-adjoint extensions $S_j := S^* \restriction \ker(\Gamma_j)$, $j \in \{0, 1\}$. Conversely, for any extension $S_0 = S_0^* \in \operatorname{Ext}_S$, there exists a (non-unique) boundary triplet $\Pi = \{\mathcal{H}, \Gamma_0, \Gamma_1\}$ for S^* such that $S_0 := S^* \restriction \ker(\Gamma_0)$.

Using the concept of boundary triplets one can parametrize all proper extensions of A in the following way.

Proposition 2.3 ([19]). *Let $\Pi = \{\mathcal{H}, \Gamma_0, \Gamma_1\}$ be a boundary triplet for S^*. Then the mapping*

$$\operatorname{Ext}_S \ni \widetilde{S} \to \Gamma \operatorname{dom}(\widetilde{S}) = \{(\Gamma_0 f, \Gamma_1 f)^\top :\ f \in \operatorname{dom}(\widetilde{S})\} =: \Theta \in \widetilde{\mathcal{C}}(\mathcal{H}) \tag{2}$$

establishes a bijective correspondence between the sets Ext_S and $\widetilde{\mathcal{C}}(\mathcal{H})$. We write $\widetilde{S} = S_\Theta$ if $\widetilde{S}$ corresponds to Θ by (2). Moreover, the following holds:
(i) *$S_\Theta^* = S_{\Theta^*}$, in particular, $S_\Theta^* = S_\Theta$ if and only if $\Theta^* = \Theta$.*
(ii) *S_Θ is symmetric (self-adjoint) if and only if Θ is symmetric (self-adjoint).*
(iii) *The extensions S_Θ and S_0 are disjoint (transversal) if and only if there is a closed (bounded) operator B such that $\Theta = \operatorname{gr}(B)$. In this case (2) takes the form*

$$S_\Theta := S_{\operatorname{gr}(B)} = S^* \restriction \ker(\Gamma_1 - B\Gamma_0). \tag{3}$$

In particular, $S_j := S^* \restriction \ker(\Gamma_j) = S_{\Theta_j}$, $j \in \{0, 1\}$, where $\Theta_0 := \begin{pmatrix} \{0\} \\ \mathcal{H} \end{pmatrix}$ and $\Theta_1 := \begin{pmatrix} \mathcal{H} \\ \{0\} \end{pmatrix} = \operatorname{gr}(\mathbb{O})$ where

$\mathbb{O}$ denotes the zero operator in $\mathcal{H}$. Note also that $\widetilde{\mathcal{C}}(\mathcal{H})$ contains the trivial linear relations $\{0\} \times \{0\}$ and $\mathcal{H} \times \mathcal{H}$ parameterizing the extensions S and S^*, respectively, for any boundary triplet Π.

2.3. Gamma field and Weyl function

It is well known that Weyl function is an important tool in the direct and inverse spectral theory of Sturm–Liouville operators. In [19], the concept of Weyl function was generalized to the case of an arbitrary symmetric operator S with $n_+(S) = n_-(S) \leq \infty$. Following [19], we briefly recall basic facts on Weyl functions and γ-fields associated with a boundary triplet Π.

Definition 2.4 ([19]). Let $\Pi = \{\mathcal{H}, \Gamma_0, \Gamma_1\}$ be a boundary triplet for S^* and $S_0 = S^* \restriction \ker(\Gamma_0)$. The operator valued functions $\gamma(\cdot) : \rho(S_0) \to [\mathcal{H}, \mathfrak{H}]$ and $M(\cdot) : \rho(S_0) \to [\mathcal{H}]$ defined by:

$$\gamma(z) := \left(\Gamma_0 \restriction \mathfrak{N}_z\right)^{-1} \qquad M(z) := \Gamma_1 \gamma(z), \quad z \in \rho(S_0), \tag{4}$$

are called the γ-field and the Weyl function, respectively, corresponding to the boundary triplet Π.

Clearly, the Weyl function can equivalently be defined by:

$$M(z)\Gamma_0 f_z = \Gamma_1 f_z, \qquad f_z \in \mathfrak{N}_z, \quad z \in \rho(S_0).$$

The γ-field $\gamma(\cdot)$ and the Weyl function $M(\cdot)$ in (4) are well defined. Moreover, both $\gamma(\cdot)$ and $M(\cdot)$ are holomorphic on $\rho(S_0)$ and the following relations:

$$\gamma(z) = \big(I + (z - \zeta)(S_0 - z)^{-1}\big)\gamma(\zeta), \ z, \zeta \in \rho(S_0), \tag{5}$$

and

$$M(z) - M(\zeta)^* = (z - \overline{\zeta})\gamma(\zeta)^*\gamma(z), \ z, \zeta \in \rho(S_0), \tag{6}$$

hold. Identity (6) yields that $M(\cdot)$ is $[\mathcal{H}]$-valued Nevanlinna function ($M(\cdot) \in R[\mathcal{H}]$), i.e. $M(\cdot)$ is $[\mathcal{H}]$-valued holomorphic function on $\mathbb{C}_{\pm}$ satisfying:

$$M(z) = M(\overline{z})^* \qquad \text{and} \qquad \frac{\text{Im}(M(z))}{\text{Im}(z)} \geq 0, \ z \in \mathbb{C}_+ \cup \mathbb{C}_-.$$

It follows also from (6) that $0 \in \rho(\text{Im}(M(z)))$ for all $z \in \mathbb{C}_{\pm}$.

2.4. Krein-type formula for resolvents

Let $\Pi = \{\mathcal{H}, \Gamma_0, \Gamma_1\}$ be a boundary triplet for S^*, $M(\cdot)$ and $\gamma(\cdot)$ the corresponding Weyl function and γ-field, respectively. For any proper (not necessarily self-adjoint) extension $\widetilde{S}_\Theta \in \text{Ext}_S$ with non-empty resolvent set $\rho(\widetilde{S}_\Theta)$ the following Krein-type formula holds (cf. [19]):

$$(S_\Theta - z)^{-1} - (S_0 - z)^{-1} = \gamma(z)(\Theta - M(z))^{-1}\gamma^*(\overline{z}), \ z \in \rho(S_0) \cap \rho(S_\Theta). \tag{7}$$

Formula (7) extends the known Krein formula for canonical resolvents to the case of any $S_\Theta \in \text{Ext}_S$ with $\rho(S_\Theta) \neq \emptyset$. Moreover, due to relations (2), (3) and (4) formula (7) is related to the boundary triplet Π. We emphasize, that this relation makes it possible to apply the Krein-type formula (7) to boundary value problems (see, e.g., [14] and references in [12]).

2.5. Scattering and Weyl function

Let S be a densely defined closed symmetric operator with finite equal deficiency indices $n_{\pm}(S)$ and $\Pi = \{\mathcal{H}, \Gamma_0, \Gamma_1\}$ is a boundary triplet for S^*, Let $S_0 = S^* \upharpoonright \ker \Gamma_0$ and S_Θ is a self-adjoint extension corresponding to $\Theta \in \tilde{C}(\mathcal{H})$. As $\dim \mathcal{H}$ is finite, by (7) $(S_\Theta - z)^{-1} - (S_0 - z)^{-1}$ is a finite rank operator and the system $\{S_\Theta, S_0\}$ is a so-called complete scattering system, i.e. the wave operators:

$$W_{\pm}(S_\Theta, S_0) = s - \lim_{t \to \pm\infty} e^{itS_\Theta}e^{-itS_0}P^{ac}(S_0),$$

exists and they are complete, i.e. their ranges coincide with the absolutely continuous subspace $\mathfrak{H}^{ac}(S_\Theta)$ of S_Θ (see, e.g. [20], [21], [22]). By $P^{ac}(S_0)$ we denote the orthogonal projection on absolutely continuous subspace $\mathfrak{H}^{ac}(S_0)$ of S_0. The scattering operator $S(S_\Theta, S_0)$ of a scattering system $\{S_\Theta, S_0\}$ is defined as:

$$S(S_\Theta, S_0) = W_+(S_\Theta, S_0)^* W_-(S_\Theta, S_0).$$

If we regard the scattering operator as an operator in $\mathfrak{H}^{ac}(S_0)$ then it becomes unitary and commutes with absolutely continuous part $S_0^{ac} = S_0 \upharpoonright \mathfrak{H}^{ac}(S_0) \cap \text{dom}(S_0)$. of S_0 and thus it is unitarily equivalent to a multiplication operator induced by a family $\{S_\Theta(z)\}$ of unitary operators in a spectral representation of S_0^{ac} ([20], Proposition 9.57). This family is called a scattering matrix of a scattering system $S(S_\Theta, S_0)$.

Since the dimension $\dim \mathcal{H}$ is finite, then the Weyl function $M(\cdot)$ corresponding to boundary triplet $\Pi = \{\mathfrak{H}, \Gamma_0, \Gamma_1\}$ is a matrix-valued Nevanlinna function. By Fatous theorem ([23]), the limit $M(\lambda + i0) = \lim_{\varepsilon \to 0+0} M(\lambda + i\varepsilon)$ exists for almost all $\lambda \in \mathbb{R}$. We denote the set of real point where the limit exists by Σ^M. We will use the notation $\mathcal{H}_{M(\lambda)} = \text{ran}(M(\lambda))$, $\lambda \in \Sigma^M$. By $P_{M(\lambda)}$ we will denote the orthogonal projection on $\mathcal{H}_{M(\lambda)}$. We will also use the notation $N_\Theta(z) = (\Theta - M(z))^{-1}$, $z \in \mathbb{C} \setminus \mathbb{R}$, where $\Theta \in \tilde{C}(\mathcal{H})$ is a self-adjoint relation corresponding to S_Θ. This function is well defined and the limit $N_\Theta(\lambda + i0) = (\Theta - M(\lambda + i0))^{-1}$ exists almost for every $\lambda \in \mathbb{R}$. This set we will denote as Σ^N.

Theorem 2.5. *([13]) Let S be a densely defined symmetric operator with finite deficiency indices in separable Hilbert space $\mathfrak{H}$, let Π be a boundary triplet corresponding to S^* with corresponding Weyl function $M(\cdot)$, S_Θ is a self-adjoint extension of S, $S_0 = S^* \upharpoonright \ker \Gamma_0$, $\Theta \in \tilde{C}(\mathcal{H})$, then in $L^2(\mathbb{R}, d\lambda, \mathcal{H}_{M(\lambda)})$ the scattering matrix of the complete scattering system $\{S_\Theta, S_0\}$ is given by:*

$$\mathfrak{S}_\Theta(\lambda) = I_{\mathcal{H}_{M(\lambda)}} + 2i\sqrt{\Im(M(\lambda + i0))}N_\theta(\lambda + i0)\sqrt{\Im(M(\lambda + i0))}$$

for $\lambda \in \Sigma^M \cap \Sigma^N$.

3. Scattering

3.1. Model description

A rigorous construction of a proposed model can be found in [17]. We will show here only the main results. We consider the Hilbert space $\mathfrak{H} = L^2(\mathbb{R}_-) \oplus L^2(\mathbb{R}_+)$ where $\mathbb{R}_- = (-\infty, 0)$ and $\mathbb{R}_+ = (0, \infty)$. On the subspaces $\mathfrak{H}_l := L^2(\mathbb{R}_-)$ and $\mathfrak{H}_r := L^2(\mathbb{R}_+)$ we consider the closed symmetric operators $H_l = -\dfrac{d^2}{dx^2} + v_l$ and $H_r = -\dfrac{d^2}{dx^2} + v_r$. We set $\mathfrak{H} := \mathfrak{H}_l \oplus \mathfrak{H}_r = L^2(\mathbb{R})$ and $H := H_l \oplus H_r$. Operator H can be regarded as the symmetric operator:

$$A = -\frac{d^2}{dx^2} + v(x), \qquad v(x) := \begin{cases} v_l & x \in \mathbb{R}_- \\ v_r & x \in \mathbb{R}_+ \end{cases}$$

with domain $\operatorname{dom}(A) = W_0^{2,2}(\mathbb{R}) := \{f \in W^{2,2}(\mathbb{R}) : f(0) = f'(0) = 0\}$. The operator A is symmetric and has deficiency indices $n_\pm(A) = 2$. For simplicity we assume that $0 \le v_r \le v_l$. It can be checked (see [17]) that the triplet $\Pi_A = \{\mathcal{H}^A, \Gamma_0^A, \Gamma_1^A\}$ with:

$$\mathcal{H}^A := \begin{matrix} \mathcal{H}^{H_l} \\ \oplus \\ \mathcal{H}^{H_r} \end{matrix} = \begin{matrix} \mathbb{C} \\ \oplus \\ \mathbb{C} \end{matrix}, \qquad \Gamma_0^A f := \begin{pmatrix} f(-0) \\ f(+0) \end{pmatrix}, \qquad \Gamma_1^A := \begin{pmatrix} -f'(-0) \\ f'(+0) \end{pmatrix},$$

defines a boundary triplet for A^*. The Weyl function $M^A(z)$ of the boundary triplet Π_A is given by:

$$M^A(z) = \begin{pmatrix} m^{H_l}(z) & 0 \\ 0 & m^{H_r}(z) \end{pmatrix} = \begin{pmatrix} i\sqrt{z - v_l} & 0 \\ 0 & i\sqrt{z - v_r} \end{pmatrix}, \qquad z \in \rho(A_0),$$

where $A_0 := A^* \restriction \ker(\Gamma_0^A)$. Notice that A_0 has Dirichlet boundary conditions.

We will view the point zero as a quantum dot or quantum cavity. In particular, the Hilbert space $\mathcal{H}^A = \mathbb{C}^2$ is considered to be the state space of the quantum dot and the self-adjoint operator B as the Hamiltonian of the dot, where $A_B := A^* \restriction \ker(\Gamma_1^A - B\Gamma_0^A)$ is a self-adjoint extension of A. The Hamiltonian B describes a two level system to which we are going to couple bosons. The state space of the bosons is the Hilbert space $\mathfrak{T} = l_2(\mathbb{N}_0)$, $\mathbb{N}_0 := \mathbb{N} \cup \{0\}$. The boson operator T is given by:

$$T\vec{\xi} = T\{\xi_k\}_{k \in \mathbb{N}_0} = \{k\xi_k\}_{k \in \mathbb{N}_0},$$
$$\vec{\xi} = \{\xi_k\}_{k \in \mathbb{N}_0} \in \operatorname{dom}(T) := \{\{\xi_k\}_{k \in \mathbb{N}_0} \in l_2(\mathbb{N}_0) : \{k\xi_k\}_{k \in \mathbb{N}_0} \in l_2(\mathbb{N}_0)\}.$$

The Hamiltonian T describes a system of bosons which do not interact mutually. The number of bosons is not fixed and varies from zero to infinity. The Hilbert space $\mathfrak{T}$ has a natural basis given by $e_k = \{\delta_{kj}\}_{j \in \mathbb{N}_0}$. Let us introduce the creation and annihilation operator b^* and b, respectively, defined by:

$$b^* e_k = \sqrt{k+1}\, e_{k+1}, \quad k \in \mathbb{N}_0, \quad \text{and} \quad b e_k = \sqrt{k}\, e_{k-1}, \quad k \in \mathbb{N}_0,$$

where $e_{-1} = 0$. One easily checks that $T = b^* b$.

In order to couple these two systems let us consider the closed symmetric operator:

$$S := A \otimes I_{\mathfrak{T}} + I_{\mathfrak{H}} \otimes T \tag{8}$$

in the Hilbert space $\mathfrak{K} := \mathfrak{H} \otimes \mathfrak{T}$. Setting the following:

$$\mathfrak{K}_l := \mathfrak{H}_l \otimes \mathfrak{T}, \qquad S_l := H_l \otimes I_{\mathfrak{T}} + I_{\mathfrak{H}_l} \otimes T,$$
$$\mathfrak{K}_r := \mathfrak{H}_r \otimes \mathfrak{T}, \qquad S_r := H_r \otimes I_{\mathfrak{T}} + I_{\mathfrak{H}_r} \otimes T,$$

we obtain:

$$\mathfrak{K} = \mathfrak{K}_l \oplus \mathfrak{K}_r \quad \text{and} \quad S = S_l \oplus S_r.$$

The corresponding Weyl function $M^S(\cdot)$ is given by:

$$M^S(z) = \begin{pmatrix} M^{S_l}(z) & 0 \\ 0 & M^{S_r}(z) \end{pmatrix}, \quad z \in \rho(S_0), \quad S_0 = S_l^D \oplus S_r^D,$$

where $S_l^D = H_l^D \otimes I_{\mathfrak{T}} + I_{\mathfrak{H}_l} \otimes T$ and $S_r^D = H_r^D \otimes I_{\mathfrak{T}} + I_{\mathfrak{H}_l} \otimes T$ – the extensions with the Dirichlet boundary conditions and:

$$M^{S_l}(z) = \frac{m^{H_l}(z - T) - \operatorname{Re}(m^{H_l}(i - T))}{\operatorname{Im}(m^{H_l}(i - T))}, \qquad z \in \mathbb{C}_\pm,$$

$$M^{S_r}(z) = \frac{m^{H_r}(z-T) - \mathrm{Re}(m^{H_r}(i-T))}{\mathrm{Im}(m^{H_r}(i-T))}, \qquad z \in \mathbb{C}_\pm.$$

Moreover, we have:

$$\begin{pmatrix} \sqrt{\mathrm{Im}(m^{H_l}(i-T))} & 0 \\ 0 & \sqrt{\mathrm{Im}(m^{H_r}(i-T))} \end{pmatrix} = \frac{1}{\sqrt[4]{2}} \begin{pmatrix} Z_l^{-1/2} & 0 \\ 0 & Z_r^{-1/2} \end{pmatrix}$$

and:

$$\begin{pmatrix} \mathrm{Re}(m^{H_l}(i-T)) & 0 \\ 0 & \mathrm{Re}(m^{H_r}(i-T)) \end{pmatrix} = \begin{pmatrix} Z_l & 0 \\ 0 & Z_r \end{pmatrix}$$

where:

$$Z_l := \sqrt{\sqrt{I_\Im + (T+v_l)^2} + T + v_l},$$

$$Z_r := \sqrt{\sqrt{I_\Im + (T+v_r)^2} + T + v_r}.$$

3.2. Scattering matrix

We want to show that the limit $\lim_{\varepsilon \to 0} M^S(\lambda + i\varepsilon)$ exists. The candidate for this limit is the function $M^S(\lambda)$, $\lambda \in \mathbb{R}$.

Lemma 3.1. *The operator-function $M^S(\lambda)$, $\lambda \in \mathbb{R}$ is a bounded operator.*

Consider:

$$M^{S_l}(\lambda) = \frac{m^{H_l}(\lambda-T) - \mathrm{Re}(m^{H_l}(i-T))}{\mathrm{Im}(m^{H_l}(i-T))} = \bigoplus_{n=0}^{\infty} \frac{m^{H_l}(\lambda-n) - \mathrm{Re}(m^{H_l}(i-n))}{\mathrm{Im}(m^{H_l}(i-n))}.$$

We then rewrite as follows:

$$\frac{m^{H_l}(\lambda-n) - \mathrm{Re}(m^{H_l}(i-n))}{\mathrm{Im}(m^{H_l}(i-n))} = \frac{i\sqrt{\lambda-n-v_l} + \frac{1}{\sqrt{2}}\sqrt{\sqrt{1+(n+v_l)^2} + n + v_l}}{\frac{1}{\sqrt{2}}\left(\sqrt{\sqrt{1+(n+v_l)^2} + n + v_l}\right)^{-1}}$$

and consider this sequence when $n > \lambda - v_l$, then the numerator can be rewritten as:

$$\frac{1}{\sqrt{2}}\sqrt{\sqrt{1+(n+v_l)^2} + n + v_l} - \sqrt{n-\lambda+v_l} =$$

$$\frac{1}{2} \frac{\sqrt{1+(n+v_l)^2} - (n+v_l-2\lambda)}{\frac{1}{\sqrt{2}}\sqrt{\sqrt{1+(n+v_l)^2} + n + v_l} + \sqrt{n-\lambda+v_l}}$$

Notice that:

$$\frac{\sqrt{2}\sqrt{\sqrt{1+(n+v_l)^2} + n + v_l}}{\frac{2}{\sqrt{2}}\sqrt{\sqrt{1+(n+v_l)^2} + n + v_l} + \sqrt{n-\lambda+v_l}}$$

has the finite limit, so it is bounded and we have to examine:

$$\sqrt{1+(n+v_l)^2} - (n+v_l-2\lambda) = \frac{1 + 4n\lambda - 4\lambda^2 + 4v_l\lambda}{\sqrt{1+(n+v_l)^2} + (n+v_l-2\lambda)}$$

which also has the finite limit and so bounded. Thus, the sequence is bounded for $n > \lambda - v_l$, so it is bounded for $n \in \mathbb{N}_0$. Analogously, we deal with M^{S_r}.

Lemma 3.2. $\lim_{\varepsilon \to 0} M^S(\lambda + i\varepsilon) = M^S(\lambda)$, $\lambda \in \mathbb{R}$.

Consider:

$$\left\|M^{S_l}(\lambda) - M^{S_l}(\lambda + i\varepsilon)\right\| = \left\|\bigoplus_{n=0}^{\infty} \frac{m^{H_l}(\lambda-n) - (m^{H_l}(\lambda+i\varepsilon-n))}{\mathrm{Im}(m^{H_l}(i-n))}\right\|.$$

We obtain:

$$\left\| \frac{m^{H_l}(\lambda - n) - (m^{H_l}(\lambda + i\varepsilon - n))}{\operatorname{Im}(m^{H_l}(i - n))} \right\| = \left\| \frac{i\sqrt{\lambda - n - v_l} - i\sqrt{\lambda + i\varepsilon - n - v_l}}{\frac{1}{\sqrt{2}}\left(\sqrt{\sqrt{1 + (n + v_l)^2} + n + v_l}\right)^{-1}} \right\| =$$

$$\left\| \frac{\sqrt{2}\sqrt{\sqrt{1 + (n + v_l)^2} + n + v_l}}{\sqrt{\lambda - n - v_l} + \sqrt{\lambda + i\varepsilon - n - v_l}} \right\| \varepsilon \le \left\| \frac{\sqrt{2}\sqrt{\sqrt{1 + (n + v_l)^2} + n + v_l}}{2\sqrt{\lambda - n - v_l}} \right\| \varepsilon.$$

The norm in the right hand side is bounded for integer n, so:

$$\frac{m^{H_l}(\lambda - n) - (m^{H_l}(\lambda + i\varepsilon - n))}{\operatorname{Im}(m^{H_l}(i - n))} \to 0, \quad \varepsilon \to +0,$$

uniformly with respect to n. Analogously we deal with M^{S_r}.

Let us show that the operator:

$$(\Theta - M^S(\lambda + i\varepsilon))^{-1}$$

exists. It is sufficient to show that $(\operatorname{Im}(M^S(\lambda)))^{-1}$ exists.

Lemma 3.3. $(\operatorname{Im}(M^S(\lambda)))^{-1}$ *exists for* $\lambda \neq n + v_l$ *and* $\lambda \neq n + v_r$.

Consider:

$$\operatorname{Im}(M^{S_l}(\lambda)) = \frac{\operatorname{Im}(m^{H_l}(\lambda - T))}{\operatorname{Im}(m^{H_l}(i - T))} = \bigoplus_{n=0}^{\infty} \frac{\operatorname{Im}(i\sqrt{\lambda - n - v_l})}{\operatorname{Im}(m^{H_l}(i - n))} = \bigoplus_{n=0}^{\infty} \frac{\operatorname{Re}(\sqrt{\lambda - n - v_l})}{\operatorname{Im}(m^{H_l}(i - n))}$$

and $\operatorname{Re}(\sqrt{\lambda - n - v_l}) = 0$ when $n \ge \lambda - v_l$ and $\operatorname{Re}(\sqrt{\lambda - n - v_l}) = \sqrt{\lambda - n - v_l}$ when $n < \lambda - v_l$. If $\lambda \neq n + v_l$ then:

$$\operatorname{Im}(M^{S_l}(\lambda))^{-1} = \bigoplus_{0}^{n < \lambda - v_l} \frac{\operatorname{Im}(m^{H_l}(i - n))}{\sqrt{\lambda - n - v_l}}.$$

Analogously, we deal with M^{S_r}.

For scattering matrix description, we need to calculate $\sqrt{\operatorname{Im}(M(\lambda + 0i))} = \sqrt{\operatorname{Im}(M(\lambda))}$.

Lemma 3.4. *Operator* $\sqrt{\operatorname{Im}(M(\lambda))}$ *has the following form:*

$$\sqrt{\operatorname{Im}(M(\lambda))} = \begin{pmatrix} \sqrt{\displaystyle\bigoplus_{n=0}^{n < \lambda - v_l} \frac{\sqrt{\lambda - n - v_l}}{\operatorname{Im}(m^{H_l}(i - n))} \oplus \bigoplus_{n \ge \lambda - v_l} 0} & 0 \\ 0 & \sqrt{\displaystyle\bigoplus_{n=0}^{n < \lambda - v_r} \frac{\sqrt{\lambda - n - v_r}}{\operatorname{Im}(m^{H_r}(i - n))} \oplus \bigoplus_{n \ge \lambda - v_r} 0} \end{pmatrix},$$

$$\operatorname{Im}(M^{S_l}(\lambda)) = \operatorname{Im}\left(\frac{m^{H_l}(\lambda - T) - \operatorname{Re}(m^{H_l}(i - T))}{\operatorname{Im}(m^{H_l}(i - T))}\right) = \frac{\operatorname{Im}(m^{H_l}(\lambda - T))}{\operatorname{Im}(m^{H_l}(i - T))}.$$

Now, as far as $m^{H_l} = i\sqrt{z - v_l}$, we obtain:

$$\frac{\operatorname{Im}(m^{H_l}(\lambda - T))}{\operatorname{Im}(m^{H_l}(i - T))} = \bigoplus_{n=0}^{\infty} \frac{\operatorname{Im}(m^{H_l}(\lambda - n))}{\operatorname{Im}(m^{H_l}(i - n))} = \bigoplus_{n=0}^{\infty} \frac{\operatorname{Im}(i\sqrt{\lambda - n - v_l})}{\operatorname{Im}(m^{H_l}(i - n))}.$$

As far as when $n < \lambda - v_l$ we have $\operatorname{Im}(i\sqrt{\lambda - n - v_l}) = \sqrt{\lambda - n - v_l})$ and when $n \ge \lambda - v_l$ we have $\operatorname{Im}(i\sqrt{\lambda - n - v_l}) = 0$, we obtain that:

$$\frac{\operatorname{Im}(m^{H_l}(\lambda - T))}{\operatorname{Im}(m^{H_l}(i - T))} = \bigoplus_{n=0}^{n < \lambda - v_l} \frac{\sqrt{\lambda - n - v_l}}{\operatorname{Im}(m^{H_l}(i - n))}.$$

Then,

$$\mathrm{Im}(M^S(\lambda)) = \begin{pmatrix} \displaystyle\bigoplus_{n=0}^{n<\lambda-v_l} \frac{\sqrt{\lambda-n-v_l}}{\mathrm{Im}(m^{H_l}(i-n))} \oplus \bigoplus_{n\geq\lambda-v_l} 0 & 0 \\[2em] 0 & \displaystyle\bigoplus_{n=0}^{n<\lambda-v_r} \frac{\sqrt{\lambda-n-v_r}}{\mathrm{Im}(m^{H_r}(i-n))} \oplus \bigoplus_{n\geq\lambda-v_r} 0 \end{pmatrix}$$

and

$$\sqrt{\mathrm{Im}(M^S(\lambda))} = \begin{pmatrix} \displaystyle\sqrt{\bigoplus_{n=0}^{n<\lambda-v_l} \frac{\sqrt{\lambda-n-v_l}}{\mathrm{Im}(m^{H_l}(i-n))} \oplus \bigoplus_{n\geq\lambda-v_l} 0} & 0 \\[2em] 0 & \displaystyle\sqrt{\bigoplus_{n=0}^{n<\lambda-v_r} \frac{\sqrt{\lambda-n-v_r}}{\mathrm{Im}(m^{H_r}(i-n))} \oplus \bigoplus_{n\geq\lambda-v_r} 0} \end{pmatrix}.$$

Let Θ be a matrix of the form:

$$\Theta = \begin{pmatrix} \displaystyle\bigoplus_{n=0}^{\infty} \begin{pmatrix} \alpha_n & \gamma_n \\ \overline{\gamma}_n & \beta_n \end{pmatrix} & 0 \\[2em] 0 & \displaystyle\bigoplus_{n=0}^{\infty} \begin{pmatrix} \kappa_n & \eta_n \\ \overline{\eta}_n & \omega_n \end{pmatrix} \end{pmatrix}.$$

Then $\Theta - M(\lambda)$ is a block-diagonal matrix with the first block of the form

$$\bigoplus_{n=0}^{\infty} \begin{pmatrix} \alpha_n - \dfrac{i\sqrt{\lambda-2n-v_l}-\mathrm{Re}(m^{H_l}(i-2n))}{\mathrm{Im}(m^{H_l}(i-2n))} & \gamma_n \\[1.5em] \overline{\gamma}_n & \beta_n - \dfrac{i\sqrt{\lambda-2n-1-v_l}-\mathrm{Re}(m^{H_l}(i-2n-1))}{\mathrm{Im}(m^{H_l}(i-2n-1))} \end{pmatrix}$$

and the second block of the form:

$$\bigoplus_{n=0}^{\infty} \begin{pmatrix} \kappa_n - \dfrac{i\sqrt{\lambda-2n-v_l}-\mathrm{Re}(m^{H_r}(i-2n))}{\mathrm{Im}(m^{H_r}(i-2n))} & \eta_n \\[1.5em] \overline{\eta}_n & \omega_n - \dfrac{i\sqrt{\lambda-2n-1-v_l}-\mathrm{Re}(m^{H_r}(i-2n-1))}{\mathrm{Im}(m^{H_r}(i-2n-1))} \end{pmatrix}.$$

Let:

$$\Delta_1(n) = \left(\alpha_n - \frac{i\sqrt{\lambda-2n-v_l}-\mathrm{Re}(m^{H_l}(i-2n))}{\mathrm{Im}(m^{H_l}(i-2n))}\right) \times$$
$$\left(\beta_n - \frac{i\sqrt{\lambda-2n-1-v_l}-\mathrm{Re}(m^{H_l}(i-2n-1))}{\mathrm{Im}(m^{H_l}(i-2n-1))}\right) - \gamma_n\overline{\gamma}_n$$

and:

$$\Delta_2(n) = \left(\kappa_n - \frac{i\sqrt{\lambda-2n-v_l}-\mathrm{Re}(m^{H_r}(i-2n))}{\mathrm{Im}(m^{H_r}(i-2n))}\right) \times$$
$$\left(\omega_n - \frac{i\sqrt{\lambda-2n-1-v_l}-\mathrm{Re}(m^{H_r}(i-2n-1))}{\mathrm{Im}(m^{H_r}(i-2n-1))}\right) - \eta_n\overline{\eta}_n.$$

Theorem 3.5. *The operator* $(\Theta - M^S(\lambda+i\varepsilon))^{-1}$ *exists. It has the block structure with the first block of the form:*

$$\bigoplus_{n=0}^{\infty} \frac{1}{\Delta_1(n)} \begin{pmatrix} \beta_n - \dfrac{i\sqrt{\lambda-2n-1-v_l}-\mathrm{Re}(m^{H_l}(i-2n-1))}{\mathrm{Im}(m^{H_l}(i-2n-1))} & -\gamma_n \\[1.5em] -\overline{\gamma}_n & \alpha_n - \dfrac{i\sqrt{\lambda-2n-v_l}-\mathrm{Re}(m^{H_l}(i-2n))}{\mathrm{Im}(m^{H_l}(i-2n))} \end{pmatrix}$$

and the second block of the form:

$$\bigoplus_{n=0}^{\infty} \frac{1}{\Delta_2(n)} \begin{pmatrix} \omega_n - \dfrac{i\sqrt{\lambda-2n-1-v_l}-\mathrm{Re}(m^{H_r}(i-2n-1))}{\mathrm{Im}(m^{H_r}(i-2n-1))} & -\eta_n \\[1.5em] -\overline{\eta}_n & \kappa_n - \dfrac{i\sqrt{\lambda-2n-v_l}-\mathrm{Re}(m^{H_r}(i-2n))}{\mathrm{Im}(m^{H_r}(i-2n))} \end{pmatrix}.$$

The expression for the scattering matrix is given in Theorem 2.5.

4. Conclusion

An extended Jaynes–Cummings model using the ideas of [8] is constructed. It is based on the theory of self-adjoint extensions of symmetric operators. The theory gives one a rigorous mathematical methodology for introducing coupling between bosons (photons), two-level quantum dot (quantum resonator) and two semi-infinite wires. Boundary triplets, gamma-field and Krein Q-functions are found. We obtain the Weyl function. This allows us to determine the scattering matrix. Mathematical details of the model are thoroughly investigated in [17].

Acknowledgements

References

[1] Aschbacher W., Jaksic V., Pautrat Y., Pillet C.-A. Transport properties of quasi-free fermions. *J. Math. Phys.*, 2007, **48**(3), P. 032101.

[2] Cornean H.D., Neidhardt H., Wilhelm L., Zagrebnov V.A. The Cayley transform applied to non-interacting quantum transport. *J. Funct. Anal.*, 2014, **266**(3), P. 14211475.

[3] Nenciu G. Independent electron model for open quantum systems: Landauer-Bttiker formula and strict positivity of the entropy production. *J. Math. Phys.*, **48**(3), P. 033302.

[4] Gerry C., Knight P. *Introductory Quantum Optics.* 2005. Cambridge University Press, Cambridge.

[5] Cummings F.W. Reminiscing about thesis work with E.T. Jaynes at Stanford in the 1950s. *Journal of Physics B: Atomic, Molecular and Optical Physics*, 2013, **46**(22), P. 220202.

[6] Rodriguez-Lara B., Moya-Cessa H., Klimov A. Combining Jaynes-Cummings and anti-Jaynes-Cummings dynamics in a trapped-ion system driven by a laser. *Physical Review A*, 2005, **71**(2), P. 023811.

[7] Neidhardt H., Wilhelm L., Zagrebnov V.A. A new model of quantum dot light emitting-absorbing devices. *J. Math. Phys. Anal. Geom.*, 2014, **10**(3), P. 350–385.

[8] Neidhardt H., Wilhelm L., Zagrebnov V.A. A new model for quantum dot light emitting-absorbing devices: proofs and supplements. *Nanosystems: Physics, Chemistry, Mathematics*, 2015, **6**(1), P. 6–45.

[9] Albeverio S., Gesztesy F., Hoegh-Krohn R., Holden H. with an appendix by P. Exner, Solvable Models in Quantum Mechanics, second ed., AMS Chelsea Publishing, Providence, 2005.

[10] Pavlov B.S., The theory of extensions and explicity-solvable models, *Russ. Math. Surv.*, 1987, **42**(6), P. 127–168.

[11] Albeverio S., Kurasov P. Singular perturbations of differential operators. Solvable Schrodinger type operators (London Mathematical Society Lecture Notes 271), Cambridge Univ. Press, Cambridge. 2000.

[12] Popov I.Y., Kurasov P.A., Naboko S.N., Kiselev A.A., Ryzhkov A.E., Yafyasov A.M., Miroshnichenko G.P., Karpeshina Yu.E., Kruglov V.I., Pankratova T.F., Popov A.I.: A distinguished mathematical physicist Boris S. Pavlov. *Nanosystems: Phys. Chem. Math.* 2016, **7**, P. 782–788.

[13] Behrndt J., Malamud M.M., Neidhardt H. Scattering matrices and Weyl function. *Proc. London Math. Soc.*, 2008, **97**(3), P. 568–598.

[14] Boitsev A.A., Neidhardt H., Popov I.Y. Dirac operator coupled to bosons. *Nanosystems: Phys. Chem. Math.*, 2016, **7**, P. 332–339.

[15] Behrndt J., Langer M., Lotoreichik V. Boundary triples for Schrödinger operators with singular interactions on hypersurfaces. *Nanosystems: Phys. Chem. Math.*, 2016, **7**, P. 290–302.

[16] Mantile A., Posilicano A. Laplacians with singular perturbations supported on hypersurfaces. *Nanosystems: Phys. Chem. Math.*, 2016, **7**, P. 315–323.

[17] Boitsev A.A., Brasche J.F., Malamud M.M., Neidhardt H., Popov I.Yu. Boundary triplets, tensor products and point contacts to reservoirs. arXiv:1710.07525v1 [math-ph], 2017, 62 pages (accepted in Ann. Henri Poincare).

[18] Derkach V.A., Malamud M.M. Generalized resolvents and the boundary value problems for Hermitian operators with gaps. *J. Funct. Anal.*, 1991, **95**(1), P. 1–95.

[19] Malamud M.M. Some classes of extensions of a Hermitian operator with lacunae, *Ukraïn. Mat. Zh.*, 1992, **44**(2), P. 215–233.

[20] Baumgartel H., Wollenberg M. *Mathematical Scattering Theory*. Akademie-Verlag, Berlin, 1983.

[21] Kato T. *Perturbation Theory for Linear Operators*. Springer-Verlag New York, Inc., New York, 1966.

[22] Yafaev D.R. *Mathematical Scattering Theory: General Theory. Translations of Mathematical Monographs, 105*. American Mathematical Society, Providence, RI, 1992.

[23] Donoghue W.F. *Monotone Matrix Functions and Analytic Continuation*. Springer Verlag, Berlin and New York, 1974.

Level crossings of eigenvalues of the Schrödinger Hamiltonian of the isotropic harmonic oscillator perturbed by a central point interaction in different dimensions

S. Fassari[1,2,3], M. Gadella[1], M. L. Glasser[1,4], L. M. Nieto[1], F. Rinaldi[2,3]

[1]Departamento de Física Teórica, Atómica y Óptica, U. Valladolid, 47011 Valladolid, Spain
[2]CERFIM, PO Box 1132, Via F. Rusca 1, CH-6601 Locarno, Switzerland
[3]Dipartimento di Fisica Nucleare, Subnucleare e delle Radiazioni,
Univ. degli Studi Guglielmo Marconi, Via Plinio 44, I-00193 Rome, Italy
[4]Department of Physics, Clarkson University, Potsdam, NY, 13699 USA

silvestro.fassari@uva.es, gadella@fta.uva.es, laryg@tds.net, luismiguel.nieto.calzada@uva.es, matfa62@gmail.com

In this brief presentation, some striking differences between level crossings of eigenvalues in one dimension (harmonic or conic oscillator with a central nonlocal δ'-interaction) or three dimensions (isotropic harmonic oscillator with a three-dimensional delta located at the origin) and those occurring in the two-dimensional analogue of these models will be highlighted.

Keywords: harmonic oscillator, point interactions, renormalisation, eigenvalues, level crossing.

1. Introduction

The aim of this note is to compare the discrete spectrum of the isotropic harmonic oscillator perturbed by a point interaction centered at the origin, the bottom of a parabolic well, across various dimensions. The physical motivation behind this detailed study is the fact that this Hamiltonian, at least in the three-dimensional case, has been used over the last twenty years to model two-dimensional quantum wires and three-dimensional quantum dots.

It is important to point out and is well known that, while in two or three dimensions there is only one type of point interaction, namely the 2/3D delta (requiring a renormalization procedure if it is to be a perturbation of the negative Laplacian or any other free Hamiltonian), in one-dimensional Quantum Mechanics we have four different types of point interactions, out of which, the only one requiring such renormalization is the nonlocal $\delta'-$interaction, defined by its quadratic form $(\cdot, |\delta'\rangle \langle \delta'|, \cdot)$ (see [1–3]). A self-adjoint Hamiltonian with the nonlocal $\delta'-$interaction can also be defined as the norm resolvent limit of a Hamiltonian involving three Dirac distributions (see [4–6]). We remind the reader that this interaction, being an element of $\mathcal{H}_{-2}\backslash\mathcal{H}_{-1}$, may not be combined with the Dirac distribution, obviously an element of $\mathcal{H}_{-1}$ (the reader is referred to [2] for a thorough description of the Sobolev spaces labelled by a negative index).

While the spectral features of the three-dimensional isotropic oscillator perturbed by a single point interaction centered at the origin have been extensively investigated (see [7–10]), less attention has been paid to those of its two-dimensional analog. The remarkable spectral feature of the three-dimensional case is the existence of level crossings: each eigenvalue created by the point perturbation, clearly affecting only the s-states of the model, regarded as a function of either the parameter α labelling the possible self-adjoint extensions or its reciprocal β (acting as the coupling constant), crosses the next lower unperturbed energy level (pertaining to an antisymmetric state with an odd value of the total angular momentum). Even more remarkable, all the level crossings take place for the same coupling parameter value.

As was shown in [11] (respectively [12, 13]), level crossings also occur in the entirely discrete spectrum of the one-dimensional harmonic (respectively conic) oscillator perturbed by a nonlocal δ'-interaction. This one-dimensional model shares the property of having all the crossings situated at the same point when either the extension parameter or the coupling parameter is chosen. However, the nature of such crossings is different from the aforementioned in three dimensions, as the eigenenergy of each antisymmetric bound state, regarded as a function of either the extension parameter α, labeling the self-adjoint extensions, or the coupling β, its reciprocal, crosses the next lower unperturbed energy level (pertaining to a symmetric state). With reference to the terminology

introduced in [14], one could describe the one-dimensional model as Fermionic and the three-dimensional model as Bosonic.

Therefore, we believe it may be worth investigating the spectral properties of the two-dimensional analog in depth given the increasing importance of this particular dimension in modern Nanophysics. As expected, level crossings also occur in the two-dimensional case. However, it will be seen that the location of these crossings is no longer at a unique parameter value. Furthermore, while in odd dimensions the interaction must be attractive in order to produce the crossings, a weaker repulsive interaction will suffice in the two-dimensional model.

2. Level crossings in the discrete spectrum of the one-dimensional harmonic or conic oscillator perturbed by a central nonlocal δ'-interaction

In this section, we shall review the findings of [11] (respectively [12, 13]) showing the occurrence of level crossings in the discrete spectrum of the harmonic (resp. conic) oscillator perturbed by a nonlocal δ'−interaction centred at the minimum of the parabolic (resp. V-shaped) potential.

It is well known that the Schrödinger Hamiltonian perturbed by a Dirac distribution need not be defined by means of renormalization, since such a perturbation is infinitesimally small in the sense of quadratic forms (see [1, 2]). Therefore, the Dirac distribution can be regarded as an element of $\mathcal{H}_{-1}$.

As anticipated earlier, the nonlocal δ'-perturbation of the one-dimensional negative Laplacian, being an element of $\mathcal{H}_{-2}\backslash\mathcal{H}_{-1}$, requires instead either the self-adjoint extension method or coupling constant renormalisation to produce a self-adjoint Hamiltonian (see [1, 2]).

The spectral effects of such a singular perturbation on the harmonic oscillator were studied in [11] starting from the explicit expression for the resolvent of the self-adjoint operator H_β acting like $H_0 = \dfrac{1}{2}\left[-\dfrac{d^2}{dx^2} + x^2\right]$ on the functions satisfying the condition $\psi(0^+) - \psi(0^-) = -\beta\psi'(0)$:

$$[H_\beta - E]^{-1} = [H_0 - E]^{-1} + \frac{2\,|\Psi(E)\rangle\,\langle\Psi(E)|}{\frac{1}{\beta} - \frac{1}{\beta_0} + \frac{2\Gamma(3/4 - E/2)}{\Gamma(1/4 - E/2)}}, \tag{1}$$

with $\beta_0 = \dfrac{\Gamma(1/4)}{2\Gamma(3/4)} \cong 1.47934$ and:

$$\Psi(x; E) = \sum_{n=0}^{\infty} \frac{(2n+1)^{1/2}\psi_{2n}(0)}{(2n+3/2 - E)}\psi_{2n+1}(x), \tag{2}$$

$\psi_n(x)$ being the n-th normalized eigenfunction of the harmonic oscillator. The latter function, having a jump discontinuity satisfying the condition $\psi(0^+) - \psi(0^-) = -\beta\psi'(0)$, is square summable since the sequence $\psi_{2n}(0)$ behaves like $n^{-1/4}$ as $n \to \infty$. Hence, the equation determining the bound state energies of H_β is:

$$\frac{1}{\beta_0} - \frac{1}{\beta} = \frac{2\Gamma(3/4 - E/2)}{\Gamma(1/4 - E/2)}. \tag{3}$$

Clearly, given that the perturbation does not affect the symmetric subspace, the even eigenvalues $E_{2n} = 2n + 1/2$ of the unperturbed harmonic oscillator are still in the discrete spectrum for any value of β. Each new odd energy level created by the perturbation is a decreasing function of the coupling parameter β (as can be easily seen by means of implicit differentiation), namely $E_{2n+1}(\beta)$. For $\beta = 0$, the operator trivially coincides with H_0, so the odd eigenvalues are also those of the harmonic oscillator $E_{2n+1} = 2n + 3/2$. Something remarkable occurs for $\beta = \beta_0$: as the left hand side of (3) vanishes, the only values of the energy that can satisfy (3) are those that make the Gamma function in the denominator diverge, which implies that $1/4 - E/2 = -n$, or equivalently $E_{2n+1}(\beta_0) = 2n + 1/2$. Therefore, the discrete spectrum of H_{β_0} consists only of the doubly degenerate eigenvalues $E_{2n}(\beta_0) = E_{2n+1}(\beta_0) = 2n + 1/2$. As $E_{2n+1}(\beta) < E_{2n}(\beta) = 2n + 1/2$ for any $\beta > \beta_0$, we have infinitely many level crossings to the right of the critical value β_0 of the coupling parameter. The plot shown in Fig. 1 depicts the three lowest level crossings.

It is worth pointing out from a physical point of view that, since the symmetry of the ground state eigenfunction changes from symmetric to antisymmetric for any $\beta > \beta_0$, the model exhibits a quantum phase transition. Furthermore, the effect produced by the singular δ'−perturbation is far stronger than the Zeldovich effect produced by the δ−interaction due to the fact that the horizontal asymptotes of the curves are situated below the horizontal lines pertaining to the unperturbed symmetric eigenvalues (see [15–17] for a detailed description of the spectrum of the 1D harmonic oscillator perturbed by Dirac distributions).
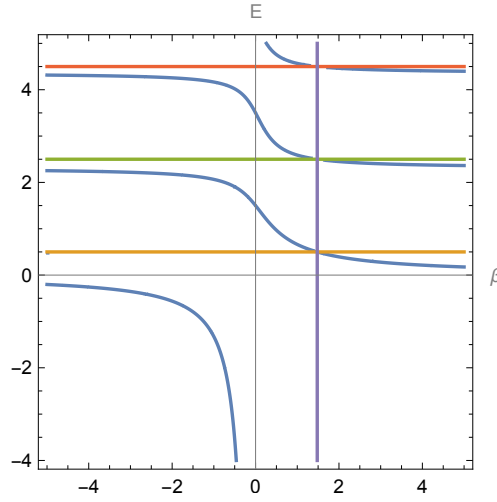
FIG. 1. The curves of the four lowest eigenenergies of H_β as functions of the coupling parameter β, and the level crossings occurring at $\beta = \beta_0 = \dfrac{\Gamma(1/4)}{2\Gamma(3/4)} \cong 1.47934$. The horizontal lines are the even energy levels of the unperturbed harmonic oscillator: $E_0 = 1/2$ (yellow), $E_2 = 5/2$ (green), $E_4 = 9/2$ (red)

The same spectral pattern has recently been encountered in the discrete spectrum of the self-adjoint Hamiltonian of the conic oscillator H_β^c acting like $H_0^c = \dfrac{1}{2}\left[-\dfrac{d^2}{dx^2} + |x|\right]$ on functions satisfying the condition $\psi(0^+) - \psi(0^-) = -\beta\psi'(0)$, whose resolvent is explicitly given by (see [12, 13] for the procedure requiring renormalization needed to define H_β^c):

$$\left[H_\beta^c - E\right]^{-1} = [H_0 - E]^{-1} + \frac{|\Psi^c(E)\rangle\langle\Psi^c(E)|}{\frac{1}{\beta} - \frac{\mathrm{Ai}(0)\mathrm{Ai}'(-2E) - \mathrm{Ai}'(0)\mathrm{Ai}(-2E)}{\mathrm{Ai}(0)\mathrm{Ai}(-2E)}}, \tag{4}$$

with:

$$\Psi^c(x; E) = \frac{1}{2^{1/2}}\sum_{n=1}^{\infty}\frac{\psi_{2n}(x)}{(E_{2n} - E)}, \tag{5}$$

where $\psi_{2n}(x)$ is the $2n$-th normalized eigenfunction (pertaining to an antisymmetric bound state) of H_0^c and E_{2n} the corresponding eigenvalue, fully investigated in [18]. The function $\Psi^c(x; E)$ is also a square summable function since the sequence $(E_{2n} - E)^{-1}$ behaves like $n^{-2/3}$ as $n \to \infty$ and has a jump discontinuity at the origin satisfying the condition $\psi(0^+) - \psi(0^-) = -\beta\psi'(0)$.

As a consequence, the bound state equation reads:

$$\frac{1}{\beta} = \frac{\mathrm{Ai}(0)\mathrm{Ai}'(-2E) - \mathrm{Ai}'(0)\mathrm{Ai}(-2E)}{\mathrm{Ai}(0)\mathrm{Ai}(-2E)}, \tag{6}$$

or equivalently:

$$\beta = \frac{\mathrm{Ai}(0)\mathrm{Ai}(-2E)}{\mathrm{Ai}(0)\mathrm{Ai}'(-2E) - \mathrm{Ai}'(0)\mathrm{Ai}(-2E)}. \tag{7}$$

Given that $\mathrm{Ai}'(-2E_{2n-1}) = 0$ for any $n \geq 1$, it follows that, if the energy is exactly equal to any odd eigenvalue (pertaining to a symmetric bound state), the right hand side of (7) is equal to:

$$\beta_0^c = -\frac{\mathrm{Ai}(0)}{\mathrm{Ai}'(0)}, \tag{8}$$

which implies that such eigenvalues cause the denominator of the rank one operator on the right hand side of (4) for the special value of the coupling parameter $\beta = \beta_0^c = -\dfrac{\mathrm{Ai}(0)}{\mathrm{Ai}'(0)} \cong 1.37172$ to vanish. This leads to their double degeneracy as eigenvalues of the Hamiltonian $H_{\beta_0^c}^c$ and the ensures level crossings at that particular value of the coupling.

The blue curves in Fig. 2 depict $E_0(\beta)$, $E_2(\beta)$ and $E_4(\beta)$, the three lowest lying energy levels pertaining to antisymmetric bound states generated by the singular perturbation as functions of the coupling parameter. The yellow horizontal line represents E_1 and the green one E_3, the energies of the two lowest symmetric bound states. Quite obviously, the spacing between two consecutive energy levels of H_0^c, the Hamiltonian of the unperturbed conic oscillator, is not constant in contrast with what happens for the harmonic oscillator. Nevertheless, the spectral features are qualitatively identical to those observed in the latter case: all the level crossings take place for the same value of the coupling parameter which is located to the right of the origin. Identically to what has already been seen in the case of the harmonic oscillator, the effect produced by this perturbation is far stronger than the one named after Zeldovich occurring for an attractive $\delta-$interaction.
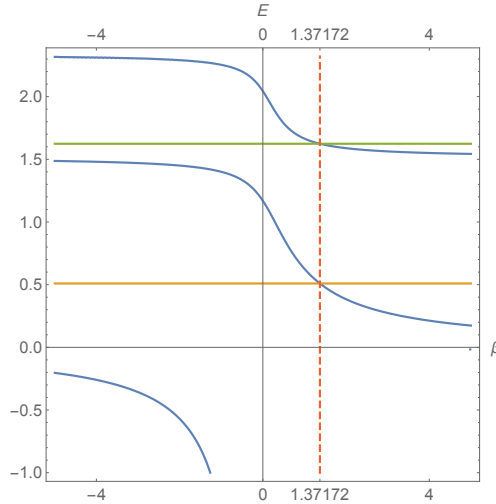
FIG. 2. The curves of the three lowest eigenenergies as functions of the coupling parameter β, and the level crossings occurring at $\beta = \beta_0^c = -\dfrac{\mathrm{Ai}(0)}{\mathrm{Ai}'(0)} \cong 1.37172$. The horizontal lines are the energy levels of the unperturbed conic oscillator: E_1 (yellow) and E_3 (green)

3. Level crossings in the discrete spectrum of the three-dimensional isotropic harmonic oscillator perturbed by a central δ-interaction

It is well known that the three-dimensional negative Laplacian perturbed by the Dirac distribution cannot be defined by means of the KLMN theorem since such a perturbation is no longer infinitesimally small in the sense of quadratic forms (see [1,2]). The same obviously holds in the presence of an harmonic confining potential.

The self-adjoint operator H_β, representing the Hamiltonian of he three-dimensional isotropic harmonic oscillator perturbed by a central $\delta-$interaction, defined either by means of the self-adjoint extension method or renormalization, has been investigated in depth in [7–10]. The entirely discrete spectrum of the operator, in particular the lowest lying eigenvalues, has also been studied in detail in those papers. The operator is rigorously defined by means of the explicit formula for its resolvent, namely:

$$[H_\beta - E]^{-1} = [H_0 - E]^{-1} + \frac{2\,|\Psi(E)\rangle\,\langle\Psi(E)|}{\frac{1}{\beta} - \frac{1}{\beta_0} + \frac{\Gamma(3/4 - E/2)}{\pi\Gamma(1/4 - E/2)}}, \tag{9}$$

with $\beta_0 = \dfrac{\pi\Gamma(1/4)}{\Gamma(3/4)} \cong 9.29495$ and:

$$\Psi(x, y, z; E) = \sum_{n_1=0}^{\infty} \sum_{n_2=0}^{\infty} \sum_{n_3=0}^{\infty} \frac{\psi_{2n_1}(0)\psi_{2n_2}(0)\psi_{2n_3}(0)}{2n_1 + 2n_2 + 2n_3 + \frac{3}{2} - E}\psi_{2n_1}(x)\psi_{2n_2}(y)\psi_{2n_3}(z), \tag{10}$$

whose norm, for any $E < 0$, is bounded by:

$$\left[\sum_{n=0}^{\infty} \frac{\psi_{2n}^2(0)}{(2n + \frac{1}{2})^{2/3}}\right]^{3/2} < \infty, \tag{11}$$

since the sequence $\psi_{2n}(0)$ behaves like $n^{-1/4}$ as $n \to \infty$.

As is well known, the eigenenergy $2n_1 + 2n_2 + 2n_3 + \dfrac{3}{2}$ in the discrete spectrum of the three-dimensional isotropic harmonic oscillator has degeneracy $\dfrac{1}{2}(2n_1 + 2n_2 + 2n_3 + 1)(2n_1 + 2n_2 + 2n_3 + 2)$. Out of all the eigenstates sharing this energy, only the one having radial symmetry will be affected by the 3D point perturbation and give rise to a new simple eigenvalue, thus lowering the original degeneracy of the level to $\dfrac{1}{2}(2n_1 + 2n_2 + 2n_3 + 1)(2n_1 + 2n_2 + 2n_3 + 2) - 1$. This new simple eigenvalue is determined as a function of the coupling parameter by the equation:

$$\frac{1}{\beta_0} - \frac{1}{\beta} = \frac{\Gamma(3/4 - E/2)}{\pi\Gamma(1/4 - E/2)}. \tag{12}$$

It is worth noting that, apart from the different constant multiplying the ratio of Gamma functions on the right hand side, the latter equation is of the same type of (3). However, the zeros of the entire function $\dfrac{1}{\pi\Gamma(1/4 - E/2)}$ are now given by $E = 2N + \dfrac{5}{2}$, the eigenenergies pertaining to the antisymmetric states, so that for the particular value $\beta = \beta_0$ the degeneracy of the next lower antisymmetric state increases by one. Hence, we get level crossings occurring for the unique value of the coupling parameter, namely $\beta_0 = \dfrac{\pi\Gamma(1/4)}{\Gamma(3/4)} \approx 9.29495$. Therefore, the 3D point perturbation must be strongly attractive in order to exhibit the level crossing phenomenon.

In Fig. 3, the lowest level crossings between the new eigenvalues created by the point perturbation and the antisymmetric levels $E = \dfrac{5}{2}, \dfrac{9}{2}, \dfrac{13}{2}$, clearly unaffected by the singular perturbation, are depicted. Therefore, also in the three-dimensional case, the effect is stronger than the Zeldovich effect that would occur in the presence of any short range interaction.
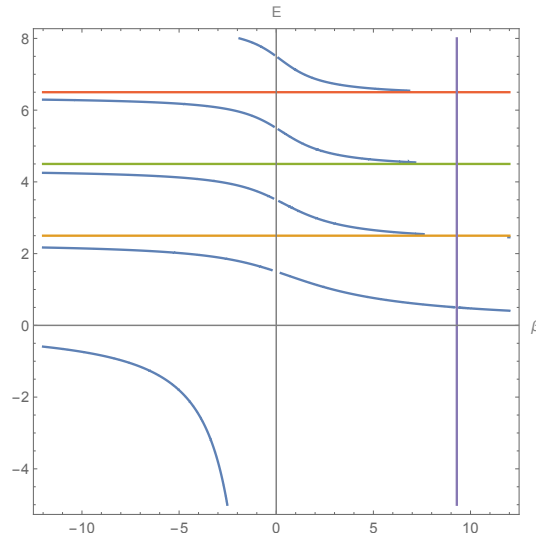
FIG. 3. The three lowest level crossings between the new eigenvalues created by the point perturbation and the antisymmetric levels $E = \dfrac{5}{2}, \dfrac{9}{2}, \dfrac{13}{2}$, clearly unaffected by the singular perturbation

4. Level crossings in the discrete spectrum of the two-dimensional isotropic harmonic oscillator perturbed by a central δ-interaction

In perfect analogy with the three-dimensional case, the two-dimensional self-adjoint Hamiltonian H_β representing the Hamiltonian of the two-dimensional isotropic harmonic oscillator perturbed by a central $\delta-$interaction, can be defined by means of the self-adjoint extension theory or by renormalization. Its discrete spectrum, in particular the lowest lying eigenvalues, has been investigated far less than the three-dimensional analog (see [19, 20]).

As the intermediate steps would be identical to those for the three-dimensional case (see [7]), we omit them and write the limit as $N \to \infty$ in the norm topology of the resolvents, that is to say the counterpart of (4) in [7]:

$$(H_\beta - E)^{-1} = (H_0 - E)^{-1} + \frac{|\Psi(E)\rangle\langle\Psi(E)|}{\dfrac{1}{\beta} - E \displaystyle\sum_{n_1=0}^{\infty}\sum_{n_2=0}^{\infty} \dfrac{\psi_{2n_1}^2(0)\psi_{2n_2}^2(0)}{(2n_1 + 2n_2 + 1)(2n_1 + 2n_2 + 1 - E)}} \tag{13}$$

with:

$$\Psi(x, y; E) = \sum_{n_1=0}^{\infty}\sum_{n_2=0}^{\infty} \frac{\psi_{2n_1}(0)\psi_{2n_2}(0)}{2n_1 + 2n_2 + 1 - E}\psi_{2n_1}(x)\psi_{2n_2}(y), \tag{14}$$

whose norm, for any $E < 0$, is bounded by:

$$\sum_{n=0}^{\infty} \frac{\psi_{2n}^2(0)}{(2n + \frac{1}{2})} < \infty \tag{15}$$

since the sequence $\psi_{2n}(0)$ behaves like $n^{-1/4}$ as $n \to \infty$.

Given that the eigenvalues of the operator H_β are exactly the poles of its resolvent, in order to achieve an accurate description of the spectrum (obviously being exclusively discrete) of the operator, we need only look for the solutions of the equation:

$$\frac{1}{\beta} = E \sum_{n_1=0}^{\infty}\sum_{n_2=0}^{\infty} \frac{\psi_{2n_1}^2(0)\psi_{2n_2}^2(0)}{(2n_1 + 2n_2 + 1)(2n_1 + 2n_2 + 1 - E)}. \tag{16}$$

The striking difference between the latter equation and its three-dimensional counterpart is that the right hand side cannot be recast as a ratio of Gamma functions; this can be seen as follows. By exploiting the well-known integral relationship between the resolvent and the semigroup for any semibounded operator for any E below the lowest point in the spectrum (see, e.g., [21] page 204), as well as the fact that the integral kernel of the semigroup of the two-dimensional harmonic oscillator is perfectly separable, we get that the right hand side of the above equation reads for any $E < 1$:

$$\frac{1}{\beta} = \frac{1}{\pi} \int_0^{\infty} \frac{e^t\left(e^{Et} - 1\right)}{e^{2t} - 1}dt = \frac{1}{\pi} \int_0^{\infty} \frac{e^{-t}\left(e^{Et} - 1\right)}{1 - e^{-2t}}dt = \frac{1}{\pi} \int_0^1 \frac{\xi^{-E} - 1}{1 - \xi^2}d\xi. \tag{17}$$

It is not difficult to show that the last integral on the right hand side can be recast as a limit of an expression involving Gamma functions so that the bound state equation becomes:

$$\alpha = \frac{1}{2\pi} \lim_{\varepsilon \to 0_+} \Gamma(\varepsilon)\left[\frac{\Gamma(1/2 - E/2)}{\Gamma(1/2 - E/2 + \varepsilon)} - \frac{\Gamma(1/2)}{\Gamma(1/2 + \varepsilon)}\right]. \tag{18}$$

By exploiting the well-known identity:

$$\Gamma(\varepsilon)\Gamma(1 - \varepsilon) = \frac{\pi}{\sin(\pi\varepsilon)},$$

and the limits:

$$\lim_{\varepsilon \to 0_+} \frac{\sin(\pi\varepsilon)}{\varepsilon} = \pi, \qquad \lim_{\varepsilon \to 0_+} \Gamma(1 - \varepsilon) = 1,$$

equation (18) can be transformed into:

$$\alpha = \frac{1}{2\pi} \lim_{\epsilon \to 0_+} \frac{1}{\epsilon}\left[\frac{\Gamma(1/2 - E/2)}{\Gamma(1/2 - E/2 + \epsilon)} - \frac{\Gamma(1/2)}{\Gamma(1/2 + \epsilon)}\right]. \tag{19}$$

The limit on the right hand side exists, which leads to an expression involving the difference of two different values of the logarithmic derivative of the Gamma function, namely:

$$\frac{1}{2\pi}\left[\frac{\Gamma'(1/2)}{\Gamma(1/2)} - \frac{\Gamma'(1/2 - E/2)}{\Gamma(1/2 - E/2)}\right] = \frac{1}{2\pi}\left[(\ln\Gamma)'(1/2) - (\ln\Gamma)'(1/2 - E/2)\right]. \tag{20}$$

By noting that:

$$(\ln\Gamma)'(x) = F(x - 1) = -\gamma - \sum_{n=1}^{\infty}\left(\frac{1}{n + x - 1} - \frac{1}{n}\right), \tag{21}$$

where γ denotes the Euler-Mascheroni constant and $F(x - 1)$ is the Digamma function, the latter expression can be recast as:

$$\frac{1}{2\pi}\left[F(-1/2) - F(-1/2 - E/2)\right] = \frac{E}{4\pi}\sum_{n=1}^{\infty} \frac{1}{\left(n - \frac{1}{2}\right)\left(n - \frac{1+E}{2}\right)}. \tag{22}$$

Hence, the equation determining the perturbed eigenvalues of our Hamiltonian can be written either in terms of the difference of two different values of the Digamma function or in terms of a simple series (reducing to a telescoping one when E is any integer with the exclusion of all odd positive ones):

$$\frac{1}{\beta} = \frac{1}{2\pi}\left[F(-1/2) - F(-1/2 - E/2)\right] = \frac{E}{4\pi}\sum_{n=0}^{\infty}\frac{1}{\left(n + \frac{1}{2}\right)\left(n + \frac{1-E}{2}\right)}. \tag{23}$$

In particular, for any E given by a positive even number, the total energy of an antisymmetric state, the series on the right hand side becomes a simple telescoping series so that it is rather straightforward to find the location of the points where level crossings occur. For the lowest antisymmetric level with $E = 2$ we find $\beta_1 = -\pi$, whereas for the upper one $E = 4$ we have $\beta_2 = -\frac{3}{4}\pi$.

Figure 4 depicts the two lowest level crossings between the new eigenvalues of the perturbed Hamiltonian as functions of the strength of the point interaction and the two lowest antisymmetric levels of the 2D harmonic oscillator clearly belonging to the spectrum of perturbed Hamiltonian. As anticipated in the introduction, the first striking difference between Fig. 4 and Fig. 3, its three-dimensional counterpart, is that in the plot of the two-dimensional model the level crossings take place to the left of the origin, which implies that in two dimensions the point perturbation need only be weakly repulsive to produce the level crossing. Furthermore, each level crossing occurs at a different value of the coupling parameter.
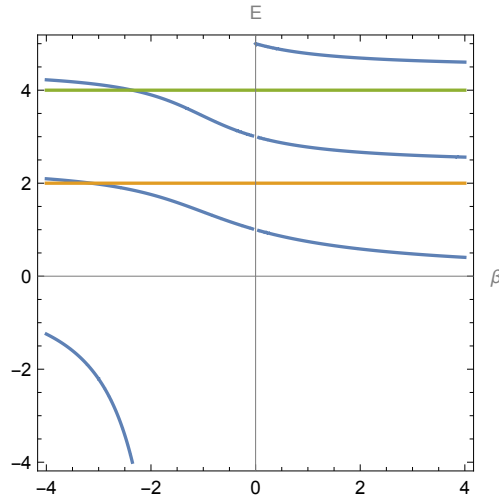
FIG. 4. Plot of the two lowest level crossings between the eigenvalues created by the point perturbation and the two lowest antisymmetric levels of the harmonic oscillator which also belong to the spectrum of the perturbed Hamiltonian

5. Final remarks

The spectral phenomenon known as "level crossing of eigenvalues" has been investigated by considering the entirely discrete spectrum of four different energy operators: the Hamiltonian of the one-dimensional harmonic oscillator perturbed by a nonlocal δ'-interaction, the Hamiltonian of the one-dimensional conic oscillator perturbed by the same singular interaction, the Hamiltonian of the two-dimensional harmonic oscillator perturbed by a δ-interaction and its three-dimensional analog. All the point perturbations considered are highly singular so that the KLMN theorem used to define the δ-perturbation in one dimension may not be invoked.

Although the level crossings in the one-dimensional models share with the three-dimensional model the property of occurring for a unique positive value of the coupling parameter (representing an attractive interaction), their nature is fundamentally different since in one dimension the eigenvalues pertaining to the antisymmetric bound states created by the singular perturbation cross the unperturbed even energy levels, exactly the opposite of what happens in three dimensions.

The two-dimensional model exhibits entirely different features; the crossings take place for different negative values of the coupling parameter so that the singular interaction need only be weakly repulsive to produce the crossings. From a mathematical point of view, the difference is due to the absence of a ratio of Gamma functions in the bound state equation and the appearance of a difference of Digamma functions as a consequence of the

logarithmic divergences of two-dimensional quantum mechanics. Further work to achieve a deeper understanding of the two-dimensional model is ongoing.

Acknowledgements

References

[1] Albeverio S., Gesztesy F., Høegh-Krohn R., Holden H. *Solvable Models in Quantum Mechanics* (AMS Chelsea Series), 2nd edition, American Mathematical Society, Providence, RI, 2004.

[2] Albeverio S., Kurasov P. *Singular Perturbations of Differential Operators*. Publishing House, Cambridge UK, 2000.

[3] Albeverio S., Dabrowski L., Kurasov P. Symmetries of Schrödinger operators with point interactions. *Lett. Math. Phys.*, 1998, **45**, P. 33–47.

[4] Exner P., Neidhardt H., Zagrebnov V.A. Potential approximations to δ': an inverse Klauder phenomenon with norm-resolvent convergence. *Commun. Math. Phys.*, 2001, **224**, P. 593–612.

[5] Fassari S., Rinaldi F. On the spectrum of the Schrödinger Hamiltonian with a particular configuration of three point interactions. *Rep. Math. Phys.*, 2009, **64**, P. 367–393.

[6] Albeverio S., Fassari S., Rinaldi F. The Hamiltonian of the harmonic oscillator with an attractive δ'-interaction centred at the origin as approximated by the one with a triple of attractive δ-interactions. *Journal of Physics A: Mathematical and Theoretical*, 2016, **49**, 025302.

[7] Fassari S., Inglese G. Spectroscopy of a three-dimensional isotropic harmonic oscillator with a delta-type perturbation. *Helv. Phys. Acta*, 1996, **69**, P. 130–140.

[8] Brüning J., Geyler V., Lobanov I. Spectral properties of a short-range impurity in a quantum dot. *J. Math. Phys.*, 2004, **45**, P. 1267–1290.

[9] Albeverio S., Fassari S., Rinaldi F. Spectral properties of a symmetric three-dimensional quantum dot with a pair of identical attractive δ-impurities symmetrically situated around the origin II. *Nanosystems: Physics, Chemistry, Mathematics*, 2016, **7** (5), P. 803–815.

[10] Albeverio S., Fassari S., Rinaldi F. Spectral properties of a symmetric three-dimensional quantum dot with a pair of identical attractive δ-impurities symmetrically situated around the origin. *Nanosystems: Physics, Chemistry, Mathematics*, 2016, **7** (2), P. 268–289.

[11] Albeverio S., Fassari S., Rinaldi F. A remarkable spectral feature of the Schrödinger Hamiltonian of the harmonic oscillator perturbed by an attractive δ'-interaction centred at the origin: double degeneracy and level crossing. *Journal of Physics A: Mathematical and Theoretical*, 2013, **46**, 385305.

[12] Fassari S., Gadella M., Glasser M.L., Nieto L.M. On the spectrum of the Schrödinger Hamiltonian of the one-dimensional conic oscillator perturbed by a point interaction. ArXiv preprint 1706.04916, 2017.

[13] Fassari S., Gadella M., Glasser M.L., Nieto L.M. Spectroscopy of a one-dimensional V-shaped quantum well with a point impurity. *Annals of Physics*, 2018, **389**, P. 48–62.

[14] Cheon T., Shigehara T. Fermion-Boson duality of one-dimensional quantum particles with generalized contact interactions. *Phys. Rev. Lett.*, 1999, **82**, 2536.

[15] Fassari S., Inglese G. On the spectrum of the harmonic oscillator with a delta-type perturbation. *Helv. Phys. Acta*, 1994, **67**, P. 650–659.

[16] Fassari S., Inglese G. On the spectrum of the harmonic oscillator with a delta-type perturbation. II. *Helv. Phys. Acta*, 1997, **70**, P. 858–865.

[17] Fassari S., Rinaldi F. On the spectrum of the Schrödinger Hamiltonian of the one-dimensional harmonic oscillator perturbed by two identical attractive point interactions. *Rep. Math. Phys.*, 2012, **69**, P. 353–370.

[18] Lörinczi J., Ma-lecki J. Spectral properties of the massless relativistic harmonic oscillator. *J. Diff. Eq.*, 2012, **253**, P. 2846–2871.

[19] Tusek M. *Analysis of Two-Dimensional Quantum Models with Singular Potentials*, Diploma Thesis, Czech Technical University, Prague, 2006.

[20] Tunali S. *Point Interactions in Quantum Mechanics*, MS Thesis, Izmir Institute of Technology, Izmir, 2014.

[21] Reed M., Simon B. *Methods in Modern Mathematical Physics IV – Analysis of Operators*, Academic Press, NY, 1978.

An introduction to the two-dimensional Schrödinger equation with nonlinear point interactions

R. Carlone[1], M. Correggi[2], L. Tentarelli[2]

[1]Università "Federico II" di Napoli, Dipartimento di Matematica e Applicazioni "R. Caccioppoli" MSA, via Cinthia, I-80126, Napoli, Italy

[2]"Sapienza" Università di Roma, Dipartimento di Matematica P.le Aldo Moro, 5, 00185, Roma, Italy

raffaele.carlone@unina.it, michele.correggi@gmail.com, tentarelli@mat.uniroma1.it

We present an introduction to the nonlinear Schrödinger equation (NLSE) with concentrated nonlinearities in $\mathbb{R}^2$. Precisely, taking a cue from the linear problem, we sketch the main challenges and the typical difficulties that arise in the two-dimensional case, and mention some recent results obtained by the authors on local and global well-posedness.

Keywords: nonlinear Schrödinger equation, nonlinear delta interactions.

1. Introduction

In the last twenty years the Schrödinger equation with point interactions has proven to be a very useful mathematical tool for modeling many interesting phenomena in several areas of theoretical physics: from foundations of quantum mechanics (e.g., [1–4]) to acoustics (e.g., [5]), from quantum field theory (e.g., [6]) to spectral theory (e.g., [7]). In addition, linear and nonlinear point interactions can be seen as singular perturbations not only of the standard Schrödinger (or heat) equation. They may also appear, for instance, in the study of the Dirac equation, a model which has recently attracted some renewed attention (see e.g., [8–10]).

Linear point interactions arise as a particular, but relevant, application of the more general *theory of self-adjoint extension* of symmetric operators; a theory that has gained new popularity in recent years also for the application to the study of evolution equations in non-standard domains, such as *quantum graphs* (see e.g., [11–26]) and *quantum hybrids* (see e.g., [27–31]).

The extension to nonlinear point interactions appeared first in [32] and its interest is driven by the possibility of investigating nonlinear problems in the context of *solvable models* (i.e., models with an explicit solution) such as, indeed, point interactions. In dimensions d=1,3 these problems have been extensively analyzed and many results have been obtained, such as local and global well-posedness (see [32,33]), occurrence of blow-up solutions (see [32,34]), and approximation by standard NLSEs with concentrating potentials (the so-called *point-like limit* – see [35,36]). We also mention that in these dimensions also linear *non-autonomous* models have been widely studied, mainly in relation to complete *ionization* phoenomena (see e.g., [37–40]).

On the contrary, to the best of our knowledge, the two-dimensional problem has failed to be understood for years, even though some of the main technical difficulties arising in this case were known (see [7,8,41]). However, the problem has been finally solved by the authors in [42], where new features of Volterra integral operators with highly singular kernels have been established (see also [43]) in order to prove local and global well-posedness of the associated Cauchy problem.

In this communication, starting from linear point interactions in $\mathbb{R}^2$, we sketch some important points of the strategy used in [42] to discuss the issues of local and global well-posedness of the nonlinear model.

2. Linear Point Interactions

In this section, we give a brief overview on linear point interactions in $\mathbb{R}^2$ (for a more detailed, we refer to [8]).

As in $\mathbb{R}^3$ (and in contrast to what occurs in $\mathbb{R}$), in $\mathbb{R}^2$ the starting point is that of giving a precise meaning to the formal operator:

$$H^f := -\Delta + \sum_{i=1}^{N} \alpha_i \delta(\cdot - \mathbf{y}_i), \qquad \mathbf{y}_1, \ldots, \mathbf{y}_N \in \mathbb{R}^2, \quad \alpha_1, \ldots, \alpha_N \in \mathbb{R}. \tag{2.1}$$

Hence, we look for a suitable self-adjoint operator in $L^2\left(\mathbb{R}^2\right)$, which correctly represent the heuristic expression in (2.1). In particular, this operator has to act as the free Laplacian far from the points were the interactions occur.

In the following, we recall how to construct such an operator by means of the theory of self-adjoint extensions. For the sake of simplicity, we consider only the case of a single point interaction placed at $\mathbf{y} \in \mathbb{R}^2$ (for the generalization to the case of a finite number of point interactions see [8]).

2.1. Definition and setting

Let us introduce the following restriction of the Laplacian:

$$H^r := -\Delta, \qquad \mathcal{D}(H^r) := C_0^\infty\left(\mathbb{R}^2\backslash\{\mathbf{y}\}\right).$$

This operator is symmetric and, furthermore, acts exactly as the standard Laplacian far from the interaction point. Hence, the strategy to find a suitable form for (2.1) is that of classifying all possible (non-trivial) self-adjoint extensions of H^r.

In fact, one can prove (see [8]) that all these extensions are given by a one-parameter family of operators $H_{\alpha,\mathbf{y}}$ with domain and action given by:

$$\mathcal{D}(H_{\alpha,\mathbf{y}}) := \left\{\psi \in L^2(\mathbb{R}^2)|\, \psi = \phi_\lambda + qG^\lambda(\cdot - \mathbf{y}), \quad \phi_\lambda \in H^2\left(\mathbb{R}^2\right), \quad q \in \mathbb{C},\right.$$

$$\left.\lim_{\mathbf{x}\to\mathbf{y}} \phi_\lambda(\mathbf{x}) = \left(\alpha + \frac{1}{2\pi}\log\sqrt{\lambda} + \frac{\gamma}{2\pi}\right)q\right\}$$

(for any $\lambda > 0$) and

$$(H_{\alpha,\mathbf{y}} + \lambda)\psi := (-\Delta + \lambda)\phi_\lambda, \qquad \forall\psi \in \mathcal{D}(H_{\alpha,\mathbf{y}}),$$

where γ is the Euler–Mascheroni constant and G^λ is the Green's function of $-\Delta + \lambda$, namely $G^\lambda(\mathbf{x}) = \frac{1}{2\pi}K_0(\sqrt{\lambda}|\mathbf{x}|)$, with $K_0(\sqrt{\lambda}|\cdot|)$ denoting the inverse (unitary) Fourier transform of $(|\mathbf{k}|^2 + \lambda)^{-1}$, i.e., the modified Bessel function of second kind of order 0 (a.k.a. Macdonald function [49, Sect. 9.6]).

Remark 2.1. In the 3d case, an analogous construction holds, but with a major difference: one can define an equivalent decomposition (up to modifying the integrability requirements at infinity) for $\lambda = 0$. Here, on the contrary, although the operator domain is independent (as in 3d) of the parameter $\lambda > 0$, the choice $\lambda = 0$ is forbidden due to the infrared singularity of the 2d Green's function (which in fact diverges when $\lambda \to 0$).

Remark 2.2. The parameter α introduced above is not the inverse scattering length. There is a relation between α, defined above with the scattering length $(4\pi\alpha^{scatt})^{-1}$ as defined in [8], and it is the following:

$$\alpha^{scatt} + \frac{\gamma}{2\pi} - \frac{\log 2}{2\pi} = \alpha.$$

The quadratic form associated with $H_{\alpha,\mathbf{y}}$, in addition, is given by:

$$\mathcal{F}_{\alpha,\mathbf{y}}(\psi) := \|\nabla\phi_\lambda\|_{L^2(\mathbb{R}^2)}^2 + \lambda\|\phi_\lambda\|_{L^2(\mathbb{R}^2)}^2 - \lambda\|\psi\|_{L^2(\mathbb{R}^2)}^2 + \left(\alpha + \frac{1}{2\pi}\log\frac{\sqrt{\lambda}}{2} + \frac{\gamma}{2\pi}\right)|q|^2, \qquad (2.2)$$

with form domain:

$$V := \left\{\psi \in L^2(\mathbb{R}^2)|\, \psi = \phi_\lambda + q\, G^\lambda(\cdot - \mathbf{y}), \phi_\lambda \in H^1\left(\mathbb{R}^2\right), \quad q \in \mathbb{C}\right\}.$$

Such a quadratic form is not positive definite. As a consequence, one finds that a bound state occurs for any value of α (another major difference with the 3d case, where the sign of the coupling constant α distinguishes between the existence/nonexistence of a bound state). More precisely:

$$\sigma\left(H_{\alpha,\mathbf{y}}\right) = \left\{-4e^{-4\pi\alpha-2\gamma}\right\} \cup [0,\infty),$$

and thus two-dimensional point interactions can be said to be always attractive.

2.2. Dynamics

As a consequence of the previous considerations (by means, for instance, of the Stone's theorem), it is well-known that, for any $\psi_0 \in D(H_{\alpha,y})$, the Cauchy problem:

$$\begin{cases} \imath \dfrac{\partial \psi_t}{\partial t} = H_{\alpha,\mathbf{y}} \psi_t, \\[2mm] \psi_{t=0} = \psi_0 \end{cases} \tag{2.3}$$

is globally well-posed. Additionally, in this case, an expression for the propagator as an integral kernel is available (see again [8, 44]). This means that the solution of the Cauchy problem can be given explicitly.

However, there exists an alternative description for the dynamics of (2.3), which has two main advantages. It makes the state description more similar to the physics intuition of what a point interaction is, and, especially, it is a suitable starting point for the generalization from linear problems to nonlinear problems, where no theory of self-adjoint operators is available.

This description is based on the following ansatz for the solutions:

$$\psi_t(\mathbf{x}) = (U_0(t)\psi_0)(\mathbf{x}) + \frac{\imath}{2\pi} \int_0^t \mathrm{d}s \, U_0(t-s, |\mathbf{x}-\mathbf{y}|) q(s), \tag{2.4}$$

where $U_0(t)$ is the integral kernel of the 2d free Schrödinger propagator, i.e.,

$$U_0(t; \mathbf{x}) = \frac{1}{2\imath t} e^{-\frac{|\mathbf{x}|^2}{4\imath t}},$$

and $q(t)$ is a complex scalar function usually called *charge*. In this way, all the relevant information on the interaction is stored in fact in $q(t)$ and hence the dynamics of the problem is completely determined by the equation satisfied by $q(t)$, that is the so-called the *charge equation*.

Remark 2.3. At an intuitive level, (2.4) is simply the Duhamel formulation of (2.3) if one assumes that $q(t)$ represent the dynamics of the wave function at the interaction point.

Before justifying the previous ansatz on ψ_t and deriving, at least formally, the charge equation, we need to introduce a technical tool (see also [42, 43, 45]). Recall that the *Volterra functions* (see, e.g., [46]) are defined as:

$$\nu(t, \alpha) := \int_0^\infty \mathrm{d}s \, \frac{t^{\alpha+s}}{\Gamma(\alpha+s+1)},$$

where $\Gamma(t) := \int_0^\infty \mathrm{d}x \, x^{t-1} e^{-x}$. In particular, we focus on the Volterra function of order -1, i.e., $\nu(t, -1) =: \mathcal{I}(t)$. This function is finite (and analytic) for every $t > 0$, whereas:

$$\mathcal{I}(t) \sim \frac{1}{t \log^2\left(\frac{1}{t}\right)} \left[1 + \mathcal{O}(|\log t|^{-1}) \right], \qquad \text{as} \quad t \downarrow 0,$$

so that $\mathcal{I} \in L^1_{\mathrm{loc}}([0, \infty))$ and $\mathcal{I} \notin L^p_{\mathrm{loc}}([0, \infty))$, for every $p > 1$. In addition,

$$\mathcal{I}(t) \sim e^t + \mathcal{O}(t^{-1}), \qquad \text{as} \quad t \to +\infty.$$

Furthermore, and above all, such a function is a *Sonine* kernel, namely there exists another function $\mathcal{J}(t)$ such that:

$$\int_0^t \mathrm{d}s \, \mathcal{I}(t-s)\mathcal{J}(s) = 1 \qquad \forall t \geq 0.$$

Precisely, $\mathcal{J}(t) := -\gamma - \log t$.

Now, we can explain why (2.4) solves (2.3), provided that $\psi_t \in \mathcal{D}(H_{\alpha,\mathbf{y}})$ for every $t \geq 0$. For the sake of simplicity we assume here $q(0) = 0$, since this is not restrictive (the argument if $q(0) \neq 0$ is analogous, up to

further computations). First, we note that:

$$\imath\partial_t\psi_t(\mathbf{x}) = (-\Delta U_0(t)\psi_0)(\mathbf{x}) - \frac{q(t)}{2\pi} + \frac{1}{2\pi}\int_0^t \mathrm{d}\tau\,\partial_\tau U_0(t-\tau;|\mathbf{x}-\mathbf{y}|)q(\tau)$$

$$= (-\Delta U_0(t)\psi_0)(\mathbf{x}) - \frac{1}{2\pi}\int_0^t \mathrm{d}\tau\,U_0(t-\tau;|\mathbf{x}-\mathbf{y}|)\dot{q}(\tau),$$

where we used the fact that $i\partial_t U_0(t)\psi_0 = -\Delta U_0(t)\psi_0$. Hence, applying the Fourier transform on $\mathbb{R}^2$, the above expression reads (setting $k = |\mathbf{k}|$):

$$\widehat{\imath\partial_t\psi_t}(\mathbf{k}) = k^2 e^{-\imath k^2 t}\widehat{\psi_0}(\mathbf{k}) - \frac{1}{2\pi}\int_0^t \mathrm{d}\tau\, e^{-\imath\mathbf{k}\cdot\mathbf{y}}\, e^{-\imath k^2(t-\tau)}\dot{q}(\tau). \qquad (2.5)$$

On the other hand, the Fourier transform of $H_{\alpha,\mathbf{y}}\psi_t$ turns out to be

$$k^2\left(\widehat{\psi_t}(\mathbf{k}) - \frac{1}{2\pi}\frac{q(t)e^{-\imath\mathbf{k}\cdot\mathbf{y}}}{k^2+\lambda}\right) - \frac{\lambda}{2\pi}\frac{q(t)e^{-\imath\mathbf{k}\cdot\mathbf{y}}}{k^2+\lambda}$$

$$= k^2 e^{-\imath k^2 t}\widehat{\psi_0}(\mathbf{k}) + \frac{1}{2\pi}\int_0^t \mathrm{d}\tau\, e^{-\imath\mathbf{k}\cdot\mathbf{y}}\,\partial_\tau\left(e^{-\imath k^2(t-\tau)}\right)q(\tau) - \frac{q(t)e^{-\imath\mathbf{k}\cdot\mathbf{y}}}{2\pi}$$

$$= k^2 e^{-\imath k^2 t}\widehat{\psi_0}(\mathbf{k}) - \frac{1}{2\pi}\int_0^t \mathrm{d}\tau\, e^{-\imath\mathbf{k}\cdot\mathbf{y}}\, e^{-\imath k^2(t-\tau)}\dot{q}(\tau),$$

which is equal to the r.h.s. of (2.5). Summing up, if $\psi_t \in \mathcal{D}(H_{\alpha,\mathbf{y}})$ for every $t \geq 0$, then the ansatz (2.4) solves (2.3). In fact, some regularity for the charge q is also required in order to make rigorous the previous computation. However, since in view of (2.4), the regularity of ψ_t is due to $q(t)$, this request is somehow hidden in the assumption $\psi_t \in \mathcal{D}(H_{\alpha,\mathbf{y}})$.

At this point it is evident that the central question is the behavior of $q(t)$, or in other words, the detection of the proper evolution equation for $q(t)$ (which will turn out to be a Volterra integral equation of the first kind). The argument below is just a formal derivation of the charge equation (a more rigorous way that exploits Laplace transform can be found in [47]), but is interesting since stresses the underlying link between this equation and the boundary condition present in the operator domain.

In order to guarantee that $\psi_t \in \mathcal{D}(H_{\alpha,\mathbf{y}})$, the boundary condition must be satisfied, i.e.,

$$\phi_{\lambda,t}(\mathbf{y}) = \frac{1}{2\pi}\int_{\mathbb{R}^2} \mathrm{d}\mathbf{k}\, e^{\imath\mathbf{k}\cdot\mathbf{y}}\,\widehat{\phi}_{\lambda,t}(\mathbf{k}) = \left(\alpha + \frac{1}{2\pi}\log\frac{\sqrt{\lambda}}{2} - \frac{\gamma}{2\pi}\right)q(t).$$

Moreover, since $\phi_{\lambda,t} = \psi_t - q(t)G^\lambda(\cdot-\mathbf{y})$,

$$\frac{1}{2\pi}\int_{\mathbb{R}^2} \mathrm{d}\mathbf{k}\, e^{\imath\mathbf{k}\cdot\mathbf{y}}\left\{e^{-\imath k^2 t}\widehat{\psi_0}(\mathbf{k}) + \frac{\imath}{2\pi}\int_0^t \mathrm{d}\tau\, e^{-\imath\mathbf{k}\cdot\mathbf{y}}\, e^{-\imath k^2(t-\tau)}q(\tau) - \frac{1}{2\pi}\frac{q(t)e^{-\imath\mathbf{k}\cdot\mathbf{y}}}{k^2+\lambda}\right\}$$

$$= \left(\alpha + \frac{1}{2\pi}\log\frac{\sqrt{\lambda}}{2} - \frac{\gamma}{2\pi}\right)q(t).$$

Combining the last diverging term on the l.h.s. with the second one via an integration by parts, we get:

$$\frac{1}{2\pi}\int_{\mathbb{R}^2} \mathrm{d}\mathbf{k}\left\{e^{\imath\mathbf{k}\cdot\mathbf{y}}\, e^{-\imath k^2 t}\widehat{\psi_0}(\mathbf{k}) - \frac{1}{2\pi(k^2+\lambda)}\int_0^t \mathrm{d}\tau\, e^{-\imath k^2(t-\tau)}\left[\dot{q}(\tau) - \imath\lambda q(\tau)\right]\right\}$$

$$= \left(\alpha + \frac{1}{2\pi}\log\frac{\sqrt{\lambda}}{2} - \frac{\gamma}{2\pi}\right)q(t).$$

The integral in $\mathbf{k}$ of the second term on the l.h.s. contains an infrared singularity for $t = \tau$ which is proportional to $\log(t - \tau)$: in fact by [48, Eqs. 3.722.1 *and* 3.722.3]

$$\int\limits_{\mathbb{R}^2} d\mathbf{k} \, \frac{e^{-\imath k^2 (t - \tau)}}{k^2 + \lambda} = -\pi e^{\imath \lambda (t - \tau)} \left[\text{ci}(\lambda(t - \tau)) - \imath \, \text{si}(\lambda(t - \tau)) \right]$$

$$= -\pi e^{\imath \lambda (t - \tau)} \left(\gamma + \log \lambda + \log(t - \tau) \right) + e^{\imath \lambda (t - \tau)} Q(\lambda; t - \tau),$$

where $\text{si}(\,\cdot\,)$ and $\text{ci}(\,\cdot\,)$ stand for the sine and cosine integral functions (see [49, Eqs. 5.2.1 *and* 5.2.2] for the definition) and, by [49, Eq. 5.2.16],

$$Q(\lambda; t - \tau) := -\pi \left(\sum_{n=1}^{\infty} \frac{(-(t - \tau)^2 \lambda^2)^n}{2n(2n)!} - \imath \, \text{si}((t - \tau)\lambda) \right)$$

(note that $Q(0; t - \tau) = -\imath \pi^2 / 2$). Hence, we obtain that:

$$(U_0(t)\psi_0)(\mathbf{y}) - \left(\alpha + \frac{1}{2\pi} \log \frac{\sqrt{\lambda}}{2} + \frac{\gamma}{2\pi} \right) q(t)$$

$$= -\frac{1}{4\pi} \int\limits_0^t d\tau \, \left(\gamma + \log(t - \tau) + \log \lambda - \frac{1}{\pi} Q(\lambda; t - \tau) \right) \partial_\tau \left(e^{\imath \lambda (t - \tau)} q(\tau) \right)$$

and taking the formal limit $\lambda \to 0$ (notice the exact cancellation of the diverging $\log \lambda$ terms)

$$(U_0(t)\psi_0)(\mathbf{y}) - \left(\alpha - \frac{1}{2\pi} \log 2 + \frac{\gamma}{2\pi} - \frac{\imath}{8} \right) q(t) = -\frac{1}{4\pi} \int\limits_0^t d\tau \, (\gamma + \log(t - \tau)) \, \dot{q}(\tau).$$

Finally, applying the convolution integral operator defined by $\mathcal{I}$ and using the Sonine property, suitably rearranging terms, one has:

$$q(t) + \int\limits_0^t d\tau \, \mathcal{I}(t - \tau) \left(4\pi\alpha - 2\log 2 + 2\gamma - \frac{i\pi}{2} \right) q(\tau) = f(t), \tag{2.6}$$

where:

$$f(t) = 4\pi \int\limits_0^t d\tau \, \mathcal{I}(t - \tau)(U_0(\tau)\psi_0)(\mathbf{y}), \tag{2.7}$$

which is what is usually called charge equation.

It is clear that the previous computations are just formal. Moreover, the actual strategy to prove that (2.4) solves (2.3) is the converse of what we made. Indeed, the main steps should be the following:

(i) proving that (2.6) has a unique solution, at least on a small interval;
(ii) proving that it also displays such a regularity that $\psi_t \in \mathcal{D}(H_{\alpha, \mathbf{y}})$ (and thus (2.4) satisfies (2.3));
(iii) proving that the solution of (2.6) (and consequently the solution of (2.3)) is global in time.

However, one can immediately see that this strategy is not the most suitable in the linear case, since classical theory of self-adjoint operators provides immediately (i)–(iii). In addition, point (ii) is not easy to prove in a direct way since the integral operator:

$$(Ig)(t) := \int\limits_0^t d\tau \, \mathcal{I}(t - \tau)g(\tau),$$

which is the main feature of the charge equation, has no regularizing properties in Sobolev spaces (due to its highly singular behavior at the origin) and this prevents establishment on the suitable regularity of $\phi_{\lambda, t}$. More in detail, even if g is a smooth function, Ig may present a very rough behavior. For instance, setting $g \equiv 1$, one can see that

$$Ig(t) = \int_0^t d\tau \, \mathcal{I}(\tau) = \nu(t, 0) \text{ is not even in } H_{\text{loc}}^\theta(\mathbb{R}^+), \text{ if } \theta > 1/2, \text{ while it belongs to } H_{\text{loc}}^{1/2}(\mathbb{R}^+).$$

On the other hand, in the nonlinear case, when the classical theory is not available, the strategy hinted before is the unique path one can follow, provided that one can manage point (ii) in spite of the singular behavior of the operator I.

Remark 2.4. The lack of regularizing properties of the integral operator I is the main difference between the 2d case and the 1d and 3d ones. Indeed, in odd dimension the resulting charge equation displays the $1/2$-Abel kernel $\dfrac{C_\beta}{t^{1-\beta}}$, $\beta \in (0,1)$, as integral kernel (in place of $\mathcal{I}$), which has sufficient smoothing properties (see [32, 50]) to overcome the regularity issues.

3. Nonlinear Point Interactions

As we mentioned before, the method based on the investigation of the Duhamel formula and the charge equation, although not necessary in the linear case, is the one that solely allows an easy generalization to the nonlinear problem.

Precisely, this extension is done by analogy, simply assuming that the strength of the interaction α depends itself on the charge in a nonlinear way (of power type), i.e.,

$$\alpha = \beta_0 \, |q(t)|^{2\sigma}, \qquad \beta_0 \in \mathbb{R}, \sigma \in \mathbb{R}^+. \tag{3.1}$$

Then, one has to follow the strategy suggested before, namely one has to prove that the function ψ_t defined by (2.4) solves (2.3) at least in a weak sense, provided that there is a unique and sufficiently regular solution of the charge equation. It is clear that, in view of (3.1), (2.6) reads:

$$q(t) + 4\pi\beta_0 \int_0^t \mathrm{d}\tau \, \mathcal{I}(t-\tau)|q(\tau)|^{2\sigma}q(\tau) - 2\left(\log 2 - \gamma + \frac{\imath\pi}{4}\right) \int_0^t \mathrm{d}\tau \, \mathcal{I}(t-\tau)q(\tau) = f(t), \tag{3.2}$$

where $f(t)$ is given again by (2.7).

This problem has been solved in [42] by the authors. However, since an exhaustive presentation of the proof would require the management of several hard and subtle technical issues, here we just give some hints on the strategy used to overcome items (i)–(iii).

3.1. Sketch of the strategy

First, we want to point out that in [42] we dealt with the weak solution of (2.3), namely with a function $\psi_t \in V$ that satisfies:

$$\begin{cases} \imath\dfrac{\mathrm{d}}{\mathrm{d}t} \langle \chi|\psi_t \rangle = \mathcal{F}_{\alpha,\mathbf{y}}\big[\chi, \psi_t\big]\big|_{\{\alpha=\beta_0|q(t)|^{2\sigma}\}}, \\ \psi_{t=0} = \psi_0, \end{cases} \tag{3.3}$$

for any $\chi = \chi_\lambda + q_\chi G^\lambda(\cdot - \mathbf{y}) \in V$, where $\langle \cdot | \cdot \rangle$ is the inner product of $L^2(\mathbb{R}^2)$ and

$$\mathcal{F}_{\alpha,\mathbf{y}}\big[\chi, \psi_t\big]\big|_{\{\alpha=\beta_0|q(t)|^{2\sigma}\}} := \int_{\mathbb{R}^2} \mathrm{d}\mathbf{x} \, \{\nabla\chi_\lambda^* \cdot \nabla\phi_{\lambda,t} + \lambda\chi_\lambda^*\phi_{\lambda,t} - \lambda\chi^*\psi_t\}$$

$$+ \left(\beta_0|q(t)|^{2\sigma} + \frac{1}{2\pi}\log\frac{\sqrt{\lambda}}{2} + \frac{\gamma}{2\pi}\right)q_\chi^*q(t).$$

The search for a strong solution seems to be out of reach at the moment. We will explain the reason below.

Remark 3.1. We stress that $\mathcal{F}_{\alpha,\mathbf{y}}\big[\cdot, \cdot\big]\big|_{\{\alpha=\beta_0|q(t)|^{2\sigma}\}}$ is nothing but the nonlinear analog of the sesquilinear form associated with the quadratic form $\mathcal{F}_{\alpha,\mathbf{y}}$ defined by (2.2) and hence is the natural choice for the definition of weak solution.

Point (i) is the simplest one since it exploits some well-known results on nonlinear Volterra integral equations (see, e.g., [51, 52]). Thus, one almost immediately finds that (3.2) has a unique continuous solution $q(t)$ on a maximal existence interval $[0, T_*)$, where T_* is possibly infinite.

On the other hand, the central and more delicate point is (ii). In particular, one can prove that, in order to have that $\psi_t \in V$ and satisfies (3.3) in the maximal existence time, it is sufficient that the $q \in H^{1/2}(0,T)$ for all $T < T_*$. However, as we suggested in the previous section, this is not an easy task due to the lack or regularizing properties of the integral operator I, defined by the Volterra function $\mathcal{I}$. In addition, since as we showed before the action of the operator I can destroy the regularity even of smooth functions, the strategy of the 1d and 3d cases (where we recall that the integral kernel $\mathcal{I}$ is replaced by the $1/2$-Abel one) namely solving smoother problems with more regular initial data and then using a density argument, is forbidden too.

Consequently, the unique available strategy, which is the one exploited in [42], is that of:

- developing a contraction argument on a possibly small interval $[0, T]$;

- repeating the same argument on consecutive intervals with suitable modifications of (3.2);
- proving that the attachments preserve the regularity at the connection points and allow to cover any closed and bounded interval strictly contained in $[0, T_*)$.

Such a procedure works since the operator I displays the following *contractive* property (see [42,43] for the proof):

$$\|Ig\|_{H^{1/2}(0,T)} \leq C_T \left(\|g\|_{L^\infty(0,T)} + \|g\|_{H^{1/2}(0,T)} \right), \tag{3.4}$$

where $C_T \to 0$, as $T \to 0$.

Finally, the proof of point (iii) consists of detecting sufficient conditions in order to claim that $T_* = +\infty$. The first step in this direction is the proof of the the conservation of the mass, i.e., $M(t) := \|\psi_t\|_{L^2(\mathbb{R}^2)}$, and, especially, of the energy, i.e.,

$$E(t) := \|\phi_{1,t}\|^2_{H^1(\mathbb{R}^2)} + \left(\frac{\beta_0}{\sigma + 1} |q(t)|^{2\sigma} + \frac{\gamma - \log 2}{2\pi} \right) |q(t)|^2.$$

Hence, a classical blow-up alternative analysis shows that in the so-called *defocusing* case, i.e., $\beta_0 > 0$, the solution is global in time, whereas in the *focusing* case, i.e., $\beta_0 < 0$, T_* may be both finite and infinite, depending on the initial datum ψ_0.

3.2. Further remarks

The methods mentioned before to manage points (ii) and (iii) have proved to be full of subtle and hard technical issues. An extensive discussion of these goes beyond the aims of this proceeding and has been done in detail in [42]. However there are points that deserve some comments.

First, we want to stress an immediate reason that makes the proof the strong version of (3.3) out of reach at the moment. This is again connected to point (ii) and, precisely, to the contracting properties of I. It is in fact possible to establish an analogous of (3.4) also for H^1-functions (actually for any $\nu \in (1/2, 1]$), which is the regularity required to get $\psi_t \in \mathcal{D}(H_{\alpha,\mathbf{y}})$ up to the proof of the boundary condition. However, in this case it is necessary to assume that $q(0) = 0$, which is an unnatural assumption and, in addition, prevents the possibility of using the attachments technique highlighted in the previous section. Thus, point (ii) cannot be proved for the H^1 regularity and this prevents at the moment the possibility of finding strong solutions of (3.3).

Furthermore, both the attachments technique and the proof of the energy conservation call for a further regularity of the charge. The former issue is due to the failure of the Hardy inequality for $H^{1/2}$-functions (see [36, 53]), that prevents the attachment of two $H^{1/2}$-functions on consecutive intervals to be in $H^{1/2}$, in general. The latter, on the contrary, is due to the integration of the derivative of the charge, which is necessary in the computations, but which have no meaning as q is not absolutely continuous, in general. However, if one proves that q is *log-Hölder* continuous, namely, that its modulus of continuity is controlled by a logarithmic function (in place of a fractional power function), then both the issues can be overcome. Indeed, in this case the attachments can be proved to be licit and one can develop a duality pairing argument in order to bypass the problem on integrating $\dot{q}$.

Unfortunately, the proof of such a further regularity for the charge requires some extra-assumptions on the initial datum ψ_0. Precisely, its regular part $\phi_{\lambda,0}$ has to satisfy:

$$(1 + k)^\varepsilon \widehat{\phi}_{\lambda,0} \in L^1(\mathbb{R}^2), \qquad \text{for some} \quad \varepsilon > 0,$$

which is a restriction with respect to the natural assumptions that only state $\psi_0 \in V$.

Finally, it is worth recalling that the contractive argument needed to manage point (ii) requests a slightly restrictive assumption on the power of the nonlinearity. Precisely, one must suppose that $\sigma \geq 1/2$. This is due to the fact that otherwise one cannot prove Lipschitz continuity of the map $g \mapsto |g|^{2\sigma} g$ between $H^{1/2}(0,T) \cap L^\infty(0,T)$ and itself, with a constant that do not blow up as $T \to 0$; namely, with a constant that do not compensate the good contractive properties of I.

References

[1] Cacciapuoti C., Carlone R., Figari R. A solvable model of a tracking chamber. *Rep. Math. Phys.*, 2007, **59**(3), P. 337–349.

[2] Carlone R., Figari R., Negulescu C. A model of a quantum particle in a quantum environment: a numerical study. *Commun. Comput. Phys.*, 2015, **18**(1), P. 247–262.

[3] Carlone R., Figari R., Negulescu C. The quantum beating and its numerical simulation. *J. Math. Anal. Appl.*, 2017, **450**(2), P. 1294–1316.

[4] Figari R., Teta A. From quantum to classical world: emergence of trajectories in a quantum system. *Math. Mech. Complex Syst.*, 2016, **4**(3–4), P. 235–254.

[5] Cacciapuoti C., Figari R., Posilicano A. Effective equation for a system of mechanical oscillators in an acoustic field. *Asymptot. Anal.*, 2015, **91**(3–4), P. 253–264.

[6] Cacciapuoti C., Fermi D., Posilicano A. Relative-zeta and Casimir energy for a semitransparent hyperplane selecting transverse modes. *Advances in quantum mechanics*, P. 71–97, Springer INdAM Ser., 18, Springer, Cham, 2017.

[7] Cacciapuoti C., Carlone R., Figari R. Perturbations of eigenvalues embedded at threshold: two-dimensional solvable models. *J. Math. Phys.*, 2011, **52**(8), 083515, 12 pp.

[8] Albeverio S., Gesztesy F., Høegh-Krohn R., Holden H. *Solvable Models in Quantum Mechanics*. Texts and Monographs in Physics, Springer-Verlag, New York, 1988.

[9] Cacciapuoti C., Carlone R., Noja D., Posilicano A. The one-dimensional Dirac equation with concentrated nonlinearity. *SIAM J. Math. Anal.*, 2017, **49**(3), P. 2246–2268.

[10] Carlone R., Malamud M., Posilicano A. On the spectral theory of Gesztesy-Šeba realizations of 1-D Dirac operators with point interactions on a discrete set. *J. Differential Equations*, 2013, **254**(9), P. 3835–3902.

[11] Adami R., Cacciapuoti C., Finco D., Noja D. Fast solitons on star graphs. *Rev. Math. Phys.*, 2011, **23**(4), P. 409–451.

[12] Adami R., Cacciapuoti C., Finco D., Noja D. On the structure of critical energy levels for the cubic focusing NLS on star graphs. *J. Phys. A*, 2012, **45**(19), 192001, 7 pp.

[13] Adami R., Cacciapuoti C., Finco D., Noja D. Constrained energy minimization and orbital stability for the NLS equation on a star graph. *Ann. Inst. H. Poincaré Anal. Non Linéaire*, 2014, **31**(6), P. 1289–1310.

[14] Adami R., Cacciapuoti C., Finco D., Noja D. Variational properties and orbital stability of standing waves for NLS equation on a star graph. *J. Differential Equations*, 2014, **257**(10), P. 3738–3777.

[15] Adami R., Serra E., Tilli P. Lack of ground state for NLSE on bridge-type graphs. *Mathematical technology of networks*, 1–11. Springer Proc. Math. Stat., 128. Springer, Cham, 2015.

[16] Adami R., Serra E., Tilli P. NLS ground states on graphs. *Calc. Var. Partial Differential Equations*, 2015, **54**(1), P. 743–761.

[17] Adami R., Serra E., Tilli P. Threshold phenomena and existence results for NLS ground states on graphs. *J. Funct. Anal.*, 2016, **271**(1), P. 201–223.

[18] Adami R., Serra E., Tilli P. Negative energy ground states for the L^2–critical NLSE on metric graphs. *Comm. Math. Phys.*, 2017, **352**(1), P. 387–406.

[19] Berkolaiko G., Kuchment P. *Introduction to quantum graphs*, Mathematical Surveys and Monographs 186, AMS, Providence, RI, 2013.

[20] Cacciapuoti C., Finco D., Noja D. Topology–induced bifurcations for the nonlinear Schrödinger equation on the tadpole graph. *Phys. Rev. E (3)*, 2015, **91**(1), article number 013206, 8 pp.

[21] Gnutzmann S., Smilansky U., Derevyanko S. Stationary scattering from a nonlinear network. *Phys. Rev. A*, 2011, **83**(3), article number 033831, 6 pp.

[22] Noja D. Nonlinear Schrödinger equation on graphs: recent results and open problems. *Philos. Trans. R. Soc. Lond. Ser. A Math. Phys. Eng. Sci.*, 2014, **372**(2007), 20130002, 20 pp.

[23] Noja D., Pelinovsky D., Shaikhova G. Bifurcations and stability of standing waves in the nonlinear Schrödinger equation on the tadpole graph. *Nonlinearity*, 2015, **28**(7), P. 2343–2378.

[24] Serra E., Tentarelli L. Bound states of the NLS equation on metric graphs with localized nonlinearities. *J. Differential Equations*, 2016, **260**(7), P. 5627–5644.

[25] Serra E., Tentarelli L. On the lack of bound states for certain NLS equations on metric graphs. *Nonlinear Anal.*, 2016, **145**, P. 68–82.

[26] Tentarelli L. NLS ground states on metric graphs with localized nonlinearities. *J. Math. Anal. Appl.*, 2016, **433**(1), P. 291–304.

[27] Carlone R., Exner P. Dynamics of an electron confined to a "hybrid plane" and interacting with a magnetic field. *Rep. Math. Phys.*, 2011, **67**(2), P. 211–227.

[28] Carlone R., Posilicano A. A quantum hybrid with a thin antenna at the vertex of a wedge. *Phys. Lett. A*, 2017, **381**(12), P. 1076–1080.

[29] Exner P., Šeba P. Quantum motion on a half–line connected to a plane. *J. Math. Phys.*, 1987, **28**(2), P. 386–391.

[30] Exner P., Šeba P. Resonance statistics in a microwave cavity with a thin antenna. *Phys. Lett. A*, 1997, **228**(3), P. 146–150.

[31] Exner P., Šeba P. A "hybrid plane" with spin-orbit interaction. *Russ. J. Math. Phys.*, 2007, **14**(4), P. 430–434.

[32] Adami R., Teta A. A Class of Nonlinear Schrödinger Equations with Concentrated Nonlinearity. *J. Funct. Anal.*, 2001, **180**(1), P. 148–175.

[33] Adami R., Dell'Antonio G., Figari R., Teta A. The Cauchy problem for the Schrödinger equation in dimension three with concentrated nonlinearity. *Ann. Inst. H. Poincaré Anal. Non Linéaire*, 2003, **20**(3), P. 477–500.

[34] Adami R., Dell'Antonio G., Figari R., Teta A. Blow-up solutions for the Schrödinger equation in dimension three with a concentrated nonlinearity. *Ann. Inst. H. Poincaré Anal. Non Linéaire*, 2004, **21**(1), P. 121–137.

[35] Cacciapuoti C., Finco D., Noja D., Teta A. The NLS equation in dimension one with spatially concentrated nonlinearities: the pointlike limit. *Lett. Math. Phys.*, 2014, **104**(12), P. 1557–1570.

[36] Cacciapuoti C., Finco D., Noja D., Teta A. The point-like limit for a NLS equation with concentrated nonlinearity in dimension three. *J. Funct. Anal.*, 2017, **273**(5), P. 1762–1809.

[37] M. Correggi, G. Dell'Antonio, Decay of a Bound State under a Time-Periodic Perturbation: A Toy Case. *J. Phys. A: Math. Gen.*, 2005, **38**, P. 4769–4781.

[38] Correggi M., Dell'Antonio G., Figari R., Mantile A. Ionization for Three Dimensional Time-Dependent Point Interactions. *Comm. Math. Phys.*, 2005, **257**(1), P. 169–192.

[39] Costin O., Costin R.D., Lebowitz J.L., Rokhlenko A. Evolution of a model quantum system under time periodic forcing: conditions for complete ionization. *Comm. Math. Phys.*, 2001, **221**(1), P. 1–26.

[40] Sayapova M.R., Yafaev D.R. The evolution operator for time-dependent potentials of zero radius. *Trudy Mat. Inst. Steklov*, 1983, **159**, P. 167–174.

[41] Carlone R., Correggi M., Figari R. Two-dimensional time-dependent point interactions. *Functional Analysis and Operator Theory for Quantum Physics*, 189–211, Eur. Math. Soc., Zürich, 2017.

[42] Carlone R., Correggi M., Tentarelli L. Well-posedness of the Two-dimensional Nonlinear Schrödinger Equation with Concentrated Nonlinearity, preprint *arXiv:1702.03651 [math-ph]*, (2017).

[43] Carlone R., Fiorenza A., Tentarelli L. The action of Volterra integral operators with highly singular kernels on Hölder continuous, Lebesgue and Sobolev functions. *J. Funct. Anal.*, 2017, **273**(3), P. 1258-1294.

[44] Albeverio S., Brzezniak Z., Dabrowski L. Time-dependent propagator with point interaction. *J. Phys. A*, 1994, **27**(14), P. 4933–4943.

[45] Samko S.G., Kilbas A.A., Marichev O.I. *Fractional integrals and derivatives. Theory and applications*. Gordon and Breach Science Publishers, Yverdon, 1993.

[46] Erdélyi A., Magnus W., Oberhettinger F., Tricomi F.G. *Higher transcendental functions. Vol. III*, Robert E. Krieger Publishing Co., Melbourne, Fla., 1981.

[47] Adami R. *A Class of Schrödinger Equations with Concentrated Nonlinearity*. Ph.D. Thesis, Università degli Studi di Roma "La Sapienza", 2000.

[48] Gradshteyn I.S., Ryzhik I.M. *Tables of Integrals, Series and Products*. Elsevier/Academic Press, Amsterdam, 2007.

[49] Abramovitz M., Stegun I.A. *Handbook of Mathematical Functions: with Formulas, Graphs, and Mathematical Tables*. National Bureau of Standards Applied Mathematics Series 55, Washington D.C., 1964.

[50] Gorenflo R., Vessella S. *Abel integral equations*, Lecture Notes in Mathematics, vol. 1461, Springer-Verlag, Berlin, 1991, Analysis and applications.

[51] Miller R.K. *Nonlinear Volterra Integral Equations*. Mathematics Lecture Note Series, W.A. Benjamin Inc., Menlo Park, Calif., 1971.

[52] Miller R.K., Sell G.R. Existence, uniqueness and continuity of solutions of integral equations. *Ann. Mat. Pura Appl. (4)*, 1968, **80**, P. 135–152.

[53] Kufner A., Persson L.E. *Weighted inequalities of Hardy type*. World Scientific Publishing Co., River Edge, NJ, 2003.

The Lieb–Mattis theorem revisited

W. Florek

Adam Mickiewicz University, Faculty of Physics
ul. Umultowska 85, 61-614 Poznań, Poland
wojciech.florek@amu.edu.pl

Simple formulation and a straightforward proof of the Lieb–Mattis theorem (LMT) do not indicate how powerful a tool it is. For more than fifty years, this theorem has been mainly discussed in its 'strong' form and applied mainly to many type of infinite spin lattices. It can be easily proved that in such cases, geometrically frustrated systems have to be excluded. However, it has been recently shown that the so-called 'weak' or general form of the LMT can be exploited considering some small, geometrically frustrated quantum spin systems. Moreover, many systems, which do not satisfy assumptions of the LMT, show identical features, including the level order characteristic for bipartite spin systems. It yields a question about possible generalizations or modifications of this theorem to involve a larger class of problems. To begin, algebraic aspects have to be understood with the invaluable role of the Perron-Frobenius theorem. The latter theorem is investigated, discussed, modified etc. in immense number of works. Many of them are important in physical applications and ways of reasoning they present can be exploited in different approaches to the LMT.

Keywords: quantum spin systems, Lieb–Mattis theorem, level order,ground state properties.

Received: 27 December 2017

Revised: 7 January 2018

1. Introduction

Physics and chemistry, both experimental and theoretical, of magnetic nanosystems have experienced rapid progress since pioneering papers on molecular magnets at the turn of the 20th and 21st centuries [1–4]. Among others, this is caused by their possible applications in molecular spintronics, magnetic hyperthermia, quantum computing and for high-density information storage or as magneto-optic devices and magnetic refrigerants. It has to be stressed that such objects are also considered as the testbeds for verification of fundamental quantum theories. At present, investigations are focused on both homo- and heterometallic complexes comprising transition and rare earth metal ions. Their most promising low temperature properties depend crucially on their quantum nature, which leads to the discrete energy levels. And properties of the most significant ground-state level are of great importance. Reliable results can be obtained within the frame of the quantum spin models, with the dominant position of large class of Heisenberg-like systems. There are several strict results (e.g. the well-known Bethe Ansatz and its generalizations) and the Lieb–Mattis theorem (LMT) [5] occupies an important place amongst them. Due to its general character it is not applicable to, for example, anisotropic systems, nevertheless it provides a simple and powerful tool to obtain rigorous results.

The Lieb–Mattis [5] theorem was announced in an earlier paper, in which similar reasoning had been applied to an antiferromagnetic linear chain of spin $s = 1/2$ [6]. Both papers have influenced investigations in condensed matter physics[1] and are still highly-cited. Their importance goes beyond condensed matter physics, what is confirmed by many databases like Scopus or Web of Science, and in both cases the number of citations per year increases recently[2]. In condensed matter physics, this is clearly related to development in investigation of, to mention only a few, entanglement, topological phases, single molecule magnets and frustration. Examples of other problems discussed with the use of the LMT or the Lieb–Schultz–Mattis theorem can be found in Refs. [7–14]. On the other hand, there are many attempts to extend these theorems (e.g. Refs. [15–18]). It can be shown [19] that the LMT is, in fact, a consequence of the Perron–Frobenius theorem (PFT) [20–24], so possible extensions of the latter one may lead to generalization of the LMT. In the case of bipartite systems, the transformation proposed in Refs. [5,6] yields a Hamiltonian as a Hermitian matrix with non-negative elements, so the PFT can be applied

---

[1]In April 2017, Ref. [6] was included in a virtual issue of *Ann. Phys.* as one of the *Most Cited in Condensed Matter Theory*; see: `https://www.journals.elsevier.com/annals-of-physics/virtual-special-issues`.

[2]According to the Web of Science Core Collection (December, 2017) Ref. [5] was cited about 600 times in total (approx. 11 per year) and 90 times in the last five years (18 per year). These numbers for Ref. [6] are as follows: more than 2300 (about 40 per year) and about 560 (more than 110 per year).

directly. Non-bipartite systems, like polygons with odd number $n > 3$ sides and antiferromagnetic coupling of the nearest neighbors, are not bipartite and, after similar transformation, some entries are negative. However, some results [25–27] indicate possibility to consider matrices with some negative elements, so it is excepted that it will give impact for reconsideration of the LMT and allow to extend the class of systems with well-determined ground-state properties.

It has to be pointed out that most problems considered are based on the so-called 'strong' version of the LMT, which, roughly speaking, excludes systems with competing interactions or geometrically frustrated [28]. The 'weak' (or general) form of this theorem allows some additional and relatively weak antiferromagnetic couplings, leading to geometric frustration in systems which are bipartite according to assumptions of the LMT [29,30], so coexistence of geometric frustration and bipartiteness is admissible. However, at the same time, it demands strong long-range couplings, what is rather non-physical in large (infinite) systems. Therefore, this feature can be observed in small systems or systems with special topology. On the other hand, the so-called Lieb–Mattis Level Order (LMLO) is realized in both, 'strong' and 'weak' cases. Moreover, it can be proved (in some cases numerically only) that larger, non-bipartite in general, analogous of bipartite systems still exhibit the LMLO [30–32]. Similarly, this effect is observed for anisotropic systems, but the total spin number S has to be replaced by the total magnetization M [33–36]. Reformulation of the LMT to include all these cases is a challenging task and to complete it, this theorem itself has to be 'revisited' and mathematical background must be meticulously examined. This paper, as its title says, is mainly devoted to the first part of this project with stress on mathematical correctness.

In the following section systems satisfying postulates of the LMT are presented. Next, in Sec. 3, the theorem itself and its mathematical background, including the PFT, are discussed. Some models not satisfying assumptions of the LMT, but showing the same properties as those being its subject, are shortly described in Sec. 4 and some open problems are indicated. The paper ends with overall conclusions in Sec. 5.

2. The domain of the Lieb–Mattis theorem

2.1. The Heisenberg Hamiltonian

The original paper of Lieb and Mattis starts with the following Hamiltonian:

$$H = 2 \sum J_{ij} \boldsymbol{S}_i \cdot \boldsymbol{S}_j;$$

the factor 2, irrelevant in proofs, suggests that this sum is taken over different non-ordered pairs $\{i, j\}$, but it was not clearly stated throughout the whole text. Some steps in considerations could be performed properly (or without special assumptions) for finite systems only, so it should be assumed that $1 \leq i, j \leq n$. In this paper, the LMT is discussed in the context of magnetic molecules (finite quantum spin systems), so this restriction does not lead to any constraints. On the other hand, it is very important that this Hamiltonian is isotropic and commutes with the square of total spin operator $\boldsymbol{S}^2$, where $\boldsymbol{S} = \sum_{i=1}^{n} \boldsymbol{s}_i$, with non-negative eigenvalues less or equal than $S_{\max}(S_{\max}+1)$ for $S_{\max} = \sum_{i=1}^{n} s_i$. With all these comments the system under question can be determined as follows.

For a given $1 < n \in \mathbb{N}$ there is set on indices $V = \{j \in \mathbb{N} \mid 1 \leq j \leq n\}$ and to each of them a spin number s_j, determining a spin operator $\boldsymbol{s}_j$, is unambiguously assigned. The set E' of all non-ordered pairs $\{j, k\}$ with $\binom{n}{2} = n(n-1)/2$ elements is constructed in the natural way (with the loss of generality $j < k$ can be assumed). A real-valued function:

$$J \colon E' \to \mathbb{R} \colon \{j, k\} \to J_{jk} = J_{kj}$$

determines weights of edges (an exchange integral is assigned to each bond) [37]. In spin models, bonds with $J_{jk} = 0$ are neglected, so a mathematical object under consideration is a simple (edge-)weighted graph with non-zero weights $J_{jk} \in \mathbb{R}$ and the set of edges $E = \{\{j, k\} \in E' \mid J_{jk} \neq 0\}$; vertex weights s_i are irrelevant in this approach. The isotropic Heisenberg Hamiltonian is determined as the following sum over *all* non-ordered pairs:

$$H = 2 \sum_{j,k=1|j<k}^{n} J_{jk} \boldsymbol{s}_j \cdot \boldsymbol{s}_k; \tag{1}$$

the 'non-existing' edges with $J_{jk} = 0$ have not been excluded in this sum, since they 'disappear' in the natural way, but considering the graph representation of this model, only the edges with non-zero weights are taken into account.
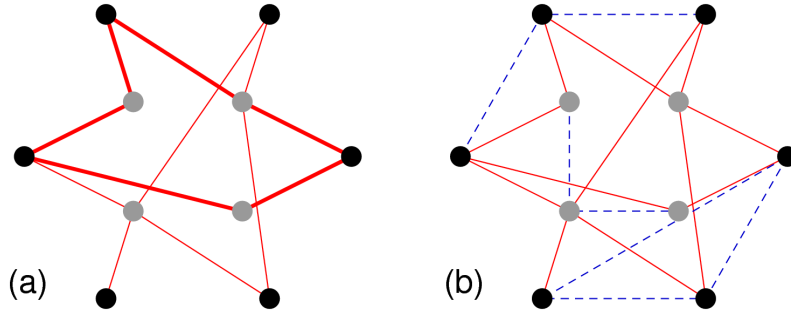
FIG. 1. (a) A bipartite (simple) graph; one of even-length cycles is distinguished by bold lines. (b) A bipartite weighted graph; for a given threshold t solid line edges have weights $w \geq t$, whereas those with weights $w \leq t$ are depicted by dashed lines. In both cases grey and black full circles denote vertices belong to U and W subsets, respectively

2.2. Bipartiteness

In graph theory, a graph is *bipartite* when its set of vertices V can be divided into two disjoint, non-empty and independent sets, i.e. $V = U \cup W$, $U \cap W = \emptyset$, $U \cap W = \emptyset$, in such a way that every edge connects vertices from different subsets only [37]. In other words, if $\{j, k\} \in E$, then vertices j and k belong to different sets U and W. Equivalently they are determined as graphs with no odd-length cycles, what is a very important property [see Fig. 1(a)].

In graph theory, the matching problem is considered taking into account weights of edges, but a graph in question is still bipartite graph if weights are neglected [37]. It means that the weights of edges do not modify the bipartiteness. The LMT demands rather *bipartite weighted graphs* than bipartite graphs with weights, i.e. weighted bipartite graphs [37]. In the former case, the bipartiteness is determined taking into account the weights of edges. A formal definition can be stated as follows: A simple edge-weighted graph with non-zero real weights is bipartite with a threshold t if its set of vertices can be decomposed into two disjoint and non-empty sets (U and W, say) such that edges $\{u, u'\}$ and $\{w, w'\}$, where $u, u' \in U$ and $w, w' \in W$, have weights $w \leq t$, whereas edges $\{u, w\}$ have weights $w \geq t$ [see Fig. 1(b)]. Note that in this case subset U and W are not independent, since vertices from the same set may be adjacent. In the special case $t = 0$, when edges with zero weights are omitted, the subgraphs with sets of vertices U and W, respectively, have edges with negative weights, whereas existing edges $\{u, w\}$ have positive weights only. Such subgraphs can be named 'negatively weighted subgraphs' and hereafter, in the context of spin systems, they will be referred to as 'ferromagnetic components (parts) of a (spin) system'[3]. It can be easily seen that in the bipartite weighted graphs with the threshold $t = 0$, all cycles contain an even number of edges with positive weights.

The LMT can be applied to spin systems, with the Hamiltonian given by Eq. (1), which can be presented as bipartite weighted graphs, but for $t > 0$ they have to be *complete* ones, which means that for each pair of vertices $u \in U$ and $w \in W$, there exist the edge $\{u, w\}$ with non-zero weight $w \geq t > 0$. Due to the inequality signs, when weights are compared with the threshold, the bipartition of a spin system may be not unique and possible thresholds leading to the same bipartition, belong to some, finite or even infinite, range. Using symbols introduced by Lieb and Mattis, the definition of a bipartite (in sense of the LMT) spin system with n spins coupled to each other according to Eq. (1) says: There exists a constant $g^2 \geq 0$ that indices $1 \leq j \leq n$ can be divided into two subsets A and B with

$$J_{jj'}, J_{k,k'} \leq g^2, \quad J_{j,k} \geq g^2, \tag{2}$$

where $j, j' \in A$ and $k, k' \in B$ [5,28][4]; such systems are referred to as LM-bipartite (LMB systems, for short). The completeness of the appropriate graph means that for $g^2 > 0$ even distant spin have to be coupled antiferromagnetically with $J \geq g^2$, what is rather non-physical assumption. Therefore, LMB spin systems with $g^2 > 0$ have to be rather small ones or have special topology like centered polygons or pyramids, as presented in Fig. 2.

---

[3]In Eq. (1) negative exchange integrals correspond to ferromagnetic couplings.

[4]Many authors apply the original Heisenberg convention, in which antiferromagnetic exchange integrals are negative, then the inequalities in Eq. (2) have to be reversed and the sign of the threshold has to be changed, i.e. $J_{jj'}$, $J_{k,k'} \geq -g^2$ and $J_{jk} \leq -g^2$. In Ref. [28] the sign was not be modified accordingly.
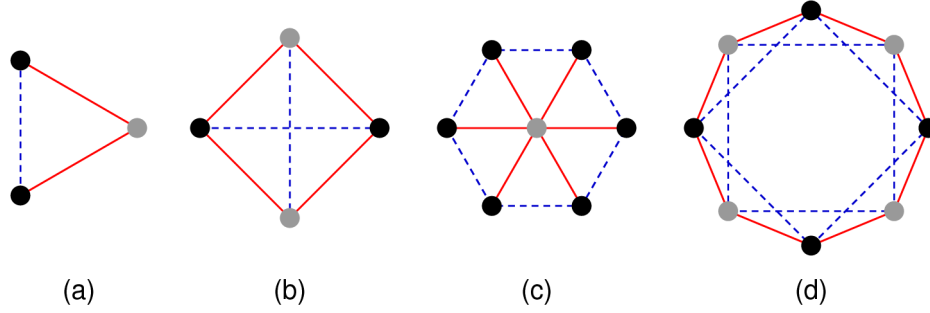
FIG. 2. The systems (a-c) are LMB ones for any threshold $g^2 > 0$, whereas that in (d) is LMB one for $g^2 = 0$ only, since there is no third-neighbour couplings. In all cases grey and black full circles denote spins from subsets A and B, respectively. Solid lines denote exchange integrals greater than or equal to the threshold g^2, whereas those with $J \leq g^2$ are depicted by dashed lines. Since $g^2 = 0$ in the case (d) then it illustrates an octanuclear antiferromagnetic ring with ferromagnetic couplings of the second-neighbours

2.3. Remarks

It was not stated by the authors, but was pointed out in Ref. [19] that the proof presented in Ref. [5] is correct when the appropriate graph is connected [37], i.e. there exists a path connecting any two vertices. In the other words, for any pair $\{j, k\}$, there exits at least one s-element sequence ($s > 0$, $l_0 \equiv j$, $l_s \equiv k$)

$$J_{j\, l_1}, J_{l_1\, l_2}, J_{l_2\, l_3}, \ldots, J_{l_{s-1}\, k} \tag{3}$$

with non-zero elements $J_{l_r\, l_{r+1}}$ for all $0 \leq r < s$. In the opposite case, there are two (or more) non-interacting subsystems X and Y (not necessarily bipartite) with the ground-state total spin numbers $S_{X(Y)}$, respectively. Hence, the whole system is highly degenerate with the total spin S being any number in the range $(|S_X - S_Y|, S_X + S_Y)$. Only for one of them equal to 0, the ground-state of the system is a uniquely determined S-multiplet with $S = S_X$ (assuming $S_Y = 0$) in the absence of accidental degeneration in the subsystems.

When $g^2 = 0$, then in each of the subsystems, only ferromagnetic exchange integrals are possible, so appropriate subsets constitute ferromagnetic components. Moreover, in this case, all cycles contains an even number of antiferromagnetic bonds, so a system in question is not geometrically frustrated [28, 30, 38, see also Fig. 2(d)]. However, for $g^2 > 0$ coexistence of LM-bipartiteness and (geometric) frustration is possible (see Figs. 2(a)–(c) and more detailed discussion in Refs. [29, 30, 32]). Even more, since systems considered are complete (and therefore connected for $g^2 > 0$) then geometric frustration is surely present, since there is at least one antiferromagnetic coupling in one of the subsystems. If such bonds do not exist then $g^2 = 0$ may be assumed and, henceforth, the geometric frustration is absent.

In the paper by Lieb and Mattis [5], there is no formal exclusion of empty sets, but assuming, for example, $B = \emptyset$ trivial results are received (see Sec. 3 below). It is only worth to mention that in such a case for each pair $\{j, k\}$, there exists at least one sequence (3) with all exchange integrals being negative. Hence, the system cannot be decomposed, but it is not necessarily ferromagnetic (cf. Ref. [5]).

3. The Lieb–Mattis theorem and its applications

3.1. The theorem

For the LMB system the numbers $S_{A(B)}$ and their absolute difference are introduced:

$$S_A = \sum_{j \in A} s_j, \quad S_B = \sum_{k \in B} s_k, \quad \mathcal{S} = |S_A - S_B|. \tag{4}$$

Lieb and Mattis proved that the ground state of the Hamiltonian (1) belongs at most to total spin $S = \mathcal{S}$. Hence, the absolute difference is the upper limit of the ground-state total spin: $S_0 \leq \mathcal{S}$. Let $E_{\min}(S)$ denotes the minimum energy of states belonging to the total spin S. The LMF says that these energies form an increasing sequence, i.e.:

$$E_{\min}(S) > E_{\min}(S - 1) \quad \text{for all} \quad S > \mathcal{S}. \tag{5}$$

This is referred to as the Lieb–Mattis level order (LMLO) and, introducing differences:

$$\Delta_S = E_{\min}(S) - E_{\min}(S - 1), \tag{6}$$
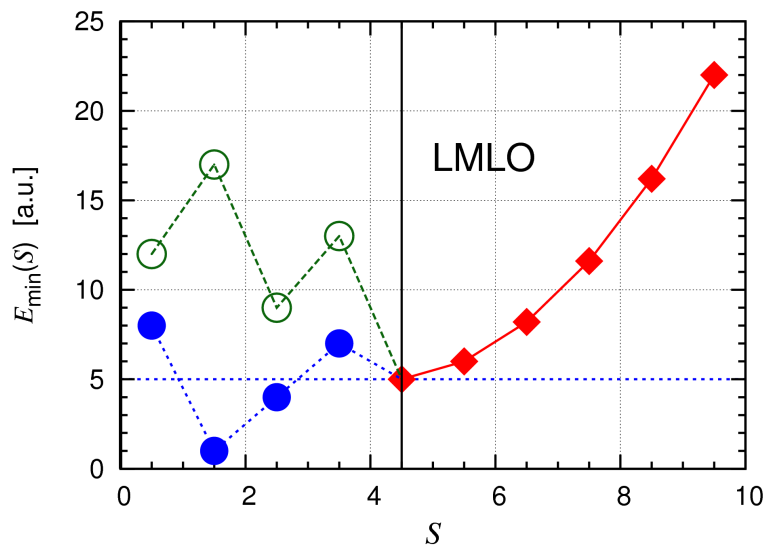
FIG. 3.   Illustration of the Lieb–Mattis level order in LM-bipartite systems. For the sake of simplicity it is assumed that the Landé band for $S \geq \mathcal{S}$ (full squares) is parabolic. Full and empty circles correspond to $g^2 > 0$ and $g^2 = 0$, respectively. Lines are a guide for the eye

can be reformulated as: Δ_S are positive for all $S > \mathcal{S}$. This effect is observed in many quantum spins systems and it is said that eigenstates with energies $E_{\min}(S)$ form the so-called Landé band [39,40]. In the special case of non-frustrated systems, i.e. for $g^2 = 0$, a stronger constraint can be proved [5]:

$$E_{\min}(S) > E_{\min}(\mathcal{S}), \quad \text{for} \quad S < \mathcal{S}, \tag{7}$$

which unambiguously determines $S_0 = \mathcal{S}$ (see Fig. 3). It has to be emphasized that the LMT says nothing about ordering of levels with $S < \mathcal{S}$. A general formulation of the LMT is also referred to as the 'weak form' with the 'strong form' assigned to the case $g^2 = 0$.

If, by chance, there are a few possible LM-bipartitions, with different threshold g^2 probably, then the most restrictive one, i.e. this with the least $\mathcal{S}$, is applied. If the case $B = \emptyset$ was allowed, then the trivial result would be obtained $S_0 \leq S_{\max} = \sum\limits_{j=1}^{n} s_j$, with the equality sign for purely ferromagnetic systems only ($g^2 = 0$ would force all non-zero weights J_{jk} to be negative in this case). Assuming systems in Fig. 2 to be homogeneous ($s_j = s$ for all $1 \leq j \leq n$) the following constraints can be easily determined: (a) $S_0 \leq s$, (b) and (d) $S_0 = 0$, and (c) $S_0 \leq 5s$. Other examples can be found in Refs. [28–30, 32, 41].

A very important example of LMB systems is the so-called sublattice Hamiltonian or the rotational band model [39, 42–44]. Spins are divided into subsets A and B with all pairs $\{j, k\}$, $j \in A$, $k \in B$, coupled antiferromagnetically with the same magnitude $J > 0$, so:

$$H = J\, \boldsymbol{S}_A \cdot \boldsymbol{S}_B, \quad \text{where} \quad S_{A(B)} = \sum\limits_{j \in A(B)} \boldsymbol{s}_j. \tag{8}$$

This system is LM-bipartite with any $0 \leq g^2 \leq J$, so the least value ($g^2 = 0$) yields $S_0 = |S_A - S_B|$ and the corresponding graph is complete bipartite one.

3.2.   Remarks about the proof

The original proof in Ref. [5] was decomposed into two parts: (i) a detailed discussion on the case $g^2 = 0$ and (ii) a short comment on the general case, so this paper goes along this way. The most crucial is a canonical transformation:

$$s_j^x \to -s_j^x, \quad s_j^y \to -s_j^y, \quad s_j^z \to +s_j^z \tag{9}$$

for all spins in a chosen subsystem, say $j \in A$. It yields all off-diagonal entries to be non-positive [5,19]. Further analysis may be done repeating Lieb and Mattis's reasoning or the Perron-Frobenius theorem (PFT) may be invoked (see below and Ref. [19]).
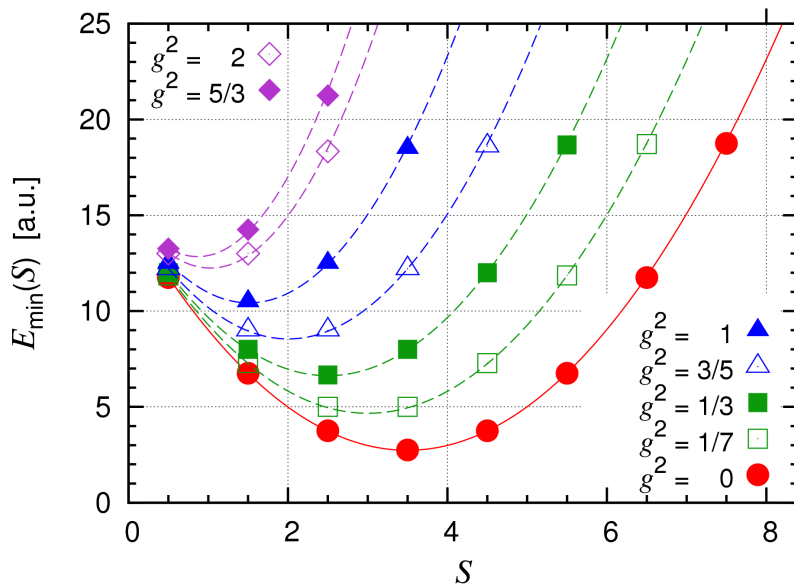
FIG. 4. The energies $E_{\min}(S)$ (the Landé band) for fictitious LM-bipartite Hamiltonians $H(g) = g^2\boldsymbol{S}^2 + S(S-7) + 15$. Symbols are defined in the legend and lines are a guide for the eye

When a Hamiltonian, commuting with $\boldsymbol{S}^2$, is LM-bipartite for $g^2 > 0$ then, it is transformed to:

$$H' = H - g^2\boldsymbol{S}^2, \tag{10}$$

which determines the LMB system with $g' = 0$. Since usually the threshold g^2 can be chosen in (infinitely) many ways, it must be done carefully – the Hamiltonian H' has to satisfy all conditions stated in the previous section, among others the corresponding bipartite weighted graph has to be connected and complete. This transformation does affect the upper limit given by $\mathcal{S}$ (the partition into sets A and B is not modified) and the LMLO for $S > \mathcal{S}$ is preserved. However, the inequality (7) does not hold, in a general case. Modifying a bit Eq. (10) one may introduce:

$$H(g) = H' + g^2\boldsymbol{S}^2,$$

and observe changes in energies $E_{\min}(S)$ for different values of g^2. A simple example is presented in Fig. 4, where $H' = S(S-7) + 15$ is assumed. The ground-state total spin S_0 decreases for increasing g^2, yielding the sequence $S_0 = 7/2, 5/2, 3/2, 1/2$ with 'critical' values of $g^2 = 1/7, 3/5$, and $5/3$ (at this points the ground-state level is formed by two S-multiplets with different total spin number S, so the degenerate frustration may be observed [45]).

However, the second (increasing) part of the universal sequence discussed in Refs. [29,30] cannot be explained in this way. It is important to emphasize that this sequence is received when the energies $E_{\min}(S)$ for $S < \mathcal{S}$ are ordered, what constitutes the special case. In a general case, different values of S_0 may appear in any order (cf. Fig. 3).

To end this section, the relation between the two theorems, Lieb–Mattis and Perron–Frobenius, is discussed. The latter one (PFT) is presented after Ref. [19]. Let A be a square matrix of size $N > 1$ with *all* entries being non-negative real numbers. If there exits $p \geq 1$ that A^p has *strictly positive* entries, then, with Λ being a set of all eigenvalues of A:

(1) $\lambda_0 = \max\limits_{\lambda \in \Lambda} |\lambda| \in \Lambda$ and it is simple (non-degenerate), i.e. it is a simple root of $\det(A - \lambda\mathbb{I}_N) = 0$, where $\mathbb{I}_N$ is the unit matrix;

(2) for any other $\lambda \in \Lambda$, $|\lambda| < \lambda_0$;

(3) the eigenvector of A associated to λ_0 has strictly positive coordinates.

These conditions are satisfied, for example, for the operator $\boldsymbol{S}^2$, so a vector with positive coordinates is associated to $S_{\max}$ in each subspace with given total magnetization M.

To use the PFT in the proof of the LMT, it is necessary to perform such modification of the Hamiltonian matrix that the above requirements are satisfied. The first step is done with the transformation (9). Since the minimum is what ones looks for, then the sign of this matrix is changed. The eigenvalues $E_{\min} \leq E \leq E_{\max}$ of the Hamiltonian (1) satisfy, as a rule, $E_{\min} < 0$, $E_{\max} > 0$, and $|E_{\min}| > E_{\max}$, so these two steps should be enough. In

the other case, to ensure that $E_{\min}$ and the corresponding eigenvector are determined properly, a shift may be done, i.e. a matrix $\gamma \mathbb{I}_N$ with enough large $\gamma > 0$ is added to obtain the matrix A. The connectivity of the corresponding graph guarantees that for some $p \geq 1$ all matrix elements of A^p are strictly positive.

4. Open problems

The LMT, with the proof sketched in the previous section, explains many features observed in investigated models of molecular nanomagnets. However, there are facts, which cannot be assigned to this theorem in the present form. It has been already mentioned above that the second part of the total spin sequence discussed in Refs. [29,30] cannot be explained by the simple analysis illustrated in Fig. 4. Moreover, in the case of ring-shaped molecules studied some features go beyond the properties given by the LMT. E.g., the differences (6) are not only positive, but also form an increasing sequence (see Fig. 5):

$$\Delta_S > \Delta_{S-1}, \quad \text{for all} \quad S > S_0; \tag{11}$$

note that is true also for $S_0 < \mathcal{S}$ [30,32]. Even if this fact is not directly mentioned, it is confirmed by magnetization steps presented (see, e.g., Refs. [34,46]).

These phenomena are clearly seen considering a very simple model of a heterogeneous centered square (see the inset in Fig. 5) with the Hamiltonian:

$$H_{\square} = J_1(\boldsymbol{s}_1 + \boldsymbol{s}_3) \cdot (\boldsymbol{s}_2 + \boldsymbol{s}_4) + J_2 \boldsymbol{s}_0 \cdot (\boldsymbol{s}_1 + \boldsymbol{s}_2 + \boldsymbol{s}_3 + \boldsymbol{s}_4). \tag{12}$$

To keep this system symmetric, it is postulated that $s_j = s$ for $1 \leq j \leq 4$ with $s_0 = s'$ in a general case. Introducing intermediate spins:

$$\boldsymbol{S}_A = \boldsymbol{s}_1 + \boldsymbol{s}_3, \quad \boldsymbol{S}_B = \boldsymbol{s}_2 + \boldsymbol{s}_4, \quad \boldsymbol{S}_{\square} = \boldsymbol{S}_A + \boldsymbol{S}_B, \quad \boldsymbol{S} = \boldsymbol{s}_0 + \boldsymbol{S}_{\square}$$

and assuming $J_1 = 1$, $J_2 = \alpha J_1$ it can be rewritten as:

$$H_{\square} = \boldsymbol{S}_A \cdot \boldsymbol{S}_B + \alpha \boldsymbol{s}_0 \cdot \boldsymbol{S}_{\square},$$

so its eigenvalues can be exactly determined with simple algebra for all values of the spin numbers $0 \leq S_{A,B} \leq 2s$, $0 \leq S_{\square} \leq 4s$, $0 \leq S \leq 4s + s'$ and the parameter $\alpha \in \mathbb{R}$ (cf. Refs. [30,34,43]). Some ranges of the parameter α can be clearly distinguished:

(1) $\alpha < 0$: The system is not LMB, so the constraint $S_0 \leq 4s + s'$ is applicable only.
(2) $\alpha = 0$: Two non-interacting systems are present, but one of them has $S_{\square} = 0$, so it has to be $S_0 = s'$ with any accidental degeneration.
(3) $0 < \alpha < 1$: there are two possibilities:
   (a) To take $\alpha < g^2 < 1$ and consider the system as one-component with $S_0 \leq 4s + s'$.
   (b) To consider a bipartition $A = \{1,3\}$, $B = \{0,2,4\}$ with $g^2 = \alpha$. However:

$$H'_{\square} = (1 - \alpha)\boldsymbol{S}_A \cdot \boldsymbol{S}_B - \alpha(\boldsymbol{s}_1 \cdot \boldsymbol{s}_3 + \boldsymbol{s}_2 \cdot \boldsymbol{s}_4),$$

   so two non-interacting subsystems, as in the case (2) above, are obtained, and therefore, formally, the LMT cannot be applied.
(4) $\alpha = 1$: It is a very particular point. Assuming $g^2 > 1$ yields H' describing the single ferromagnetic component, whereas $g^2 = 1$ leads to two ferromagnetic components ($A' = \{1,3\}$, $B' = \{2,4\}$) and isolated spin $\boldsymbol{s}_0$.
(5) $\alpha > 1$: The domain of the LMT is reached, at last. The system is LMB for any $1 \leq g^2 \leq \alpha$ and for the least value $g^2 = 1$ one has:

$$H' = -(\boldsymbol{s}_1 \cdot \boldsymbol{s}_3 + \boldsymbol{s}_2 \cdot \boldsymbol{s}_4) + (\alpha - 1)\boldsymbol{s}_0 \cdot \boldsymbol{S}_{\square}$$

   with obvious LM-bipartition $A' = \{1,2,3,4\}$, $B' = \{0\}$, so $\mathcal{S} = |4s - s'|$.

The results obtained for $s = 1$, $s' = 2$ are presented in Fig. 5. It is evident that the LMLO is present for all $\alpha \in \mathbb{R}$, even with the stronger constraint given by Eq. (11). Also the sequence of the ground-state total spin $S_0(\alpha)$ (see the inset in Fig. 5) is consistent with the previous discussion [29,30,32,47, see also Fig. 4], though g^2 can be assumed constant here. Analogous results were also obtained for the isosceles triangle [29,30].

All the above features follow the special properties of ring-shaped molecules investigated and can be explained by 'specialized' forms of the LMT or more detailed studies, including careful analysis of the energy spectrum for $S < \mathcal{S}$ and discussion on the special cases: two isolated subsystems or one-component systems (cf. Ref. [19]). It is very likely that in some cases such considerations will allow to apply the PFT in its original form. However, the same properties have been confirmed by exact diagonalization calculations for larger systems [29,30,32,46], which, in general, are not LMB systems. In such cases the crucial transformation (9), performed for any decomposition into
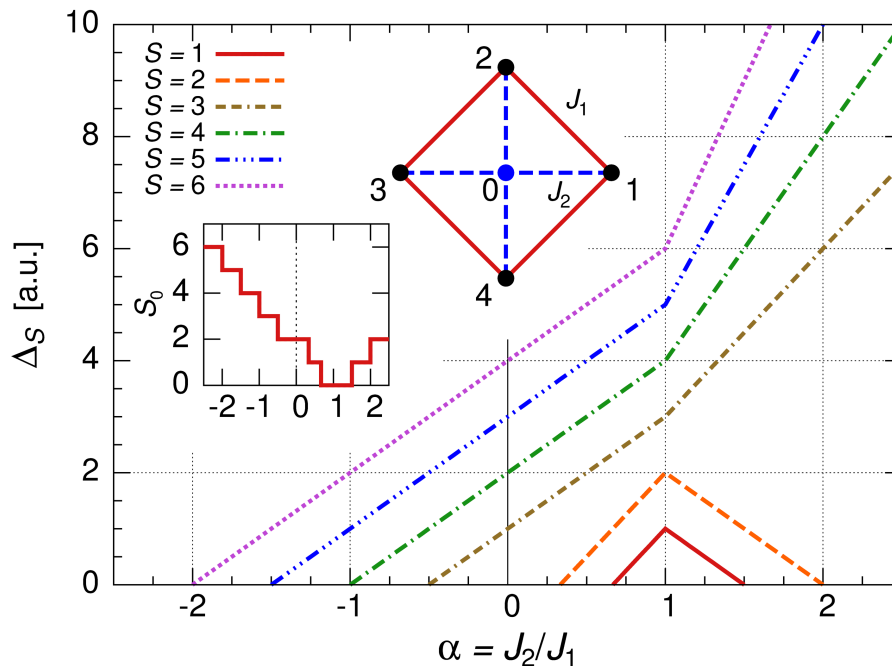
FIG. 5. The LMLO in a heterogeneous centred square presented in the inset ($s_0 = 2$, $s_1 = s_2 = s_3 = s_4 = 1$, $J_1 > 0$). Irrelevant segments (with $S < S_0$) are omitted. Zeros of Δ_S are placed at critical values $\alpha_c^{(k)} = -2, -3/2, -1, -1/2, 1/3, 2/3, 3/2, 2$ (for $1 \leq k \leq 8$, respectively), where the ground-state total spin number S_0 is changed (see the inset)

two non-empty subsystems, leaves some negative entries in the corresponding Hamiltonian matrices. It is expected that among a huge number of works on some generalizations of the PFT, at least some of them, e.g. [25–27], will provide new tools and ways of reasoning, which will help in generalization of the LMT to larger systems which, already, show main features of the LMB ones.

5. Conclusion and final remarks

The Lieb–Mattis theorem has been applied to many quantum spin systems and considered and generalized in various ways. However, the LMB systems with $g^2 > 0$ have not been carefully analyzed, since they appear under exceptional conditions. Progress in synthesis of molecular nanomagnets has shown that the coexistence of geometric frustration and LM-bipartition is possible and this observation has put forward interest in a general ('weak') form of the LMT. As it has been discussed above there are two main questions. At first, some features not included in the theorem itself, like the universal sequences of the ground-state total spin or the LMLO with the stronger condition (11), have to be investigated and explained. Secondly, the domain of the LMB should be thoroughly studied and necessary modifications should be done to include, for example, the whole range of the parameter α in Fig. 5 or larger, not LM-bipartite in general, systems. It can be presumed that a part of these problems can be solved applying the Perron-Frobenius theorem in its standard version, but in some cases generalizations of the PFT have to be taken into account.

Single-ion anisotropy plays the crucial role in investigations of single-molecule magnets and in many cases of anisotropic models some features analogous to LMLO are also observed [33,35,36,48,49]. However, in such cases the total spin is not a good quantum number, so the LMLO should be rather related to the total magnetization. Sometimes, for relatively small anisotropy parameters it is assumed that the total spin is, loosely speaking, 'an approximated good quantum number' and energy levels are labelled with S, even in the presence of anisotropy [40]. Such approach stands in contradictions to rigorous mathematical considerations presented above. Moreover, it was shown that such approximation can be accepted for levels with extreme energies, since they are quite stable, but there are abrupt changes of mean values of the total spin number for levels with intermediate energies [50,51]. On the other hand, it has to be carefully studied whether this is an intrinsic effect or it simply follows splitting of S-multiples observed in the isotropic regime. It should be emphasized that subspaces with a fixed magnetization are very important in the proof of the LMT, then rhombic anisotropy has to be excluded.

Acknowledgements

References

[1] Gatteschi D., Sessoli R., Villain J. *Molecular Nanomagnets*. Oxford University Press, Oxford, 2006.

[2] Winpenny R. E. P. *Molecular Cluster Magnets*. World Scientific Publ. Co., Singapore 2012.

[3] *Molecular Nanomagnets and Related Phenomena*, (Ed.: S. Gao), Springer, Berlin-Heidelberg 2015.

[4] Miller J., Gatteschi D. Molecule-based magnets. *Chem. Soc. Rev.*, 2011, **40** (6), P. 3053–3368.

[5] Lieb E., Mattis D. Ordering energy levels of interacting spin systems. *J. Math. Phys.*, 1962, **3**, P. 749–751.

[6] Lieb E., Schultz T., Mattis D. Two soluble models of an antiferromagnetic chain. *Annals of Physics*, 1961, **16**, P. 407–466.

[7] Buican M., Gromov A. Anyonic chains, topological defects, and conformal field theory. *Commun. Math. Phys.*, 2017, **356**, P. 1017–1056.

[8] Rajak A., Nag T. Survival probability in a quenched Majorana chain with an impurity. *Phys. Rev. E*, 2017, **96**, 022136.

[9] Nevado P., Fernández-Lorenzo S., Porras D. Topological edge states in periodically driven trapped-ion chains. *Phys. Rev. Lett.*, 2017, **119**, 210401.

[10] Cheng M., Zaletel M., et al. Translational symmetry and microscopic constraints on symmetry-enriched topological phases: A view from the surface. *Phys. Rev. X*, 2016, **6**, 041068.

[11] Ruppeiner G., Bellucci S. Thermodynamic curvature for a two-parameter spin model with frustration. *Phys. Rev. E*, 2015, **91**, 012116.

[12] Miyao T. Quantum Griffiths inequalities. *J. Stat. Phys.*, 2016, **164**, P. 255–303.

[13] Tylutki M., Astrakharchik G. E., Recati A. Coherent oscillations in small Fermi-polaron systems. *Phys. Rev. A*, 2017, **96**, 063603.

[14] Pan L., Liu Y., et al. Exact ordering of energy levels for one-dimensional interacting Fermi gases with $SU(N)$ symmetry. *Phys. Rev. B*, 2017, **96**, 075149.

[15] Oshikawa M. Commensurability, excitation gap, and topology in quantum many-particle systems on a periodic lattice. *Phys. Rev. Lett.*, 2000, **84**, P. 1535–1538.

[16] Nachtergaele B., Sims R. *Commun. Math. Phys.*, 2007, **276**, P. 437–472.

[17] Zaletel M.P., Vishwanath A. Constraints on topological order in Mott insulators. *Phys. Rev. Lett.*, 2015, **114**, 077201.

[18] Nomura K., Morishige J., Takaichi I. Extension of the Lieb-Schultz-Mattis theorem. *J. Phys. A: Math. Theor.*, 2015, **48**, 375001.

[19] Nachtergaele B., Spitzer W., Starr S. Ferromagnetic ordering of energy levels. *J. Stat. Phys.*, 2004, **116**, P. 719–738.

[20] Perron O. Zur Theorie der Matrizen. *Math. Ann.*, 1907, **64**, P. 248–263.

[21] Frobenius G. *Über Matrizen aus nicht negativen Elementen*. S.-B. Preuss Acad. Wiss., Berlin 1912, pp. 456–477.

[22] Simon B. *The Statistical Mechanics of Lattice Gases*, Vol. 1, Princeton Univ. Press, 1993.

[23] MacCluer C.R. The many proofs and applications of Perron's theorem. *SIAM Review*, 2000, **42**, P. 487–498.

[24] Hawkins T. Continued fractions and the origins of the Perron-Frobenius theorem. *Arch. Hist. Exact Sci.*, 2008, **62**, P. 655–717.

[25] Rump S.M. Theorems of Perron-Frobenius type for matrices without sign restrictions. *Lin. Alg. Appl.*, 1997, **266**, P. 1–42.

[26] Tarazaga P., Raydan M., Hurman A. Perron-Frobenius theorem for matrices with some negative entries. *Lin. Alg. Appl.*, 2001, **328**, P. 57–68.

[27] Noutsos D. On Perron-Frobenius property of matrices having some negative entries. *Lin. Alg. Appl.*, 2006, **412**, P. 132–153.

[28] Schnack J. Effects of frustration on magnetic molecules: a survey from Olivier Kahn until today. *Dalton Trans.*, 2010, **39**, P. 4677–4686.

[29] Kamieniarz G., Florek W., Antkowiak M. Universal sequence of ground states validating the classification of frustration in antiferromagnetic rings with a single bond defect. *Phys. Rev. B*, 2015, **92**, 140411.

[30] Florek W., Antkowiak M., Kamieniarz G. Sequences of ground states and classification of frustration in odd-numbered antiferromagnetic rings. *Phys. Rev. B*, 2016, **94**, 224421.

[31] Schnack J. Frustration effects in antiferromagnetic molecules: The cuboctahedron. *Polyhedron*, 2009, **28**, P. 1620–1623.

[32] Antkowiak M., Florek W., Kamieniarz G. Universal sequence of the ground states and energy level ordering in frustrated antiferromagnetic rings with a single bond defect. *Acta Phys. Pol. A*, 2017, **131**, P. 890–892.

[33] Caciuffo R., Guidi T., et al. Spin dynamics of heterometallic Cr_7M wheels M = Mn, Zn, Ni) probed by inelastic neutron scattering. *Phys. Rev. B*, 2005, **71**, 174407.

[34] Furrer A., Krämer K.W., et al. Magnetic and neutron spectroscopic properties of the tetrameric nickel compound $[Mo_{12}O_{28}(\mu_2\text{-}OH)_9(\mu_3\text{-}OH)_3\{Ni(H_2O)_3\}_4]\cdot13H_2O$. *Phys. Rev. B*, 2010, **81**, 214437.

[35] Antkowiak M., Kozłowski P., et al. Detection of ground states in frustrated molecular rings by in-field local magnetization profiles. *Phys. Rev. B*, 2013, **87**, 184430.

[36] Antkowiak M., Kucharski Ł., Kamieniarz G. Non-uniform coupling model of the frustrated chromium-based ring Cr_8Ni. *EPJ Web of Conferences*, 2014, **75**, 05007.

[37] Wilson R.J. *Introduction to Graph Theory*, Adison Wesley Longman Ltd., 4th edition, London, 1996.

[38] Toulouse G. Theory of the frustration effect in spin glasses: I. *Communications de Physique*, 1977, **2**, P. 115-119; Reprinted in *Spin Glass Theory and Beyond* (Eds.: Mézard M., Parisi G., Virasoro M.A.), World Scientific Publ. Co., Singapore, 1987, P. 99–103.

[39] Waldmann O. Spin dynamics of finite antiferromagnetic Heisenberg spin rings. *Phys. Rev. B*, 2001, **65**, 024424.

[40] Kamieniarz G., Kozłowski P., et al. Phenomenological modeling of molecular-based rings beyond the strong exchange limit: Bond alternation and single-ion anisotropy effects. *Inorg. Chimica Acta*, 2008, **361**, P. 3690–3696.

[41] Sobocińska M., Antkowiak M., et al. New tetranuclear manganese clusters with $[Mn_3^{II}Mn^{III}]$ and $[Mn_2^{II}Mn_2^{III}]$ metallic cores exhibiting low and high spin ground state. *Dalton Trans.*, 2016, **45**, P. 7303–7311.

[42] Schnack J., Luban M., Modler R. Quantum rotational band model for the Heisenberg molecular magnet $Mo_{72}Fe_{30}$. *Europhys. Lett.*, 2001, **56**, P. 863–869.

[43] Florek W., Kaliszan L.A., Kunert H.W., Machatine A.G.J. Small antiferromagnetic spin systems – sublattice Hamiltonians. *Physica B*, 2010, **405**, P. 3811–3817.

[44] Florek W., Kaliszan L.A. Small antiferromagnetic spin systems: Just beyond the rotational band model. *Acta Phys. Pol. A*, 2015, **127**, P. 330–332.

[45] Kahn O. Competing spin interactions and degenerate frustration for discrete molecular species. *Chem. Phys. Lett.*, 1997, **265**, P. 109–114.

[46] Sharples J.W., Collison D., et al. Quantum signatures of a molecular nanomagnet in direct magnetocaloric measurements. *Nature Commun.*, 2014, **5**, 5321.

[47] Ako A.M., Waldmann O., et al. Odd-numbered Fe^{III} complexes: Synthesis, molecular structure, reactivity, and magnetic properties. *Inorg. Chem.*, 2007, **46**, P. 756–766.

[48] Kozłowski P, Antkowiak M., Kamieniarz G. Frustration signatures in the anisotropic model of a nine-spin $s = 3/2$ ring with bond defect. *J. Nanopart. Res.*, 2011, **13**, P. 6093–6102.

[49] Baker M.L., Guidi T., et al. Spin dynamics of molecular nanomagnets unravelled at atomic scale by four-dimensional inelastic neutron scattering. *Nature Phys.*, 2012, **8**, P. 906–911.

[50] Florek W., Jaśniewicz-Pacer K, Kaliszan L. A., Kamieniarz G. Single-ion anisotropy in a four-spin system: mixing of S-states. *Cen. Eur. J. Chem.*, 2009, **7**, P. 211–214.

[51] Florek W., Kaliszan L.A., Jaśniewicz-Pacer K., Antkowiak M. Numerical analysis of magnetic states mixing in the Heisenberg model with the dihedral symmetry. *EPJ Web of Conferences*, 2013, **40**, 14003.

Kinetic model of electron transport in cylindrical nanowire with rough surface

S. A. Botman, S. B. Leble

Immanuel Kant Baltic Federal University, ul. Aleksandra Nevskogo, 14, Kaliningrad, 236016, Russia

sbotman@innopark.kantiana.ru, sleble@kantiana.ru

In this work, the problem of electron transport in cylindrical nanowires is considered. A model of nanowire is proposed with the irregularities/scatterers concentrated mainly in the vicinity of the surface. It is treated as a waveguide with some scattering indicatrix introduced to describe specular and nonspecular scattering. Employing the kinetic approach, Kolmogorov equation is used to calculate subsequently aproximate nonequlibrium distribution function and derive explicit formula for the resistivity of the system.

1. Introduction

One of the important feature of low dimensional systems is that they can exhibit properties which differ markedly from the corresponding bulk systems [1]. The problem of transport in these systems has commanded great attention over the past decades from both experimental and theoretical physicists [2–5]. Although numerous approaches to the electron transport modeling problem were developed, most of them rely on Kolmogorov equation [6] in the view of the fact that conductivity process is a nonequilibrium one.

The key component of kinetic approach is collision integral determination, which can be done in various ways. An expression for the integral can be obtained directly by calculating Bloch waves scattering amplitudes [7,8] or by introducing some semiempirical scattering indicatrix. Fuchs proposed model for DC conductivity in thin metal films based on combination of specular and nonspecular electron scattering on film boundary [9]. This approach was adopted and enhanced in a number of works [10–12].

The main goal of this work is to study Kolmogorov equation for conductivity electron within rough surface cylindrical nanowire with certain type of scattering indicatrix implied. In contrast with multiple scattering expansion, we use an expansion with respect to a small parameter [1] characterizing a weak deviation from equilibrium that leads to conventional Fredholm integral equations of convolution type. Its investigation gives simple solutions obtained using Fourier transform.

2. Kinetic model

2.1. Scattering models

Let's consider electron transport problem for cylindrical nanowire. As a source of electrons, we take the base of the cylinder, i.e. a round plate, that emits the electrons distributed by Fermi–Dirac function. Resistivity of such a system arises from the scattering of the electrons on phonons, other electrons or structural defects. For low-dimensional structures, the surface can be treated as defect and is believed to have biggest contribution to resistivity at low temperatures [3].

It is natural to introduce cylindrical coordinate system (ρ, ϕ, z) with respect to the symmetry of the system so that axis z is aligned with the center of cylinder. Also, one may introduce cylindrical coordinate system (v_ρ, v_ϕ, v_z) in velocity subspace of phase space. Assuming orts in velocity subspace are denoted as $(\vec{e}_\rho, \vec{e}_\phi, \vec{e}_z)$, the confinement condition for scattered electron can be expressed as follows:

$$\left(\vec{v'}, \vec{e}_\rho\right) \leq 0, \tag{1}$$

where $\vec{v'}$ – velocity of electron after scattering on surface.

Generally, if the precise scattering cross section $\Sigma(\vec{v}, \vec{v'}, \vec{r})$ is known, it can be reduced to averaged cross section:

$$\sigma(\vec{v}, \vec{v'}, \rho) = \iint \Sigma(\vec{v}, \vec{v'}, \vec{r}) \, dz d\phi. \tag{2}$$
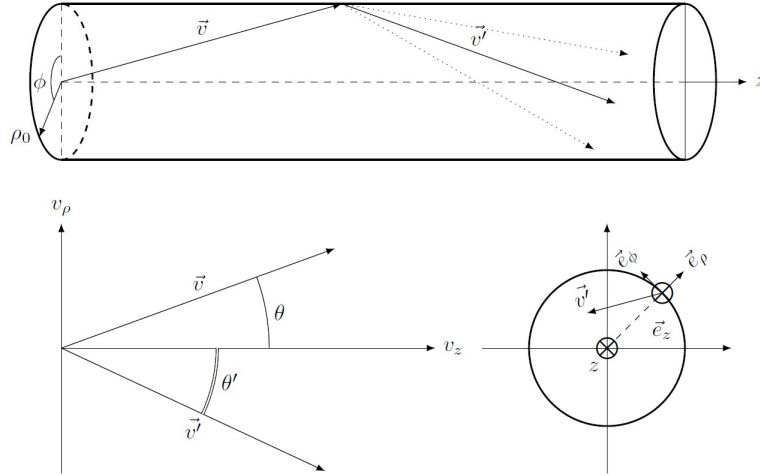
FIG. 1. Electron scattering on rough boundary of cylindrical nanowire introduced (top). Velocities of electron before and after scattering in velocity subspace (bottom left). Illustration of confinement condition (bottom right)

However, the problem of finding exact form of Σ is of immense complexity. That is why the usual approach is to directly introduce semiempirical averaged scattering cross section σ, such as specular reflection and elastic random angle scattering [12].

The differential cross section for elastic specular scattering on a boundary will have the following form:

$$\sigma = \delta(\rho - \rho_0)\delta(v'_z - v_z)\delta(v'_\rho - v_\rho)\delta(v'_\phi - v_\phi - \pi). \qquad (3)$$

Assuming that the nanowire is homogeneous and scattering cross section does not dependent upon the position on the surface, one may drop ϕ coordinate (with respective velocity component) from consideration, so the remaining coordinates are $\rho \in [0, \infty)$, $z \in (-\infty, \infty)$ and the problem turns into a two-dimensional one. Thus, for elastic the scattering of an electron on a perfectly smooth boundary ($v'_z = v_z$, $v'_\rho = -v_\rho$), the differential cross section appears as follows:

$$\sigma = \delta(\rho - \rho_0)\delta(v'_z - v_z)\delta(v'_\rho + v_\rho)\Theta(-v'_\rho), \qquad (4)$$

where ρ_0 – nanowire radius, δ – Dirac delta function, Θ – Heaviside step function. The latter multiplier in (4) is the confinement condition (1).

The main difference of rough boundary with smooth one is that the velocity angle of scattered particle follows some distribution. However, preserving the condition of elastic scattering conserves the velocity modulus. In order to take into account this conservation law, one may introduce the velocity modulus v and velocity direction θ (assuming that $\theta = 0$ corresponds to direction along z-axis). Thus, for rough wall scattering, the differential cross section will have the following form:

$$\sigma = \delta(\rho - \rho_0)\delta(v' - v)G(\theta' + \theta)\Theta(-\theta')\Theta(\theta' + \pi), \qquad (5)$$

where G – some distribution function. The sum within brackets of G implies that the maximum scattering probability corresponds to the case when the incident angle equals the scattering angle.

Or, in more general case, taking into account extent of the outer surface, one may transform (5) as follows:

$$\sigma = A(\rho)\delta(v' - v)G(\theta' + \theta)\Theta(-\theta')\Theta(\theta' + \pi), \qquad (6)$$

where $A(\rho)$ – some radial distribution of scatterers (one may choose $F(\rho) = \Theta(\rho_0 - \rho)$ in case of infinitely thin surface layer). and G – some functions, that describe scattering probability with respect to angles.

2.2. Kinetic equation

Let's now consider the kinetic problem for electrons moving in a cylindrical nanowire with an applied electrostatic field. In the simplest case, for transport studies we assume that the external electrical field with intensity E is applied along the z-axis and system is finite and restrained by electrode contacts from both sides.

The Kolmogorov equation for this case will have the following form:

$$\frac{\partial f}{\partial t} + eE\frac{\partial f}{\partial v_z} + v_z\frac{\partial f}{\partial z} + v_\rho\frac{\partial f}{\partial \rho} + v_\phi\frac{\partial f}{\partial \phi} = -f\int \sigma(r, \vec{v}, \vec{v'})d\vec{v'} + \int \sigma(r, \vec{v'}, \vec{v})f(\vec{v} = \vec{v'})d\vec{v'}, \qquad (7)$$

where, $f = f(t, \vec{r}, \vec{v})$ – distribution function, $\sigma = \sigma(\vec{r}, \vec{v}, \vec{v'})$ – scattering cross section, e – elementary electric charge.

Electrons on cathode follow the Fermi–Dirac distribution:

$$n_F(v) = \left[\exp\left(\frac{mv^2/2 - E_F}{k_B T} \right) + 1 \right]^{-1}, \tag{8}$$

where T – temperature, k_B – Boltzmann constant, E_F – Fermi energy, m – electron mass.

Next, it is safe to assume that equilibrium distribution function can be chosen as follows:

$$f_e = n_F(v)F(\rho), \tag{9}$$

where $F(\rho)$ – some radial distribution of charge carriers (one may choose $F(\rho) = \Theta(\rho_0 - \rho)$ in case of infinitely thin surface layer).

Henceforward, we will consider the simplest case of stationary ($\partial f / \partial t = 0$) and homogeneous ($\partial f / \partial z = 0$, $\partial f / \partial \phi = 0$) electron current. In this case, equation (7) turns into:

$$eE\frac{\partial f}{\partial v_z} + v_\rho \frac{\partial f}{\partial \rho} = -f \int \sigma(\rho, \vec{v}, \vec{v'})d\vec{v'} + \int \sigma(\rho, \vec{v}, \vec{v'})f(\vec{v} = \vec{v'})d\vec{v'}, \tag{10}$$

where $f = f(\rho, v_\rho, v_z)$ (phase space of the system is reduced to three dimensions).

Let's assume that deviation f_d of nonequilibrium distribution function f from equilibrium one f_e is small, i.e. $f = f_e + \varepsilon f_d$, where we introduced ε – small parameter ($|\varepsilon| \ll 1$).

It should be noted that substitution of $\vec{v}$-symmetric function f_e into right part of (10) gives zero. Considering this fact, and taking into account that f_d is $\vec{v}$-antisymmetric, putting for brevity $\epsilon = 1$, one finally obtains:

$$eE\frac{\partial f_e}{\partial v_z} + v_\rho \frac{\partial f_e}{\partial \rho} = -f_d \int \sigma(\rho, \vec{v}, \vec{v'})d\vec{v'} + \int \sigma(\rho, \vec{v}, \vec{v'})f_d(\vec{v} = \vec{v'})d\vec{v'}. \tag{11}$$

2.3. Rough boundary case

Let's now consider more general case of the rough boundary. This means a reflection angle is not equal to incident one, though scattering is elastic and velocity module is preserved. For this case, we substitute (6) into (11) and switch to integration over v' and ϕ'. In this case, the equation (11) will have the following form:

$$eE\frac{\partial f_e}{\partial v_z} + v_\rho \frac{\partial f_e}{\partial \rho} = -f_d(\rho, v, \theta)A(\rho)v \int\limits_{-\pi}^{0} G(\theta' + \theta)d\theta' + A(\rho)v \int\limits_{-\pi}^{0} G(\theta' + \theta)f_d(\rho, v, \theta')d\theta'. \tag{12}$$

Next, we introduce the integral operator:

$$\hat{K}f(\rho, v, \theta) = \int\limits_{-\pi}^{0} G(\theta' + \theta)f_d(\rho, v, \theta')d\theta', \tag{13}$$

$$g = -\frac{eE\,F(\rho)\dfrac{\partial n_F}{\partial v_z} + v_\rho n_F \dfrac{\partial F(\rho)}{\partial \rho}}{A(\rho)\,v}, \tag{14}$$

where we took into account probability normalization condition $\int_{-\pi}^{0} G(\theta' + \theta)d\theta' = 1$.

Thus, (12) turns into:

$$f_d = g + \hat{K}f_d, \tag{15}$$

which in fact is a Fredholm equation of the second kind. It is useful to introduce a new variable $\alpha = -\theta'$ so that the kernel of integral equation $G(\theta - \alpha)$ is defined on the square i.e. $\theta, \alpha \in [0, \pi]$.

2.4. Fourier transform solution

In order to study equation (15), lets rewrite it in more general form:

$$\varphi = g + \lambda \hat{K}\varphi, \tag{16}$$

where φ – unknown function, $\hat{K}$ – integral operator of convolution type, g – nonhomogeneous term, λ – parameter:

$$\varphi(x) = \lambda \int K(x - s)\varphi(s)ds + g(x). \tag{17}$$

Here, integration is performed over an infinite region and function K is defined by extending G with zero outside $[0, \pi]$ intervals.

In general form, solution of (16) can be expressed as follows via the resolvent:

$$\varphi = (1 - \lambda \hat{K})^{-1} g. \tag{18}$$

In order to check for the existence of the solution (18) one may follow the Fredholm alternative and solve the corresponding homogeneous equation:

$$\varphi = \lambda \hat{K} \varphi. \tag{19}$$

Let us apply Fourier transform to each element of equation (19):

$$\varphi = \frac{1}{\sqrt{2\pi}} \int \tilde{\varphi}(\omega_1) e^{i\omega_1 s} d\omega_1, \tag{20}$$

$$K(x - s) = \frac{1}{\sqrt{2\pi}} \int \tilde{K}(\omega_2) e^{i\omega_2(x-s)} d\omega_2. \tag{21}$$

Thus:

$$\int \tilde{\varphi}(\omega) e^{i\omega x} d\omega = \frac{\lambda}{\sqrt{2\pi}} \iiint \tilde{K}(\omega_2) e^{i\omega_2(x-s)} \tilde{\varphi}(\omega_1) e^{i\omega_1 s} d\omega_1 d\omega_2 ds. \tag{22}$$

Let's multiply the left and right part of this equation by $e^{-i\omega_0 x}$ and integrate over x:

$$\sqrt{2\pi} \int \tilde{\varphi}(\omega) \delta(\omega - \omega_0) d\omega = \frac{\lambda}{\sqrt{2\pi}} \iiint \tilde{K}(\omega_2) \tilde{\varphi}(\omega_1) e^{i(\omega_1 - \omega_2)s} \left(\int e^{i(\omega_2 - \omega_0)x} dx \right) d\omega_1 d\omega_2 ds =$$

$$= \lambda \iiint \tilde{K}(\omega_2) \tilde{\varphi}(\omega_1) e^{i(\omega_1 - \omega_2)s} \delta(\omega_2 - \omega_0) d\omega_1 d\omega_2 ds. \tag{23}$$

Next, the remaining integrals can be trivially taken:

$$\tilde{\varphi}(\omega_0) = \frac{\lambda}{\sqrt{2\pi}} \iint \tilde{K}(\omega_0) \tilde{\varphi}(\omega_1) e^{i(\omega_1 - \omega_0)s} d\omega_1 ds =$$

$$= \frac{\lambda}{\sqrt{2\pi}} \tilde{K}(\omega_0) \int \tilde{\varphi}(\omega_1) \delta(\omega_1 - \omega_0) d\omega_1 = \frac{\lambda}{\sqrt{2\pi}} \tilde{K}(\omega_0) \tilde{\varphi}(\omega_0). \tag{24}$$

Or, changing the variables:

$$\left(1 - \frac{\lambda}{\sqrt{2\pi}} \tilde{K}(\omega) \right) \tilde{\varphi}(\omega) = 0. \tag{25}$$

Apparently, equation (25) will have no nontrivial solutions apart from cases when $K \sim \delta(x - s)$. Applying the Fredholm alternative to this problem (by setting $\lambda = 1$ and defining $\hat{K}$ accordingly) proves that inhomogeneous equation (16) will have solution.

Using the same approach for the inhomogeneous equation gives us:

$$\tilde{\varphi}(\omega) = \frac{\lambda}{\sqrt{2\pi}} \tilde{K}(\omega) \tilde{\varphi}(\omega) + \tilde{g}(\omega). \tag{26}$$

This equation is algebraic and thus can be solved easily:

$$\tilde{\varphi}(\omega) = \frac{\tilde{g}(\omega)}{1 - \frac{\lambda}{\sqrt{2\pi}} \tilde{K}(\omega)}. \tag{27}$$

Finally, solution of equation (16) can be found by applying inverse Fourier transform to both parts of (27):

$$\varphi(x) = \int \frac{\tilde{g}(\omega)}{\sqrt{2\pi} - \lambda \tilde{K}(\omega)} e^{ix\omega} d\omega. \tag{28}$$

Although expression (28) gives us formal solution for equation (15), its practical application is limited because as the problem of finding Fourier images $\tilde{g}$ and $\tilde{K}$ is not a trivial task.

2.5. Electron transport

The solution of (15) can also be obtained as follows:

$$f_d(\rho, v, \theta) = g(\rho, v, \theta) + \int\limits_0^\pi R(\theta - \alpha) g(\rho, v, \alpha)\, d\alpha, \tag{29}$$

where R – the resolvent of integral operator (14). It can be shown using Fourier transofrm [13] that equation (29) can be expressed as follows:

$$\tilde{f}_d(\omega) = [1 + \tilde{R}(\omega)] \tilde{g}(\omega), \tag{30}$$

The resolvent Fourier image can be found using equation (27):

$$\tilde{R}(\omega) = \frac{\tilde{K}(\omega)}{\sqrt{2\pi} - \tilde{K}(\omega)}. \tag{31}$$

Let us now choose the extended scattering amplitude function G as follows:

$$G(x) = \frac{1}{\sqrt{2\pi}\gamma} \exp\left(-\frac{1}{2\gamma^2} x^2\right), \tag{32}$$

which in fact is normal distribution. Here γ – parameter which corresponds to standard deviation. Then, one may plug Fourier image of (32) into equation (31), arriving at:

$$\tilde{R}(\omega) = \frac{2\pi}{2\pi - \sqrt{\gamma} \exp\left(-\frac{\gamma^2}{2}\omega^2\right)} - 1. \tag{33}$$

Assuming the spread of scattering angles is small i.e. $\gamma \ll 1$, one may neglect the second term of denominator in the relation (33), that yields $\tilde{R}(\omega) \approx 0$. Thus, for the zero order approximation of nonequilibrium distribution function one may use the function g:

$$f_d^0 = \frac{eEm}{k_B T} \frac{v_z}{v} \exp\left(\frac{\frac{m}{2}(v_z^2 + v_\rho^2) - E_F}{k_B T}\right) n_F^2 \frac{F(\rho)}{A(\rho)} - \frac{v_\rho}{v} \frac{1}{A(\rho)} \frac{\partial F(\rho)}{\partial \rho} n_F. \tag{34}$$

Let's now switch velocity coordinate system as ($v_z = v\cos(\theta)$, $v_\rho = v\sin(\theta)$):

$$f_d^0 = B(\rho, v)\cos(\theta) - C(\rho, v)\sin(\theta), \tag{35}$$

where:

$$B(\rho, v) = eE \frac{m}{k_B T} \exp\left(\frac{\frac{mv^2}{2} - E_F}{k_B T}\right) n_F^2(v, T) \frac{F(\rho)}{A(\rho)} = -\frac{eE}{v} \frac{\partial n_F(v)}{\partial v} \frac{F(\rho)}{A(\rho)}, \tag{36}$$

$$C(\rho, v) = \frac{1}{A(\rho)} \frac{\partial F(\rho)}{\partial \rho} n_F(v). \tag{37}$$

Generally, current density of the waveguide can be obtained as follows:

$$\vec{j}(\vec{r}) = e \int \vec{v} f_d(\vec{r}, \vec{v}) d\vec{v}. \tag{38}$$

For z-projection of homogeneous current density one obtains:

$$j_z(\rho) = e \int\limits_{-\infty}^\infty \int\limits_{-\infty}^\infty f_d\, v_z dv_\rho dv_z = e \int\limits_{-\pi}^\pi \int\limits_0^\infty f_d\, v^2 \cos(\theta) dv d\theta. \tag{39}$$

The total current through transverse surface can be calculated as:

$$J = \int\limits_0^{\rho_0} j_z(\rho) d\rho. \tag{40}$$

Next, taking into account parity of functions, integral of the second term in (35) will give zero. The form of expression (35) allows to perform variable separation and if the exact $A(\rho)$ and $F(\rho)$ are known, radial dependence

can be integrated out. Thus, one may obtain the temperature dependency of the system resistivity in zero order approximation:

$$R = -\frac{1}{S_0} \left[\int\limits_0^\infty v \frac{\partial n_F(v)}{\partial v}\, dv \right]^{-1}, \tag{41}$$

where S_0 – constant resulting from θ and ρ integration:

$$S_0 = e^2 \int\limits_0^{\rho_0} \frac{F(\rho)}{A(\rho)} d\rho \int\limits_{-\pi}^{\pi} \cos^2(\theta)d\theta = \pi e^2 \int\limits_0^{\rho_0} \frac{F(\rho)}{A(\rho)} d\rho. \tag{42}$$

The integral in (41) nontrivially depends on temperature. It can be shown using the Sommerfeld expansion that:

$$-\int\limits_0^\infty v \frac{\partial n_F(v)}{\partial v}\, dv = \frac{1}{\sqrt{2m}} \int\limits_0^\infty \frac{n_F(E)}{\sqrt{E}} dE \approx \frac{\sqrt{E_F}}{2\sqrt{2m}} + \frac{\pi^2}{12} \frac{(k_B T)^2}{\sqrt{2m E_F^3}}, \tag{43}$$

where Fermi energy also depends on temperature: $E_F(T) \approx E_F(0) \left(1 - \frac{\pi^2}{12} \frac{(k_B T)^2}{E_F^2(0)} \right)$, where $E_F(0)$ depens only on fundamental constants [14].

3. Results and discussion

It was shown that Kolmogorov equation for electrons in cylindrical nanowire with surface scattering introduced can be conceived of as Fredholm equation of the second kind. Existence of a solution was proved by applying Fredholm alternative in the Resolvent form, that is approved by transition to the Fourier transformed equation. Zero order approximation of solution was illustrated by the case of a gently sloping surface irregularities used to study resistivity temperature dependence of system under consideration in explicit form.

References

[1] Dresselhaus M. S. et al. *Springer Handbook of Nanotechnology*. Springer, 2010.

[2] Dingle R. B. The electrical conductivity of thin wires. *Proceedings of the Royal Society of London. Series A, Mathematical and Physical Sciences*, 1950, **201**(1067), P. 545–560.

[3] Lin Y., Sun X., and Dresselhaus M. S. Theoretical investigation of thermoelectric transport properties of cylindrical Bi nanowires. *Physical Review B*, 2000, **62**(7), P. 4610–4623.

[4] Pavlov B. S. and Strepetov A. V. Exactly solvable model of electron scattering by an inhomogeneity in a thin conductor *Theoretical and Mathematical Physics*, 1992, **90**(2), P. 152–156.

[5] Leble S. B. Kolmogorov equation for Bloch electrons and electrical resistivity models for nanowires. *Nanosystems: Physics, Chemistry, Mathematics*, 2017, **8**(2), P. 247–259.

[6] Kolmogoroff A. Über die analytischen Methoden in der Wahrscheinlichkeitsrechnung. *Mathematische Annalen*, 1931, **104**(1), P. 415–458.

[7] Lobanov I. S., Popov I. Yu. Scattering by a junction of zig-zag and armchair nanotubes. *Nanosystems: Physics, Chemistry, Mathematics*, 2012, **3**(2), P. 6–28.

[8] Botman S. A. and Leble S. B. Electrical conductivity model for quasi-one-dimensional structures. *Nanosystems: Physics, Chemistry, Mathematics*, 2017, **8**(2), P. 231–235.

[9] Fuchs K. The conductivity of thin metallic films according to the electron theory of metals. In *Mathematical Proceedings of the Cambridge Philosophical Society*, 1938, **34**(1), P. 100–108.

[10] Chaplik A. V. and Entin M. V. Energy spectrum and electron mobility in a thin film with non-ideal boundary. *Soviet Journal of Experimental and Theoretical Physics*, 1969, **28**(3), P. 514–517.

[11] Krokhin A., Makarov N. M., and Yampolskii V. A. Theory of the surface scattering of electrons in metals with gently sloping surface irregularities. *Soviet Physics-JETP*, 1991, **72**(2), P. 289–294.

[12] Makarov N. M., Moroz A. V., and Yampolskii V. A. Classical and quantum size effects in electron conductivity of films with rough boundaries. *Physical Review B*, 1995, **52**(8), P. 6087–6101.

[13] Manjirov A. V. and Polyanin A. D. *Reference book on integral equation*. Factorial press, 2000.

[14] Ashcroft N., Mermin N., Wei D. *Solid State Physics: Revised Edition.* Amazon press, 2016.

N wells at a circle. Splitting of lower eigenvalues

T. F. Pankratova

ITMO University, 49 Kronverkskiy, St. Petersburg, 197101, Russia

tanpankrat@yandex.ru

A stationary Schrödinger operator on $\mathbb{R}^2$ with a potential V having N nondegenerate minima which divide a circle of radius r_0 into N equal parts is considered. Some sufficient asymptotic formulae for lower energy levels are obtained in a simple example. The ideology of our research is based on an abstract theorem connecting modes and quasi-modes of some self-adjoint operator A and some more detailed investigation of low energy levels in one well (in $\mathbb{R}^d$).

Keywords: Shrödinger operator, potential, splitting, eigenvalues and eigenfunctions.

1. Introduction. Modes and quasi-modes

We use terms modes and quasi-modes following V. I. Arnold [1]. An eigenvalue and eigenvector of some operator A, i.e. a pair (λ, u) which satisfies equation $Au = \lambda u$ exactly, is called a mode. Some value and vector which satisfy this equation approximately with some error of order ε is called a quasi-mode. More precisely, the result is as follows:

Let A be a self-adjoint operator in a Hilbert space H, λ_0 – a real value, orthonormal vectors $u_1, u_2, ..., u_N \in D(A)$, Q is a positive constant, $\varepsilon = \max_{1 \leq i \leq N} \|(A - \lambda_0) u_i\|$, $0 < 4\sqrt{3}N\varepsilon < Q$, $\lambda_1, ..., \lambda_N$ are the eigenvalues of the matrix M with the inputs $\{M_{ik}\} = \{\langle Au_i, u_k \rangle\}$ ($\langle \cdot, \cdot \rangle$ means a scalar product in H), every eigenvalue is counted according to its multiplicity.

Theorem 1. *Suppose the interval $I = [\lambda_0 - Q, \lambda_0 + Q]$ contains at most N eigenvalues of A. Then, the interval $I_1 = \left[\lambda_0 - Q + 4\sqrt{3}N\varepsilon, \lambda_0 + Q - 4\sqrt{3}N\varepsilon\right]$ contains exactly N eigenvalues of A. There exist constants p and q such that if $0 < \varepsilon < p$ then, any interval $\delta_j = \left[\lambda_j - q\varepsilon^2, \lambda_j + q\varepsilon^2\right]$ is included in I_1 and contains an eigenvalue of A. Any connected component of the set $\bigcup_{j=1}^{N} \delta_j$ contains exactly as many eigenvalues of A as there are intervals δ_j forming it.*

Theorem 1 allows us to describe eigenvectors and eigenvalues of A based on the knowledge only of its quasi-modes. If δ_j does not intersect with δ_{j+1}, the distance between their middle points gives us a good approximation of the distance between the two nearest eigenvalues. The first proposition of Theorem 1 guaranties the absence of additional eigenvalue of A in our interval.

2. A self-adjoint Schrödinger operator on $\mathbb{R}^d$

Let us consider the Schrödinger equation:

$$-\frac{h^2}{2}\Delta u + Vu = Eu, \tag{1}$$

where $\Delta = \sum_{i=1}^{d} \frac{\partial^2}{\partial_i^2}$ is the Laplace operator, V is a real valued function defined on $\mathbb{R}^d$ having nondegenerate minima (wells) with some kind of symmetry, h (small parameter) is the Planck constant (in special system of units). Let A be the corresponding Schrödinger operator defined by the left hand side of equation (1) in $L_2(\mathbb{R}^d)$.

If V in (1) has a finite number of identical wells which differ only by space translations and $V(x) > C$ beyond the region of the wells where C exceeds the value of V at minimum, lower part of the spectrum of operator A is organized in the following way. There is a set of finite groups of eigenvalues (each of them is related

to some quantum vector $n \in \mathbb{N}^d$), the distance between the groups being of the order h, and the distance between eigenvalues in each group, the splitting, being exponentially small with respect to h.

It is possible to find explicit formulae for the widths of these splittings using semi-classical asymptotics for each well. The problem was considered in different ways by different authors and almost completely solved in one dimensional case [1–8]. The case $d > 1$ is much more complicated. There are many results obtained in this area (see [9–17] and the list is far from exhaustive). The semiclassical asymptotics of the discrete spectrum and strict estimates of the splittings are described in [9] and other works of these authors (using the theory of pseudo differential operators). The semiclassical expansion for the eigenfunctions and the rigorous asymptotics for the splitting widths in the lowest levels were obtained in [10] (with the use of Maslov's canonical operator). The possibility to solve this problem in that case was discussed during the Diffraction Day Conference 2014 in the talk of A. Anikin and M. Rouleux [12].

In the present work, in order to write down strict asymptotic formulae for splittings in two-dimensional case, one has to use Theorem 1. It is necessary to find a sufficiently accurate semiclassical approximation to eigenstates for a single well in some vicinity of a minimum, independent of h. Such an approximation was constructed in [11, 13]. The formal series on powers of h were obtained. Coefficients in all terms were found in some domain independent of h. Terms for eigenfunctions are analytic for analytic potential. If we truncate the series at the m-th term the remaining sums satisfy the equation (1) with an error of the order of $h^{m+1} \exp(-S/h)$, where S is a nonnegative function defined in [11]. The possibility to take m as large as we like and exponential decreasing of all terms beyond some vicinity of a minimum allows one to construct sufficient *quasi-modes*. Each *quasi-mode* has to be constructed from semiclassical approximations of lower eigenfunctions in the region of the bottom of each well vanishing beyond it.

In this work, a simple example is considered. Here, the circle containing N minima of V is f line of minimum of the corresponding functional b and it is easy to find b in a plain form.

3. An example. N wells at a circle

Let $d = 2$. Let V in equation (1) in polar coordinates be of the following form:

$$V = \frac{\omega_1^2}{2} (r - r_0)^2 + \frac{\omega_2^2}{2} \sin^2 \frac{N\phi}{2}, \qquad (2)$$

ω_1, ω_2 are some positive Diophantine numbers. (This means that there exist positive numbers α and β such that for any $k \in \mathbb{Z}^2$, $k \neq 0$, $|\langle k, \omega \rangle| \geq \frac{\beta}{|k|^\alpha}$).

It is easy to see that the points $M_j \left(r_0; \frac{2\pi j}{N} \right)$, $j = 0, 1, ..., N-1$, are nondegenerate minima of V, $M_j \in \Gamma$, Γ is a circle $r = r_0$ and

$$V(r, \phi) = V \left(r; \phi + \frac{2\pi j}{N} \right). \qquad (3)$$

We put a Cartesian system of coordinates $(x_j; y_j)$ in the vicinity of the bottom of each well in such a way that $M_j = M_j(0; 0)$ in this coordinates, axis x_j is tangential to a circle Γ at the point M_j and y_j is normal to it. One can find the following Taylor series for V:

$$V(X_j) = \frac{1}{2} \left(\hat{\omega}_1^2 x_j^2 + \hat{\omega}_2^2 y_j^2 \right) + \sum_{|k| \geq 3} v_k X_j^k,$$

$$X_j = (x_j; y_j), \quad k = (k_1; k_2), \quad X_j^k = x_j^{k_1} y_j^{k_2}, \quad |k| = k_1 + k_2, \quad \hat{\omega}_i > 0, \quad i = 1, 2,$$

in a vicinity of M_j. The form of this series does not depend on j because of equality (3).

In order to use Theorem 1, let us find semiclassical approximations $\left(\hat{u}_n, \hat{E}_n \right)$ for some first quantum vectors $n = (n_1, n_2)$, $n_1 = 0, 1, ...$; $n_2 = 0, 1, ...$; in each domain $D_j = \{|x_j| \leq \gamma, |y_j| \leq \hat{\gamma}\}$. They are the same for all D_j, $j = 0, 1, ...N-1$. Let us take numbers γ and $\hat{\gamma}$ such that two neighboring domains D_j and D_{j+1} intersect. Let domain $G_{j,j+1} = D_j \bigcap D_{j+1}$ be such an intersection. Let the point $\hat{M}_j = \hat{M}_j \left(r_0; \frac{\pi (2j+1)}{N} \right) \in G_{j,j+1}$, $j = 0, 1, ..., N-1$. Then, we multiply $\hat{u}_n$ by cutting functions $\chi^{[j]} = \chi^{[j]}(x_j, y_j) = \chi_1^{[j]}(x_j) \chi_2^{[j]}(y_j)$, where

$\chi_1^{[j]}(x_j)$ and $\chi_2^{[j]}(y_j)$ are smooth cutting functions, i.e.

$$\chi_1^j(x_j) = \left\{ \begin{array}{ll} 1, & |x_j| \leq \gamma, \\ 0, & |x_j| \geq \gamma + \varepsilon_1, \end{array} \right. \qquad \chi_2^j(y_j) = \left\{ \begin{array}{ll} 1, & |y_j| \leq \hat{\gamma}, \\ 0, & |y_j| \geq \hat{\gamma} + \varepsilon_2, \end{array} \right. \qquad \hat{u}_n \chi^{[j]} = \hat{\hat{u}}_n^{[j]}.$$

Function $\hat{u}_n^{[j]}$ is equal to zero beyond rectangular $\{|x_j| \geq \gamma + \varepsilon_1, |y_j| \geq \hat{\gamma} + \varepsilon_2\}$. We construct N quasi-modes $\tilde{u}_{n,k}$, $k = 1, ..., N$, as a linear combination of cut-off functions $\hat{u}_n^j$, i.e. $\tilde{u}_{n,k} = \sum\limits_{j=1}^{N} \alpha_{j,k} \hat{u}_n^{[j]}$, $k = 1, ..., N$. We find numbers $\alpha_{j,k}$ in order to orthonormalize the system $\{\tilde{u}_{n,k}\}_{k=1}^{N}$. Now, we can use Theorem 1 in a way similar to one presented in [8].

We find that for our example with N wells (eq. (2)) for each quantum vector N eigenvalues E_n^k, $k = 1, ..., N$, of operator A has the following form:

$$E_n^k = \hat{E}_n + \mu_k^{[n]} + O\left(\varepsilon^2\right),$$

where:

$$\hat{E}_n = \sum_{j=1}^{m} E_{n,j} h^j; \quad E_{n,1} = \left(n_1 + \frac{1}{2}\right)\hat{\omega}_1 + \left(n_2 + \frac{1}{2}\right)\hat{\omega}_2,$$

$$\mu_k^{[n]} = a \cdot \exp\left(-h^{-1}b\right) \cdot \cos\frac{\pi k}{N+1}, \quad k = 1, ..., N, \quad \mu_k^{[n]} = O\left(\varepsilon\right), \quad b = \int\limits_{M_{k-1} M_k} \sqrt{2V} dS,$$

$M_{k-1} M_k$ is a line of minimum of functional b. In our case it is a part of the circle Γ. At this circle, $\sqrt{2V} = \omega_2 \sin\frac{N\phi}{2}$, $dS = r_0 d\phi$. Hence, $b = \frac{4}{N} r_0 \omega_2$.

Now, we can write down the splitting formula for lower eigenvalues of operator A:

$$\Delta E_n^k = E_n^{k+1} - E_n^k = d_k \exp\left(-\frac{b}{h}\right)(1 + O(h)), \quad k = 1, ..., N.$$

One can regard this example as a simple model for some possibly more complicated situation.

References

[1] Arnol'd V.I., Modes and quasimodes. *Functional Analysis and Its Applications*, 1972, **6** (2), P. 94–101.

[2] Slavyanov S.Yu. Asymptotics of singular Sturm–Liouville problems with respect to a large parameter in the case of close transition points. *Differential Equations*, 1969, **5**, P. 313–325.

[3] Simon B. Semiclassical analysis of low lying eigenvalues, I. Non-degenerate minima: Asymptotic Expansions. *Ann. Inst. Henri Poincare*, 1983, **38**, P. 295–307.

[4] Simon B. Semiclassical analysis of low lying eigenvalues, II. Tunneling. *Ann. Inst. Henri Poincare*, 1984, **120**, P. 89–118.

[5] Maslov V.P. *The complex WKB-method in nonlinear equations*. Nauka, Moscow, 1981 (in Russian).

[6] Jona-Lasinio G., Martinelli F., Scoppola E. New approach to the semiclassical limit of quantum mechanics. *Comm. Math. Phys.*, 1981, **80**, P. 223–254.

[7] Harrel E.M. Double wells. *Comm. Math. Phys.*, 1980, **75**, P. 239–261.

[8] Pankratova T.F. Quasimodes and splitting of eigenvalues. *Soviet Math. Dokl.*, 1984, **29**, P. 597–601.

[9] Helffer B., Sjostrand J. Multiple wells in the semiclassical limit III – Interaction through non-resonant wells. *Math. Nachr.*, 1985, **124**, P. 263–313.

[10] Dobrokhotov S.Yu., Kolokoltsov V.N. Splitting amplitudes of the lowest energy levels of the Schrodinger operator with double well potential. *Theor. Math. Phys.*, 1993, **94** (3), P. 300–305.

[11] Pankratova T.F. Semiclassical eigenstates at the bottom of a multidimensional well. *Ann. Inst. Henri Poincare*, 1995, **62** (4), P. 361–382.

[12] Anikin A., Rouleux M. Multidimensional tunneling between potential wells at non degenerate minima. *Proc. Int. Conf. Days on Diffraction*, 2014, P. 17–22.

[13] Pankratova T.F. Tunneling in multidimensional wells. *Nanosystems: Phys. Chem. Math.*, 2015, **6** (1), P. 113–121.

[14] Anikin A.Yu. Asymptotic behaviour of the Maupertuis action on a libration and a tunneling in a double well. *Rus. J. Math. Phys.*, 2013, **20** (1), P. 1–10.

[15] Anikin A.Yu. Libration and splitting of the ground state in multidimensional double well problem. *Theor. Math. Phys.*, 2013, **175** (2), P. 609–619.

[16] Bruning J., Dobrokhotov S.Yu., Semenov E.S. Unstable closed trajectories, librations and splitting of the lowest eigenvalues in quantum double well problem. *Regul. Chaotic Dyn.*, 2006, **11** (2), P. 167–180.

[17] Takada S., Nakamura H. Effects of vibrational excitation on multidimensional tunneling: General study and proton tunneling in tropolone. *J. Chem. Phys.*, 2015, **102**, P. 3977–3992.

Inverse dynamic problems for canonical systems and de Branges spaces

A. S. Mikhaylov[1,2], V. S. Mikhaylov[1,2]

[1]St. Petersburg Department of V. A. Steklov Institute of Mathematics of the Russian Academy of Sciences, 7 Fontanka, St. Petersburg, 191023 Russia

[2]St. Petersburg State University, 7/9 Universitetskaya nab., St. Petersburg, 199034 Russia

mikhaylov@pdmi.ras.ru, vsmikhaylov@pdmi.ras.ru

We show the equivalence of inverse problems for different dynamical systems and corresponding canonical systems. For canonical system with general Hamiltonian we outline the strategy of studying the dynamic inverse problem and procedure of construction of corresponding de Branges space.

Keywords: inverse problem, Boundary Control method, de Branges spaces, Schrödinger operator, Dirac system, Jacobi matrices, canonical systems.

1. Introduction

This is an accompanying paper to [1], in which the authors have shown the relationship between the de Branges method and the Boundary Control (BC) method on a basis of three dynamical systems: wave equation with a potential on a half-line, Dirac system on a half-line and dynamical system with discrete time for semi-infinite discrete Schrödinger operator. For each system, they constructed the related de Branges space using natural dynamic objects and operators, used in the BC method. In the present note, we will show the equivalence of dynamic inverse problems (IP) for different dynamical systems (wave equation, Dirac system, Jacobi matrices), and IPs for equivalent canonical systems. We note that every original system will be equivalent to canonical system with different dynamics (the dependence on t is given by one of the following operators: $\frac{d^2}{dt^2}$, $i\frac{d}{dt}$, ∂_t, where ∂_t is a difference operator).

Let $H \in L_{1,loc}(0, L; \mathbb{R}^{2\times2})$ be a locally summable on $(0, L)$, $L \leq \infty$ matrix-valued function $H \geq 0$, called Hamiltonian, $J := \begin{pmatrix} 0 & 1 \\ -1 & 0 \end{pmatrix}$, vector $Y = \begin{pmatrix} Y_1 \\ Y_2 \end{pmatrix}$. We choose the "proper" dynamics and fix the general dynamical canonical system, the initial boundary value problem (IBVP) of which will be the subject of our interest:

$$iH\frac{dY}{dt} - J\frac{dY}{dx} = 0, \quad x \geq 0, \, t \geq 0.$$

For such a system we set up an IP and outline the strategy of solving it by the BC method, provided the Hamiltonian is smooth and strictly positive. We also provide a method of construction of the de Branges space for such a Hamiltonian in natural dynamic terms following [1].

In the second section, we expose all necessary information on de Branges spaces and canonical systems following [2] and [3]. In the third section, we deal with dynamical systems for Schrödinger operator on a half-line, wave equation on a half-line, Dirac operator on a half-line and a semi-infinite Jacobi matrices. We formulate dynamic IP for each system, then we transform IBVP for each system to the IBVP for certain canonical system, formulate IP for canonical system, and show that it is equivalent the original ones.

In the fourth section, we will show that one specific choice of dynamics give a finite speed of wave propagation in a canonical system, provided the Hamiltonian is smooth and strictly positive. We note that the finiteness of the wave propagation is important: initially the BC method was developed and applied in the case of multidimensional wave equation [4,5] on a bounded manifold, but later on the BC method was successfully applied to parabolic and Schrödinger equations (where the speed is infinite) as well [6–8]. We provide algorithms of solving dynamic IP and construction of de Branges space for such a Hamiltonian. Based on these results, we formulate the hypothesis for constructing the de Branges space for general Hamiltonian by the dynamic method.

2. de Branges spaces

Here, we provide the information on de Branges spaces in accordance with [2, 3]. The entire function $E : \mathbb{C} \mapsto \mathbb{C}$ is called a *Hermite–Biehler function* if $|E(z)| > |E(\overline{z})|$ for $z \in \mathbb{C}_+$. We use the notation $F^{\#}(z) = \overline{F(\overline{z})}$. The *Hardy space* H_2 is defined by: $f \in H_2$ if f is holomorphic in $\mathbb{C}^+$ and $\sup_{y>0} \int_{-\infty}^{\infty} |f(x+iy)|^2 \, dx < \infty$. Then the *de Branges space* $B(E)$ consists of entire functions such that:

$$B(E) := \left\{ F : \mathbb{C} \mapsto \mathbb{C}, \ F \text{ entire}, \int_{\mathbb{R}} \left| \frac{F(\lambda)}{E(\lambda)} \right|^2 \, d\lambda < \infty, \ \frac{F}{E}, \frac{F^{\#}}{E} \in H_2 \right\}.$$

The space $B(E)$ with the scalar product:

$$[F, G]_{B(E)} = \frac{1}{\pi} \int_{\mathbb{R}} \overline{F(\lambda)} G(\lambda) \frac{d\lambda}{|E(\lambda)|^2},$$

is a Hilbert space. For any $z \in \mathbb{C}$ the *reproducing kernel* is introduced by the relation

$$J_z(\xi) := \frac{\overline{E(z)} E(\xi) - E(\overline{z}) \overline{E(\overline{\xi})}}{2i(\overline{z} - \xi)}. \tag{1}$$

Then

$$F(z) = [J_z, F]_{B(E)} = \frac{1}{\pi} \int_{\mathbb{R}} \overline{J_z(\lambda)} F(\lambda) \frac{d\lambda}{|E(\lambda)|^2}.$$

We observe that a Hermite–Biehler function $E(\lambda)$ defines J_z by (1). The converse is also true [9, 10]: a Hilbert space of analytic functions with reproducing kernel is a de Branges space (provided some nonrestrictive conditions on the set of function and on the norm hold true).

Let $H \in L_{1,loc}(0, L; R^{2 \times 2})$ be a Hamiltonian and the vector $Y = \begin{pmatrix} Y_1 \\ Y_2 \end{pmatrix}$ be solution to the following Cauchy problem:

$$-J \frac{dY}{dx} = \lambda H Y, \tag{2}$$
$$Y(0) = C,$$

for $C \in \mathbb{R}^2$, $C \neq 0$. Without loss of generality, it is assumed that $\operatorname{tr} H(x) = 1$. Then, the function $E_x(\lambda) = Y_1(x, \lambda) + iY_2(x, \lambda)$ is a Hermite–Biehler function ($E_L(\lambda)$ makes sense if $L < \infty$), it is called de Branges function of the system (2) since one can construct de Branges space based on this function. On the other hand, E_L serves as an inverse spectral data for the canonical system (2). The solution to (2) and $Y(0) = (1, 0)^T$ is denoted by $\Theta(x, \lambda)$. The main result of the theory [3, 9] says that the opposite is also true: every Hermite–Biehler function satisfying some condition comes from some canonical system.

3. Dynamical canonical systems for wave equation, Dirac system and Jacobi system with discrete time

In this section, we use some ideas from [3] to rewrite IBVPs for different dynamical systems as IBVPs for canonical dynamical systems. Everywhere below, $T > 0$ is fixed.

3.1. Wave equation with a potential on a half-line

For a potential $q \in L_{1,\text{loc}}(\mathbb{R}_+)$, we consider the IBVP for the 1d wave equation on a half-line:

$$\begin{cases} u_{tt}(x, t) - u_{xx}(x, t) + q(x)u(x, t) = 0, & x \geq 0, \ t \geq 0, \\ u(x, 0) = u_t(x, 0) = 0, \ u(0, t) = f(t). \end{cases} \tag{3}$$

Here, f is an arbitrary $L^2_{loc}(\mathbb{R}_+)$ function referred to as a *boundary control*. The *response operator* $R_q^T : L_2(0, T) \mapsto L_2(0, T)$ with the domain $\mathcal{D} = C_0^{\infty}(0, T)$ is introduced by $\left(R_q^T f\right)(t) := u_x^f(0, t)$, it plays a role of a dynamic inverse data [11–13]. The IP is to recover q on $(0, T)$ from R_q^{2T}.

We consider the solutions $y_{1,2}$ to following Cauchy problems:

$$\begin{cases} -y_{1,2}''(x) + q(x)y_{1,2}(x) = 0, & x \geq 0, \\ y_1(0) = 1, \ y_1'(0) = 0, \ y_2(0) = 0, \ y_2'(0) = 1, \end{cases} \tag{4}$$

and look for the solution to (3) in the form:

$$u^f(x,t) = c^1(x,t)y_1(x) + c^2(x,t)y_2(x). \tag{5}$$

Plugging this representation to (3) yields:

$$c_{tt}^1 y_1 + c_{tt}^2 y_2 = -qc^1 y_1 - qc^2 y_2 + c_{xx}^1 y_1 + 2c_x^1 y_1' + c_1 y_1'' + c_{xx}^2 y_2 + 2c_x^2 y_2' + c_2 y''$$
$$= \left(c_x^1 y_1 + c_x^2 y_2\right)_x + c_x^1 y_1' + c_x^2 y_2'.$$

If we demand the equality $c_x^1 y_1 + c_x^2 y_2 = 0$, then unknown $c^{1,2}$ satisfies the following system:

$$\begin{cases} c_{tt}^1 y_1 + c_{tt}^2 y_2 = c_x^1 y_1' + c_x^2 y_2', \\ c_x^1 y_1 + c_x^2 y_2 = 0. \end{cases} \tag{6}$$

We note that due to the boundary conditions in (4) and (6), we have that:

$$u_x^f(0,t) = c_x^1(0,t)y_1(0) + c^1(0,t)y_1'(0) + c_x^2(0,t)y_2(0) + c^2(0,t)y_2'(0) = c^2(0,t).$$

On expressing $c_x^{1,2}$ from (6), and bearing in mind the equality $\det \begin{pmatrix} y_1 & y_2 \\ y_1' & y_2' \end{pmatrix} = 1$, we obtain that:

$$\begin{cases} c_x^1 = -c_{tt}^1 y_1 y_2 - c_{tt}^2 y_2^2, \\ c_x^2 = c_{tt}^1 y_1^2 + c_{tt}^2 y_1 y_2. \end{cases}$$

On introducing the notations $C = \begin{pmatrix} c^1 \\ c^2 \end{pmatrix}$, $J = \begin{pmatrix} 0 & 1 \\ -1 & 0 \end{pmatrix}$, $H = \begin{pmatrix} y_1^2 & y_1 y_2 \\ y_1 y_2 & y_2^2 \end{pmatrix}$ and counting the initial and boundary conditions on u^f at $t = 0$ and at $x = 0$, we obtain that C satisfies the following IBVP:

$$\begin{cases} HC_{tt} - JC_x = 0, & x \geq 0, t \geq 0, \\ C(x,0) = 0, C_t(x,0) = 0, & x \geq 0, \\ c^1(0,t) = f(t), & t \geq 0. \end{cases} \tag{7}$$

The response operator $\widetilde{R}_q^T : L_2(0,T) \mapsto L_2(0,T)$ for (7) is introduced by the equality $\left(\widetilde{R}_s^T f\right)(t) := c^2(0,t)$. On the other hand, using (5) and second line in (6), we have that:

$$\left(R_q^T f\right)(t) := u_x^f(0,t) = c_x^1(0,t)y_1(0) + c^2(0,t)y_2'(0) = c^2(0,t) = \left(\widetilde{R}_s^T f\right)(t).$$

So we can see that IPs for (3) and for (7) are equivalent.

3.2. Wave equation on a half-line

For a smooth positive density $\rho \in C^2(\mathbb{R}_+)$, $\rho(x) \geq \delta > 0$, we consider the IBVP for a wave equation on a half-line:

$$\begin{cases} \rho(x)u_{tt}(x,t) - u_{xx}(x,t) = 0, & x \geq 0, \ t \geq 0, \\ u(x,0) = u_t(x,0) = 0, \ u(0,t) = f(t). \end{cases} \tag{8}$$

Where the function $f \in L_{loc}^2(\mathbb{R}_+, \mathbb{C})$ is interpreted as a *boundary control*. The *response operator* $R_\rho^T : L_2(0,T) \mapsto L_2(0,T)$ with the domain $\mathcal{D} = C_0^\infty(0,T)$ is defined by $R_\rho^T f := u_x^f(0,t)$. We introduce the *eikonal* $\tau(x) := \int_0^x \rho^{\frac{1}{2}}(s)\, ds$, from physical point of view, it is a time at which a wave initiated at $x = 0$ fills the segment $(0,x)$, let $\Omega^l = \{x > 0 \,|\, \tau(x) < l\}$. Then, the natural set up of IP is to recover $\rho(x)|_{\Omega^T}$ from R_ρ^{2T}, see [14].

We introduce the new function:

$$C(x,t) = \begin{pmatrix} c^1 \\ c^2 \end{pmatrix} := \begin{pmatrix} u_t \\ iu_x \end{pmatrix},$$

and a Hamiltonian $H := \begin{pmatrix} \rho(x) & 0 \\ 0 & 1 \end{pmatrix}$. Then it is easy to see that Y satisfies the canonical system:

$$\begin{cases} iHC_t - JC_x = 0, & x \geq 0, t \geq 0, \\ C(x,0) = 0, & x \geq 0, \\ c^1(0,t) = g(t) := f'(t), & t \geq 0. \end{cases} \tag{9}$$

The response operator $\widetilde{R}_\rho^T : L_2(0,T) \mapsto L_2(0,T)$ for (9) with the domain $\mathcal{D} = C_0^\infty(0,T)$ is introduced by $\left(\widetilde{R}_s^T g\right)(t) := c^2(0,t)$. We can see that IPs for (8) and for (9) are equivalent.

3.3. Dirac system on a half-line

With a matrix potential $V = \begin{pmatrix} p & q \\ q & -p \end{pmatrix}$, $p, q \in C^1_{loc}(\mathbb{R}_+)$, vector $u = \begin{pmatrix} u_1 \\ u_2 \end{pmatrix}$ we associate the IBVP for a Dirac system:

$$\begin{cases} iu_t + Ju_x + Vu = 0, & x \geq 0,\, t \geq 0, \\ u\big|_{t=0} = 0, & x \geq 0, \\ u_1\big|_{x=0} = f, & t \geq 0, \end{cases} \tag{10}$$

Here f is an arbitrary $L^2_{loc}(\mathbb{R}_+, \mathbb{C})$ function referred to as a *boundary control*. The *response operator* R^T_D : $L_2(0, T) \mapsto L_2(0, T)$ with the domain $\mathcal{D} = C^\infty_0(0, T)$ is introduced by $\left(R^T_D f\right)(t) := u_2(0, t)$, it plays a role of a dynamic inverse data. The IP is to recover V on $(0, T)$ from R^{2T}_D, see [15].

Let $Y^{1,2}$ be solutions to the following Cauchy problems:

$$\begin{cases} JY^{1,2}_x + VY^{1,2} = 0, \\ Y^1_1(0) = 1, \quad Y^1_2(0) = 0, \quad Y^2_1(0) = 0, \quad Y^2_2(0) = 1. \end{cases}$$

We will look for the solution to (10) in the form:

$$u(x, t) = c^1(x, t)Y^1(x) + c^2(x, t)Y^2(x). \tag{11}$$

Plugging this representation in (10) yields:

$$i\left(c^1_t Y^1 + c^2_t Y^2\right) + c^1_x JY^1 + c^2_x JY^2 + c_1 JY^1_x + c_2 JY^2_x + c_1 VY^1 + c_2 VY^2$$
$$= i\left(c^1_t Y^1 + c^2_t Y^2\right) + J\left(c^1_x Y^1 + c^2_x Y^2\right) = 0,$$

on introducing $C = \begin{pmatrix} c^1 \\ c^2 \end{pmatrix}$, we see that the above equality is equivalent to:

$$i\begin{pmatrix} Y^1_1 & Y^2_1 \\ Y^1_2 & Y^2_2 \end{pmatrix} C_t + J\begin{pmatrix} Y^1_1 & Y^2_1 \\ Y^1_2 & Y^2_2 \end{pmatrix} C_x = 0.$$

We introduce the notation: $A = \begin{pmatrix} Y^1_1 & Y^2_1 \\ Y^1_2 & Y^2_2 \end{pmatrix}$, $B = JAJ$. Then the above system is equivalent to:

$$iAC_t - BJC_x = 0,$$

on multiplying it by B^{-1} and introducing the Hamiltonian by $H = B^{-1}A$, we obtain:

$$iHC_t - JC_x = 0.$$

Counting that $\det B = \det A = 1$, we evaluate:

$$H = B^{-1}A = \begin{pmatrix} Y^1Y^1 & Y^1Y^2 \\ Y^1Y^2 & Y^2Y^2 \end{pmatrix},$$

Bearing in mind the initial and boundary conditions in (10), we see that C satisfies the following IBVP:

$$\begin{cases} iHC_t - JC_x = 0, & x \geq 0,\, t \geq 0, \\ C(x, 0) = 0, & x \geq 0, \\ c^1(0, t) = f(t), & t \geq 0. \end{cases} \tag{12}$$

The response operator $\widetilde{R}^T_D : L_2(0, T) \mapsto L_2(0, T)$ for (12) is introduced by $\left(\widetilde{R}^T_D f\right)(t) := c^2(0, t)$. The representation (11) implies that IPs for (10) and for (12) are equivalent.

3.4. Semi-infinite Jacobi matrices

Let $0 = b_0 < b_1 < b_2 < \ldots < b_n < \ldots$ be a partition of $[0, +\infty)$. We introduce the notations: $\Delta_j := (b_{j-1}, b_j)$, $l_j = |\Delta_j| = b_j - b_{j-1}$. Let for each j we define $e_j \in \mathbb{R}^2$, $|e_j| = 1$, $e_j \neq \pm e_{j\pm 1}$, and $e_j(x) = e_j$, $x \in \Delta_j$. We define a Hamiltonian H:

$$H(x)f(x) = (f(x), e_j(x))\, e_j(x) = \begin{pmatrix} e^2_{1j}(x) & e_{1j}(x)e_{2j}(x) \\ e_{1j}(x)e_{2j}(x) & e^2_{2j}(x) \end{pmatrix} \begin{pmatrix} f^1(x) \\ f^2(x) \end{pmatrix}.$$

Consider functions of the type (i.e. functions from the domain of operator, corresponding to such a Hamiltonian, see [RR]):

$$f(x) = \begin{pmatrix} f^1(x) \\ f^2(x) \end{pmatrix} = f_j e_j(x) + \xi_j(x)e^\perp_j(x), \quad x \in \Delta_j, f_j \in \mathbb{R}, \quad e^\perp_j = Je_j, \tag{13}$$

and note that $(f, e_j) = f_j$. For such a Hamiltonian H we study the equation:

$$Jf' = Hg, \tag{14}$$

where the function g has a form (13), $g = g_j e_j(x) + \eta_j(x)e_j^\perp(x)$, $x \in \Delta_j$. The equality in (14) implies that

$$\xi_j'(x)Je_j^\perp(x) = g_j e_j(x), \quad x \in \Delta_j,$$

which yields the following expression for $\xi_j(x)$ for some s_j:

$$\xi_j(x) = s_j + g_j(b_j - x), \quad x \in \Delta_j. \tag{15}$$

We use the continuity condition at $x = b_{j-1}$ to obtain:

$$f_{j-1}e_{j-1} + s_{j-1}e_{j-1}^\perp = f_j e_j + (s_j + g_j l_j) e_j^\perp.$$

Multiplying the above equality by e_j we get:

$$s_{j-1} = \frac{1}{\left(e_j, e_{j-1}^\perp\right)} \left(f_j - f_{j-1}\left(e_j, e_{j-1}^\perp\right)\right), \tag{16}$$

and multiplying by e_{j-1} we obtain:

$$f_{j-1} = f_j\left(e_j, e_{j-1}\right) + (s_j + g_j l_j)\left(e_j^\perp, e_{j-1}\right). \tag{17}$$

Using (16), (17) we can express g_j via f_{j-1}, f_j, f_{j+1}:

$$g_j l_j = \frac{1}{\left(e_j, e_{j-1}^\perp\right)} f_{j-1} + \left(\frac{(e_{j+1}, e_j)}{\left(e_{j+1}, e_j^\perp\right)} - \frac{(e_j, e_{j-1})}{\left(e_j^\perp, e_{j-1}\right)}\right) f_j - \frac{1}{\left(e_j^\perp, e_{j+1}\right)} f_{j+1}. \tag{18}$$

Making the substitution:

$$u_j = g_j \sqrt{l_j}, \quad v_j = f_j \sqrt{l_j}, \tag{19}$$

from (18) we obtain the relation:

$$u_j = \frac{1}{\left(e_j, e_{j-1}^\perp\right)\sqrt{l_{j-1}l_j}} v_{j-1} + \frac{1}{l_j}\left(\frac{(e_{j+1}, e_j)}{\left(e_{j+1}, e_j^\perp\right)} - \frac{(e_j, e_{j-1})}{\left(e_j^\perp, e_{j-1}\right)}\right) v_j - \frac{1}{\left(e_j^\perp, e_{j+1}\right)\sqrt{l_j l_{j+1}}} v_{j+1}. \tag{20}$$

On introducing the notations:

$$\rho_j = \frac{-1}{\left(e_{j+1}, e_j^\perp\right)\sqrt{l_j l_{j+1}}}, \quad j \geq 1,$$

$$q_j = \frac{1}{l_j}\left(\frac{(e_j, e_{j+1})}{\left(e_j^\perp, e_{j+1}\right)} - \frac{(e_j, e_{j-1})}{\left(e_j^\perp, e_{j-1}\right)}\right), \quad j \geq 2,$$

we can rewrite (20) in a form:

$$u_j = \rho_{j-1}v_{j-1} + q_j v_j + \rho_j v_{j+1}, \quad j \geq 2,$$

and q_1 is found from the condition at zero. So finally we obtain the following result: if f and g having representation (13) are connected by (14), then u and v defined by (19) satisfy:

$$Av = u, \quad A = \begin{pmatrix} q_1 & \rho_1 & 0 & 0 & 0 \\ \rho_1 & q_2 & \rho_2 & 0 & 0 \\ 0 & \rho_2 & q_3 & \rho_3 & 0 \\ 0 & 0 & \cdot & \cdot & \cdot \end{pmatrix}.$$

We can introduce the dependence on (continuous) time t: let $f(x, t)$, $g(x, t)$ have form:

$$f(x, t) = f_j(t)e_j(x) + \xi(x, t)e_j^\perp(x), \quad x \in \Delta_j,$$

$$g(x, t) = g_j(t)e_j(x) + \eta(x, t)e_j^\perp(x), \quad x \in \Delta_j,$$

then if $g(x, t) = if_t(x, t)$, then f solves:

$$Jf_x = iHf_t.$$

On the other hand (19) implies the relationship $u_j(t) = iv_{j_t}(t)$, which yields that v solves $iv_t - Av = 0$. Adding initial and boundary conditions gives well-posed IBVP for dynamical system with continuous time governed by Jacobi matrix:

$$\begin{cases} iv_t - Av = 0, & x \geq 0, \, t \geq 0, \\ v_n(0) = 0, & n \geq 1, \\ v_1(t) = h(t), & t \geq 0. \end{cases} \tag{21}$$

The response operator $R_J^T : L_2(0, T) \mapsto L_2(0, T)$ with the domain $D = C_0^\infty(0, T)$ for this system is introduced by the rule $\left(R_J^T h\right)(t) := v_2(t)$. On the other hand, IBVP (21) is equivalent to (we assume that $e_1 = (1, 0)^T$):

$$\begin{cases} iHf_t - Jf_x = 0, & x \geq 0, \, t \geq 0, \\ f(x, 0) = 0, & x \geq 0, \\ f^1(0, t) = j(t) := \dfrac{h(t)}{\sqrt{l_1}}, & t \geq 0. \end{cases} \tag{22}$$

For the system (22), the response operator $\widetilde{R}_J^T : L_2(0, T) \mapsto L_2(0, T)$ with the domain $D = C_0^\infty(0, T)$ is introduced by the rule $\left(R_J^T h\right)(t) := f^2(0, t)$. Note that by (13), $f^2(0, t) = \xi_1(0, t)$. From (15), the relationship $g(x, t) = i f_t(x, t)$ and (16), we have that:

$$\left(R_J^T h\right)(t) = s_1(t) + g_1(t)l_1 = \frac{f_2(t)}{\left(e_2, e_1^\perp\right)} - f_1(t) + if^1(0, t)l_1$$

$$= \frac{f_2(t)}{\left(e_2, e_1^\perp\right)} - \frac{h(t)}{\sqrt{l_1}} + ih(t)\sqrt{l_1} = -\rho_1 v_2(t)\sqrt{l_1} - h(t)\left(\frac{1}{\sqrt{l_1}} - i\sqrt{l_1}\right).$$

So IP for (21) and (22) from corresponding response operators are equivalent. We note that we can introduce the different type of continuous dynamics for Jacobi matrices (for example the dynamics of the type $\dfrac{d}{dt^2}$ was considered in [16]).

We can also introduce the dependence on the discrete time $t \in \mathbb{N}$ by letting $f_t(x)$, $g_t(x)$ have form:

$$f_t(x) = f_{j,t} e_j(x) + \xi_t(x) e_j^\perp(x), \quad x \in \Delta_j, \, t \in \mathbb{N},$$
$$g_t(x) = g_{j,t} e_j(x) + \eta_t(x) e_j^\perp(x), \quad x \in \Delta_j, \, t \in \mathbb{N}.$$

If f, g are related by $g_t(x) = f_t(x) + f_{t-1}(x) =: \partial_t f(x)$, then counting (14), f solves:

$$Jf_x = H\partial_t f.$$

The equality (19) implies $u_j = \partial_t v_j$, which yields that v satisfies $\partial_t v_{\cdot,t} - Av_{\cdot,t} = 0$. Adding initial and boundary conditions gives the following IBVP:

$$\begin{cases} \partial_t v_{\cdot,t} - Av_{\cdot,t} = 0, & t \in \mathbb{N} \\ v_{n,1} = v_{n,0}(0) = 0, & n \geq 1, \\ v_{1,t} = h_t, & t \in \mathbb{N}. \end{cases} \tag{23}$$

where $h_t \in l_2$ is referred to as a *boundary control*. The response operator $R_{J,d}^T$ with the domain $D = \mathrm{R}^T$ for this system is introduced by $R_{J,d}^T : \mathbb{R}^T \mapsto \mathbb{R}^T$, $\left(R_{J,d}^T h\right)_t = v_{2,t}$, $t = 1 \ldots, T$. The forward and inverse problem was studied in [17, 18]. The IBVP (23) is equivalent to, which is equivalent to the following IBVP for a canonical system:

$$\begin{cases} H\partial_t f - Jf_x = 0, & x \geq 0, \, t \in \mathbb{N}, \\ f_0(x) = 0, & x \geq 0, \\ f_t^1(0) = j_t := \dfrac{h_t}{\sqrt{l_1}}, & t \in \mathbb{N}. \end{cases} \tag{24}$$

For the system (24) the response operator $\widetilde{R}_{J,d}^T : l_2 \mapsto l_2$ is introduced by the rule $\left(R_J^T j\right)(t) := f_t^2(0)$. By (13), $f_t^2(0) = \xi_{1t}(0)$, from (15), the relationship $g_t(x) = \partial_t f(x)$ and (16), we have that:

$$\left(R_{J,d}^T h\right)_t = s_{1t} + g_{1t}l_1 = \frac{f_{2t}}{\left(e_2, e_1^\perp\right)} - f_{1t} + if_t^1(0)l_1$$

$$= \frac{f_{2t}}{\left(e_2, e_1^\perp\right)} - \frac{h_t}{\sqrt{l_1}} + ih_t\sqrt{l_1} = -\rho_1 v_{2,t}\sqrt{l_1} - h_t\left(\frac{1}{\sqrt{l_1}} - i\sqrt{l_1}\right).$$

So, IP for (23) and (24) from corresponding response operators are equivalent.

We see that different dynamic systems after transformations come to dynamical canonical systems with different dynamics ($i\dfrac{d}{dt}$, $\dfrac{d}{dt^2}$, and even discrete one ∂_t).

We will investigate the dynamics given by $i\dfrac{d}{dt}$, the canonical system with this dynamics possess property of finite speed of wave propagation.

4. Canonical systems with smooth strictly positive Hamiltonian

We consider the IBVP for a canonical system. Assuming that the Hamiltonian satisfies conditions: $H = H^* \in C^2(0, T; \mathbb{R}^{2\times 2})$, $H \geq \delta > 0$, $\operatorname{tr} H = 1$, we set $Y^f = \begin{pmatrix} y^1 \\ y^2 \end{pmatrix}$ to be a solution to:

$$\begin{cases} iH\dfrac{d}{dt}Y - J\dfrac{d}{dx}Y = 0, & x \geq 0,\, t \geq 0, \\ Y(x,0) = 0, & x \geq 0, \\ y^1(0,t) = f(t), & t \geq 0. \end{cases} \tag{25}$$

Where the *boundary control* $f \in \mathcal{F}^T := L_2(0, T; \mathbb{C})$. The *response operator* $R^T : \mathcal{F}^T \mapsto \mathcal{F}^T$ is introduced as $\left(R^T f\right)(t) := y_2^f(0, t)$. The inverse problem we will be dealing with consists in a recovering $H(x)$, on an interval $(0, l)$ for some $l > 0$ from given R^{2T}.

4.1. One-velocity wave system

We rewrite (25): differentiate the first line in (25) w.r.t. t and use equation to get:

$$HY_{tt} + JH^{-1}JY_{xx} + JH_x^{-1}JY_x = 0,$$

which is equivalent to the equation:

$$HY_{tt} - \frac{1}{\det H}HY_{xx} + JH_x^{-1}JY_x = 0.$$

Counting the initial and boundary condition, we obtain that Y satisfies the following IBVP for one-velocity system:

$$\begin{cases} \det H Y_{tt} - Y_{xx} + \det H H^{-1}JH_x^{-1}JY_x = 0, & x \geq 0,\, t \geq 0, \\ Y(x,0) = Y_t(x,0) = 0, & x \geq 0, \\ \begin{pmatrix} y^1(0,t) \\ y^2(0,t) \end{pmatrix} = G(t) := \begin{pmatrix} f(t) \\ (Rf)(t) \end{pmatrix}, & t \geq 0. \end{cases} \tag{26}$$

Here, the velocity is given by $c(x) = \dfrac{1}{\sqrt{\det H(x)}}$. The response operator $R_w^T : L_2(0, T; \mathbb{C}) \mapsto L_2(0, T; \mathbb{C})$ with the domain $\mathcal{D} = C_0^\infty(0, T, \mathbb{C})$ for (26) is introduced as $\left(R_w^T G\right)(t) := Y_x^G(0, t)$. The *eikonal* function is introduced by $\tau(x) := \displaystyle\int_0^x \sqrt{\det H(s)}\, ds$, and $\Omega^l = \{x > 0 \,|\, \tau(x) < l\}$. Then the natural setup of IP is to recover $H(x)|_{\Omega^T}$ from R_w^{2T}.

We see that the IP for the system (26), is equivalent to IP for (25). But there is one important disadvantage – in studying IP for (26) which comes from (25), we need to use the specific set of controls of the type $\begin{pmatrix} f \\ Rf \end{pmatrix}$, which makes application of the BC method problematic. Instead, we will reduce (25) to Dirac-type system, and follow the scheme offered in [15].

4.2. Dirac-type dynamical system

We introduce the following transformation: let

$$U = \begin{pmatrix} \cos\phi(x) & \sin\phi(x) \\ -\sin\phi(x) & \cos\phi(x) \end{pmatrix}$$

be a unitary matrix such that $U^* H U = D := \begin{pmatrix} d_1(x) & 0 \\ 0 & d_2(x) \end{pmatrix}$, where $d_1, d_2 \geq \delta > 0$, $d_1 + d_2 = 1$. If $Y = U\widetilde{Y}$, then $\widetilde{Y}$ satisfies the following IBVP for Dirac-type dynamical system:

$$\begin{cases} iD\dfrac{d}{dt}\widetilde{Y} + J\dfrac{d}{dx}\widetilde{Y} - \phi'(x)\widetilde{Y} = 0, & x \geq 0,\, t \geq 0, \\ \widetilde{Y}(x,0) = 0, & x \geq 0, \\ \widetilde{y}^1(0,t) = g(t) := \cos\phi(0)f(t) + \sin\phi(0)(Rf)(t), & t \geq 0. \end{cases} \tag{27}$$

The response operator $R_{CD}^T : L_2(0, T) \mapsto L_2(0, T)$ is introduced by $\left(R_{CD}^T g\right)(t) := \widetilde{y}^2(0, t)$. We can see that $\widetilde{y}^2(0, t) = -\sin\phi(0)f(t) + \cos\phi(0)(Rf)(t)$, so IP for (25) and for (27) are equivalent.

Thus our first goal will be to study the dynamic IP for the following Dirac-type system:

$$
\begin{cases}
iD\dfrac{d}{dt}V + J\dfrac{d}{dx}V + \psi(x)V = 0, & x \geq 0,\ t \geq 0, \\
V(x,0) = 0, & x \geq 0, \\
v^1(0,t) = f(t), & t \geq 0,
\end{cases}
\tag{28}
$$

where D as above is a diagonal matrix with twice differentiable entries and unit trace, $\psi \in C^2(\mathbb{R}_+)$. The function $f \in \widetilde{\mathcal{F}}^T := L_2(0,T;\mathbb{C})$ is a *boundary control*. The response $R_D^T : \widetilde{\mathcal{F}}^T \mapsto \widetilde{\mathcal{F}}^T$ is introduced by $\left(R_D^T f\right)(t) := v^2(0,t)$. The IP consists in recovering $D|_{\Omega^T}$, $\psi|_{\Omega^T}$ from R^{2T}. We outline the scheme offered in [1, 15]:

Proposition 1. *The solution to (28) admits the following representation:*

$$
V(x,t) = A(x)f(t - \tau(x)) + \int\limits_0^{x(t)} w(x,s)f(t - \tau(s))\,ds,
$$

where $\tau(s) = \displaystyle\int_0^s \sqrt{d_1(\alpha)d_2(\alpha)}\,d\alpha$ is eikonal, $x(t)$ is a function inverse to $\tau(x)$, the kernel $w = \begin{pmatrix} w^1 \\ w^2 \end{pmatrix}$ is twice differentiable in $\{(x,s)\,|\,0 \leq \tau(x) \leq s \leq T\}$, $A = \begin{pmatrix} a^1 \\ a^2 \end{pmatrix}$, where $a^{1,2}$ are solutions to the following system:

$$
i\sqrt{d_1}\,a_x^1 = \sqrt{d_2}\,a_x^2,
$$
$$
\sqrt{d_2}\left(\psi a^1 + a_x^2\right) = i\sqrt{d_1}\left(\psi a^2 - a_x^1\right).
$$

We introduce the *outer space*, the space o states of (28): $\mathcal{H}^T := L_2(0,\tau(T);\mathbb{C})$ and a *control operator* $\widetilde{W}^T : \widetilde{\mathcal{F}}^T \mapsto \mathcal{H}^T$ acting by the rule:

$$
\left(\widetilde{W}^T f\right)(x) := V^f(x,T).
$$

The Proposition 1 implies that $\widetilde{W}^T$ is not an isomorphism, and the system (28) is not boundary controllable. To restore the controllability, we introduce the auxiliary system:

$$
\begin{cases}
iD\dfrac{d}{dt}U - J\dfrac{d}{dx}U - \psi(x)U = 0, & x \geq 0,\ t \geq 0, \\
U(x,0) = 0, & x \geq 0, \\
u^1(0,t) = g(t), & t \geq 0,
\end{cases}
\tag{29}
$$

and note that solutions to (28) and (29) are connected by the formula $V^f = \overline{U^{\overline{f}}}$. The extended outer space is defined by $\mathcal{F}^T := L_2(0,T;\mathbb{C}^2)$, and the *extended control operator* $W^T : \mathcal{F}^T \mapsto \mathcal{H}^T$ is introduced by:

$$
W^T \begin{pmatrix} f \\ g \end{pmatrix} := V^f(x,T) + U^g(x,T).
$$

Proposition 2. *The extended control operator is an isomorphism between $\mathcal{F}^T$ and $\mathcal{H}^T$.*

The set $\mathcal{U}^T := W^T \mathcal{F}^T$ is called extended reachable set. The Proposition 2 says that $\mathcal{U}^T = \mathcal{H}^T$.

We consider the operator of the Dirac-type system on a half-line: let $\mathbf{D} := D^{-1}J\dfrac{d}{dx} + D^{-1}\psi$ on $L_2(\mathbb{R}_+,\mathbb{C}^2) \ni \Phi = \begin{pmatrix} \Phi_1 \\ \Phi_2 \end{pmatrix}$ with a Dirichlet condition $\Phi_1(0) = 0$. Denote by $\theta(x,z) = \begin{pmatrix} \theta_1 \\ \theta_2 \end{pmatrix}$ a solution to the following Cauchy problem for $z \in \mathbb{C}$:

$$
\begin{cases}
J\theta_x + V\theta = zD\theta, & x > 0, \\
\theta_1(0,z) = 0, \quad \theta_2(0,z) = 1.
\end{cases}
\tag{30}
$$

Let $d\rho$ be a spectral measure of $\mathbf{D}$, and $F : L_2(\mathbb{R}_+; \mathbb{C}^2) \mapsto L_{2,\rho}(\mathbb{R}_+)$ be the corresponding Fourier transform:

$$\left(F \begin{pmatrix} f_1 \\ f_2 \end{pmatrix} \right) (\lambda) = F(\lambda) = \int_0^\infty (f_1(x)\theta_1(x,\lambda) + f_2(x)\theta_2(x,\lambda))\ dx,$$

$$f_1(x) = \int_{-\infty}^\infty F(\lambda)\theta_1(x,\lambda)\ d\rho(\lambda), \quad f_2(x) = \int_{-\infty}^\infty F(\lambda)\theta_2(x,\lambda)\ d\rho(\lambda),$$

$$\int_0^\infty (f_1^2(x) + f_2^2(x))\ dx = \int_{-\infty}^\infty F^2(\lambda)\ d\rho(\lambda).$$

We introduce the *extending connecting operator* $C^T : \mathcal{F}^T \mapsto \mathcal{F}^T$ by the quadratic form:

$$\left(C^T \begin{pmatrix} f_1 \\ g_1 \end{pmatrix}, \begin{pmatrix} f_2 \\ g_2 \end{pmatrix} \right)_{\mathcal{F}^T} = \left(W^T \begin{pmatrix} f_1 \\ g_1 \end{pmatrix}, W^T \begin{pmatrix} f_2 \\ g_2 \end{pmatrix} \right)_{\mathcal{H}^T}, \quad C^T = (W^T)^* W^T. \tag{31}$$

The important fact in the BC method is that:

Proposition 3. *The extending connecting operator is a positive isomorphism in $\mathcal{F}^T$, it admits the representation in terms of dynamic inverse data R^{2T}, and spectral inverse data $d\rho(\lambda)$.*

We introduce the linear manifold of Fourier images of extended states (Fourier image of extended reachable set) at time $t = T$:

$$B_D^T := \left\{ K(\lambda) \,|\, K(\lambda) = \left(FW^T \begin{pmatrix} k_1 \\ k_2 \end{pmatrix} \right)(\lambda), \begin{pmatrix} k_1 \\ k_2 \end{pmatrix} \in \mathcal{F}^T \right\} = F\mathcal{U}^T.$$

Equipped with the scalar product, generated by C^T:

$$[F, G]_{B_D^T} := \left(C^T \begin{pmatrix} f_1 \\ f_2 \end{pmatrix}, \begin{pmatrix} g_1 \\ g_2 \end{pmatrix} \right)_{\mathcal{F}^T}, \quad F, G \in B_D^T,$$

this linear space becomes a Hilbert space of analytic functions. It is also possible to define a reproducing kernel in this space (it is given in terms of a solution to a Krein equation), which makes B_D^T a de Branges space. Solution of dynamic and spectral IPs for (28) and construction of corresponding de Branges space will be the subject of forthcoming publications.

4.3. Dynamic approach to de Branges spaces

Based on the arguments from the previous subsection, we can formulate the hypothesis about de Branges space for canonical system (25) with general Hamiltonian. First, we introduce the auxiliary system:

$$\begin{cases} iH \dfrac{d}{dt}Z + J \dfrac{d}{dx}Z = 0, & x \geq 0,\ t \geq 0, \\ Z(x,0) = 0, & x \geq 0, \\ z^1(0,t) = g(t), & t \geq 0. \end{cases} \tag{32}$$

The *extending control operator* $W^T : \mathcal{F}^T \mapsto \mathcal{F}^T$ acting in extended control space $\mathcal{F}^T := L_2(0,T; \mathbb{C}^2)$ is defined by $W^T \begin{pmatrix} f \\ g \end{pmatrix} := Y^f(x,T) + Z^g(x,T)$. The *extending connecting operator* C^T is given by analog to (31). Then, the de Branges space corresponding to (25) is a Fourier image of extended reachable set, equipped with a scalar product, generated by C^T.

We note that the construction of de Branges space by dynamic methods for general Hamiltonian in fact is equivalent to solving the dynamic IP for system (25) with general H. We note that the in studying the IP in this case, one inevitably face with two obstacles: the smoothness of H, and changing the rank of H, which reflects in the lack of the boundary controllability of the dynamical system. The authors suggest that studying the inverse dynamic problem for a Krein string [10, 19] will be instructive and can help to overcome difficulties connected with general Hamiltonian.

Acknowledgements

References

[1] Mikhaylov A.S., Mikhaylov V.S. The Boundary Control method and de Branges spaces. Schrödinger equation, Dirac system and Discrete Schrödinger operator. *Journal of Mathematical Analysis and Applications*, 2018, **460** (2), P. 927–953.

[2] Remling C. Schrödinger operators and de Branges spaces. *J. Funct. Anal.*, 2002, **196** (2), P. 323–394.

[3] Romanov R.V. Canonical systems and de Branges spaces. URL: `http://arxiv.org/abs/1408.6022`, 2014.

[4] Belishev M.I. An approach to multidimensional inverse problems for the wave equation. *Soviet Math. Dokl.*, 1988, **36** (3), P. 481–484.

[5] Belishev M.I. Boundary control in reconstruction of manifolds and metrics (the BC method). *Inverse Problems*, 1997, **13** (5), R1–R45.

[6] Avdonin S.A., Lenhart S., Protopopescu V. Determining the potential in the Schrödinger equation from the Dirichlet to Neumann map by the boundary control method. *J. Inverse Ill-Posed Probl.*, 2005, **13**, P. 317–330.

[7] Belishev M.I. Recent progress in the boundary control method. *Inverse Problems*, 2007, **23** (5), R1–R67.

[8] Belishev M.I. Boundary control and tomography of Riemannian manifolds (the BC-method). *Uspekhi Matem. Nauk*, 2017, **72** (4), P. 3–66 (in Russian).

[9] de Branges L. *Hilbert space of entire functions*. Prentice-Hall, NJ, 1968.

[10] Dym H., McKean H.P. *Gaussian processes, function theory, and the inverse spectral problem*. Academic Press, New York etc., 1976.

[11] Avdonin S.A., Mikhaylov V.S. The boundary control approach to inverse spectral theory. *Inverse Problems*, 2010, **26** (4), 045009 (19 pp).

[12] Belishev M.I., Mikhaylov V.S. Unified approach to classical equations of inverse problem theory. *Journal of Inverse and Ill-Posed Problems*, 2012, **20** (4), P. 461–488.

[13] Mikhaylov A.S., Mikhaylov V.S. Relationship between different types of inverse data for the one-dimensional Schrödinger operator on a half-line. *Zapiski Nauchnykh Seminarov POMI*, 2016, **451**, P. 134–155.

[14] Belishev M.I. Boundary control and inverse problems: a one-dimensional version of the boundary control method. *J. Math. Sci. (N. Y.)*, 2008, **155** (3), P. 343–378.

[15] Belishev M.I., Mikhaylov V.S. Inverse problem for one-dimensional dynamical Dirac system (BC-method). *Inverse Problems*, 2010, **26** (4), 045009 (19 pp).

[16] Teschl G. Jacobi operators and completely integrable nonlinear lattices. *Mathematical Surveys and Monographs*, **72**, American Mathematical Society, Providence, RI, 2000.

[17] Mikhaylov A.S., Mikhaylov V.S. Dynamical inverse problem for the discrete Schrödinger operator. *Nanosystems: Physics, Chemistry, Mathematics*, 2016, **7** (5), P. 842–854.

[18] Mikhaylov A.S., Mikhaylov V.S. Dynamic inverse problem for the Jacobi matrices. URL: `https://arxiv.org/abs/1704.02481`, 2017.

[19] Krein M.G. On the one method of effective solving the inverse boundary value problem. *Dokl. Akad. Nauk. USSR*, 1954, **94** (6), P. 987–990.

Cyclic-periodic ZRP structures. Scattering problem for generalized Bloch functions and conductivity

S. Leble

Immanuel Kant BFU, Al. Nevsky st.14, Kaliningrad, 236016, Russia

lebleu@mail.ru

Problems of quantum description of nanostructures transport properties is investigated in a framework of the structure symmetry group. Corresponding states of conductivity electrons are defined as irreducible representations of the group. The right/left Bloch functions are written and the Floquet theorem is formulated. The results are used for formulating the zero range potential (ZRP) conditions for arbitrary orbital quantum number whose construction is presented via Darboux dressing chain built in a space of distributions. The electron spin variables are taken into account. A spectrum of the non-relativistic Hamiltonian with a system of a nanostructure ZRPs is found from the matrix eigenvalue problem. The scattering problem on an extra ZRP is formulated in terms of the right/left Bloch functions. As an example, the discrete spectrum and scattering on N-ZRP-centers is solved and compared with experimental data for benzene molecule.

Keywords: Nanostructures, zero-range potential, Bloch wave, scattering problem, charge transport.

Received: 8 January 2018

Revised: 31 January 2018

1. Introduction

1.1. General remarks

Problems of quantum description of nanostructures transport properties are directly connected with geometry of the object and corresponding electron states in a field of atomic systems. The conventional quantum mechanics of an electrons pure state is derived from the mathematical results of Floquet [1] from which grows the fundamental notion of the Bloch function. Thus, the quantum state is defined as an eigenfunction of commuting translational symmetric Hamiltonian and shift operators. It is well-known that the quantum mechanical description based on pure state cannot explain transport phenomenon because the discrete spectrum of energy does not allow to be accelerated in weak electric field. Only account of extra energy originated from atoms heat motion give such a possibility to move through a crystal. It means that we should apply quantum statistics method that allow to introduce a nano-object temperature and its impact on conductivity. Moreover, having a non-equilibrium system in external field we should go up to kinetic equations. As fundamental basis for such purposes, the Bogolubov chain equation is used, which, upon reduction, leads to either Boltzmann or Kolmogorov one-particle equations depending on the statement of the problem [2].

The zero-range potential (ZRP) method has proven to be an efficient tool in describing quantum structures with arbitrary geometry at sufficiently low energies (large de Broglie wavelength) such that detailed structure of atomic potential can be neglected [3–5]. Important understanding of its mathematical nature was found in theory of extensions [6,7]. Speaking mainly either about one-dimensional spectral and scattering problems over the whole x-axis domain or half-axis r-domain for a radial Shrödinger equation, several interesting models demonstrate excellent results for many-particle systems.

This has been further developed into generalized zero-range potential (gZRP) method that takes into account effects of higher order partial waves in describing scattering properties [8–10]. Application of the regular ZRP method can be extended to describe not only small, typically atomic, structures but also larger molecular systems [12]. By definition, the method is focused on scattering problem, i.e. the continuous spectrum. For molecular systems, this also works well for discrete spectrum [5, 14]. The spectral properties for such extended systems as nanotubes demonstrate waveguide properties [13]. In the case of finite extended systems as wire crystals or nanotubes, one may use boundary or von Karman periodic conditions.

In our previous papers [14] and in the Master thesis of Ponomarev [Leble supervision], we studied stationary states of electron in the field of ZRPs that are positioned on a ring and cylinder surface in points that form a system with finite-group rotational symmetry with respect to the cylinder axis. We would mention here the important development of the theory with magnetic field account [15] and a development of computational techniques for

complex ZRP systems with symmetry [16]. We also studied a scattering of a free electron on benzene-like ring systems of s-ZRP, comparing it with experiment.

In the present work, we develop these results, pose and solve a scattering problem of electrons in a tube Bloch states on a defect or a deformation potential that is modeled also by a ZRP. The main concept in such a problem is the *irreducible representation of the tube symmetry group*, formulated as a main theorem. Such functions form automatically an eigenset of complete set of commuting observables (Sec. 2.1). Both finite and infinite tubes electron spectrum are studied and compared. We introduce Hamiltonians with ZRPs eigenvalue problems for arbitrary angular momentum (orbital quantum number). In the next section (Sec 3) we reformulate the Darboux theorem that link ZRP with different values of the orbital quantum number and open a transition to nonzero range localized potentials. Further, the electron spin variable is taken into account in the same line of ZRP conditions. Next , in the Sec. 4 a normalization of the Bloch functions via electron flux is used to pose a scattering problem for such functions as a basis. The discrete and continuous spectra in a frame of scattering problem are studied for a degenerate case of N-ZRP-centers (Sec. 5). In this section, some calculations are presented for benzene molecule configuration that was compared with both experimental and calculated data.

1.2. Method of zero-range potentials

The idea of the ZRP method is to replace a real potential with potential presented by a distribution, placed at a given point that mimics the physical scattering behavior of the far zone. The behavior in the case of a point potential placed at the origin is conventionally studied via the radial Schrödinger equation at $r \in [0, \infty)$ for the free space ($r > 0$) [5]:

$$-\frac{d^2R}{dr^2} + \frac{2}{r}\frac{dR}{dr} + \frac{l(l+1)}{r^2}R = k^2R, \tag{1}$$

where $k^2 = \dfrac{2mE}{\hbar^2}$, k is the wave number, m, E are mass and energy of a particle (electron), respectively, $\hbar$ is Planck's constant, $R(r)$ is the radial part of the wave function.

It is well-known that the general solution can be formed as a linear combination of spherical Bessel and Neumann functions, $j_l(kr)$ and $y_l(kr)$, respectively:

$$R(r) = C_l\left(j_l(kr) - \tan\eta_l \cdot y_l(kr)\right), \tag{2}$$

with $s_l = \exp(2i\eta_l)$ being a scattering matrix.

Taking into account the following asymptotic behavior at $kr \to 0$:

$$j_l(kr) \approx \frac{(kr)^l}{(2l+1)!!}, \tag{3}$$

$$y_l(kr) \approx -\frac{(2l-1)!!}{(kr)^{l+1}}, \tag{4}$$

written with notion of the odd factorial $(2l+1)!! = (2l+1)\cdot(2l-1)\cdot\ldots\cdot 3\cdot 1$, $(-1)!! = 1$, we obtain asymptotic behavior of finite-energy solution at the origin:

$$R(r) \approx C_l\tan\eta_l\frac{(2l-1)!!}{(kr)^{l+1}}. \tag{5}$$

From the Eq. (2), the constant C_l can be expressed as:

$$C_l = \frac{(2l+1)!!}{k^l(2l+1)!}\left.\frac{d^{2l+1}}{dr^{2l+1}}\left(r^{l+1}\psi\right)\right|_{r=0}. \tag{6}$$

Elimination of C_l from (6), and the equality corresponding to (5), yields:

$$\left.\frac{1}{r^{l+1}\psi}\frac{d^{2l+1}}{dr^{2l+1}}\left(r^{l+1}\psi\right)\right|_{r=0} = \frac{(2l+1)!}{(2l+1)!!}\cdot\frac{1}{(2l-1)!!}\cdot\frac{k^{2l+1}}{\tan\eta_l}, \tag{7}$$

leads to the condition in the origin:

Proposition 1.1 (Zero range potential, l-ZRP). *The solution of Shrödinger equation with zero potential, that feeds the boundary condition:*

$$\left.\frac{1}{r^{l+1}\psi}\frac{d^{2l+1}}{dr^{2l+1}}\left(r^{l+1}\psi\right)\right|_{r=0} = -\frac{2^l l!}{(2l-1)!!}1/a_l^{2l+1}, \tag{8}$$

with

$$a_l^{2l+1} = -\frac{\tan\eta_l}{k^{2l+1}} \tag{9}$$

results in the desired physical behavior of solution at a significant distance from the point-center.

Quantity a_l is termed as the partial wave scattering length and it is independent of particular energy value at low energies [5], see also (2) by which we conclude that

Proposition 1.2 (Scattering length). *The scattering length a_l is defined by:*

$$\tan \eta_l \approx -\frac{A_2}{A_1 \, (2l+1)!! \, (2l-1)!!} k^{2l+1},$$

that demonstrates the r.h.s. of (8) *energy independence.*

At low energies, it is often enough to consider the ZRP as a spherical point, thus neglecting higher partial waves. The solution to the (1) should be a subject to the simple boundary condition:

$$\frac{d \log (r\psi)}{dr}\bigg|_{r=0} = -\beta, \tag{10}$$

where $\beta = 1/a_0$ is the s-wave inverse scattering length. Such ZRP we will mark as s-ZRP.

In the next section, we enhance the standard ZRP approach by means of application of a dressing procedure [10,20]. We notice and make use of the fact that a certain class of *Darboux transformations* DT of spherically symmetric ZRPs yields also a potential of zero range but, in general, with different effective characteristic (scattering length of the original ZRP is altered), including l-ZRP. Transformation parameters of a single atomic potential can be chosen based on solution of conventional bounded state problem solved for a system of ZRPs (molecule) such that resulting solution mimics the scattering behavior for the molecule as a whole.

2. Cylindrical tube with surface-centered point potentials

An interesting structure, related to mesoscopic physics, is the long tube with cross-sections periodically filled with point-centers forming symmetrical structures.

We focus on bounded state solutions for finite and an infinitely long tube made of plane N-fold symmetrical structures considered by means of unidirectional translation (Fig. 1). We also formulate a general approach to electron-impurity scattering of directed Bloch waves.
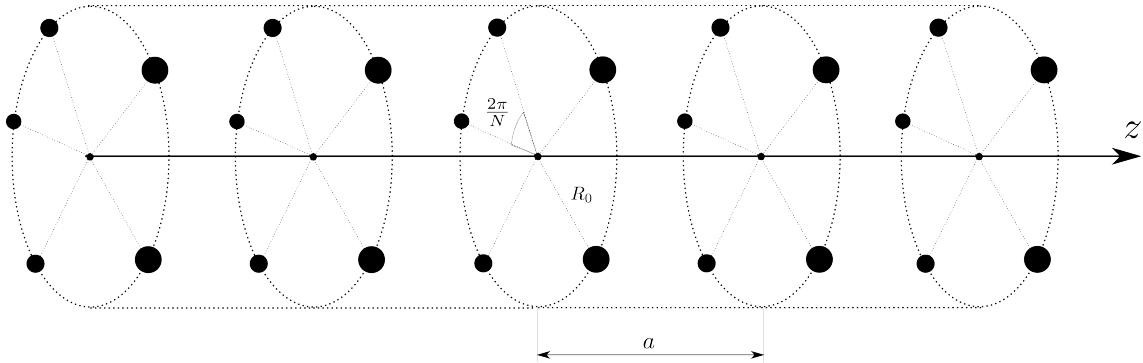
FIG. 1. The tube geometry

2.1. Bloch function

We start from general remarks, taking a spectral 3D problem based on stationary Shrödinger equation (SE):

$$\hat{H}\psi = E\psi. \tag{11}$$

Let $A \in G$ be a group of the point-centers set symmetry and the finite group $R_j \in G_c$ be a subgroup of rotations on angles $\theta_j = \dfrac{2\pi j}{N}$, $j = 0, ..., N-1$ in a plane, orthogonal to the z-axis. Let also the translations along z-axis be denoted as t_{na}, $n = 0, ..., M$ and form the cyclic group $t_{na} \in G_T$, hence the group elements are the pairs $A = (R_j, t_{na})$. The case of infinite group will be studied separately in Sec. 2.4. The particular case relates to the structure of Fig. 1 is described by the direct product:

$$G = G_c \star G_T, \tag{12}$$

therefore the sum by the group reads:

$$\sum_G = \sum_{G_c} \sum_{G_T}. \tag{13}$$

Let the group be represented by transformations in the position space $\vec{r} \in R^3$. It is straightforward to see that A is equivalent to the combined operations of a rotation:

$$R_j = \begin{pmatrix} \cos\theta_j & \sin\theta_j & 0 \\ -\sin\theta_j & \cos\theta_j & 0 \\ 0 & 0 & 1 \end{pmatrix} \tag{14}$$

and translation:

$$t_a \begin{pmatrix} x \\ y \\ z \end{pmatrix} = \begin{pmatrix} x \\ y \\ z+a \end{pmatrix}. \tag{15}$$

The representation of the elements A is written as:

$$A\vec{r} = R_j\vec{r} + t_a^n\vec{r} = \begin{pmatrix} \cos\theta_j x + \sin\theta_j y \\ -\sin\theta_j y + \cos\theta_j \\ z+na \end{pmatrix}. \tag{16}$$

The transformations form an Abelian group, $R_j t_a = t_a R_j$.

The principal element of the construction is the function:

$$g_\pm(r_0,\, k) = \frac{e^{\pm ikr_0}}{r_0}, \tag{17}$$

where $\vec{r}_0 = \vec{r} - \vec{R}$, $\vec{R} = (0, -R, 0)$, that is a solution of the e.v. problem equation (11) with zero potential at $(r_0 = (\vec{r} - \vec{R}, \vec{r} - \vec{R})^{1/2} > 0)$, corresponding to the energy (Hamiltonian eigenvalue) $E = \dfrac{\hbar^2 k^2}{2m}$. Note that the origin is placed at symmetry axis of the centers positions (Fig. 1). The basic idea: it is convenient to define a class of solutions via summation by a group of symmetry.

Proposition 2.1. *The operator T_A defines the sum:*

$$\sum_{A \in G} C_A T_A g_\pm(r_0,\, k), \tag{18}$$

its action is given by:

$$T_A g_\pm(r_0,\, k) = g_\pm(r_A,\, k), \tag{19}$$

$$r_A = \sqrt{(\vec{R} - A\vec{r}, \vec{R} - A\vec{r})}.$$

The function (18) *is a solution of the SE* (11) *at $r_A > 0$.*

Let the irreducible representations of the symmetry group is denoted as $D^{\vec{\mu}}(A)$, where:

$$\vec{\mu} = \{\mu_1, \mu_2\}, \tag{20}$$

the integers, numerating irreducible representations run the values $j_1 = 0, ..., N-1; j_2 = 0, ..., M-1$. Hence, the following lemma holds:

Lemma 2.2 (Irreducible representations). *The pair of functions, defined by:*

$$\phi_\pm^{\vec{\mu}} = C_\pm \sum_{A \in G} D^{\vec{\mu}}(A) T_A g_\pm(\vec{r},\, k) \tag{21}$$

transforms as irreducible representation of G.

Proof: Action of the operator T_A yields:

$$T_B \phi_\pm^{\vec{\mu}}(\vec{r},\, k) = A_\pm \sum_{A \in G} D^{\vec{\mu}}(A) T_B T_A g_\pm(\vec{r},\, k) = D^{\vec{\mu}}(B^{-1}) \phi_\pm^{\vec{\mu}}, \tag{22}$$

we change the summation by A to summation by C as follows:

$$T_B T_A = T_{BA} = T_C, \quad A = B^{-1}C, \quad D^{\vec{\mu}}(A) = D^{\vec{\mu}}(B^{-1}C) = D^{\vec{\mu}}(B^{-1})D^{\vec{\mu}}(C).$$

It is convenient to choose alternative parametrization of the group, using the cylindrical coordinate system ρ, ϕ, z, having in mind that all centers in a plane xy are lying on a circumference of a radii R. We also introduce a vector $\vec{p} = \{\phi, z\}$ in a ϕz plane, hence the rotations are equivalent to a shifts in ϕ, so:

$$T_A g_\pm \left(\rho, \phi, z, k\right) = g_\pm \left(\rho, \phi + \frac{2\pi j}{N}, z + na, k\right). \tag{23}$$

Moving to a realistic geometry of the tube and using periodic von Karman conditions we restrict the natural n variable change so as $|n| \leq M$, i.e. $g_\pm \left(\rho, \phi, z + Ma, k\right) = g_\pm \left(\rho, \phi, z, k\right)$. The group element, or the transformation is parametrized by the vector:

$$\vec{s} = \{s_1, s_2\} = \{\frac{2\pi j}{N}, na\}. \tag{24}$$

The transformation $A \in G$ is written as $A\vec{p} = \vec{p} + \vec{s}$. Next, we denote:

$$g_\pm \left(\rho, \phi, z, k\right) = g_\pm \left(\rho, \vec{p}, k\right). \tag{25}$$

For the symmetry group is Abelian and subgroups are cyclic, the irreducible representations are one-dimensional. Conventionally choosing it as unitary, we write:

$$D^{\vec{\mu}}(A) = \exp[i(\vec{\mu}, \vec{s})], \tag{26}$$

the integers, numerating irreducible representations run the values $j_1 = 0, ..., N-1; j_2 = 0, ..., M-1$ as in (20):

$$\vec{\mu} = \{\mu_1, \mu_2\} = \{j_1, \frac{2\pi j_2}{aM}\}. \tag{27}$$

.

Corollary 2.3 (Bloch function). *The functions $\phi_\pm^{\vec{\mu}}$ (21) are eigenvectors of the Hamilton operator $\hat{H}$ and symmetry transformations T_B operators.*

This statement is also valid for the subgroup of translation $B \in G_T$. We take the joint eigenfunctions (21) of the operators $\hat{H}$ as a definition of *"generalized Bloch function" (GBF)*.

2.2. Floquet and Wigner theorems

The result leads directly to analog of Floquet theorem [1].

Theorem 2.4 (Floquet theorem). *The function:*

$$\exp[i(\vec{\mu}, \vec{p})]\phi_\pm^\mu \left(\rho, \vec{p}, k\right)$$

is invariant with respect to action:

$$T_A \exp[i(\vec{\mu}, \vec{p})]\phi_\pm^\mu \left(\rho, \vec{p}, k\right) = \exp[i(\vec{\mu}, \vec{p})]\phi_\pm^\mu \left(\rho, \vec{p}, k\right). \tag{28}$$

The **proof** follows directly from equality:

$$T_A \exp[i(\vec{\mu}, \vec{p})]\phi_\pm^{\vec{\mu}} \left(\rho, \vec{p}, k\right) =$$
$$A_\pm \exp[i(\vec{\mu}, \vec{p} + \vec{s})] \sum_{B \in G} D^{\vec{\mu}}(B) T_A T_B g_\pm \left(\rho, \vec{p}, k\right) = \tag{29}$$
$$\exp[i(\vec{\mu}, \vec{p} + \vec{s})] D^{\vec{\mu}}(A)\phi_\pm^{\vec{\mu}} \left(\vec{r}, k\right)$$

and the lemma 2.2.

The direct Wigner theorem application leads to the statement

Proposition 2.5 (Wigner theorem). *The transition to the irreducible representation of symmetry transformations basis $\phi_\pm^{\vec{\mu}}$ (21) diagonalize the Hamilton operator $\hat{H}$ with natural numeration of energy levels by $\vec{\mu}$.*

The s-ZRP potential conditions for the Bloch functions (21):

$$\phi_\pm^{\vec{\mu}} = C_\pm \sum_{A \in G} \exp[i(\vec{\mu}, \vec{s})] T_A g_\pm \left(\vec{r}, k\right) \tag{30}$$

are given by:

$$\frac{\partial \left(\left|\vec{r} - A\vec{R}\right| \cdot \phi_\pm^{\vec{\mu}}\right)}{\partial \left|\vec{r} - A\vec{R}\right|}\Bigg|_{\left|\vec{r} - A\vec{R}\right| = 0} = -\beta \left(\left|\vec{r} - A\vec{R}\right| \phi_\pm^{\vec{\mu}}\right)\Big|_{\left|\vec{r} - A\vec{R}\right| = 0}, \tag{31}$$

that for arbitrary $A \in G$ results in the eigenvalue, corresponding to the irreducible representation $\vec{\mu}$. Plugging the basic solution (35), transformed as:

$$T_A g_\pm \left(\vec{r} - \vec{R}, \, k \right) = \frac{e^{\pm ikr_A}}{r_A}, \tag{32}$$

into (31) with real $\kappa_{\vec{\mu}}$: $k = i\kappa_{\vec{\mu}}$ in the limit $\left| \vec{r} - A\vec{R} \right| = r_A = 0$, calculation yields:

$$\frac{\partial \left(r_A \sum'_{B \in G} \exp[i(\vec{\mu}, \vec{s}_B)] g_\pm \left(\vec{r} - B\vec{R}, i\kappa_{\vec{\mu}} \right) \right)}{\partial r_A} \Bigg|_{r_A = 0} =$$

$$\sum'_{B \in G} \exp[i(\vec{\mu}, \vec{s}_B)] g_\pm \left(\vec{r} - B\vec{R}, k \right) \Bigg|_{r_A = 0} - \kappa_{\vec{\mu}} \exp[i(\vec{\mu}, \vec{s}_B)] +$$

$$r_A \frac{\partial \left(\sum'_{B \in G} \exp[i(\vec{\mu}, \vec{s}_B)] g_\pm \left(\vec{r} - B\vec{R}, i\kappa_{\vec{\mu}} \right) \right)}{\partial r_A} \Bigg|_{r_A = 0} = \tag{33}$$

$$-\beta \left(r_A \sum_{B \in G} \exp[i(\vec{\mu}, \vec{s}_B)] g_\pm \left(\vec{r} - B\vec{R}, i\kappa_{\vec{\mu}} \right) \right) \Bigg|_{r_A = 0}.$$

The sum marked by "prime" $\sum'$ do not include the term A. Continuing to reach the limit, we change $\vec{r} = A\vec{R}$, arriving at:

$$\sum'_{B \in G} \exp[i(\vec{\mu}, \vec{s}_B)] g_+ \left(A\vec{R} - B\vec{R}, i\kappa_{\vec{\mu}} \right) = (\kappa_{\vec{\mu}} - \beta) \exp[i(\vec{\mu}, \vec{s}_A)]. \tag{34}$$

Plugging the parameters s_B, and

$$g_+ \left(A\vec{R} - B\vec{R}, -\kappa_{\vec{\mu}} \right) = \frac{e^{-\kappa_{\vec{\mu}} r_{AB}}}{r_{AB}}, \tag{35}$$

where the vector $A\vec{R} - B\vec{R} = (R_j - R_i)\vec{R} + (n - m)a\vec{e}_z$ and:

$$r_{AB} = \sqrt{(A\vec{R} - B\vec{R}, A\vec{R} - B\vec{R})}, \tag{36}$$

are the distances between atoms, arriving at equation for evaluation of $\kappa_{\vec{\mu}}$:

$$\sum'_{B \in G} \exp[i(\vec{\mu}, \vec{s}_B - \vec{s}_A)] \frac{e^{-\kappa_{\vec{\mu}} r_{AB}}}{r_{AB}} = \kappa_{\vec{\mu}} - \beta. \tag{37}$$

It is convenient to denote the group parameters as:

$$\vec{s}_A = \{s_{1A}, s_{2A}\} = \{\frac{2\pi j_A}{N}, n_A a\}. \tag{38}$$

.

Remark 2.6 (Sum by neighbors). This equation is the working formula for the discrete spectrum calculation. The exponent in the nominators decays at distances of closest neighbors, so we can account only such terms to estimate the result.

By the result of the Floquet theorem, denoting group invariants as:

$$\varphi_\pm^{\vec{\mu}} (\rho, \vec{p}, k) = \exp[i(\vec{\mu}, \vec{p})] \phi_\pm^{\vec{\mu}} (\rho, \vec{p}, k), \tag{39}$$

we express the Bloch functions in terms of the group invariants as:

$$\phi_\pm^{\vec{\mu}} (\rho, \vec{p}, k) = \exp[-i(\vec{\mu}, \vec{p})] \varphi_\pm^{\vec{\mu}} (\rho, \vec{p}, k), \tag{40}$$

or:

$$\phi_\pm^{\vec{\mu}} (\rho, \vec{p}, k) = \phi_\pm^{\vec{\mu}} = C_\pm \sum_{B \in G} \exp[i(\vec{\mu}, \vec{s})] T_B g_\pm (\vec{r}, k) =$$

$$C_\pm \sum'_{B \in G} \exp[i(\vec{\mu}, \vec{s}_B)] T_B g_\pm (\vec{r}, k) + C_\pm \exp[i(\vec{\mu}, \vec{s}_A)] T_A g_\pm (\vec{r}, k) = \tag{41}$$

$$\exp[-i(\vec{\mu}, \vec{p})] \varphi_\pm^{\vec{\mu}} (\rho, \vec{p}, k).$$

2.3. On spectrum for finite tube

Plugging the vectors $\vec{\mu}$ (20) and $\vec{s}_A - \vec{s}_B$, one arrives at:

$$\sum_{B \in G}' \exp\left[i\left(j_1 \frac{2\pi(j_A - j_B)}{N} + (n_A - n_B)\frac{2\pi j_2}{M}\right)\right]\frac{e^{-\kappa_{\vec{\mu}} r_{AB}}}{r_{AB}} = \kappa_{\vec{\mu}} - \beta. \tag{42}$$

The vector $A\vec{R} - B\vec{R} = (R_j - R_i)\vec{R} + (n - m)a\vec{e}_z$ in matrix form is written as:

$$(R_j - R_i)\vec{R} + (n - m)a\vec{e}_z = \begin{pmatrix} -R(\sin\theta_j - \sin\theta_i) \\ -R(\cos\theta_j - \cos\theta_i) \\ (n - m)a \end{pmatrix}, \tag{43}$$

and, hence:

$$r_{AB} = R\sqrt{2}\sqrt{1 - \cos(\theta_j - \theta_i) + \frac{(n - m)^2 a^2}{2R^2}}. \tag{44}$$

Plugging $\theta_j = 2\pi\dfrac{j}{N}$ and $a = 2R\sin\dfrac{\pi}{N}$, we arrive at the expression, convenient for numeric solution of (42):

$$r_{AB} = R\sqrt{2}\sqrt{1 - \cos\left(2\pi\frac{j - i}{N}\right) + 2(n - m)^2 \sin^2\frac{\pi}{N}}. \tag{45}$$

Recall that the label of an irreducible representation is $\{j_1, \dfrac{2\pi j_2}{aM}\}$ and by choosing the element A as unit, we formulate the proposition:

Proposition 2.7 (Discrete spectrum). *The Hamiltonian of the multiatom ZRP system (Fig. 1), has the discrete spectrum, the eigenvalues of it are numerated by the irreducible representations numbers $j_{1,2}$ written as:*

$$E_{\vec{\mu}} = -\frac{\hbar^2 \kappa_{\vec{\mu}}^2}{2m}, \qquad n = 0, \ldots, [M/2], \tag{46}$$

by treating transcendental equation with respect to $\kappa_{\vec{\mu}}$ (by means of numerical methods, e.g. the Newton–Raphson algorithm):

$$\sum_{j=0}^{N-1}\sum_{n=1}^{M} \exp\left[-i\left(j_1\frac{2\pi j}{N} + j_2\frac{2\pi n}{M}\right)\right]\frac{e^{-\kappa_{\vec{\mu}} r_{1B}}}{r_{1B}} = \kappa_{\vec{\mu}} - \beta, \tag{47}$$

where $r_{1B} = R\sqrt{2}\sqrt{1 - \cos(2\pi\dfrac{j}{N}) + 2n^2\sin^2\dfrac{\pi}{N}}$. The corresponding eigenfunctions are:

$$\phi^{\vec{\mu}} = C_{j_1 j_2} \sum_{j=0}^{N-1}\sum_{n=1}^{M} \exp\left[-i\left(j_1\frac{2\pi j}{N} + j_2\frac{2\pi n}{M}\right)\right]\frac{e^{-\kappa_{\vec{\mu}} r_A}}{r_A}, \tag{48}$$

where $r_A = \left|\vec{r} - R_j\vec{R} - na\vec{e}_z\right|$, the constant $C_{j_1 j_2}$ can be found from the normalization condition.

The spectrum is naturally discrete but the eigenvalues are collected in groups, that in a sense inherits the continuous spectrum of the Hamiltonian for infinite tube of the next section. It can be understood attending the Remark 2.6. Ground state $j_1 = j_2 = 0$ is non-degenerate:

$$\phi^{00} = C_{00} \sum_{j=0}^{N-1}\sum_{n=1}^{M} \frac{e^{-\kappa_{00} r_A}}{r_A}. \tag{49}$$

with energy determined via κ_{00} by the equation:

$$\sum_{j=0}^{N-1}\sum_{n=1}^{M} \frac{e^{-\kappa_{00} r_{1B}}}{r_{1B}} = \kappa_{00} - \beta. \tag{50}$$

Some alternative technique details of the spectrum calculations are described in [14] and for details see [29].

2.4. Infinite tube. Bands

Let us take the case of integer n, say $M = \infty$, then, using the Floquet theorem we write similar to (49) the complete set of bounded solutions:

$$\phi^{k,j_1} = C_0 \sum_{j=1}^{N} \sum_{n=-\infty}^{+\infty} \exp\left[-i\left(j_1\frac{2\pi j}{N} + kna\right)\right]\frac{e^{-\kappa_{j_1} r_A}}{r_A}, \tag{51}$$

where $r_A = \left|\vec{r} - R_j\vec{R} - na\vec{e}_z\right|$, the constant C_0 can be found from the normalization condition for continuous spectrum. The first sum (index n) is carried over cross-section planes with centers while the second sum (index j) is over centers in a plane numerated, as before, from 1 to N, and positions of centers are:

$$\vec{R}_{nj} = R_j\vec{R} + na\vec{e}_z, \tag{52}$$

with $a\vec{e}_z$ being a shift vector corresponding to distances between the nearest cross-section planes with centers and $\vec{R}_j$ denoting positions of centers in a plane orthogonal to z-axis.

The corresponding energy $E_k^{(j_1)}$ can be found from the general equation (31) rewritten as (47), dividing the sum into two parts:

$$\sum_{j=1}^{N-1} \sideset{}{'}\sum_{n=-\infty}^{\infty} \exp\left[-i\left(j_1\frac{2\pi j}{N} + kna\right)\right]\frac{e^{-\kappa_{\vec{\mu}} r_{1B}}}{r_{1B}} + \sideset{}{'}\sum_{n=-\infty}^{\infty} \exp[-ikna]\frac{e^{-\kappa_{j_1} 2nR\sin\frac{\pi}{N}}}{2nR\sin\frac{\pi}{N}} = \kappa_{j_1} - \beta, \tag{53}$$

where $r_{1B} = 2R\sqrt{\sin^2\left(\pi\frac{j}{N}\right) + n^2\sin^2\frac{\pi}{N}}$.

The series in the second term is summed up as follows ($\kappa_{j_1} = \kappa$):

$$\sideset{}{'}\sum_{n=-\infty}^{\infty} e^{ikna}\frac{e^{-\kappa|n|a}}{|n|\,a} = \sum_{n=1}^{+\infty}\frac{e^{-(\kappa-ik)na}}{ma} + \sum_{n=1}^{+\infty}\frac{e^{-(\kappa+ik)na}}{na}. \tag{54}$$

Denoting $\lambda_\pm = e^{-(\kappa\pm ik)a}$, we notice that $|\lambda_\pm| < 1$. This allows us to write:

$$\sum_{n=1}^{+\infty}\frac{\lambda^n}{n} = \sum_{n=1}^{+\infty}\int_0^\lambda \tilde{\lambda}^{n-1}d\tilde{\lambda} = \int_0^\lambda \underbrace{\sum_{n=0}^{\infty}\tilde{\lambda}^n}_{=\frac{1}{1-\tilde{\lambda}}}d\tilde{\lambda} = -\log(1-\lambda).$$

$$\begin{aligned}
\sideset{}{'}\sum_{m=-\infty}^{+\infty} e^{ikma}\frac{e^{-\kappa|m|a}}{|m|\,a} &= -\frac{1}{a}\log\left[(1-\lambda_-)(1-\lambda_+)\right] = \\
&= -\frac{1}{a}\log\left[2e^{-\kappa a}(\cosh\kappa a - \cos ka)\right] = \\
&= -\frac{1}{a}\log\left[2(\cosh\kappa a - \cos ka)\right] + \kappa.
\end{aligned}$$

The result of substitution leads to the theorem:

Proposition 2.8. *Given the irreducible representation j_1 of the group G_c and the infinite set of point potentials forming the tube along the symmetry group G, we state that the spectrum of energy is continuous, the dependence $E_k^{(j_1)}(k)$ for the j_1-th band state is found as solution of the transcendental equation:*

$$\sum_{j=1}^{N-1} \sideset{}{'}\sum_{n=-\infty}^{\infty} \exp\left[-i\left(j_1\frac{2\pi j}{N} + kna\right)\right]\frac{e^{-\kappa_{j_1} r_{1B}}}{r_{1B}} + \left(\beta - \frac{1}{a}\log\left[2(\cosh\kappa_{j_1} a - \cos ka)\right]\right) = 0, \tag{55}$$

with respect to $\kappa_{j_1} = \sqrt{-\left(2m/\hbar^2\right)E_k^{(j_1)}}$.

3. Back to zero-range potentials for $l \neq 0$ and spin account

3.1. Darboux transformation and its application

Following mainly [14], consider one-dimensional Sturm–Liouville equation:

$$L\psi = \lambda\psi, \tag{56}$$

where:

$$L = -\frac{d^2}{dx^2} + u(x). \tag{57}$$

We apply algebraic-differential transformation, referred as Darboux transformation (DT):

$$D = \frac{d}{dx} - \sigma(x). \tag{58}$$

The following theorem takes place:

Theorem 3.1 (Darboux Theorem). *The transformed equation preserve the same form and eigenvalue:*

$$L^{[1]}\psi^{[1]} = \lambda\psi^{[1]}, \tag{59}$$

where $\psi^{[1]} = D\psi$, $L^{[1]} = -\dfrac{d^2}{dx^2} + u^{[1]}(x)$ *and the transformed potential is:*

$$u^{[1]}(x) = u(x) - 2\sigma'(x). \tag{60}$$

where:

$$\sigma(x) = \frac{\Phi_1'}{\Phi_1} \tag{61}$$

with Φ_1 *being a particular solution to the original equation with* λ_1:

$$-\Phi_1'' + u(x)\Phi_1 = \lambda_1\Phi_1$$

.

In case of multiple application of the DT, the expression (61) is generalized into Crum formulas:

Theorem 3.2 (Crum observation). *Let:*

$$\psi^{[N]} = D^{[N]}\psi = \frac{W(\Phi_1, \ldots, \Phi_N, \psi)}{W(\Phi_1, \ldots, \Phi_N)}, \tag{62}$$

where W denote determinants of the Wronskian matrices. resulting in the following transformation of the potential:

$$u^{[N]}(x) = u(x) - 2\frac{d^2}{dx^2}\Big[\log W(\Phi_1, \ldots, \Phi_N)\Big]. \tag{63}$$

We move towards the radial Schrödinger equation (1) and notice that it can be brought to the form (56) eligible for direct application of obtained transformation formulas. Namely, performing substitution $\psi = \chi/r$, one readily obtains:

$$-\chi'' + \frac{l(l+1)}{r^2}\chi = k^2\chi, \tag{64}$$

that contains only the centrifugal term originating from the orbital moment operator.

That is to say, having in mind to save zero potentials, that we can apply DT to equation (1), meaning that all original wave functions ψ should be multiplied by r, whereas the potential term

$$u(r) = \frac{l(l+1)}{r^2} \tag{65}$$

remains unchanged.

Thus, the formulas (62), (63) in spherical coordinates should be replaced with:

$$u^{[N]}(r) = u(r) - 2\frac{d^2}{dr^2}\Big[\log W(r\Phi_1, \ldots, r\Phi_N)\Big] \tag{66}$$

and:

$$\psi^{[N]} = D^{[N]}\psi = \frac{W(r\Phi_1, \ldots, r\Phi_N, r\psi)}{rW(r\Phi_1, \ldots, r\Phi_N)}. \tag{67}$$

Following an idea of the previous works [10, 20], we first show how gZRP can be induced by application of DT.

We start by choosing a spherical Bessel function as the seed solution:

$$\psi_l(r) = C j_l(kr) \tag{68}$$

and apply N-th order Darboux transformation taking spherical Hankel functions with specific parameters κ_m as prop functions:

$$\Phi_m(r) = C h_l^{(1)}(-i\kappa_m r), \qquad m = 1, \ldots, N. \tag{69}$$

Note that we represent here and later on generic constant as C without prescribing any specific value, such that it can absorb constant multipliers (where their meaning is not important) without changing notation.

We can employ Crum's formula (62) and consider the asymptotic behavior of spherical functions at $r \to \infty$:

$$j_l(kr) \approx \frac{\sin(kr - l\pi/2)}{kr}, \tag{70}$$

$$y_l(kr) \approx -\frac{\cos(kr - l\pi/2)}{kr}, \tag{71}$$

$$h_l^{(1)}(kr) = j_l(kr) + iy_l(kr) \approx (-i)^{l+1}\frac{\exp(ikr)}{kr}, \tag{72}$$

$$h_l^{(2)}(kr) = j_l(kr) - iy_l(kr) \approx i^{l+1}\frac{\exp(-ikr)}{kr}. \tag{73}$$

Then, the Wronskians are transformed into Vandermonde determinants.

The asymptotic of the potential (66) and the solution (67) are expressed in terms of Vandermonde determinants:

$$\Delta(\kappa_1, \ldots, \kappa_N, ik) = \begin{vmatrix} 1 & \kappa_1 & \kappa_1^2 & \ldots & \kappa_1^N \\ 1 & \kappa_2 & \kappa_2 & \ldots & \kappa_2^N \\ \ldots & \ldots & \ldots & \ldots & \ldots \\ 1 & \kappa_N & \kappa_N^2 & \ldots & \kappa_N^N \\ 1 & ik & (ik)^2 & \ldots & (ik)^N \end{vmatrix} = C\prod_{m=1}^{N}(\kappa_m - ik).$$

$$\psi_l^{[N]}(r) = C\left[(-i)^l\frac{\exp(ikr)}{kr}\frac{\Delta(\kappa_1, \ldots, \kappa_N, ik)}{\Delta(\kappa_1, \ldots, \kappa_N)} - i^l\frac{\exp(-ikr)}{kr}\frac{\Delta(\kappa_1, \ldots, \kappa_N, -ik)}{\Delta(\kappa_1, \ldots, \kappa_N)}\right]. \tag{74}$$

Theorem 3.3 (ZRP by DT). *Given a seed solution* (68) ***for arbitrary choice of*** N ***and parameters*** κ_m***,*** $m = 1, \ldots, N$ *of prop functions* (69) *provides DT-invariance of the ZRP.*

This leads to the following:

Corollary 3.4 (s-states). *For* $l = 0$:

$$\log W(r\Phi_1, \ldots, r\Phi_N) = \sum_{m=1}^{N}\kappa_m r + C,$$

according to ***dressed potential*** (66):

$$u^{[N]}(r) \equiv 0, \qquad r > 0.$$

The scattering length is:

$$a_0 = \sum_{m=1}^{N}\kappa_m^{-1} = \beta^{-1}. \tag{75}$$

For arbitrary l, denoting:

$$s_l = \prod_{m=1}^{N}\frac{(\kappa_m - ik)}{(\kappa_m + ik)} = -\prod_{m=1}^{N}\frac{(k + i\kappa_m)}{(k - i\kappa_m)}, \tag{76}$$

we recognize in the expression (74) the asymptotes of spherical Hankel functions, hence:

$$\psi_l^{[N]}(r) = C\left[s_l h_l^{(1)}(kr) - h_l^{(2)}(kr)\right]. \tag{77}$$

The final expression (77), being alternative form of radial function coincides with (2) if:

Proposition 3.5 (S-matrix).

$$s_l = \exp(2i\eta_l) = \prod_{m=1}^{N}\frac{(\kappa_m - ik)}{(\kappa_m + ik)}. \tag{78}$$

So, the DT technique reproduces the result of introduction obtained in a systematic way.

Now, alternatively to gZRP, instead of taking into account the impact of higher harmonics, we consider the transformation of spherically symmetric solution (i.e. $l = 0$) with the parameters κ_m to be chosen according to spectral data of the entire molecule obtained, for example, from the discrete spectrum of molecule modeled by regular ZRP method.

We return to:

$$a_l^{2l+1} k^{2l+1} = -i \frac{ik \sum_{n=1}^{N} \prod_{\substack{m=1 \\ m \neq n}}^{N} \kappa_m + \ldots + (ik)^N}{\prod_{m=1}^{N} \kappa_m + \ldots + (ik)^{N-1} \sum_{n=1}^{N} \kappa_n}. \tag{79}$$

The conditions may be directly applied to the Bloch functions of the Sec. 2.1.

Freedom of choice of transformation parameters gives the possibility of inducing *desired poles of scattering matrix* (76) and, thereby, perform transition from atomic to molecular ZRP by choosing κ_m, $m = 1, \ldots, M$ such that the new potential allows M bounded states obtained by solving conventional formulation of the discrete spectrum problem for the set of M standard ZRPs making up the molecule. Molecular ZRP can be qualitatively characterized by *effective scattering length computed according to* (75) and thus used in such simplified scattering calculations in complicated problems involving, for example, a chain of molecules and give a model for conductivity.

3.2. Spin variable account

The Pauli equation for zero external field [24] is the equation for two-component spinor that is eigenvector of commuting operators M and M_z having in cylindrical coordinates the form:

$$M_z = -i\hbar \frac{\partial}{\partial \varphi} + \frac{\hbar}{2} \sigma_z,$$
$$M = \sigma_i M_i - \hbar/2, \tag{80}$$

with eigenvalues $\hbar(m + \frac{1}{2})$, k'. The components ψ_i are expressed in terms of spherical functions as follows:

$$\frac{1}{\sin\theta} \frac{\partial Z}{\partial \phi} - \frac{\partial Z}{\partial \theta} = k'Y,$$
$$\frac{1}{\sin\theta} \frac{\partial Y}{\partial \phi} + \frac{\partial Y}{\partial \theta} = k'Z, \tag{81}$$

so, that:

$$\psi_1 = f(r)Y,$$
$$\psi_2 = g(r)Z. \tag{82}$$

The equations coincide with ones of Dirac theory (we use notations from [24]) in the nonrelativistic limit. A transition to real auxiliary functions is performed by:

$$f(r) = \frac{f_1 + if_2}{\sqrt{2}},$$
$$g(r) = \frac{f_1 - if_2}{\sqrt{2}}. \tag{83}$$

The radial functions f_i in nonrelativistic limit f_i^0, $|f_2| \ll |f_1|$, $f_1^0 = rR$ are defined by the equation that coincides by form with radial Shrödinger equation:

$$\frac{d^2 R}{dr^2} + \frac{2}{r} \frac{dR}{dr} - \frac{k'(k'-1)}{r^2} R + \frac{2m}{\hbar^2}(E - U(r)) = 0, \tag{84}$$

where the quantum number k' is expressed in terms of the nonrelativistic quantum number l:

$$k'(k'-1) = l(l+1). \tag{85}$$

The minimal value of k' is $k' = 1$, that corresponds to $l = 0$, otherwise $k' = -l, l+1$. The system of equations for f_i^0:

$$-\frac{\hbar}{2mc}\left(\frac{df_1^0}{dr} - \frac{k'}{r} f_1^0\right) = f_2^0,$$
$$\frac{df_2^0}{dr} + \frac{k'}{r} f_2^0 = \frac{E - U}{2mc} f_1^0, \tag{86}$$

leads to (84) for f_1^0, while the first of (86) reads as expression of f_2^0 via f_1^0. We can start from ZRP theory for (84), expressing the Pauli theory solutions (82) in nonrelativistic limit in terms of R as the solution of (84).

The general form of the solution is:

$$f_2^0 = -\frac{\hbar}{2mc}\left(\frac{df_1^0}{dr} - \frac{k'}{r}f_1^0\right),$$

$$f_1^0 = rR,$$

(87)

while:

$$f(r) = \frac{1}{\sqrt{2}}\left(1 - i\frac{\hbar}{2mc}\left(\frac{d}{dr} - \frac{k'}{r}\right)\right)rR = \frac{1}{\sqrt{2}}(1 - i\hat{a})rR,$$

$$g(r) = \frac{1}{\sqrt{2}}\left(1 + i\frac{\hbar}{2mc}\left(\frac{d}{dr} - \frac{k'}{r}\right)\right)rR = \frac{1}{\sqrt{2}}(1 + i\hat{a})rR,$$

(88)

where:

$$\hat{a} = \frac{\hbar}{2mc}\left(\frac{d}{dr} - \frac{k'}{r}\right) = \frac{\hbar}{2mc}r^{k'}\frac{d}{dr}r^{-k'}.$$

(89)

Next, such identity holds:

$$\begin{pmatrix} 1 + i\hat{a} & 0 \\ 0 & 1 - i\hat{a} \end{pmatrix}\begin{pmatrix} \psi_1 \\ \psi_2 \end{pmatrix} = \begin{pmatrix} 1 + i\hat{a} & 0 \\ 0 & 1 - i\hat{a} \end{pmatrix}\begin{pmatrix} f(r)Y \\ g(r)Z \end{pmatrix} =$$

$$\begin{pmatrix} (1 + \hat{a}^2)rRY \\ (1 + \hat{a}^2)rRZ \end{pmatrix} = (1 + \hat{a}^2)rR\begin{pmatrix} Y \\ Z \end{pmatrix},$$

(90)

where:

$$\hat{a}^2 = \frac{\hbar^2}{4m^2c^2}r^{k'}\frac{d^2}{dr^2}r^{-k'}.$$

(91)

The ZRP potential in this case is defined by asymptotic behavior of R (2) as in (4) and (5) within the algorithm shown in introduction, Eqs. (7–9). A constants $C_\pm$ in these cases are defined from:

$$\frac{1}{\sqrt{2}}(1 \pm i\hat{a})rR(r) \approx C_\pm\frac{1}{\sqrt{2}}(1 \pm i\hat{a})r\left(\frac{(kr)^l}{(2l+1)!!} - \frac{(2l-1)!!}{(kr)^{l+1}}\tan\eta_{l\pm}\right),$$

(92)

with $s_{l\pm} = \exp\left(2i\eta_{l\pm}\right)$ being a scattering matrices (having in mind the link between k' and l). The sign "–" stands for f and "+" marks g. We designate next $f_+ = g$, $f_- = f$ for brevity. The leading singularity terms at $r \to 0$ are given by:

$$k^{l+1}r^{l+1}f_\pm|_{r=0} = \pm\frac{(2l-1)!!}{\sqrt{2}}C_\pm\tan\eta_{l\pm}\frac{\hbar}{2mc}(l + k'),$$

(93)

and:

$$C_\pm = \frac{\sqrt{2}\,(2l+1)!!}{k^l(2l+1)!}\frac{d^{2l+1}}{dr^{2l+1}}r^lf_\pm|_{r=0}.$$

(94)

Combining yields:

$$r^{l+1}f_\pm|_{r=0} = \pm\tan\eta_{l\pm}\frac{\hbar}{2mc}(l + k')(2l-1)!!\frac{(2l+1)!!}{k^{2l+1}(2l+1)!}\frac{d^{2l+1}}{dr^{2l+1}}r^lf_\pm|_{r=0}.$$

(95)

This gives the general ZRP conditions for the spinor wave function components taking into account the spin variable. The case of s-wave $l = 0, k' = 1$ leads to:

$$krf_\pm|_{r=0} = \pm\tan\eta_{0\pm}\frac{\hbar}{mc}\frac{d}{dr}f_\pm|_{r=0}.$$

(96)

Some alternative condition is formulated in [28].

4. Bloch wave scattering problem by a ZRP

4.1. Flux normalization

It is essential to note that for every allowed energy we will have two Bloch functions marked by the sign as index $\pm$. Bloch functions for k and $-k$ will give us appropriate flux in opposite directions. We shall name such Bloch functions as "left" and "right". We consider the tube as quasi-one-dimensional structure; therefore, let us differentiate the basic solutions with respect to the variable z, which is the axis of symmetry:

$$\frac{\partial}{\partial z}g_\pm(r, k) = \left(\pm ik - \frac{1}{r}\right)\frac{z}{r}\frac{e^{\pm ikr}}{r}.$$

(97)

The flux component can be calculated by the definition:

$$j_z(\psi) = -i\frac{\hbar}{2m}\left(\psi^*\frac{d}{dz}\psi - \psi\frac{d}{dz}\psi^*\right). \tag{98}$$

Direct substitution (21) into (98) yields at $r \to \infty$:

$$j_z(\phi_\pm) = \pm 2A_\pm^* A_\pm \frac{\hbar k}{m}\sum_{A,B} D^{\vec\mu*}(A)D^{\vec\mu}(B)g_\pm^*\left(r_A,\,k\right)g_\pm\left(r_A,\,k\right). \tag{99}$$

Lemma 4.1 (Flux). *Let the transverse to the tube axis plane be denoted as S. The flux through S along z is constant:*

$$\partial_z\int_S j_z(\phi_\pm)dS = 0.$$

Proof: Differentiation of j_z by z and use the Hermicity of Δ_{tr} ($\Delta = \partial_z^2 + \Delta_{tr}$) yields the Statement of the Lemma.

A normalization of the left/right Bloch functions $\phi_\pm$ is defined via

Definition 4.2 (Normalization). The normalization constants $A_\pm$ for the right and left Bloch waves are defined by the conditions for the stream:

$$\int_S j_z(\phi_\pm)dS =$$
$$\pm|A_\pm|^2\frac{2\hbar k}{m}\sum_{A,B}\exp[i\vec\mu(\vec s_B - \vec s_A)]\int_S g_\pm^*\left(r_B,\,k\right)g_\pm\left(r_A,\,k\right)dS = \pm 1, \tag{100}$$

with (26) account.

4.2. Scattering problem for Bloch electron formulation

A scattering problem may be formulated by means of left and right Bloch waves:

$$\phi = \phi_+^{\vec\mu} + f_-\phi_-^{\vec\mu} = \sum_{a\in G} D^{\vec\mu}(a)T_a(g_+ + f_-g_-), \tag{101}$$

represents incoming and reflected wave at $z < 0$, while at $z > 0$ it is:

$$f_+\phi_+^\mu.$$

Let a ZRP scatterer is placed at $z = 0$. As an aim of future development, it is chosen as a defect of displacement (deformation potential) positioned at $\vec r_0$.

According to the idea of **ZRP method**, we write the solution to the scattering problem as:

$$\phi = \phi_+^\mu + f_-\phi_-^\mu = \sum_{a\in G} D^\mu(a)T_a(g_+ + fg_-), \tag{102}$$

subject to the conditions (10) at the appropriate point $\vec R_0$ with some other scattering length:

$$\left.\frac{\partial\log\left(\left|\vec r - \vec R_0\right|\cdot\phi(\vec r)\right)}{\partial\left|\vec r - \vec R_0\right|}\right|_{\left|\vec r - \vec R_0\right|=0} = -\beta_0, \qquad i = 1,\,\ldots,\,M. \tag{103}$$

A one-dimensional scattering problem by ZRP for Dirac comb Bloch functions was considered in [17]. Condition of nonzero solution (zero determinant of the matrix of coefficients) gives the energy spectrum structure:

$$\cos(Ka) = \cos(ka) + \frac{m\beta}{\hbar^2}\frac{\sin(ka)}{k}. \tag{104}$$

Equation (99) is true for any x. Substitution of solution into (99) gives:

$$j(\psi_\rightleftarrows) = \frac{\hbar k}{m}|A_\pm|^2\frac{\pm\sin(Ka)\sin(ka)}{1 - \cos(\pm Ka + ka)}. \tag{105}$$

Next, equation (105) is used for flux normalization:

$$j(\psi_\rightleftarrows) = \pm 1. \tag{106}$$

Corollary 4.3 (Conduction). *A conductivity of the tube with defects, modeled by s-ZRPs may be calculated directly on basis of the scattering amplitude f_- evaluated as a solution of* (103). *More complicated models with $l \neq 0$ account may be used within the prescribed algorithm.*

Below, we demonstrate the presented approach by applying it to a general cyclic molecule with eventual focus on a **benzene molecule**.

5. Case study: $M = 1$, a cyclic molecule

We here consider a molecular system as a degenerate case of the tube with $M = 1$ of N point-centers, typically atoms or groups, modeled by ZRPs which fixed positions in the xy-plane, see Fig. 1. Obviously, the group of symmetry in the plane is the cyclic $G_c = C_N$.

5.1. Bounded states problem

For discrete spectrum as in the Sec. 2.3 we chose a real κ, with the fundamental solution of the Schrödinger equation with zero potential:

$$g\left(r, \kappa\right) = \frac{e^{-\kappa r}}{r}. \tag{107}$$

According to the general idea, we write solution to the bounded state problem as subject to the particular case of conditions (31):

$$\sum_{B \in G_c}' \exp\left[i\mu \frac{2\pi(j_A - j_B)}{N}\right] \frac{e^{-\kappa_\mu r_{AB}}}{r_{AB}} = \kappa_\mu - \beta, \tag{108}$$

where $\mu = j_1 = 0, ..., N - 1$ is an irreducible representation number. The distances between atoms are found from (45), after choice of A as unit element, that now simplifies as:

$$r_{IB} = 2R \sin\left(\frac{\pi j}{N}\right). \tag{109}$$

The equations then reads:

$$\sum_{j=0}^{N-1} \exp\left[-i\mu \frac{2\pi j}{N}\right] \frac{e^{-\kappa_\mu 2R \sin(\frac{\pi j}{N})}}{2R \sin(\frac{\pi j}{N})} = \kappa_\mu - \beta. \tag{110}$$

We note that the expression is formally valid for $\mu = 0, \ldots, N - 1$, however we note that there is only $[N/2]$ different values κ_μ because equations differ only by the factors $\exp\left[-i\mu \frac{2\pi j}{N}\right]$, which coincides with $\exp\left[-i(N - \mu)\frac{2\pi j}{N}\right]$, where $[\cdot]$, here and subsequently, marks integer part of an argument (i.e. the floor function).

Theorem 5.1 (Bound states). *The eigenvalue problem for n ZRP is equivalent to the algebraic system* (110). *Energy levels are numerated by an irreducible representation number, such that:*

$$E_\mu = -\frac{\hbar^2 \kappa_\mu^2}{2m}, \qquad \mu = 0, \ldots, [N/2], \tag{111}$$

by treating transcendental equation with respect to κ_μ. In case of even number of atoms N) the only non-degenerate eigenvalues are the ground state $\mu = 0$:

$$\psi_0(\vec{r}) = C_0 \sum_{j=0}^{N-1} \frac{e^{-\kappa_0 r_A}}{r_A}, \tag{112}$$

where $r_A = \left|\vec{r} - R_j \vec{R}\right|$ and the state with the highest energy $\mu = N/2$:

$$\psi_{N/2}(\vec{r}) = C_{M/2} \sum_{j=0}^{N-1} (-1)^j \frac{e^{-\kappa_{N/2} r_A}}{r_A}, \tag{113}$$

other states are doubly-degenerate:

$$\psi_\mu(\vec{r}) = C_\mu \sum_{j=0}^{N-1} \exp\left[-i\mu \frac{2\pi j}{N}\right] \frac{e^{-\kappa_\mu r_A}}{r_A}. \tag{114}$$

For odd number of atoms, the classification of states and levels is similar.

5.2. Continuous spectrum. Scattering problem

Let incident free particle fly axially on N-atom potential, centered in transverse xy plane symmetric structure as in previous section. A Schrödinger equation solution with energy $E = \dfrac{\hbar^2 k^2}{2\mu}$ is now taken as the superposition that accounts for the s-waves corresponding the identity irreducible representation:

$$\psi(\vec{r}) = e^{ikz} + \sum_{j=0}^{N-1} g\left(\left|\vec{r} - \vec{R}_j\right|, -ik\right), \tag{115}$$

at $r \to \infty$, the solution (115) tends to:

$$\psi(\vec{r}) = e^{ikz} + f(\theta,\, \phi)\frac{e^{ikr}}{r}. \tag{116}$$

Theorem 5.2 (Scattering amplitude). *Let the positions of the cyclic molecule atoms are determined as $\vec{R}_j = R_j\vec{R}$. The scattering amplitude at long distances in direction $\vec{n} = \vec{r}/r = (\sin\theta\cos\phi,\, \sin\theta\sin\phi,\, \cos\theta)^T$ is given by:*

$$f(\theta,\, \phi) = C_0 \sum_{j=0}^{N-1} e^{-ik\vec{n}\cdot\vec{R}_j}. \tag{117}$$

where

$$C_0 = \frac{-1}{\beta + ik + 2\sum_{j=1}^{(N+\chi_N)/2-1} g\left(r_j, -ik\right) + \chi_{N-1}\cdot g\left(r_{N/2}, -ik\right)}, \tag{118}$$

where $\chi_N = \dfrac{N/2 - [N/2]}{N/2 - [(N-1)/2]}$ is an indicator of parity of the number of atoms N.

Proof. The ZRP conditions (50) are modified as:

$$C_0 \sum_{j=0}^{N-1} \frac{e^{-ikr_{1B}}}{r_{1B}} = ik - \beta. \tag{119}$$

recall also that (109) is written as:

$$r_{1B} = r_j = 2R\sqrt{\sin(\frac{\pi j}{N})}. \tag{120}$$

The asymptotic at infinity is based on one term of the expansion $\left|\vec{r} - \vec{R}_j\right| \approx r - \dfrac{\vec{r}}{r}\cdot\vec{R}_j$. From the equation, it follows that:

$$C_0 = \begin{cases} \dfrac{-1}{\beta + ik + 2\sum_{j=1}^{(N-1)/2} g\left(r_j, -ik\right)}, & \text{odd } N, \\[3mm] \dfrac{-1}{\beta + ik + 2\sum_{j=1}^{N/2-1} g\left(r_j, -ik\right) + g\left(r_{N/2}, -ik\right)}, & \text{even } N. \end{cases}$$

This can be unified as in the theorem formulation. It is also useful to recall the relation (120) and rewrite the sum explicitly:

$$\sum_{j=1}^{(N+\chi_N)/2-1} g\left(r_j, -ik\right) = \frac{1}{2R} \sum_{j=2}^{(N+\chi_N)/2} \frac{\exp\left(2ikR\sin\left(\frac{\pi j}{N}\right)\right)}{\sin\left(\frac{\pi j}{N}\right)} \tag{121}$$

The differential cross-section is determined by:

$$\frac{d\sigma}{d\Omega} = |f(\theta,\, \phi)|^2, \tag{122}$$

as well as the total scattering cross-section:

$$\sigma = \int\limits_0^{2\pi}\int\limits_0^{\pi} |f(\theta,\, \phi)|^2 \sin\theta d\theta d\phi. \tag{123}$$

This also can be expressed according to the optical theorem:

$$\sigma = \frac{4\pi}{k}\operatorname{Im}\left\{f(0,\, \phi)\right\}. \tag{124}$$

Therefore:

$$\sigma \;=\; \frac{4\pi N}{k} \mathrm{Im}\left\{C_0\right\} = \frac{4\pi N}{k} \frac{k+P}{(k+P)^2 + (\beta+Q)^2},$$ (125)

where we denote:

$$P \equiv \frac{1}{R}\left\{ \sum_{j=1}^{(M+\chi_N)/2-1} \frac{\sin\left(2kR\sin\left(\pi j/N\right)\right)}{\sin\left(\pi j/N\right)} + \frac{\chi_{N-1}}{2}\sin\left(2kR\right)\right\},$$ (126)

$$Q \equiv \frac{1}{R}\left\{ \sum_{j=1}^{(N+\chi_N)/2-1} \frac{\cos\left(2kR\sin\left(\pi j/N\right)\right)}{\sin\left(\pi j/N\right)} + \frac{\chi_{N-1}}{2}\cos\left(2kR\right)\right\}.$$ (127)

We note that for the case of a single ZRP scatterer (i.e. $N = 1$) characterized by:

$$\left.\frac{d\log\left(r\psi(r)\right)}{dr}\right|_{r=0} = -\beta_0,$$ (128)

the formula (118) should be obviously replaced with:

$$C_0 = -\frac{1}{\beta_0 + ik},$$ (129)

resulting in the very simple formula for total scattering cross-section:

$$\sigma = \frac{4\pi}{k}\mathrm{Im}\left\{C_0\right\} = \frac{4\pi}{k^2 + \beta_0^2}.$$ (130)

As it was announced, we believe that a simplified theoretical model of molecular structures can be built by replacing each multiatomic molecule with some ZRP once its spectrum is known. Indeed, in particular for scattering on one molecule instead of (125), one would attempt to use (130) with β_0 to be chosen from the discrete spectrum levels κ_m according to the obtained formula (75).

5.3. Results for benzene molecule

It is important to verify the method of ZRP addressing a relatively simple atomic system, e.g., molecule. Focusing on particular case of a benzene molecule C_6H_6 which can be considered as a cyclic structures formed by $C - H$ constituents described by ZRPs, we set $N = 6$ and start with the bounded state problem solution.

The structure of the discrete spectrum is as it described by the Theorem 5.1 for the even number of centers, i.e. there are 4 energy levels with 2 middle ones being doubly degenerate. Numerical solution of the transcendental equations (110) yields the values of energy levels which are compared with those obtained by the well-known Hückel method on the Fig. 2. The spectrum, namely distances between the energy levels, reveals good correspondence of ZRP approach to the qualitative Hückel calculations dictating energies from the ground to the highest level to be $E_0 - 2A$, $E_0 - A$, $E_0 + A$, $E_0 + 2A$, respectively [18, 25].

To analyze continuous spectrum, we consider total scattering cross-section dependence on energy.

We compare the results given by the standard (atomic) ZRP model of the molecule (125) and those followed from single ZRP description of the molecule, i.e. (130) using the inverse of effective scattering length for β_0 evaluation. As one can observe on the plots given below (Fig. 3), for differently estimated values of radius of benzene molecule (e.g. see the introduction of [27]), there is moderate coincidence between conventional set of atomic ZRPs model and proposed single molecular ZRP approach.

Also, we notice that better correspondence of the molecular ZRP results to those obtained with the set of standard ZRPs can be achieved if in the dressing procedure one includes only the ground state and the state with maximal energy, i.e. $E_j = -\dfrac{\hbar^2 \kappa_j^2}{2\mu}$, $j = 0, 3$. This can be viewed as if we follow the described general procedure of application DT for every level, but for each doubly degenerate level with $E_j = -\dfrac{\hbar^2 \kappa_j^2}{2\mu}$, $j = 1, 2$ we perform an additional DT again with the prop function of type (69) but choosing a negative transformation parameter $\kappa = -\kappa_j$, $j = 1, 2$ (corresponding to the same energy level). This results in cancellation of consecutive contributions of the DTs with opposite to each other spectral parameters gives:

$$\beta = \left(\kappa_0^{-1} + \kappa_3^{-1}\right)^{-1},$$ (131)

Benzene energy levels comparison [eV]
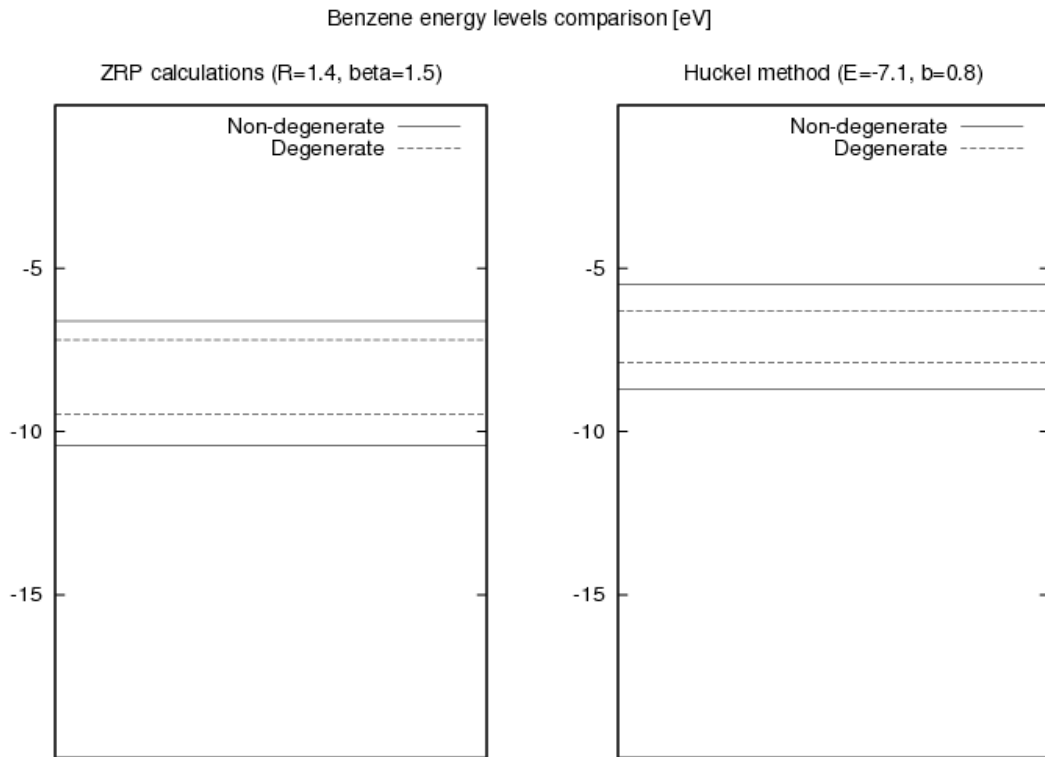
FIG. 2. The energy levels of benzene molecule. The ZRP calculations against Hückel model
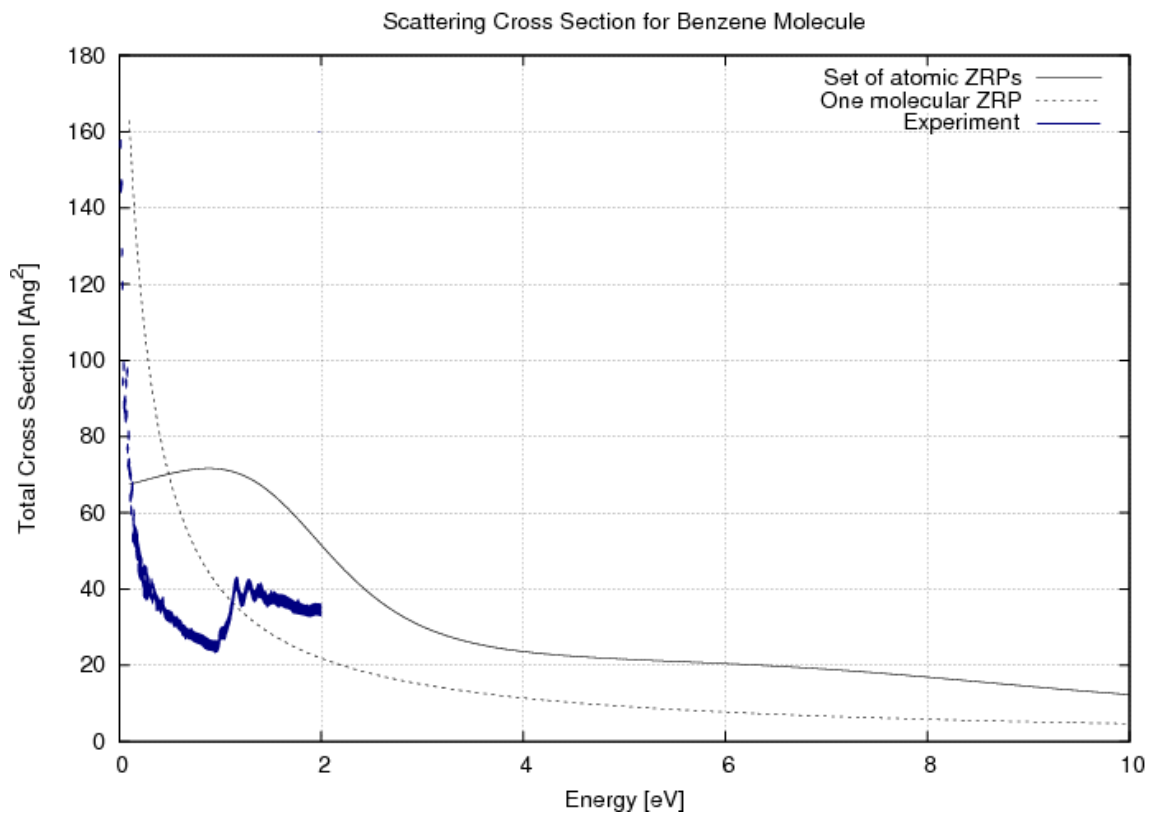
FIG. 3. The cross-section of scattering by $N = 6$ benzene molecule, lying in xy plane. The theory against experiment

This result is not surprising since, as it can be seen from the scattering matrix formalism, such pair of DTs yields consecutive adding and removal of a pole on the imaginary positive k half-axis (which corresponds to a bounded state) of (76): $s_0 \cdot \dfrac{k + i\kappa_j}{k - i\kappa_j} \cdot \dfrac{k - i\kappa_j}{k + i\kappa_j} = s_0$, $j = 1, 2$.

That is effective characteristic involves only the lowest and the highest energy level parameters. In case of odd number of atoms this would involve only the ground state energy parameter κ_0. Refined in this way, the molecular potential gives results are demonstrated by plots at [29].

6. Conclusions

The main results:

1. For arbitrary discrete symmetry, a generalization of Floquet theorem is formulated and proved. The Floquet–Bloch functions are constructed in terms of covariant summation by the symmetry group. The obtained formulas are valid as for scattering problem as for bounded states for the cases of quantum ring and quantum wire, respectively. The results are formulated for Abelian group but the proofs are based only on group-theoretical formalism, hence they may be generalized in straightforward manner.

2. Energy corresponding to the given states can be calculated numerically by solving the transcendent equations that were obtained with account of arbitrary angular momentum and electron spin.

3. In case of the quantum ring, solution to scattering problem can be further simplified depending on the range of interest in terms of energy of incident wave: either the stationary phase method can be used to estimate the resulting integral in high-energy range or simply small-argument direct series expansion for the case of large wavelengths in comparison to the size of the ring.

4. Eventually computed scattering cross-section might be used in estimates of electrical conductivity for solids that contain these quantum rings structures as inclusions or surface additions.

5. The presented method of extension of conventional atomic ZRP approach is made to describe molecular structures based on their discrete spectrum. Bounded state energies, either found from conventional ZRP calculations or in whatever alternative way, determine effective characteristic of newly introduced single ZRP that is expected to adequately describe properties of a molecule.

6. Certainly, replacement of arbitrary molecules with spherically symmetric point-centers is a crude approximation valid only in low-energy limit, however, as was demonstrated, even in case of highly anisotropic molecules, like benzene, the model gives not perfect but reasonable quality results while at the same time allowing significant simplification in formulation of more complicated molecular structures problems with molecules instead of atoms as ZRP constituents.

7. Although we believe that the molecular ZRP method should be tested on more examples in order to prove its quantitative merit, it seems to be a beneficial tool at least to obtain estimates of results on physically reasonable analytical grounds.

References

[1] Floquet G. Sur les équations différentielles linéaires á coefficients periodiques. *Annales de l'École Normale Supérieure*, 1883, **12**, P. 47–88.

[2] Leble S.B. Kolmogorov equation for Bloch electrons and electrical resistivity models for nanowires. *Nanosystems: Physics, Chemistry, Mathematics*, 2017, **8** (2), P. 247–259.

[3] Fermi E. Sopra lo spostamento per pressione delle righe elevate delle serie spettrali. *Il Nuovo Cimento*, 1934, **11**, P. 157–166.

[4] Breit G. The scattering of slow neutrons by bound protons: methods of calculation. *Phys. Rev.*, 1947, **71**, P. 215.

[5] Demkov Yu.N., Ostrovskii V.N. *Zero-range potentials and their applications in atomic physics*. Plenum, New York, 1988.

[6] Pavlov B.S. The theory of extensions and explicitly-solvable models. *Russian Math. Surveys*, 1987, **42** (6), P. 127–168.

[7] Albeverio S., Gesztesy F., Hoegh-Krohn R., Holden H. *Solvable models in quantum mechanics*. Springer, New York, 1988.

[8] Huang K., Yang C.N. Quantum-mechanical many-body problem with hard-sphere interaction. *Phys. Rev.*, 1957, **105**, P. 767–775.

[9] Derevianko A. Revised Huang-Yang multipolar pseudopotential. *Phys. Rev. A*, 2005, **72**, 044701.

[10] Leble S.B., Yalunin S. A dressing of zero-range potentials and electron molecule scattering problem at low energies. *Phys. Lett. A*, 2005, **339**, P. 83–88.

[11] Pavlov B.S., Strepetov A.V. Exactly solvable model of electron scattering by an inhomogeneity in a thin conductor. *Theoret. and Math. Phys.*, 1992, **90** (2), P. 152–156.

[12] Leble S.B., Yalunin S. Generalized zero range potentials and multi-channel electron molecule scattering. *Rad. Phys. Chem.*, 2003, **68**, P. 181–186.

[13] Adamyan V.M., Blinova I.V., Popov A.I., Popov I.Yu. Waveguide bands for a system of macromolecules. *Nanosystems: physics, chemistry, mathematics*, 2015, **6** (5), P. 611–617.

[14] Leble S., Ponomarev D.V. Dressing of zero-range potentials into realistic molecular potentials of finite range. *Task Quarterly*, 2010, **14** (1–2), P. 29–34.

[15] Grishanov E.N., Popov I.Y. Electron spectrum for aligned SWNT array in a magnetic field. *Superlattices and Microstructures*, 2016, **100**, P. 1276–1282.

[16] Grishanov E.N., Popov I.Y. Computer simulation of periodic nanostructures. *Nanosystems: Physics, Chemistry, Mathematics*, 2016, **7** (5), P. 865–868.

[17] Botman S., Leble S. Bloch wave scattering on pseudopotential impurity in 1D Dirac comb model. `ArXiv:1511.04758v1 [cond-mat.mes-hall]`, 2015.

[18] Coulson C.A., O'Leary B., Mallion R.B. *Hückel theory for organic chemists*. Academic Press, London, 1978.

[19] Crum M.M. Associated Sturm-Liouville systems. *Quart. J. Math. Oxford Ser.*, 1955, **6** (2), P. 121–127.

[20] Doktorov E.V., Leble S.B. *Dressing method in mathematical physics*. Springer, London, 2006.

[21] Drukarev G.F. The zero-range potential model and its application in atomic and molecular physics. *Adv. Quantum Chem.*, 1979, **11**, P. 251–274.

[22] Bordag M., Muñoz-Castañeda J.M. Dirac lattices, zero-range potentials, and self-adjoint extension. *Phys. Rev. D*, 2015, **91**, 065027.

[23] Idziaszek Z., Callarco T. Pseudopotential method for higher partial wave scattering. *Phys. Rev. Lett.*, 2006, **96**, 013201.

[24] Fock V. *Fundamentals of quantum mechanics*. Mir, Moscow, 1982.

[25] Le Bellac M. *Quantum Physics*, Cambridge University Press, 2006.

[26] Matveev V.B., Salle M.A. *Darboux transformations and solitons*. Springer-Verlag, Berlin, Heidelberg, 1991.

[27] Nakahara M., Wakai C., Matubayasi N. Jump in the Rotational Mobility of Benzene Induced by the Clathrate Hydrate Formation. *J. Phys. Chem.*, 1995, **99** (5), P. 1377–1379.

[28] Szmytkowski R. Zero-range potentials for Dirac particles: Scattering and related continuum problems. *Phys. Rev. A*, 2005, **71**, 052708(1–19).

[29] Ponomarev D.V. Electronic states in zero-range potential models of nanostructures with a cyclic symmetry. MSc. Thesis. Supervisor: prof. S. Leble. Gdansk, Gdansk University of Technology, 2010.

Magnetic response of a quantum wire of elliptical cross-section in a magnetic field perpendicular to the axis of the wire

V. A. Margulis[1], V. V. Karpunin[2], K. I. Mironova[1]

[1]Ogarev Mordovian State University, Bolshevistskaya 68, Saransk, 340005, Russia

[2]Mordovian State Pedagogical Institute named after M. E. Evseviev, Studencheskaya 11 A, Saransk, 340007, Russia

theorphysics@mrsu.ru, karpuninvv@mail.ru

The magnetic response of a quantum wire of elliptical cross section is investigated. An explicit analytic expression is found for the spectrum and wave functions of an electron in the wire. Using an approach based on finding the classical partition function, an expression is obtained for the magnetic response of the electron gas in the wire. The dependence of the response on the magnitude and direction of the magnetic field is found.

Keywords: magnetic moment, quantum wire.

1. Introduction

Effects arising in the magnetic field perpendicular to the axis of the wire in electronic systems are due to the fact that the motion in the plane of confinement and perpendicular to it is connected by a magnetic field whose direction is determined by the angle θ, $\mathbf{B} = B(\sin\theta, \cos\theta)$ [1–4]. The effect of the spin-orbit interaction on the magnetization of low-dimensional systems has been investigated [5–13]. The energy spectrum of electrons in low-dimensional systems has been studied in [14]. As shown in [1,2], in the case of the parabolic confinement potential (well or wire), the problem of finding the spectrum and wave functions of the one-electron Hamiltonian can be solved exactly.

The magnetoresistance of the wire in a magnetic field whose direction is at different angles with the wire axis has been studied experimentally in Refs [15]. It is shown that at different angles the Aharonov-Bohm oscillations are manifested in the magnetoresistance.

The jumps of the magnetic moment for the wire in the form of a thin-walled cylinder were found in [16]. We note that theoretical studies of the magnetic moment of the wire in a magnetic field transverse to the axis are not known to us. In [17], the electron-impurity scattering coefficient of Bloch waves for one dimensional Dirac comb potential is used for calculating the temperature dependence of conductivity within kinetic theory. Nonlinear light absorption and its time evolution at high optical excitation levels in GaSe and InSe layered crystals have been experimentally investigated in [18].

We use an asymmetric parabolic potential V for modeling of a quantum waveguide with elliptical cross-section. In this case, the confinement potential is:

$$V(x, z) = \frac{m^*}{2}(\omega_1^2 x^2 + \omega_2^2 z^2), \tag{1}$$

here ω_1 and ω_2 is effective frequencies of potential, m^* is the effective electronic mass. In this model, the characteristic lengths are $l_i = \sqrt{\hbar/m^*\omega_i}$, where $i = 1, 2$ equal to the semi-axes of the cross-section of the wire. We choose the gauge of the magnetic field in the form $\mathbf{A} = (0, B_z x - B_x z, 0)$. The axis of the wire is located along the axis oy. The Hamiltonian describing the one-electron states has the form:

$$H = \frac{1}{2m^*}\left[p_x^2 + (p_y - \frac{e}{c}B_z x + \frac{e}{c}B_x z)^2 + p_z^2\right] + V(x, z) \tag{2}$$

The solution of the Schrödinger equation with the Hamiltonian (2) can be written in the form:

$$\Psi(x, y, z) = \frac{1}{\sqrt{L}}\exp\left(\frac{i}{\hbar}p_y y\right)\varphi(x, z), \tag{3}$$

where φ satisfies the equation $\widehat{H}\varphi = E\varphi$, and L is the length of the wire. This $L^{-1/2}$ is the normalization constant of the plane wave in the y direction. The Hamiltonian $\widehat{H}$ has the form

$$\widehat{H} = \frac{1}{2m^*}\left[p_x^2 + \left(p_y - \frac{e}{c}B_z x + \frac{e}{c}B_x z\right)^2 + p_z^2\right] + V(x, z),\tag{4}$$

expression (2) is not identical (4) because p_y is eigenvalue of the operator p_y.

Let us shift the coordinate system xoz along the axis x by x_0, and along the axis z by z_0, and then we require the reduction of the linear in the axis x and z terms in h. Then we obtain equations for x_0, y_0:

$$\begin{cases} -p_y\omega_z + m^*[(\omega_1^2 + \omega_z^2)x_0 - \omega_x\omega_z z_0] = 0 \\ p_y\omega_x + m^*[(\omega_2^2 + \omega_x^2)z_0 - \omega_x\omega_z x_0] = 0, \end{cases}\tag{5}$$

where $\omega_x = |e|B_x/m^*c$, $\omega_z = |e|B_z/m^*c$, $B_x = B\sin\theta$. θ is the angle defined by the magnetic field and the x axis.

Solving the system (5), we get relations

$$x_0 = \frac{\omega_z p_y}{M\omega_1^2}; \quad z_0 = -\frac{\omega_x p_y}{M\omega_2^2}.\tag{6}$$

After the shift in the axes $x' = x - x_0$, $z' = z - z_0$, the Hamiltonian $\hat{H}$ takes the form:

$$\widehat{H} = -\frac{\hbar^2}{2m^*}\Delta + \frac{p_y^2}{2m^*} + (\omega_x z_0 - \omega_x x_0)p_y +$$

$$\frac{m^*}{2}[(\omega_1^2 + \omega_z^2)(x'^2 + x_0^2) +$$

$$+(\omega_2^2 + \omega_x^2)(z'^2 + z_0^2) - 2\omega_x\omega_z(x'z' + x_0 z_0)],\tag{7}$$

where Δ is a two-dimensional Laplace operator.

We rotate the coordinate system by an angle α to get rid of the term $\sim x'z'$. The angle α satisfies the relation:

$$\mathrm{tg}2\alpha = \frac{2\omega_x\omega_z}{\omega_2^2 - \omega_1^2 + \omega_x^2 - \omega_z^2}.\tag{8}$$

The Hamiltonian $\hat{H}$ takes the form:

$$\widehat{H} = -\frac{\hbar^2}{2m^*}\Delta + \frac{p_y^2}{2M} + \frac{m^*\Omega_1^2}{2}x^2 + \frac{m^*\Omega_2^2}{2}z^2.\tag{9}$$

Characteristic frequencies are:

$$2\Omega_{1,2}^2 = \omega_1^2 + \omega_2^2 + \omega_c^2 \pm \sqrt{(\omega_2^2 - \omega_1^2 - \omega_c^2\cos 2\theta)^2 + \omega_c^4\sin^2 2\theta}.\tag{10}$$

The spectrum $\hat{H}$, as follows from (9), has the form:

$$\varepsilon = \frac{p_y^2}{2M} + \hbar\Omega_1\left(n_1 + \frac{1}{2}\right) + \hbar\Omega_2\left(n_2 + \frac{1}{2}\right), \quad n_1, n_2 = 0, 1, 2...,\tag{11}$$

where:

$$M = m^*\left(1 + \frac{\omega_x^2}{\omega_2^2} + \frac{\omega_z^2}{\omega_1^2}\right) = m^*\left(1 + \frac{\omega_c^2}{\omega_2^2}\sin^2\theta + \frac{\omega_c^2}{\omega_1^2}\cos^2\theta\right).\tag{12}$$

Eigen functions $\varphi(x, z)$ have the form:

$$\varphi(x, z) = \Phi_{n_1}\left[(x - x_0)\cos\alpha + (z - z_0)\sin\alpha\right] \times \Phi_{n_2}\left[(x - x_0)\sin\alpha + (z - z_0)\cos\alpha\right],\tag{13}$$

where Φ_{n_1} and Φ_{n_2} are the oscillatory functions. $\Phi_s(y) = C_s\exp(-y^2/2l^2)H_s(y/l)$, C_s is the normalization constant, $H_s(y/l)$ is Hermite polynomial.

2. Magnetic moment

The purpose of this paper is to find the magnetic moment $\mathbf{M}$ of the wire placed in a perpendicular magnetic field. The calculation of the magnetic moment is based on finding the thermodynamic potential Ω of the gas in the wire. Then $\mathbf{M}$ is determined by the formula $\mathbf{M} = -(\partial\Omega/\partial\mathbf{B})_{T,V}$, where T is temperature and V is volume.

There are two approaches to finding Ω. One approach is based on the Poisson formula [19, 20], and the other [21], is based on finding the classical partition function of states Z. Both approaches were used earlier to find the magnetic response of nanostructures [22–24]. In this paper, we use the classical partition function Z for finding the monotonic and oscillating part of the magnetic moment:

$$Z = \sum_{n_1,n_2,p_y} \exp(-\varepsilon_{n_1,n_2,p_y}/T). \tag{14}$$

Using the formula (11), from (14) we get:

$$Z = \frac{D\sqrt{T}}{4}\left[\sinh\left(\frac{\hbar\Omega_1}{2T}\right)\sinh\left(\frac{\hbar\Omega_2}{2T}\right)\right]^{-1}, \tag{15}$$

where $D = \sqrt{2\pi M}L/(2\pi\hbar)$.

Introducing $\zeta = 1/T$, we obtain for Ω the expression [21]:

$$\Omega = \frac{1}{2\pi i}\int_{\gamma-i\infty}^{\gamma+i\infty}\frac{Z(\zeta)}{\zeta^2}d\zeta\int_0^\infty e^{\varepsilon\zeta}\frac{\partial f_0}{\partial\varepsilon}d\varepsilon. \tag{16}$$

Here, $f_0(\varepsilon) = (\exp((\varepsilon-\mu)/T)+1)^{-1}$ is the Fermi distribution function $0 < \gamma < 1/T$. In (16) the expression for Ω contain the integral:

$$\frac{1}{2\pi i}\int_{\gamma-i\infty}^{\gamma+i\infty}\frac{\exp\varepsilon\zeta\,d\zeta}{\zeta^{5/2}\sinh\beta_1\zeta\sinh\beta_2\zeta}, \tag{17}$$

where $\beta_{1,2} = \hbar\Omega_{1,2}/2$. This integral is calculated in the Appendix:

$$\frac{1}{2\pi i}\int_{\gamma-i\infty}^{\gamma+i\infty}\frac{\exp(\varepsilon\zeta)d\zeta}{\zeta^{5/2}\sinh\beta_1\zeta\sinh\beta_2\zeta} = \frac{1}{\pi}\int_0^\infty\frac{\exp(-\varepsilon t)dt}{t^{5/2}\sinh\beta_1 t\sinh\beta_2 t} + \frac{2}{\pi^{5/2}}\sum_{k=1}^\infty\frac{(-1)^k}{k^{5/2}}\times$$

$$\left[\beta_1^{3/2}\frac{\cos(k\pi\varepsilon/\beta_1+\pi/4)}{\sin(\pi k\beta_2/\beta_1)} + \beta_2^{3/2}\frac{\cos(k\pi\varepsilon/\beta_2+\pi/4)}{\sin(\pi k\beta_1/\beta_2)}\right]. \tag{18}$$

Replacing in (16) $(\varepsilon-\mu)/T = \xi$, where μ is the chemical potential of the electronic gas and replacing the value $-\mu/T$ on $-\infty$, we obtain from (16) and (18) the expression for $\Omega = \Omega^{mon} + \Omega^{osc}$, where:

$$\Omega^{mon} = -\frac{DT}{4}\times\int_0^\infty\exp(-\mu t)\left[t^{3/2}\sin(\pi Tt)\sinh\beta_1 t\sinh\beta_2 t\right]^{-1}dt. \tag{19}$$

The oscillating part Ω^{osc} has the form of a Fourier series:

$$\Omega^{osc} = -\frac{TD}{2\sqrt{\pi}}\sum_{k=1}^\infty\frac{(-1)^{k+1}}{k^{3/2}}\left[\frac{\beta_1^{1/2}\cos(\pi\mu k/\beta_1+\pi/4)}{\sinh(\pi^2 kT/\beta_1)\sin(\pi k\beta_2/\beta_1)} + \frac{\beta_2^{1/2}\cos(\pi\mu k/\beta_2+\pi/4)}{\sinh(\pi^2 kT/\beta_2)\sin(\pi k\beta_1/\beta_2)}\right]. \tag{20}$$

It is convenient at first calculate the derivatives:

$$\frac{\partial\Omega_{1,2}}{\partial B} = \frac{e\omega_c}{m^*c\Omega_{1,2}}\left(1\pm\frac{\omega_1^2-\omega_2^2+\omega_c^2}{\Omega_1^2-\Omega_2^2}\right). \tag{21}$$

Differentiating Ω^{osc} only rapidly oscillating factors in the field, and taking account of (20), we obtain:

$$\frac{M^{osc}}{\mu_B^*} = -\frac{1}{2}TL\sqrt{M}\mu\omega_c\times\left\{\frac{1}{(\hbar\Omega_1)^{5/2}}\left(1+\frac{\omega_1^2-\omega_2^2+\omega_c^2}{\Omega_1^2-\Omega_2^2}\right)\times\right.$$

$$\sum_{k=1}^\infty\frac{(-1)^k}{\sqrt{k}}\frac{\sin\left(\frac{2\pi k\mu}{\hbar\Omega_1}+\frac{\pi}{4}\right)}{\sinh\left(\frac{2\pi^2 kT}{\hbar\Omega_1}\right)\sin\left(\pi k\frac{\Omega_2}{\Omega_1}\right)} + \frac{1}{(\hbar\Omega_2)^{5/2}}\left(1+\frac{\omega_1^2-\omega_2^2+\omega_c^2}{\Omega_2^2-\Omega_1^2}\right)\times$$

$$\sum_{k=1}^{\infty} \frac{(-1)^k}{\sqrt{k}} \frac{\sin\left(\frac{2\pi k\mu}{\hbar\Omega_2} + \frac{\pi}{4}\right)}{\sinh\left(\frac{2\pi^2 kT}{\hbar\Omega_2}\right) \sin\left(\pi k\frac{\Omega_1}{\Omega_2}\right)} \bigg\}, \tag{22}$$

here $\mu_B^* = e\hbar/2m^*c$.

In the case $\omega^2 = \omega_1^2 = \omega_2^2$, however $\Omega_1 \neq \Omega_2$, $\Omega_1 = \sqrt{\omega^2 + \omega_c^2}$, $\Omega_2 = \omega$. In this connection, for the circular cross section the formula (22) has the form

$$\frac{M_{osc}}{\mu_B^*} = -TL\sqrt{M}\mu\omega_c \times \left[\frac{1}{(\hbar\sqrt{\omega^2 + \omega_c^2})^{5/2}} \times \right.$$

$$\left. \sum_{k=1}^{\infty} \frac{(-1)^k}{\sqrt{k}} \frac{\sin((2\pi k\mu/\hbar\sqrt{\omega^2 + \omega_c^2}) + \pi/4)}{\sinh(2\pi^2 kT/\hbar\sqrt{\omega^2 + \omega_c^2}) \sin(\pi k\omega/\sqrt{\omega^2 + \omega_c^2})} \right]. \tag{23}$$

It can be noted that passage to the limit to a wire of circular cross section $\omega_c \neq 0$ is possible, since in this case $\Omega_1 \neq \Omega_2$. In the case, when $\omega_c \to 0$, such passage to the limit is impossible. The reason for this is related to the fact that the calculation of the magnetic moment in the work is based on finding the partition function Z (15). The oscillating part is formed by the sum of the residues at the poles of the first order at the points z_k.

$$\text{res}\left[\frac{\exp(\varepsilon z)}{z^{5/2} \sinh\beta_1 z \sinh\beta_2 z}, \ z_k \right]. \tag{24}$$

If $\Omega_1 = \Omega_2, \omega_c = 0$, the poles become of the second order:

$$\text{res}\left[\frac{\exp(\varepsilon z)}{z^{5/2} \sinh^2 \beta z}, \ z_k \right] = \lim_{z \to z_k} \left[\frac{\exp(\varepsilon z)(z - z_k)^2}{z^{5/2} \sinh^2 \beta z} \right]. \tag{25}$$

Because of this circumstance, using formula (A.7) and hence (23) in this case cannot be found as $\lim_{\omega_c \to 0} M_{osc}$ because poles are changes.

The dependence of the magnetic response on the magnetic field is shown in Figs. 1 – 4. Let us now consider the limit of the potential Ω in the case of weak fields: $\omega_c \to 0$, $\mu \gg \hbar\Omega_{1,2}$, $\hbar\Omega_{1,2}/T \gg 1$. We note that in this limit, the oscillating part Ω^{osc} consists of rapidly oscillating terms of the series (20) and their contribution to Ω tends to zero. To evaluate Ω^{mon}, we use (16). Then, as shown in [25] at low temperatures, the expression is given by:

$$-\Omega = z(\mu) + \frac{\pi^2 T^2}{6} z^{''}(\mu), \tag{26}$$

where

$$z(\varepsilon) = \frac{1}{2\pi i} \int_{\gamma-i\infty}^{\gamma+i\infty} e^{\varepsilon\xi} Z(\xi) \frac{d\xi}{\xi^2}, \tag{27}$$

here $Z(\xi)$ is determined by the formula (15). With the constraint $\hbar\Omega_i/T \gg 1$ from (15) follows the estimate

$$Z(\xi) \simeq \frac{D}{\sqrt{\xi}} \exp\left[-\frac{\hbar(\Omega_1 + \Omega_2)}{T} \right]. \tag{28}$$

We substitute (28) in (27) and use the formula [26]:

$$\frac{1}{2\pi i} \int_{\gamma-i\infty}^{\gamma+i\infty} t^{\gamma-1} e^{-pt} dt = \begin{cases} 0, & p > 0, \\ 1/((-p)^{\gamma}\Gamma(1-\chi)), & p < 0, \end{cases} \quad \text{at } \gamma > 0, \ \text{Re}\,\chi < 1. \tag{29}$$

Then

$$z(\varepsilon) = \frac{D}{\Gamma(5/2)} \left(\varepsilon - \frac{\hbar\Omega_1 + \hbar\Omega_2}{2} \right)^{3/2}, \tag{30}$$

where $\Gamma(\alpha)$ – Euler function, $\Gamma(5/2) = 3\sqrt{\pi}/4$.

The second derivative $z(\varepsilon)$ has the form:

$$z^{''}(\varepsilon) = \frac{D}{\sqrt{\pi}} \frac{1}{\sqrt{\varepsilon - \frac{\hbar(\Omega_1 + \Omega_2)}{2}}}, \tag{31}$$
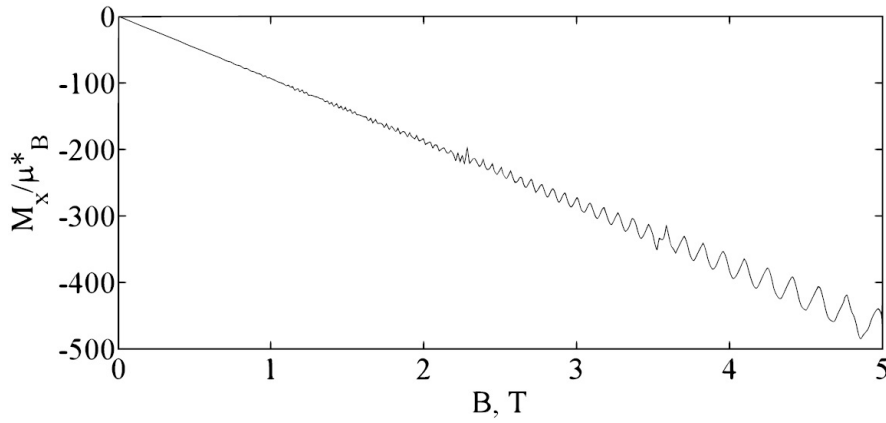
FIG. 1. Dependence of the magnetic response of a quantum wire on the magnitude of the magnetic field for the angle $\theta = \pi/8.324$, the effective frequencies of the confinement potential are $\omega_1 = 2.177 \times 10^{12} \ c^{-1}$; $\omega_2 = 3.353 \times 10^{12} \ c^{-1}$. The temperature T is 7 K
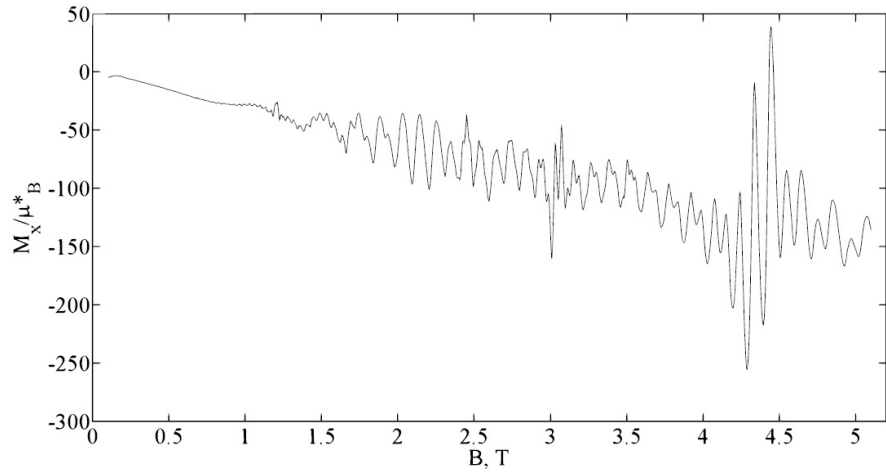
FIG. 2. Dependence of the magnetic response of a quantum wire on the magnitude of the magnetic field for the angle $\theta = \pi/9.524$, the effective frequencies of the confinement potential are $\omega_1 = 3.177 \times 10^{12} \ c^{-1}$; $\omega_2 = 6.353 \times 10^{12} \ c^{-1}$. The temperature T is 3 K
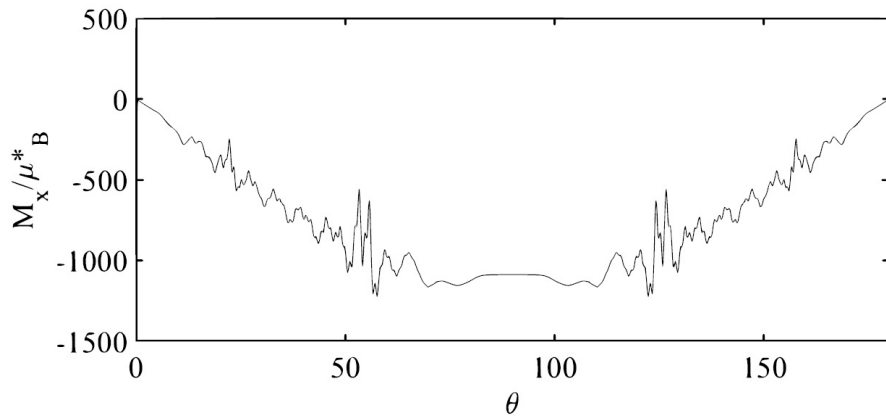
FIG. 3. The dependence of the magnetic response of a quantum wire on the direction of the magnetic field (in the interval from 0 to 180), the value of which is $B = 1.52$ Tl, at effective frequencies of the confinement potential are $\omega_1 = 2.177 \times 10^{12} \ c^{-1}$; $\omega_2 = 3.353 \times 10^{12} \ c^{-1}$. The temperature T is 2 K
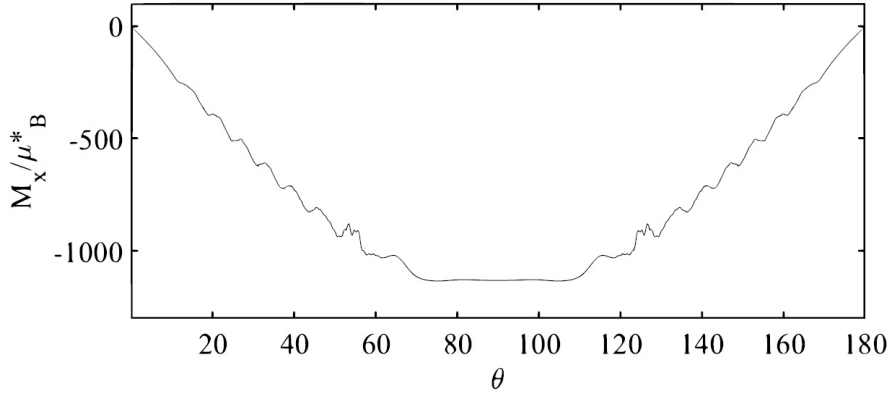
FIG. 4. The dependence of the magnetic response of a quantum wire on the direction of the magnetic field (in the interval from 0 to 180), the value of which is $B = 1.52$ Tl, at effective frequencies of the confinement potential are $\omega_1 = 2.177 \times 10^{12}$ c^{-1}; $\omega_2 = 3.353 \times 10^{12}$ c^{-1}. The temperature T is 5 K

Then, for Ω^{mon}, we obtain:

$$-\Omega^{mon}(\mu) = \frac{4D}{3\sqrt{\pi}} \left(\mu - \frac{\hbar\Omega_1 + \hbar\Omega_2}{2} \right)^{3/2} + \frac{D}{\sqrt{\pi}} \frac{\pi^2 T^2}{6} \frac{1}{\sqrt{\mu - \frac{\hbar\Omega_1 + \hbar\Omega_2}{2}}}. \tag{32}$$

The second term in (32) is small in comparison with the first $\sim O(T^2/\mu^2)$, so this can be neglected.

For the estimate Ω^{mon}, we confine ourselves to the case $\omega_1 = \omega_2$. Then, $D \simeq D_0 \sqrt{1 + \omega_c^2/\omega^2}$, where $D_0 = D(B = 0)$. Frequencies $\Omega_1 = \omega$, $\Omega_2 = \sqrt{\omega^2 + \omega_c^2}$.

$$-\Omega^{mon}(\mu) = \frac{4D}{3\sqrt{\pi}} \left(\mu - \hbar\omega - \frac{\hbar\omega_c^2}{4\omega} \right)^{3/2} \left(1 + \frac{\omega_c^2}{2\omega^2} \right). \tag{33}$$

From (33) we obtain the estimate:

$$-\frac{1}{\mu_B^*} \frac{\partial \Omega^{mon}}{\partial B} \simeq \frac{8D_0}{3\sqrt{\pi}} \frac{\omega_c}{\hbar\omega^2} (\mu - \hbar\omega)^{3/2} - \frac{2D_0\omega_c}{\sqrt{\pi}\omega} (\mu - \hbar\omega)^{1/2}. \tag{34}$$

In (34) to within $\hbar\omega/\mu$ we can confine ourselves to the first term. Then for the magnetic moment, we obtain:

$$\frac{M^{mon}}{\mu_B^*} = \frac{8D_0}{3\sqrt{\pi}} \frac{\omega_c}{\hbar\omega^2} (\mu - \hbar\omega)^{3/2}. \tag{35}$$

From (35), one can estimate the magnetic susceptibility of an electron gas in a wire $\chi = -(1/V)\partial^2\Omega/\partial B^2$. Here, the normalization volume $V = \hbar L/m^* \sqrt{\omega_1\omega_2}$. Then, for susceptibility χ, we obtain the following expression:

$$\chi = \frac{4D_0}{3\sqrt{\pi}L} \left(\frac{e^2}{m^*c^2} \right) \frac{(\mu - \hbar\omega)^{3/2}}{\hbar\omega}. \tag{36}$$

3. Conclusion

As can be seen from formula (35) and (Fig. 1), the main dependence is linear on the magnetic field. Peaks grow linearly with increasing magnetic field.

We consider the wire with an elliptical section, not a circular section, since the latter type of section is a special case. In particular, in the case of a circular cross section, the value M entering the spectrum does not depend on the angle of field direction θ, $M = m^* \left(1 + \omega_c^2/\omega^2 \right), \omega^2 = \omega_1^2 = \omega_2^2$.

It follows from the formula (36) that the electron gas in the wire is paramagnetic $\chi > 0$ and the cause of this is the dependence $M(B)$. Obviously, the expressions (20) and (22) for Ω^{osc} and M^{osc} lose their meaning for those values of the field B for which the ratio Ω_1/Ω_2 or Ω_2/Ω_1 is equal to an integer (the commensurability condition). The question of the convergence of Fourier series of the type entering into (20) and (22) is considered in detail in [2], where it is shown that with probability one the series converge to an analytic function and, therefore, they can be differentiated term by term in components fields at all points where the commensurability conditions are not satisfied.

In Fig. 1–4, we plotted the dependence of the magnetic moment on the magnitude and direction of the field at typical values for the spectrum parameters. It is important to note that oscillatory dependencies arise not only on the graph $M(B)$, but also $M(\theta)$. In both cases, the oscillations are not periodic.

4. Appendix

We introduce the notation:

$$J = \frac{1}{2\pi i} \int\limits_{\gamma-i\infty}^{\gamma+i\infty} \frac{\zeta^{3/2} e^{\varepsilon\zeta} d\zeta}{\sinh\beta_1\zeta \sinh\beta_2\zeta}. \tag{A.1}$$

For the calculation J, we extend the integrand to the complex plane with a cut along the negative part of the real line. Consider a contour Γ consisting of both C_R, C_ρ segments and a segment $[\rho, R]$ T $[R, \rho]$, and $[\gamma - iR, \gamma - iR]$ (Fig.5).
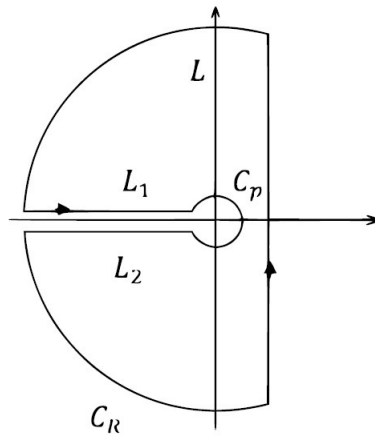
FIG. 5. Contour Γ

The integrand in J is

$$\frac{d^4}{d\varepsilon^4}\left(\frac{e^{\varepsilon\zeta}}{\zeta^{5/2}\sinh\beta_1\zeta\sinh\beta_2\zeta}\right). \tag{A.2}$$

This function has simple poles at points $z_k = i\pi k/\beta_1$, and $z_k = i\pi k/\beta_2$, where $k = \pm 1, \pm 2, \dots$. It is easy to show that the integrals over C_R, C_ρ tend to zero for $R \to \infty$ and $\rho \to 0$, respectively. The sum of the integrals over the upper and lower sides of the cut in the same range gives:

$$\frac{1}{\pi} \int\limits_0^\infty \frac{t^{3/2} e^{-\varepsilon t} dt}{\sinh\beta_1 t \sinh\beta_2 z}. \tag{A.3}$$

We take into account that:

$$\frac{1}{2\pi i} \oint\limits_\Gamma \frac{\zeta^{3/2} e^{\varepsilon\zeta} d\zeta}{\sinh\beta_1\zeta \sinh\beta_2\zeta} = \sum_{k=-\infty}^\infty \operatorname{res}\left[\frac{z^{3/2} e^{\varepsilon z}}{\sinh\beta_1 z \sinh\beta_2 z}, z_k\right]. \tag{A.4}$$

Then we get the relation:

$$\frac{1}{2\pi i} \int\limits_{\gamma-i\infty}^{\gamma+i\infty} \frac{\zeta^{3/2} e^{\varepsilon\zeta} d\zeta}{\sinh\beta_1\zeta \sinh\beta_2\zeta} = \frac{1}{\pi} \int\limits_0^\infty \frac{t^{3/2} e^{-\varepsilon t} dt}{\sinh\beta_1 t \sinh\beta_2 t} + \sum_{k=-\infty}^\infty \operatorname{res}\left[\frac{z^{3/2} e^{\varepsilon z}}{\sinh\beta_1 z \sinh\beta_2 z}, z_k\right]. \tag{A.5}$$

We note that $J(\varepsilon)$ is the inverse Laplace transform of the integrand. From the theorem on the differentiation of the integral and the image to the parameter ε, it follows that:

$$\frac{1}{2\pi i} \int\limits_{\gamma-i\infty}^{\gamma+i\infty} \frac{e^{\varepsilon\zeta} d\zeta}{\zeta^{5/2}\sinh\beta_1\zeta \sinh\beta_2\zeta} = \frac{1}{\pi} \int\limits_0^\infty \frac{e^{-\varepsilon t} dt}{t^{5/2}\sinh\beta_1 t \sinh\beta_2 t} +$$

$$+ \sum_{k=-\infty}^{\infty} \text{res} \left[\frac{e^{\varepsilon z}}{z^{5/2} \sinh \beta_1 z \sinh \beta_2 z}, \; z_k \right].$$ (A.6)

Summing up the residues in (A.6), we obtain:

$$\frac{1}{2\pi i} \int_{\gamma-i\infty}^{\gamma+i\infty} \frac{e^{\varepsilon\zeta} d\zeta}{\zeta^{5/2} \sinh \beta_1 \zeta \sinh \beta_2 \zeta} = \frac{1}{\pi} \int_0^\infty \frac{e^{-\varepsilon t} dt}{t^{5/2} \sinh \beta_1 t \sinh \beta_2 t} +$$

$$+ \frac{2}{\pi^{5/2}} \sum_{k=1}^{\infty} \frac{(-1)^k}{k^{5/2}} \left[\frac{\beta_1^{3/2} \cos(\pi k\varepsilon/\beta_1 + \pi/4)}{\sin(\pi k\beta_2/\beta_1)} + \frac{\beta_2^{3/2} \cos(\pi k\varepsilon/\beta_2 + \pi/4)}{\sin(\pi k\beta_1/\beta_2)} \right].$$ (A.7)

Acknowledgment

References

[1] Merlin R. Subband-Landau-level coupling in tilted magnetic fields: Exact results for parabolic wells. *Sol. State Commun.*, 1987, **64**, P. 99–101.

[2] Geyler V.A., Margulis V.A. Specific heat of quasi-two-dimensional systems in a magnetic field. *Phys. Rev.* **B**, 1997, **55**, P. 2543–2548.

[3] Bychkov Yu.A., Mel′nikov V.I., Rashba E.I. Effect of spin-orbit coupling on the energy spectrum of a 2D electron system in a tilted magnetic field. *Sov. JETP*, 1990, **71**, P. 401–405.

[4] Drichko I.L., Smirnov I.Yu., Suslov A.V., Mironov O.A., Leadley D.R. Magnetoresistivity and acoustoelectronic effects in a tilted magnetic field in p-Si/SiGe/Si structures with an anisotropic g factor. *JETP*, 2010, **111**, P. 495–502.

[5] Herzog F., Heedt S., Goerke S., Ibrahim A., Rupprecht B., Heyn Ch., Hardtdegen H., Schpers Th., Wilde M.A. and Grundler D. Confinement and inhomogeneous broadening effects in the quantum oscillatory magnetization of quantum dot ensembles. *J. Phys.: Condens. Matter*, 2016, **28**, P. 045301.

[6] Wilde M.A. and Grundler D. Alternative method for the quantitative determination of Rashba-and Dresselhaus spin-orbit interaction using the magnetization. *New Journal of Physics*, 2013, **15**, P. 115013.

[7] Wilde M. A., Rupprecht B., Herzog F., Ibrahim A., and Grundler D. Spin-orbit interaction in the magnetization of two-dimensional electron systems. *Phys. Status Solidi B*, 2014, **251**, P. 1710–1724.

[8] Rupprecht B., Heedt S., Hardtdegen H., Schapers Th., Heyn Ch., Wilde M.A., and Grundler D. Frequency anomaly in the Rashba-effect induced magnetization oscillations of a high-mobility two-dimensional electron system. *Phys. Rev.* **B**, 2013, **87**, P. 035307.

[9] Rupprecht B., Krenner W., Wurstbauer U., Heyn Ch., Windisch T., Wilde M.A., Wegscheider W., and Grundler D. Magnetism in a Mn modulation-doped InAs/InGaAs heterostructure with a two-dimensional hole system. *J.Appl.Phys.*, 2010, **107**, P. 093711.

[10] Wilde M.A., Schwarz M.P., Heyn Ch., Heitmann D., and Grundler D. Experimental evidence of the ideal de Haas-van Alphen effect in a two-dimensional system. *Phys. Rev.* **B**, 2006, **73**, P. 125325.

[11] Ruhe N., Springborn J.I., and Heyn Ch. Simultaneous measurement of the de Haas-van Alphen and the Shubnikov-de Haas effect in a two-dimensional electron system. *Phys. Rev.* **B**, 2006, **74**, P. 235326.

[12] Wilde M. A., Rhode M., Heyn Ch., Heitmann D., and Grundler D. Direct measurements of the spin and valley splittings in the magnetization of a Si/SiGe quantum well in tilted magnetic fields. *Phys. Rev.* **B**, 2005, **72**, P. 165429.

[13] Wilde M.A., Springborn J.I., Heyn Ch., Heitmann D., Grundler D. Magnetization of GaAs quantum wires with quasi one-dimensional electron systems. *Physica E*, 2004, **22**, P. 729–732.

[14] Apalkov V.M. and Portnoi M.E. Tuning gaps and phases of a two-subband system in a quantizing magnetic field. *Phys. Rev.* **B**, 2002, **65**, P. 125310.

[15] Gitsu D.V., Huber T.E., Konopko L.A., and Nikolaeva A.A. Aharonov-Bohm Oscillations in Bi Nanowires. *AIP Conference Proceedings*, 2006, **850**, P. 1409–1410.

[16] Tsindlekht M.I., Genkin V.M., Felner I., Zeides F., Katz N., Gazi S., Chromik S., Dobrovolskiy O.V., Sachser R., Huth M. Magnetic moment jumps in flat and nanopatterned Nb thin-walled cylinders. *Physica C: Superconductivity and its Applications*, 2017, **533**, P. 101–104.

[17] Botman S.A., Leble S.B. Electrical conductivity model for quasionedimensional structures. *Nanosystems: Physics, Chemistry, Mathematics*, 2017, **8**(2), P. 231–235.

[18] Kyazimzade A.G., Salmanov V.M., Huseynov A.G., Mamedov R.M., Salmanova A.A., Ahmedova F.Sh. Nonlinear optical and quantadimensional effects in monoselenide of gallium and indium. *Nanosystems: Physics, Chemistry, Mathematics*, 2017, **8**(5), P. 654–660.

[19] Landau L.D., Lifshitz E.M. *Statistical Physics, Third Edition, Part 1: Volume 5 (Course of Theoretical Physics, Volume 5)*, Butterworth-Heinemann; 3 edition, January 15, 1980, 544 p.

[20] Shoenberg D. *Magnetic Oscillations in Metals*. Cambridge University Press, 1984, 570 p.

[21] Perelomov A.M. *Generalized Coherent States and their Applications*, Springer-Verlag Berlin Heidelberg, 1986, 320 p.

[22] Geyler V.A., Margulis V.A., Nesmelov A.G., Chuchaev I.I. Magnetic Susceptibility of a Quasi-Two-Dimensional System in a Tilted Magnetic Field. *Phys. Sol. St.*, 1994, **36**, P. 1090–1094.

[23] Margulis V.A., Mironov V.A. Magnetic moment of a 2D electron gas with spin-orbit interaction. *JETP*, 2009, **108**, P. 656–660.

[24] Margulis V.A., Mironov V.A. Magnetic moment of the Volcano ring. *Phys. Sol. St.*, 2008, **50**, P. 152–158.

[25] Margulis V.A. Magnetization and polarization of the electron gas in multiferroics. *Low Temp. Phys.*, 2014, **40**, P. 363–366.

[26] Prudnikov A.P., Brychkov Yu.A., Marichev O.I. *Integrals and series, Elementary Functions*, N.Y.: Gordon and Breach, 1986, 800 p.

The effect of geometric confinement on gas separation characteristics of additive poly[3-(trimethylsilyl)tricyclononene-7]

E. A. Chernova[1], M. A. Bermeshev[2], D. I. Petukhov[1], O. V. Boytsova[1,3], A. V. Lukashin[1], A. A. Eliseev[1]

[1]Lomonosov Moscow State University, Leninskiye Gory, Moscow, 119991, Russia

[2]A. V. Topchiev Institute of Petrochemical Synthesis (TIPS) Russian Academy of Sciences, Leninsky prospect, 29, Moscow, 119991, Russia

[3]Kurnakov Institute of General and Inorganic Chemistry, Russian Academy of Sciences, Leninsky prospect, 31, Moscow, 119991, Russia

alexey.lukashin@gmail.com, eliseev@inorg.chem.msu.ru

Composite membranes based on a hydrophobic glassy poly[3-(trimethylsilyl)tricyclononene-7] (PTCNSi-1) confined in the channels of anodic alumina with different pore diameters are discussed. Formation of continuous polymer film with partial penetration of polymer into the rigid pores of anodic alumina was achieved by spin-coating technique under vacuum suction. Mass-transport characteristics of composite membranes reveal a slight reduction of composite membrane permeability for condensable gases, and many-fold permeability drop for permanent gases as compared to the bulk film. This results in an ideal selectivity rise over 35 for C_4H_{10}/CH_4 pair compared to 12.6 for bulk PTCNSi-1. The effect is attributed to a solubility-controlled mobility of polymer segments confined in the AAO channels and formation of rigid shallow polymer layer at AAO/polymer interface, which suppress transport of gases. The correlation between intrinsic properties of the polymer (hydrophobicity, Kuhn segment) and its transport characteristics in the confined state is discussed. The evolution of the permeance and pure-gas selectivity of the composite membranes during ageing is also reported.

Keywords: geometric confinement, polynorbornene, anodic alumina, condensable gases, permanent gases, selectivity.

Received: 21 December 2017

Revised: 31 December 2017

1. Introduction

Geometric confinement of matter is a fundamental approach used both in artificial devices and natural systems to resolve the problem of space-saving design and gain the benefit of unusual material properties appearing due to size effects [1–3].

Geometric confinement requires restrictive systems that include, but are not limited to: microfabricated nanochannels, structural cavities of porous solid materials, thin films, micelles or microdroplets [4–7]. One of the frequently used geometric constrictors is represented by anodic aluminum oxide (AAO) templates exposing well defined system of cylindrical channels with easily adjustable diameter, controlled porosity and extremely narrow pore size distribution [8–10]. Expectedly, confinement effects appear when the characteristic size of a container coincides with the characteristic size of the filler resulting in its structural changes or affecting its functional properties [10].

The effect is well pronounced for both crystalline and amorphous materials, including polymers [11, 12]. As a result, the microstructure of a material changes in response to steric confinement and can be modified by controlling restrictor sizes [13, 14]. In the case of polymers, space restriction causes suppression of polymer chains segmental mobility and increases the rigidity of the chains. Toughening of confined polymers extends to a limit of the strength of individual molecules as it was observed for polysterene in 7 nm silica pores [14]. Strong densification of polymer has also been evidenced with gradual suppression of G-actin in phospholipid-stabilized emulsion droplets, which resulted even in cortex formation [1].

The effect of space confinement of polymer chains holds a great promise in membrane applications, as soon as mass-transport properties of polymers are determined by free volume elements and chain dynamics [15]. The special case involves gas-separation membranes with thermodynamic selectivity exhibiting a strong dependence on polymer chain mobility. It is natural to expect that the decrease of chains mobility in rigid channels can result in decreased permanent gas transport across the confined polymer, while the permeance of condensable gases will mostly be preserved due to attenuation of polymer-wall interactions. As a result, the separation factor of polymeric membranes can be enhanced.

In our previous study, we showed that the spatial restriction of polymer of intrinsic microporosity (PIM-1) in the channels of anodic alumina (AAO) leads to a dramatic decrease in permanent gases permeance [16]. As a result, the maximal ideal C_4H_{10}/CH_4 separation factor of 1400 was achieved for the confined polymer in contrast to 58 for the bulk film. The severe confinement effect was ascribed to high rigidity of PIM-1 macromolecules and strong interaction between hydrophilic functional groups of the polymer and OH-groups of AAO channels. The strong intermolecular interaction causes to the formation of a dense adhered layer on the walls of AAO, hindering the movement of macromolecules in the channels. This makes composite membranes nearly impermeable for permanent gases, while polymer swelling by condensable gases releases polymer chains and enhances the gas flow.

It is obvious, that polymer's nature should provide a major influence on its behavior under spatial confinement. The intrinsic properties of a particular polymer, such as the presence of surface functional groups and the size of the Kuhn segment, can dramatically influence its interaction with a restrictive system. To examine this issue, a hydrophobic glassy polymer, additive poly[3-(trimethylsilyl)tricyclononene-7] (PTCNSi-1) that weakly interacts with surface OH-groups of AAO was chosen as a test object to compare the confinement effect with the results provided earlier for PIM-1 [4]. Here, we report the influence of AAO channel diameter on the PTCNSi-1 microstructure and behavior under geometric confinement, as well as the evolution of polymer transport characteristics with time.

2. Experimental section

Anodic alumina membranes were prepared by anodic oxidation. The detailed procedure of membrane preparation, their structural parameters and mass-transport characteristics can be found in our previous studies [16, 17]. The porous structure of AAO supports was adjusted to provide the flow resistance negligible compared to that of a polymer film [18, 19]. The films with 10 – 15 % porosity, 100 μm thickness and channel diameters ranging from 25 to 80 nm were used as constricting supports.

PTCNSi-1 with the molecular weight of 550 kDa and Kuhn segment of 6.0 ± 0.6 nm (the coil size is 56 nm) was synthesized by addition polymerization [20]. Composite membranes were prepared by spin-coating of polymer solution in toluene under vacuum. Polymer solutions were deposited onto AAO supports at rotation speeds of 2300 to 3300 rpm. The concentrations of polymer solution were varied from 1 to 6 wt.%. The optimal concentration providing the homogeneous coverage of AAO surface and leading to intrusion of polymer species to AAO channels was found to be 3 wt.%.

The permeance of AAO supports and composite membranes was measured for the gases in the following order: CH_4, N_2, O_2, CO_2, and n-C_4H_{10}. Two-compartment cross-flow cell and permeance setup equipped with SLA5850 mass-flow controllers (Brooks, England), PD-100-DI pressure transducers (OVEN, Russia) and T-Station 75 vacuum system (BOC Edwards, England) was used as described in detail in [4]. The measurements were performed at ambient temperature (22 ± 2 °C) and continuous flow of feeding gas at the atmospheric pressure using both differential (continuous pumping) and integral (closed volume) schemes with flow registered using either flow controllers or pressure transducers. The permeances, evaluated using both schemes were found to be identical for highly permeable gases (C_4H_{10} and CO_2). Integral scheme was used to measure the permeances of permanent gases to achieve better accuracy.

The microstructure of AAO supports and composite membranes was studied by SEM using Leo Supra 50 VP (21 kV, VPSE detector) and Carl Zeiss NVision 40 (5 kV, InLens detector) electron microscopes. AAO supports were dissolved in 3 M NaOH aqueous solution and to study the microstructure of polymer replicas by SEM.

3. Results and discussion

3.1. Microstructure of the membranes

Typically, the structure of composite membranes includes an outer and inner selective polymer layers. The outer selective layer is represented by a uniform defect-free coating, whereas the inner selective layer is represented by polymer nanofibers confined in the AAO channels. The inner layer is accounted to govern the flow resistivity of the membrane (Fig. 1a). According to SEM, polymeric fibers are uniformly distributed over the membrane area providing the high membrane performance (Fig. 1b).

3.2. The dependence of transport parameters on AAO pore diameter

The composite membranes show a decrease in gas permeability towards permanent and condensable gases as compared to the 1 μm bulk film (Table 1). The ratio of the polymer permeance in the bulky state to the permeance in the confined state towards different gases (the permeance loss factor) was used to estimate the degree of polymer chain suppression in AAO channels. Among permanent gases, the permeance loss factor generally decreases in the order $CH_4 > N_2 > O_2$ for all the membranes. The observed tendency correlates with the kinetic
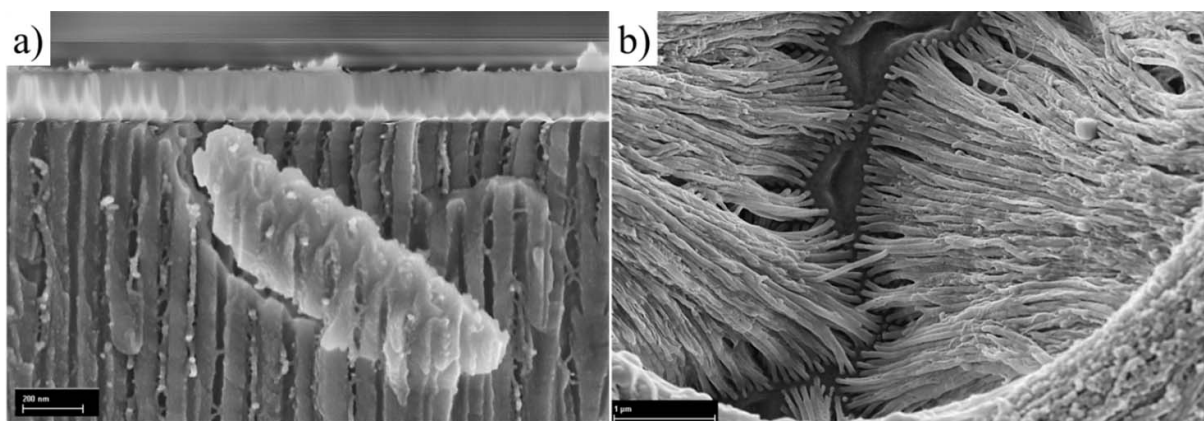
FIG. 1. Microstructure of composite membranes: a) cross-sectional view of C-40 sample close to the top surface after dense polymer layer removal; b) replica of the selective layer of C-40 sample

diameters of permanent gas molecules. Among them, CH_4 has the largest size, and its propagation through the confined polymer layer is more hindered. The absolute values of permeance loss factors for permanent gases are also strongly affected by substrate pore diameters, revealing two-fold decrease in CH_4 transport efficiency with decreasing pore sizes in the supports from 80 to 25 nm (Table 1). Notably, a similar trend was observed for PIM-1 composite membranes [16], attaining maximum permeance suppression for methane over 15.

TABLE 1. Permeability of composite membranes

	AAO pore diameter, nm	Gas				
		CH_4	C_4H_{10}	CO_2	O_2	N_2
Kinetic diameter, nm [23]		0.380	0.430	0.330	0.346	0.364
Permeance, L/m^2/bar/h						
Bulk film, 1 mkm		370±18	4750±238	1930±97	360±18	140±7
C-25	25±5	64±3	2310±116	699±35	134±7	46,5±2
C-40	40±5	79±4	2737±137	581±29	171±8	55±3
C-80	80±10	129±6	2350±117	601±30	238±12	92±5
bulk PIM-1 [16]		120±6	7460±473	980±49	230±11	91±4
PIM-1/C25 [16]	25±5	8±2	11400±547	420±18	77±37	9±4
Permeance loss factor						
Bulk film/C-25		5.78	2.06	2.76	2.69	3.01
Bulk film/C-40		4.68	1.73	3.32	2.11	2.54
Bulk film/C-80		2.87	2.02	3.21	1.51	1.52
Bulk film PIM-1/C-25		15	0.65	2.33	2.98	10.11

The situation changes in the case of transport of condensable gases through composite membranes. The permeance of those becomes nearly immune to the constrictor size effect, resulting in nearly the same permeance, irrespective of substrate pore diameter. On the other hand, permeance loss factors befall dependent on the nature of penetrant: the value of the permeance loss factor changes from ~ 2 for C_4H_{10} to ~ 3 for CO_2 for all

the membranes with different pore diameters. This behavior differs from earlier published data for PIM-1/AAO membranes.

This phenomenon can be explained by the difference in the intrinsic properties of the PTCNSi-1 and PIM-1, which have different chemical natures (Fig. 2). PIM-1 contains hydrophilic functional groups and its macromolecules are highly rigid: even the entire chain can be considered as one Kuhn segment [21]. Conversely, PTCNSi-1 is a semi-flexible hydrophobic glassy polymer with Kuhn segment of 6 nm [22]. The adsorption of hydrophobic macromolecules to the hydrophilic walls and surface of the AAO support can be considered poor enough. Thus, the adhered surface layer of PTCNSi-1 on the walls of AAO channels is flexible and doesn't provide a strong reduction in polymer chain mobility. Reduction in Kuhn segment also reduces the thickness of inflexible shallow layer, which suppresses transport of low-soluble gases. As a result, the response of this polymer to the geometric confinement is expectedly weaker.
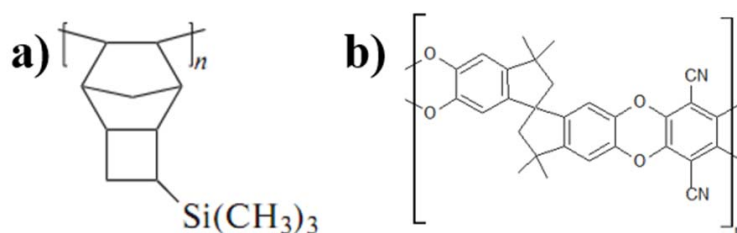
FIG. 2. The monomer units a) PTCNSi-1; b) PIM-1

Highly soluble condensable gases generally reduce polymer-wall interaction and strongly affect small scale mobility of polymer chains in both the cases. For the weakly-bound polymer (PTCNSi-1), this results in complete extinguishing of constrictor size effects (Table 1), while for the strongly interacting macromolecules (PIM-1), it just reduces the thickness of inflexible shallow layer, attenuating the confinement effect [16].

Nevertheless, the confinement effect is well pronounced even for weakly bound polymers with rather small Kuhn segment. The pure-gas selectivity of PTCNSi-1/AAO composite membranes is enhanced as compared to the bulk film (Table 2). The 2,8- and 2,6-fold increase in C_4H_{10}/CH_4 pure-gas selectivity is observed for the C-25 and C-40 samples, respectively, while selectivity of the C-80 membrane slightly exceeds that of the bulk film. The enhancement of CO_2/CH_4 separation factor generally follows the tendency observed for C_4H_{10}/CH_4 gas pair with twice higher ideal separation factors as compared to the bulk film. A very slight increase in O_2/N_2 selectivity is also observed for C-25 and C-40 composite membranes.

TABLE 2. The dependence of selectivity on AAO channels diameter

Selectivity	C_4H_{10}/CH_4	CO_2/CH_4	O_2/N_2
Bulk film 1 mkm	12.9±0.6	5.2±0.3	2.5±0.1
C-25	36±2	10.9±0.5	2.9±0.1
C-40	34±2	7.3±0.4	3.1±0.2
C-80	18.2±1	4.6±0.2	2.6±0.1

These observations determine the key role of constrictor-polymer and gas-polymer interaction in the transport of gases through constrained polymer membranes. At present, the results available for both PTCNSi-1 and PIM-1 constrained polymers can be interpreted in the following way. Interaction of polymer with inorganic matrix at AAO/polymer interface results in the formation of rigid shallow polymer layer which extends into polymer volume, depending on the intrinsic rigidity of the polymer. Generally, the higher is Kuhn segment in the polymer the thicker toughened layer is formed. The low-scale mobility of polymer segments in this layer is strongly hindered, suppressing transport of gases by diffusional jumps. Dissolution of condensable gases in polymer volume and their interaction with constrained macromolecules reduces the rigidity of the toughened layer and effectively increases permeability of condensable gases. The solubility-controlled mobility of polymer segments results in a colossal rise of ideal separation factors for condensable/permanent gas pairs. Thus, the effect of constrictor

is both provided by the substrate/polymer interfacial energy and Kuhn segment/pore size ratio. Unfortunately, quantitative interpretation of the confinement effect is still impractical due to the absence of experimental data on gases solubility for the confined polymers. We even failed to find data on solubility coefficients of gases in bulk PTCNSi-1, so the influence of solubility of gases on the permeance of composite membranes cannot be directly considered.

3.3. Physical ageing

To trace the evolution of constrained polymer, the physical ageing of composite membrane C-40 was studied over 50 days. The decrease in permanent and condensable gases permeance exhibits similar trends with the permeance loss factors rather close for different gases (Fig. 3b, Table 3). Significant change in polymer permeability and similar behavior of the permeance for different gases points to the structural changes appearing in the confined polymer. As soon as the highest impact into the transport of permanent gases is provided by an internal volume of polymer fibers rather than the rigid shallow layer interacting with AAO interface, the possible mechanism of physical ageing is the growth of shallow toughened layer thickness with time.
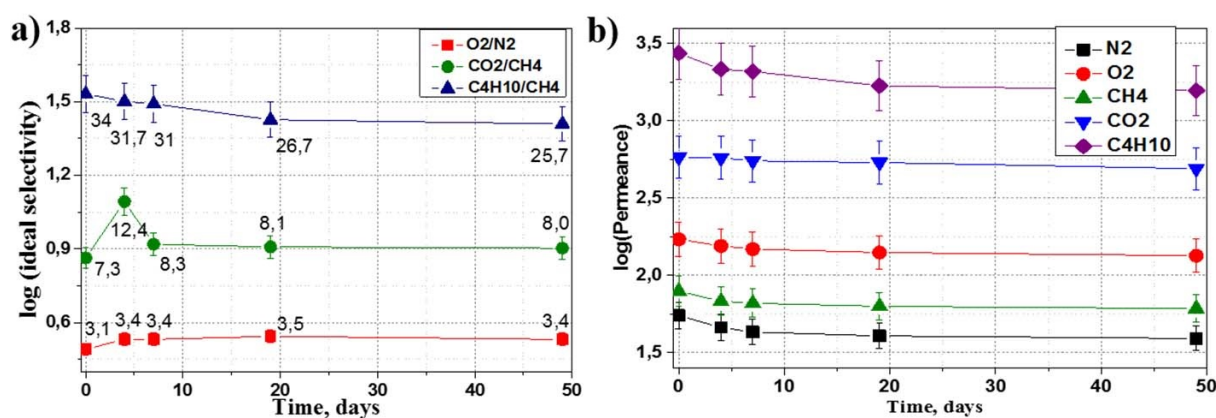
FIG. 3. Time-evolution of a) permeance; b) selectivity of C-40 membrane

TABLE 3. Time-evolution of permeance and loss in permeance of the C-40 membrane

Permeance, L/m^2/bar/h					
Time, days	CH$_4$	C$_4$H$_{10}$	CO$_2$	O$_2$	N$_2$
0	79±4	2737±137	581±29	171±9	55±3
4	68±3	2153±108	575±29	155±8	46±2
7	66±3	2086±104	550±27	148±7	43±2
19	63±3	1685±84	537±27	140,5±7	40,6±2
50	61±3	1570±79	490±24	134±6	39±2
Total permeance loss, %					
Time, days	CH$_4$	C$_4$H$_{10}$	CO$_2$	O$_2$	N$_2$
50	23	42	16	22	29

On the other hand, the decrease of permeance of highly-soluble C$_4$H$_{10}$ is more influenced by the gradual densification of the shallow layer. Thus, the fastest permeance loss of butane with ageing, can be interpreted as a continuous growth of polymer rigidity and substrate-polymer interaction energy in time in contrast to growth of the toughened layer. This assumption is indirectly proved by inability to restore the initial butane permeability of composite film even after 2 days of butane exposure.

Thus, we can conclude that the change in permeance of confined polymers in the course of the physical ageing is a result of synergetic effects of both structural changes and the growth of the thickness of shallow toughened layer interacting with inorganic matrix. This behavior of permeance evolution with time can be correlated with the influence of geometric confinement. Indeed, the 100 mm-thick film of PTCNSi-1 homologue (PTCNSi-2 with two Si(CH$_3$)$_3$ groups in side chains) exhibits only 3 – 5 % reduction in permeance of N$_2$ and O$_2$ during 3 weeks of ageing [20]. Expectedly, spatial confinement amplifies and accelerates relaxation of polymer chains into more stable conformations.

Notably, the asymptotes of pure gas selectivity of composite films with ageing don't conform with ideal selectivities of a bulk polymer. Stabilization of pure gas selectivity for C$_4$H$_{10}$/CH$_4$ pair is achieved at the level of ~ 25 as compared to ~ 13 in a bulk film, while CO$_2$/CH$_4$ selectivity stabilizes at 8.0 as compared to 5.2 in a bulk film. Even permanent gas O$_2$/N$_2$ pair exhibits an asymptote of 3.4, which is higher than a value of 2.5 for bulk PTCNSi-1 (Fig. 3a).

The resulting selectivity increase caused by confinement of macromolecules in the rigid substrates is substantial for technological uses. We believe the reported constrictor effects on membrane performance will contribute to the development of new polymeric membrane materials and encourage improvement of the existing polymeric membrane's performance.

4. Conclusions

Composite membranes based on hydrophobic glassy polymer, PTCNSi-1, confined in the channels of anodic aluminium were obtained by spin-coating technique of polymer solution in toluene under vacuum. Mass-transport characteristics of confined polymer illustrate uneven reduction of permeance for permanent and condensable gases, as compared to the bulk film, which results in 2-fold increase in C$_4$H$_{10}$/CH$_4$ and CO$_2$/CH$_4$ ideal selectivity. The comparison of presented results with earlier published data on PIM-1/AAO membranes showed the correlation between intrinsic properties of the polymer (hydrophobicity and Kuhn segment) and its transport characteristics in the confined state. According to our model, adsorption of polymer chains on the pore walls of the inorganic matrix gives rise to the formation of a rigid toughened polymer layer extending into polymer volume depending on the intrinsic rigidity of the polymer. The thickness of the toughened layer is proportional to the Kuhn segment in the polymer. The small-scale mobility of macromolecules in this layer is restricted and causes reduction of polymer gas permeance, especially for permanent gases. Swelling of polymer by condensable gases lowers the rigidity of the confined layer, enhancing the permeability of constricted polymer towards condensable gases. As a result, the solubility-controlled mobility of polymer segments causes a substantial rise of ideal separation factors for condensable/permanent gas pairs.

We believe that the government of polymer microstructure by geometric confinement will provide a powerful tool for controlling the performance of composite membrane materials. Combination of appropriate type of polymer and confinement conditions will give rise to a variety of high-performance membranes, not only for gas separation technology, but also for pervaporation and nanofiltration.

References

[1] Claessens M., Tharmann R., Kroy K., Bausch A.R. Microstructure and viscoelasticity of confined semiflexible polymer networks. *Nature Physics*, 2006, **2** (3), P. 186–189.

[2] Maier J. Nanoionics: ion transport and electrochemical storage in confined systems. *Nature Materials*, 2005, **4**, P. 805–815.

[3] Huber P. Soft matter in hard confinement: phase transition thermodynamics, structure, texture, diffusion and flow in nanoporous media. *J. Phys. Condens. Matter*, 2015, **27** (10), 103102.

[4] Eliseev A.A., Falaleev N.S., et al. Size-Dependent Structure Relations between Nanotubes and Encapsulated Nanocrystals. *Nano Lett.*, 2017, **17** (2), P. 805–810.

[5] Eliseev A.A., Petukhov D.I., et al. Morphological modification of the surface of polymers by the replication of the structure of anodic aluminum oxide. *JETP Lett.*, 2010, **92** (7), P. 453–456.

[6] Jones R.L., Kumar K.S., et al. Chain Conformation in Ultrathin Polymer Films Using Small-Angle Neutron Scattering. *Macromolecules*, 2001, **34** (3), P. 559–567.

[7] Buttersack C., Rudolph H., Mahrholz J., Buchholz K. High Specific Interaction of Polymers with the Pores of Hydrophobic Zeolites. *Langmuir*, 1996, **12** (13), P. 3101–3106.

[8] Krutyeva M., Wischnewski A., Richter D. Polymer dynamics in nanoconfinement: Interfaces and interphases. *EPJ Web of Conferences*, 2015, **83**, 02009.

[9] Krutyeva M., Wischnewski A., et al. Effect of Nanoconfinement on Polymer Dynamics: Surface Layers and Interphases. *Phys. Rev. Lett.*, 2013, **110** (10), 108303.

[10] Lukatskaya M., Trusov L., et al. Controlled way to prepare quasi-1D nanostructures with complex chemical composition in porous anodic alumina. *Chem. Commun.*, 2011, **47** (8), P. 2396–2398.

[11] Tung W., Composto R., Riggleman R., Winey K. Local Polymer Dynamics and Diffusion in Cylindrical Nanoconfinement. *Macromolecules*, 2015, **48** (7), P. 2324–2332.

[12] Volynskii A.L., Yarysheva A.Yu, et al. Specific features of structure and properties of solutions, melts and solid states of polymers in confined nanometric volumes. *Russ. Chem. Rev.*, 2014, **83** (11), P. 1003–1026.

[13] Steinhart . Supramolecular Organization of Polymeric Materials in Nanoporous Hard Templates. In *Self-Assembled Nanomaterials II: Nanotubes*, Springer, Heidelberg, 2008, P. 123–187.

[14] Isaacson S., Lionti K., et al. Fundamental limits of material toughening in molecularly confined polymers. *Nat. Mater.*, 2015, **15**, P. 294–298.

[15] Nagel C., Günther-Schade K., et al. Free Volume and Transport Properties in Highly Selective Polymer Membranes. *Macromolecules*, 2002, **35** (6), P. 2071–2077.

[16] Chernova E., Petukhov D., et al. Enhanced gas separation factors of microporous polymer constrained in the channels of anodic alumina membranes. *Sci. Rep.*, 2016, **6**, 31183.

[17] Petukhov D.I., Eliseev A.A. Gas permeation through nanoporous membranes in the transitional flow region. *Nanotechnology*, 2016, **27** (8), 85707.

[18] Petukhov D.I., Napolskii K.S., et al. Comparative study of structure and permeability of porous oxide films on aluminum obtained by single- and two-step anodization. *ACS Appl. Mater. Interfaces*, 2013, **5** (16), P. 7819–7824.

[19] Petukhov D.I., Berekchiyan M.V., et al. Experimental and Theoretical Study of Enhanced Vapor Transport through Nanochannels of Anodic Alumina Membranes in a Capillary Condensation Regime. *J. Phys. Chem. C*, 2016, **120** (20), P. 10982–10990.

[20] Gringolts M., Bermeshev M., et al. New High Permeable Addition Poly(tricyclononenes) with $Si(CH_3)_3$ Side Groups. *Synthesis, Gas Permeation Parameters, and Free Volume, Macromolecules*, 2010, **43** (17), P. 7165–7172.

[21] Shantarovich V.P., Suzuki T., et al. Structural heterogeneity in glassy polymeric materials revealed by positron annihilation and other supplementary techniques. *Phys. status solidi*, 2007, **4** (10), P. 3776–3779.

[22] Yevlampieva N.P., Bermeshev M.V., et al. Additive poly[3-(trimethylsilyl)tricyclononene-7]: Molecular properties and chain rigidity. *Polym. Sci. Ser. A*, 2016, **58** (3), P. 324–335.

[23] Breck D.V. *Zeolite molecular sieves. Structure, chemistry and use*. John Wiley and Sons, New York, 1974, 771 p.

$Ca_{1-x-y}Yb_xPr_yF_{2+x+y}$ solid solution powders as a promising materials for crystalline silicon solar energetics

S. V. Kuznetsov[1], O. A. Morozov[2], V. G. Gorieva[2], M. N. Mayakova[1], M. A. Marisov[2], V. V. Voronov[1], A. D. Yapryntsev[3], V. K. Ivanov[3], E. I. Madirov[2], A. S. Nizamutdinov[2], V. V. Semashko[2], P. P. Fedorov[1]

[1]Prokhorov General Physics Institute, RAS, 38 Vavilova str., Moscow, 119991 Russia

[2]Kazan Federal University, 18 Kremljovskaya, Kazan, 420008 Russia

[3]Kurnakov Institute of General and Inorganic Chemistry, RAS, 31 Leninsky pr., Moscow,119991 Russia

kouznetzovsv@gmail.com

We have synthesized single-phase powders of $Ca_{1-x-y}Yb_xPr_yF_{2+x+y}$ solid solutions with an average particle size of about 35 nm by co-precipitation from aqueous nitrate solutions. After annealing at 600 °C during 1 hour, the particle size was increased up to 150–200 nm. Individual luminescence bands of praseodymium are distinguishable in the luminescence spectrum. The intensity of the luminescence of ytterbium increased by a factor of 1000 in comparison with the unannealed samples. The highest luminescence intensity of ytterbium was detected for the $Ca_{0.9495}Yb_{0.0500}Pr_{0.0005}F_{2.0505}$.

1. Introduction

Solar energy is one of the most abundant energy sources [1,2] and crystalline silicon solar panels became a quite traditional tool for its utilization. The use of silicon has its major advantage in its chemical availability, as well as well-developed manufacturing and recycling technology, including recycling of the rare-earth-containing components. Other solar panels, such as GaAs, CdTe, Cu(In,Ga)Se$_2$ multiple layer devices, can also be utilized for the solar energy conversion [1], but their manufacturing and recycling is more complicated and expensive due to their toxicity. In other words, the use of GaAs, CdTe, and/or Cu(In,Ga)Se$_2$ doesn't obey "green chemistry" principles. Unfortunately, silicon solar panels possess relatively low coefficients for converting solar power to electric energy (under 25 % even for the best samples [1,2]). This is why silicon solar cells are frequently modified by luminescent coatings. These phosphor films can transform solar energy from the spectral region of photon nonsusceptibility (ultra-violet and visible range) of crystalline silicon solar cells to the region of their photoresponse (infra-red range).

Down-conversion luminescence, especially quantum cutting mechanism is one of the promising pathways of increasing crystalline silicon solar cell efficiency [1,3]. Quantum cutting allows for splitting each energy UV photon to two infra-red photons [4]. When Pr is excited at a wavelength of 185 nm, a quantum conversion efficiency of more than 100 % was obtained.

Later publications concerning down-conversion phenomenon also demonstrated quantum yields of more than 100 % for several materials [1].

Fluorite-type solid solutions $M_{1-x}R_xF_{2+x}$ (M = Ca, Sr, Ba, R – rare earth) exists in all MF$_2$-RF$_3$ systems [5]. Single-phase solid solutions in the systems $Ca_{1-x}R_xF_{2+x}$ are formed up to x = 0.2 [6], $Sr_{1-x}R_xF_{2+x}$ x = 0.6 [7]. For systems based on BaF$_2$-RF$_3$, single-phase solid solutions with low dopant content cannot be synthesized [8–10]. Effective up- and down-conversion luminescence is carried out through the interaction of the cations introduced in the matrix. Calcium fluoride matrix possesses certain technological advantages, for it has crystal lattice parameters close to that of silicon, so CaF$_2$-based films can easier be attached to silicon substrates by epitaxy [11–13].

Thus it is of great interest to study CaF$_2$ matrix with Pr^{3+}-Yb^{3+} ions pair doped due to the existence of resonant transitions $^3P_0-^1G_4$ of Pr^{3+} and $^2F_{7/2} - ^2F_{5/2}$-transitions of Yb^{3+} ions [14] which is promising for quantum cutting by means of energy transfer from Pr^{3+} ions to Yb^{3+} ions. Therefore, the goal of the present study was the investigation of chemical and physical properties of $Ca_{1-x-y}Yb_xPr_yF_{2+x+y}$ solid solutions for determining the chemical compositions suitable for increasing the efficiency of crystalline silicon solar panels.

2. Experimental

We used 99.99 wt% pure ytterbium and praseodymium nitrate hexahydrates, calcium nitrate tetrahydrate (all reagents were manufactured by LANHIT, Russia), 99.99 wt% pure 46–49 wt% aqueous hydrogen fluoride (SigmaTec, Russia) and double distilled water as the starting materials, without further purification. Fluorite-type CaF_2:Yb:Pr solid solution precipitates were synthesized according to our previously published protocol [15]. 0.5 M calcium, praseodymium, ytterbium nitrate aqueous solutions were added dropwise to the two-fold excess of 5.0 M aqueous HF under vigorous magnetic stirring. The process of co-precipitation is based on the fact that the solubility of alkaline-earth and rare-earth fluorides in water is low (about 10^{-5}-10^{-4} M) [16,17]. After CaF_2:Yb:Pr precipitate was formed, the mother solution was decanted. Precipitates formed were washed with double distilled water until negative nitrate anion test with diphenylamine. This qualitative reaction is based on the oxidation of diphenylamine, which has a sensitivity to nitrate ions. Colorless diphenyl benzidine is first formed, which upon further oxidation is converted into a diphenyl benzidine quinoid derivative having a blue color. Obtained powders were dried in air at 45 °C for 5 hours and annealed in platinum crucibles (also in air) at 600 °C for 1 hour.

All samples were analyzed using a Bruker D8 Advanced (Cu Kα radiation) diffractometer. Particle sizes and morphology were determined by a Carl Zeiss NVision 40 scanning electron microscope. Differential thermal analysis (DTA) and differential thermal gravimetric analysis (DTG) was performed on a MOM Q-1500 D derivato-graph with platinum crucible on air (rate of heating/cooling - 10 degrees/min). Fluorescence of the samples was excited by a 443 nm cw laser diode with a pumping power density of 152.8 W/cm^2. The luminescence spectra were recorded with Stellarnet EPP 2000 spectrometer using a 5 mm filter (ZhS-16) and corrected for the spectral sensitivity of spectrometer. The luminescence kinetics were registered with the use of scanning monochromator with 600 l/mm diffraction grating and under pulsed excitation with 444 nm laser light from OPO system Lotis TII LT2211. The luminescence light was converted by photomultiplier tube FEU62 and digitalized by BORDO oscilloscope.

3. Results

Typical X-ray diffraction pattern of CaF_2:Yb:Pr unannealing sample is presented in Fig. 1a. All observed reflections are in a good agreement with JCPDS Card #77-2245 data, i.e., XRD results confirmed that synthesized samples contain only one fluorite-type phase. According to our previous experimental data for similar samples, the luminescence intensity of unannealed samples was low. One of the main reasons for this is the presence of hydroxyl anions in the crystal lattice, which result in quenching of luminescence. We chose the annealing temperature based on DTA/DTG study (Fig. 2). It's clear, that the dehydration proceeds in several stages and finishes at about 500–550 °C. Weight loss upon was 3.7 wt%. Based on this we chose the 600 °C and 1 hour as annealing conditions. Fig. 1b represents XRD data for annealed sample. Lines in the X-ray pattern of the sample dried at 45 °C (Fig. 1a), were much broader than the lines for the sample annealed at 600 °C (Fig. 1b). Annealing leads to an increased crystallite size. We calculated the unit cell parameters for the samples before and after annealing (Table 1). Annealing at 600 °C resulted in an anticipated small decrease in the unit cell parameter value in comparison with the data for the same composition samples dried at 45 °C: see also [18] for the similar dehydration effect studies. The weight loss upon for dehydration in Table 1 and in TG data in DTA/DTG study were similar.

Typical scanning electron microscopy (SEM) images of the samples dried at 45 °C are presented in Fig. 3a,b,c. SEM results confirm that particle sizes vary from 20 nm to 80 nm (average particle size is about 35 nm). Fig. 3b presents SEM image taken in EBSD regime, which allow for atomic contrast regime. The uniform color of the image on Fig. 3b confirms the single phase composition of the powders. Annealing at 600 °C caused the increase in the particle sizes up to ∼150–200 nm (Fig. 3d,e). Evaluation of chemical composition based on EDX analysis is summarized in Table 2. The content of praseodymium in the solid solutions is close to it's nominal content in initial aqueous solution. The content of ytterbium fluoride in solid solutions is somewhat higher than in aqueous solution. The EDX composition determination error is 0.5 mol.%. This means that the concentration of praseodymium in the samples may also be greater than in the case of ytterbium. The mean value of ytterbium distribution coefficient between solid and aqueous phases is about 1.45. This means that the crystallization proceeds in an incongruent manner.

Characteristic luminescence spectra of the samples before and after annealing are presented in Fig. 4a. The luminescence intensity of the unannealed sample appeared to be very low as it has been predicted and intensity of Yb^{3+} luminescence at the wavelengths around 1 micrometer was almost at the level of noise. In the visible spectral range, we have registered broad luminescence band located in the region of praseodymium luminescence. After annealing/dehydration stage, the luminescence spectra have changed. In the visible spectral range, characteristic
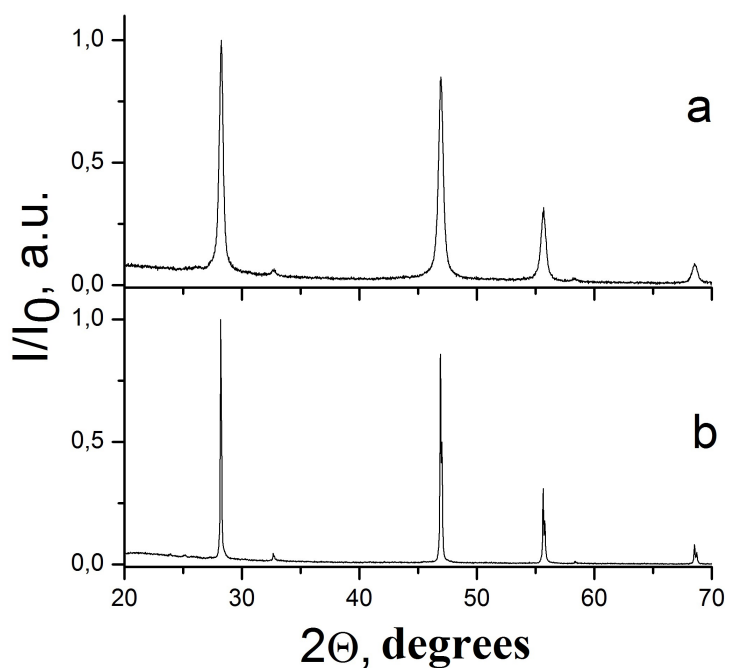
FIG. 1. XRD patterns of CaF$_2$:Yb (5.0mol%):Pr (0.1 mol%) powder: dried at 45 °C (a), and annealed at 600 °C (b)

TABLE 1. XRD results for CaF$_2$:Yb:Pr solid solutions

No*	Nominal doping Pr/Yb, mol. %	After drying at 45 °C	After annealing at 600 °C	Weight loss upon, wt.%
		a, Å	a, Å	
1	0.01/7.0	5.4757(7)	5.4700(6)	4.5
2	0.01/10.0	5.463(2)	5.460(3)	3.8
3	0.01/12.0	5.4799(4)	5.4774(4)	4.2
4	0.05/5.0	5.461(2)	5.464(1)	4.3
5	0.05/7.0	5.476(1)	5.4694(7)	4.1
6	0.05/10	5.4741(8)	5.47643(8)	4.7
7	0.05/12.0	5.4757(7)	5.472(1)	4.1
8	0.05/20.0	5.4826(7)	5.4850(8)	4.8
9	0.1/1	5.460(2)	5.4627(2)	5.7
10	0,1/5	5.4747(3)	5.4737(6)	5.6
11	0.1/10	5.490(2)	5.4759(4)	5.5
12	0.1/20	5.4802(9)	5.481(1)	4.9
13	1/5	5.475(1)	5.469(1)	5.6
14	1/10	5.4731(5)	5.4804(3)	2.7

* – The sample labeling used in Table 1 is maintained across the whole paper for the reader's convenience.
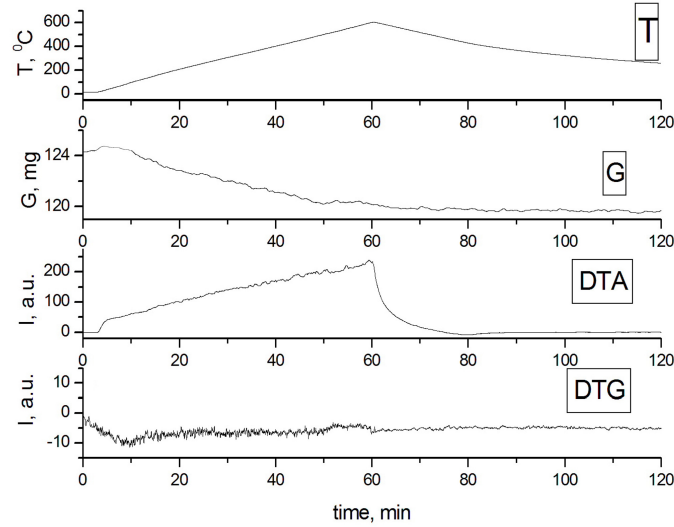
FIG. 2. DTA/DTG analysis of CaF$_2$:Yb(7.0 mol.%):Pr(0.01 mol.%) precipitate. T – temperature, G – weight, DTA – differential thermal analysis, DTG – differential thermal gravimetry. The weights at annealing was 3.7 wt.%

TABLE 2. EDX results for CaF$_2$:Yb:Pr samples

Sample number – temperature of drying	Pr/Yb, mol.%		The effective praseodymium/ytterbium distribution coefficient
	Nominal doping	Doping based on EDX	
10–45	0.1/5.0	*/6.8	–/1.36
10–600	0.1/10.0	*/7.1	–/1.42
11–600	0.1/10.0	*/15.5	–/1.55
13–45	1.0/5.0	1.1/7.9	1.1/1.58
14–45	1.0/10.0	1.1/14.9	1.1/1.49

* The content of praseodymium is below the limit of reliable determination.

spectral lines of praseodymium ions have been resolved which agree with literature data [19] and consistent with data for other fluoride systems containing Pr^{3+} [20–22]. These lines correspond to numerous transitions from ^{3}P$_J$ manifold to ^{3}H$_J$ and ^{3}F$_J$ manifolds. The intensity of ytterbium luminescence at around 1-micrometer spectral range has increased one thousand fold. It means that annealing stage is an efficient tool for dehydration and increasing of ytterbium luminescence.

Luminescence spectra for series of annealed samples with different Pr^{3+} and Yb^{3+} ions content have been investigated. Characteristic spectra are presented in Fig. 4b. The inset shows luminescence lines in visible spectral range in enlarged intensity scale. The known Pr^{3+} ion luminescence lines are registered in the visible spectral range. The intense luminescence within 900–1100 nm range corresponding to ^{2}F$_{5/2}-^2$F$_{7/2}$ transitions of Yb^{3+} ions was detected. This indicates a successful transfer of excitation energy from praseodymium to ytterbium. Intense luminescence of ytterbium at $\lambda = 1~\mu$m overlaps the photosensitivity region of crystalline silicon solar cells [1, 3]. We observe a decrease of Pr^{3+} luminescence intensity with higher Yb^{3+} content for samples with low levels of Pr^{3+} doping which proves down-conversion approach for the selected ions pair. This also indicates the applicability of this approach to increase the efficiency of solar cells. At the same time, the decrease of shorter wavelength peak of Yb^{3+} luminescence is observed with the increase of Yb^{3+} content, which speaks about reabsorption process.

Unfortunately, the effort to increase the down-conversion yield by an increase of Pr^{3+} ion content does not yield positive results. In Fig. 5a one can see that luminescence lines intensity of Pr^{3+} ions increase while the
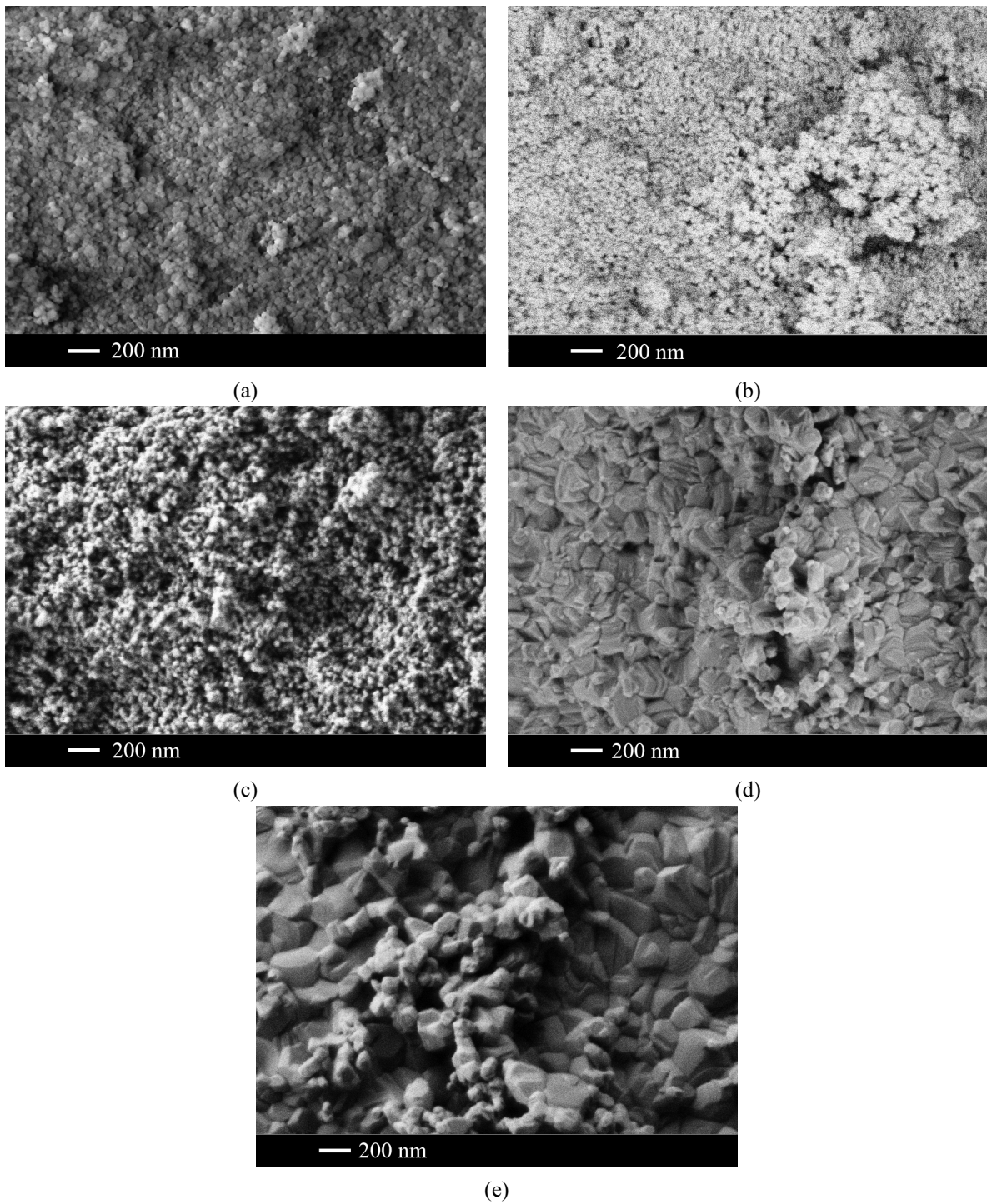
FIG. 3. (a) SEM image of sample 10 after drying at 45 °C. (b) SEM image (EBSD regime) of sample 13 after drying at 45 °C. (c) SEM image of sample 14 after drying at 45 °C. (d) SEM image of sample 10 after annealing at 600 °C. (e) SEM image of sample 11 after annealing at 600 °C.
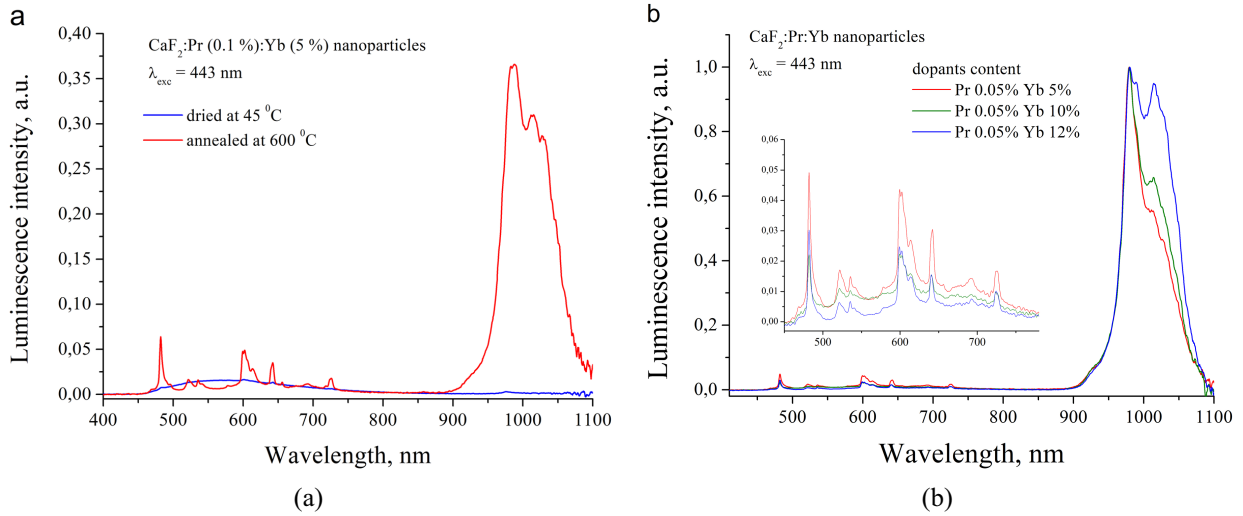
FIG. 4. Luminescence spectra for sample of CaF_2 with Pr^{3+} (0.1 %) and Yb (5 %) before and after annealing (a), luminescence of a series of CaF_2:Pr:Yb samples annealed at 600 °C (b)

intensity of Yb^{3+} ions drops for samples with 5 % of Yb^{3+} when increasing the Pr^{3+} content from 0.05 % to 1 %. Apparently, we have the opposing process of radiationless decay of Yb^{3+} ions excited state.

In order to clarify this, we have studied the Yb^{3+} luminescence decay kinetics in the series of samples with constant Yb^{3+} content and varying Pr^{3+} content. In the Fig. 5b luminescence decay curves of Yb^{3+} detected at 978 nm are presented. It is clearly seen that Yb^{3+} luminescence lifetime drops with increased Pr^{3+} ion content.
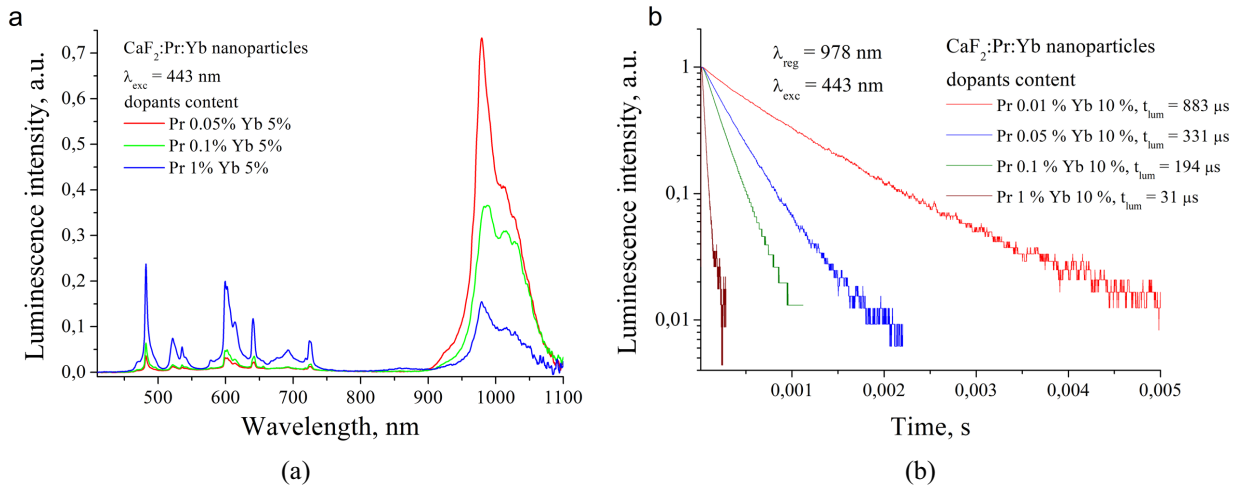
FIG. 5. Luminescence spectra (a) and Yb^{3+} luminescence decay (b) for samples of CaF_2 with constant Yb^{3+} content (10 %) and various Pr^{3+} content

Apparently, this quenching occurs due to close location of $^2F_{5/2}$ and $^1G_4$ manifolds for Yb^{3+} and Pr^{3+} ions respectively in the band gap of CaF_2 matrix which provides energy transfer from Yb^{3+} to Pr^{3+} ions. This process brings more restrictions to search for optimal Yb and Pr ions composition in CaF_2 for means of efficient down-conversion. The highest level of luminescence intensity among all the studied samples was observed for the composition CaF_2:Pr (0.05 mol.%):Yb (5.0 mol.%).

4. Conclusions

Single-phase precipitates with an average particle size of about 35 nm were formed upon precipitation of $Ca_{1-x-y}Yb_xPr_yF_{2+x+y}$ solid solutions from the corresponding aqueous nitrate solutions. Crystallization of fluoride phases proceeds according to the incongruent mechanism. The mean value of the ytterbium distribution coefficient

was about 1.45. These samples dried at 45 °C had weak luminescence intensities. The annealing step for dehydration was found to be necessary for intensity luminescence increasing. According to DTA/DTG study, the temperature of annealing must be higher than 550 °C. The annealing conditions chosen for further study were 600 °C, 1 hour. After annealing, the particle size increased up to 150–200 nm. Individual luminescence bands of praseodymium are distinguishable in the luminescence spectrum. The intensity of the luminescence of ytterbium increased by 1000-fold. At the same time, we have observed the quenching of Yb^{3+} ions luminescence at high levels of Pr^{3+} content apparently due to energy transfer from $^2F_{5/2}$ manifold of Yb^{3+} to $^1G_4$ manifold of Pr^{3+} ion. The highest luminescence intensity of ytterbium was determined for a $Ca_{0.9495}Yb_{0.0500}Pr_{0.0005}F_{2.0505}$ solid solution. This composition is substantial interest for further experiments aimed at the creation of luminescent coatings on crystalline silicon designed to increase the efficiency of solar panels.

Acknowledgements

References

[1] Huang X., Han S., Huang W., Liu X. Enhancing solar cell efficiency: the search for luminescent materials as spectral converters. *Chem. Soc. Rev.*, 2013, **42**, P. 173–201.

[2] Green M.A., Bremner S.P. Energy conversion approaches and materials for high-efficiency photovoltaics. *Nature Mater.*, 2017, **16**, P. 23–34.

[3] Richardson B.S. Enhancing the performance of silicon solar cells via the application of passive luminescence conversion layers. *Solar Energy Materials & Solar Cells*, 2006, **90**, P. 2329–2337.

[4] Piper W.W., DeLuca J.A., Ham F.S. Cascade fluorescent decay in Pr^{3+}-doped fluorides: Achievement of a quantum yield greater than unity for emission of visible light. *J. Lumin.*, 1974, **8**, P. 344–348.

[5] Sobolev B.P. *The Rare Earth Trifluorides. Part 1. The High Temperature Chemistry of the Rare Earth Trifluorides*. Institut d'Estudis Catalans, Barcelona, Spain, 2000, 520 pp.

[6] Fedorov P.P., Mayakova M.N., Kuznetsov S.V., et. al. Synthesis of CaF_2-YF_3 nanopowders by co-precipitation from aqueos solutions. *Nanosystems: Physics, Chemistry, Mathematics*, 2017, **8**(4), P. 462–470.

[7] Mayakova M.N., Luginina A.A., Kuznetsov S.V., et. al. Synthesis of SrF_2-YF_3 nanopowders by co-precipitation from aqueous solutions. *Mendeleev Communications*, 2014, **24**(6), P. 360–362.

[8] Kuznetsov S.V., Fedorov P.P., Voronov V.V., et. al. Synthesis of $Ba_4R_3F_{17}$ (R stands for Rare-Earth Elements) Powders and Transparent Compacts on Their Base. *Rus. J. Inorg. Chem.*, 2010, **55**(4), P. 484–493.

[9] Fedorov P.P., Mayakova M.N., Kuznetzov S.V., et. al. Co-precipitation of yttrium and barium fluorides from aqueous solutions. *Materials Research Bulletin*, 2012, **47**, P. 1794–1799.

[10] Karbowiak M., Cichos J. Does $BaYF_5$ nanocrystal exist? – The BF_2-YF_3 solid solution revisited using photoluminescence spectroscopy. *J. Alloy Compd.*, 2016, **673**, P. 258–264.

[11] ElFajri A., Moussetad M., Tardy P., Barriere A.S. Electrical study of Pr^{3+} ion environment in $Ca_{1-x}Pr_xF_{2+x}$ thin films. *Phys. Status solidi (a)*, 2000, **179**, P. 373–386.

[12] Sokolov N.S., Suturin S.M. MBE growth of calcium and cadmium fluoride nanostructures on silicon. *Appl. Surf. Sci.*, 2002, **175–176**, P. 619–628.

[13] Blunier S., Zogg H., Maissen C., et. al. Lattice and thermal misfit dislocation in epitaxial CaF_2/Si(111) and BaF_2-CaF_2/Si(111) structures. *Phys. Rev. Lett.*, 1992, **68**(24), P. 3599–3602.

[14] Yagoub M.Y.A., Swart H.C., Coetsee E. Concentration quenching, surface and spectral analyses of SrF_2:Pr^{3+} prepared by different synthesis techniques. *Opt. Mater.*, 2015, **42**, P. 204–209.

[15] Fedorov P.P., Mayakova M.N., Kuznetsov S.V., Voronov V.V. Low temperature phase formation in the CaF_2–HoF_3 system. *Russ. J. Inorg. Chem.*, 2017, **62**(9), P. 1173–1176.

[16] Batsanova L.R. Rare-earth fluorides. *Rus. Chem. Rev.*, 1971, **40**(6), P. 465–484.

[17] *Gmelin Handbuch der anorganischen Chemie. Syst. Nummer 39: Seltenerdelemente. Teil C.3: Sc, Y, La und Lanthanide. Fluoride, Oxifluoride und zugehogige Alkalidoppelverbindungen.* Berlin, Springer Vlg., 1976, 439 pp.

[18] Rozhnova Yu.A., Kuznetsov S.V., Luginina A.A., et. al., New $Sr_{1-x-y}R_x(NH_4)_yF_{2+x-y}$ (R = Yb, Er) solid solution as precursor for high efficiency up-conversion luminophor and optical ceramics on the base of strontium fluoride. *Mater. Chem. Phys.*, 2016, **172**, P. 150–157.

[19] Dieke G.H., Crosswhite H.M. The spectra of the doubly and triply ionized rare earths. *Appl. Opt.*, 1963, **2**, P. 675–686.

[20] Kuzmanoski A., Pankratov V., Feldmann C. Energy transfer of the quantum-cutter couple Pr^{3+}–Mn^{2+} in CaF_2:Pr^{3+},Mn^{2+} nanoparticles. *J. Lumin.*, 2016, **179**, P. 555–561.

[21] Meijerink A., Wegh R., Vergeer P., Vlugt T. Photon management with lanthanides. *Opt. Mater.*, 2006, **28**, P. 575–581.

[22] Pudovkin M.S., Morozov O.A., Pavlov V.V., Korableva S.L., Lukinova E.V., Osin Y.N., Evtugyn V.G., Safiullin R.A., Semashko V.V. Physical Background for Luminescence Thermometry Sensors Based on Pr^{3+}:LaF_3 Crystalline Particles. *J. Nanomaterials*, 2017, Article No 3108586.

The microstructure effect on the Au/TiO$_2$ and Ag/TiO$_2$ nanocomposites photocatalytic activity

D. A. Kozlov[1], V. A. Lebedev[1,2], A. Yu. Polyakov[1], K. M. Khazova[1], A. V. Garshev[1,2,3]

[1]Faculty of Materials Science, Lomonosov Moscow State University, 1-73 Leninskiye gory, Moscow, 119991, Russia

[2]Faculty of Chemistry, Lomonosov Moscow State University, 1-3 Leninskiye gory, Moscow, 119991, Russia

[3]Baikov Institute of Metallurgy and Material Science RAS, 49 Leninskiy prospekt, Moscow, 119334, Russia

kozlov@inorg.chem.msu.ru, vasya_lebedev@mail.ru, a.yu.polyakov@gmail.com, khazovakm@gmail.com, garshev@inorg.chem.msu.ru

In this work the systematic study of the Au/TiO$_2$ and Ag/TiO$_2$ nanocomposites was evaluated. Aeroxide P25 preparation was taken as a titania precusor. Composites were obtained using different wet chemistry techniques: impregnation by previously prepared nanoparticles(NPs) sols, *in-situ* reduction by sodium borohydride, sodium citrate and UV irradiation. The varying of the synthesis method due to the reduction rate differences results in the different interaction between metal NPs and titanium dioxide, and hence different metal/TiO$_2$ contacts were observed. All the obtained samples were analyzed by XRD, TRS, SEM with EDX and TEM with EDX. According to the statistical analysis of the TEM images the correlation between the metal NPs rate formation and their anisotropy was shown, which may allow us to consider the anisotropy as a descriptor of the contact quality. Combining the results of the optical spectroscopy with the NPs TEM statistical analysis, we confirmed the correlation between observable anisotropy and the contact quality. Finally, the effect of the synthesis method on the photocatalytic activity (PCA) of nanocomposites was shown. Since the work functions of Au and Ag differ, the opposite effects on PCA are expected. Thus, in the case of the Au/TiO$_2$ nanocomposites, the positive effect associated with NPs anisotropy on the PCA was demonstrated. Alternatively, in the case of the Ag/TiO$_2$ nanocomposites the PCA evolution was detected only in the case of small NPs formation.

Keywords: photocatalysis, titania, nanocomposites, TiO$_2$, gold nanoparticles, silver nanoparticles, anisotropy.

Received: 24 January 2018

Revised: 5 February 2018

1. Introduction

Currently, photocatalysis is widely used in numerous light-driven technologies, *e.g.* for water purification [1], waste degradation [2–4], water splitting [5] and CO$_2$ reduction [6]. TiO$_2$-based materials are one of the most popular photocatalysts, demonstrating high PCA due to required energy bands positions and an acceptable band gap of 3.2 eV, which corresponds to the near UV range [7]. However, the effective wavelength range for the photocatalysis mediated by pure TiO$_2$ is limited by UV. PCA of titania-based materials in the visible range can be improved by increasing their absorbance at 400–700 nm wavelengths [8]. For this, the morphology and structure of photocatalyst can be modified by the introduction of dopant additives [9] or accurate (and rather complicated) tuning of the shape of titania NPs [10, 11]. At the same time, large-tonnage production of commercial TiO$_2$ catalysts, such as Aeroxide P25, is based on the pyrolysis of titanium compounds [12, 13]. Therefore, post-processing modification of TiO$_2$ NPs is more economically feasible for production of visible-range photocatalysts. Such methods include design of the contact titania with other materials, *e.g.* metal and semiconductor NPs, carbon-based materials, dye molecules. The main disadvantage of the carbon-modified titania is a significant shading and loading of the photocatalyst surface, since optimal carbon materials addition is usually 20–30% that can affect on the absorption ability [8]. Dye-sensitized titania is widely applied for the solar cells [14], but suffers significantly from the photocatalytic dye degradation.

Loading of the titania surface with semiconductor NPs results in a visible-light induced PCA and increases the total (UV and visible) PCA in the case of II-type heterojunction formation. As demonstrated in our earlier article [15], the PCA of nanocomposite based on Aeroxide P25 and WO$_3$·H$_2$O was increased by *ca.* 30% higher in comparison with the pristine Aeroxide P25. Similarly, Han et al. [16] reported PCA increasing upon loading TiO$_2$ with semiconductor Cu$_2$O NPs However, modification of titania with metal NPs (such as Ag, Au, Pd, Pt, Cu) is known to be much more effective for achievement of PCA in visible range [17–19].

The formation of the Schottky contact between the metal and semiconductor components of the nanocomposite may increase PCA due to an interparticle charge carriers transfer [20] leading to the spatial separation and, hence, longer lifetimes of photogenerated nonequilibrium electrons and holes. The ohmic contact formation does not result in the charge carriers separation, and hence increase of the PCA is not expected. Moreover, there are few possible mechanisms [21] of energy transfer from plasmonic NPs to the semiconductor, which beneficially effects PCA. According to the work functions of bulk gold and anatase, which are 5.23 eV [22] and 5.10 eV [23] respectively, we can expect Schottky contact formation in this case, whereas Ag/TiO$_2$ contact should be ohmic due to work function of silver, which is 4.25–4.37 eV [24]. Based on the bulk materials band structure, the principal scheme of the Au/TiO$_2$ and Ag/TiO$_2$ contacts are presented on the Fig. 1.
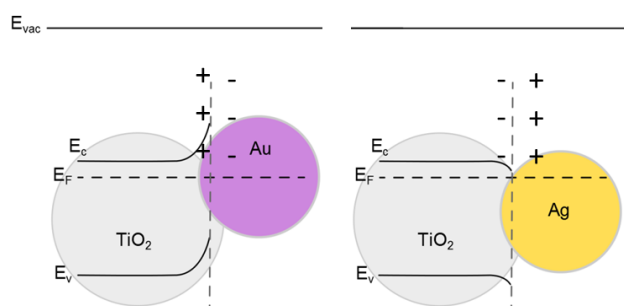
FIG. 1. Principial scheme Au/TiO$_2$ and Ag/TiO$_2$ contacts structures based on the bulk materials work functions

At the same time, many authors declared the positive effect of silver NPs on the PCA of titanium dioxide. Some recent reports addressing the Ag NPs effect on the PCA of TiO$_2$ are summarized in the Table 1. It should be noted that a significant increase (1.5–2 times) is observed mainly for the <10 nm NPs. Alternatively, in the case of larger NPs, the nanocomposites demonstrated decreased PCA. This observation can be explained by a significant increase of Fermi level in silver NPs, which was confirmed elsewhere [25] by Kelvin probe microscopy of gold and silver NPs. Similar size effect was observed by Cozzoli et al. [26], namely the PCA increase was associated with the charge carriers separation observed only in the case of 8-10 nm silver NPs. The measurements of the equilibrium potential of irradiated Au/TiO$_2$ nanocomposites reported by Subramanian et al. [27] revealed a size-related shift of Fermi level in Au NPs. The greater shift of the Fermi level was observed in smaller Au NPs (20 mV for 8 nm diameter, 40 mV for 5 nm and 60 mV for 3 nm Au NPs) and caused the increase of PCA.

The shape and size variations primarily effect on the optical properties of plasmonic NPs due to the changes of the surface plasmon resonance (SPR) parameters. Particullary, red shift of the SPR wavelength was observed upon increasing the diameter of gold nanospheres [42]. Eustis et al. [43] showed that the increase of the aspect ratio of anisotropic elliptical gold particles also leads to an increased SPR wavelength. A number of methods were developed for mathematical simulation of light scattering and absorption by plasmonic NPs, *e.g.* Discrete Dipole Approximation (DDA), Finite Element Methods (FEM). Several analytical methods (Mie theory, quasistatic theory) [44] were also reported. Kelly et al. [45] used DDA and analytical methods to calculate theoretically the effect of different factors (size, medium permittivity, aspect ratio) affecting the SPR peak position. Therefore, the red shift of the SPR peak position can be caused by increasing of the NPs diameter, aspect ratio, refractive index of the medium, whereas blue shift may be caused by snipping of the non-spherical particles.

As shown above, the effect of plasmonic NPs size on PCA of TiO$_2$ is studied rather well. At the same time, the impact of the contact between Au or Ag and TiO$_2$ counterparts has insufficient experimental confirmation. Here we employed different synthesis techniques, namely impregnation with pre-synthesized NPs, reduction of Ag$^+$ and AuCl$_4^-$ ions with sodium borohydride (rapid reaction), as well as sodium citrate and UV irradiation (slower reactions) to produce the series of Au/TiO$_2$ and Ag/TiO$_2$ nanocomposites. We used TEM to characterize the NPs morphology and to estimate the shape anisotropy which was chosen as a simplified descriptor of the contact quality. These data were compared with the measured and simulated UV-visible-NIR absorption spectra of the nanocomposites. The composition and structure of the nanocomposites was also studied by XRD, SEM-EDX and STEM-EDX. Finally, we discussed the impact of plasmonic NPs morphology (effective size, shape anisotropy) and their contact with TiO$_2$ on the PCA of the designed nanocomposites.

TABLE 1. The articles review data of the metal nanoparticles size effect on the PCA of Ag/TiO$_2$ nanocomposite

Ag NPs size	Method of PCA measurement*	Relative increase of PCA	Ref
1–2 nm	MO Photodegradation	1.15	[28]
1.5–2 nm	Phenol photodegradation	1.5	[29]
2 nm	Photodegradation of acetone	1–1.2	[30]
2–4 nm	RhB Photodegradation	1.5	[31]
3 nm	MB Photodegradation	3.7	[19]
3 nm	Photodegradation of Safranin-O	1.6	[32]
3–5 nm	Photodegradation pentachlorophenol	2	[33]
5 nm	MB Photodegradation	2.8	[19]
5 nm	MB Photodegradation	Visible light irradiation	[34]
7 nm	Selective oxidation of benzyl alcohol	2	[35]
7 nm	RhB Photodegradation	2	[36]
8 nm	MB Photodegradation	2	[19]
9 nm	MO Photodegradation	1.2	[37]
7–10 nm	MB Photodegradation	1.1	[38]
10 nm	Catalytic oxidation of benzene	None	[39]
20 nm	MO Photodegradation	1.5	[40]
24 nm	RhB Photodegradation	Visible light irradiation	[41]

*MB — Methylene Blue, MO — Methyl Orange, RhB — Rhodamine B

2. Simulation

To determine the SPR peak position position in the media with different permittivity, we calculated the dependence of the extinction cross sections on the wavelength for gold and silver NPs with a diameter of 20 nm. The calculation was provided by the Mie theory:

$$\sigma(\lambda) = \frac{24\pi^2 a^3 \sqrt{\varepsilon_m^3(\lambda)}}{\lambda \ln 10} \cdot \left[\frac{\varepsilon_i(\lambda)}{(\varepsilon_r(\lambda) + 2\varepsilon_m(\lambda))^2 + \varepsilon_i(\lambda)^2} \right], \tag{1}$$

where a — a particle size, $\varepsilon_i(\lambda)$ and $\varepsilon_r(\lambda)$ — imaginary and real parts of the NPs material permittivity as a function of a wavelength, and $\varepsilon_m(\lambda)$ — a permittivity of the medium.

The DDA modelling were performed using the DDSCAT software [46]. Values of the real and imaginary parts of the complex dielectric permittivity of gold and silver were taken from the article [47] in the both cases. Size of model particle was chosen at least of 30000 dipoles. Effective size was recalculated as $a_{eff} = \frac{1}{2} \cdot d_{eff}$. To reduce the angular dependency, for each λ, d_{eff} nine target orientations were averaged for two incident polarizations.

3. Experimental

3.1. Synthesis

3.1.1. Reduction with sodium borohydride. Aqueous solutions of gold or silver precursors (HAuCl$_4$ or AgNO$_3$, respectively) were added to reach the metal amount of 5% w.p. in the final nanocomposite. The pH value was adjusted by drop-wise addition of $2M$ NaOH or HNO$_3$ solutions and was measured by ESK 10601/7 electrode, filled with NH$_4$NO$_3$ solution to prevent the seepage of chlorine ions to the mixture. Samples were obtained only in the acidic media (pH 2–6) due to oxide and hydroxide precipitation possibility in the case of silver and basic reduction in the case of gold [48]. After the pH adjustment, suspension was stirred for the 30 min, and then a fresh ice-cold NaBH$_4$ solution was added with 30% molar excess relative to the metal ions concentration. The principial reactions may be written as follows:

$$Ag^+ + BH_4^- + 4H_2O \rightarrow B(OH)_4^- + 3.5H_2 \uparrow + H^+ + Ag, \tag{2}$$

$$AuCl_4^- + BH_4^- + 4H_2O \rightarrow B(OH)_4^- + 2.5H_2 \uparrow + 3H^+ + 4Cl^- + Au. \tag{3}$$
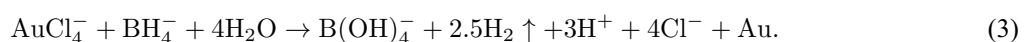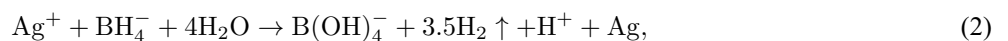
The side process of sodium borohydride hydrolysis may be described as follows [49]:

$$BH_4^- + 4H_2O \rightarrow B(OH)_4^- + 4H_2 \uparrow. \tag{4}$$
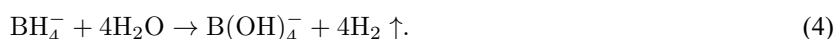
In the case of $AuCl_4^-$ reduction, the solution color was changed from light-yellow to dark red-wine over 3–5 min. This corresponds to the relatively rapid formation of gold NPs. In the case of Ag^+ reduction, the colorless solution becomes yellowish brown in a similar timeframe as in the case of gold. The obtained products were separated by centrifugation (8000 rpm, 15 min), and triple rinsed with the DW (160 ml each time). The final precipitate was dried at 80°C during 12 h. It should be noted, that rinse water was colorless, and the absence of observable concentration of metal NPs in the rinse water is the evidence of the nanocomposite formation. Samples obtained using this method were labelled as Au/TiO$_2$ (b) and Ag/TiO$_2$ (b).

3.1.2. Reduction with sodium citrate. Syntheses utilizing sodium citrate as a reducing agent were evaluated by the similar method: DW solution of sodium citrate was added to the titania aqueous suspension with the metal precursor. During the reduction process temperature was maintained at 90°C to increase the reaction rate. The ratio of metal ions and sodium citrate was about 1:9. In the case of gold NPs formation, it took about 20 min to change color of the reaction solution from yellow to light violet. In the case of silver NPs formation the reaction was carried out for 6 h and the color of reaction mixture was changed from colorless to dark brown. The principal reactions of the metal ions reduction by the citrate anions may be written as follows [50–52]:

$$2Ag^+ + C_6H_5O_7^{3-} \rightarrow C_5H_4O_5^{2-} + CO_2 \uparrow + H^+ + 2Ag, \tag{5}$$

$$2AuCl_4^- + 3C_6H_5O_7^{3-} \rightarrow 3C_5H_4O_5^{2-} + 3CO_2 \uparrow + 3H^+ + 8Cl^- + 2Au. \tag{6}$$
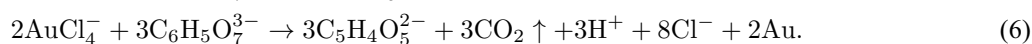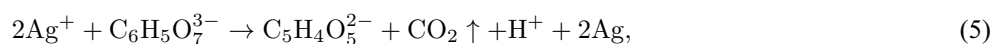
The obtained products were separated, washed and dried under same conditions. The rinse water was colorless as well as in the case of reduction by borohydride. Samples obtained using this method were labelled as Au/TiO$_2$ (cit) and Ag/TiO$_2$ (cit).

3.1.3. Reduction with UV light. To functionalize titania with metal NPs under UV light, an aqueous suspension of titania, included 20 mg titania powder with 100 ml of metal precursor solution (concentration corresponded to 5% w.p. of metal in the final product), was irradiated by the UV lamp MADIX Y1207 (electric power 20 W) under a vigorous stirring. In the case of Ag/TiO$_2$ nanocomposites, the suspension was irradiated for 20 min, whereas in the case of Au/TiO$_2$, the reaction could be as long as 3 h. The completion of reaction was indicated by the finishing of the color changing. Then, samples were separated by the centrifugation, washed and dried under same conditions. Samples obtained using this method were labelled as Au/TiO$_2$ (UV) and Ag/TiO$_2$ (UV).

3.1.4. Reference samples. Au/TiO$_2$ and Ag/TiO$_2$ nanocomposites were also prepared by mixing of the titania suspension with previously prepared gold or silver NPs sols. Metals NPs sols syntheses were carried out at same condition as in the case of citrate reduction, but without the precence of titania. To obtained mixtures containing metal and semiconductor NPs were freezed using a liquid nitrogen and then freeze-dried by Labconco Freezone lyophilizer. Dried samples were washed with the centrifugation in DW water. Since rinse water after the sample precipitation was also colorless, we assume that non-redispersibility of NPs was caused by the formation of nanocomposite of metal NPs with titania. Samples obtained using this method were labelled as Au/TiO$_2$ (imp) and Ag/TiO$_2$ (imp).

3.2. Analysis

3.2.1. X-Ray Diffraction. Phase composition of the nanocomposites was investigated by the X-ray Diffraction (XRD) at $CuK_{\bar{\alpha}}$ radiation on the Rigaku D/MAX 2500 diffractometer with the rotating anode. X-Ray patterns were collected at the $10–90°2\theta$ range, $0.02°2\theta$ step, with 1 s acquisition in each point. To deconvolute titania, gold and silver peaks $30–50°2\theta$ range was investigated with the 10 s acquisition at each point. XRD profile analysis were performed using Jana2006 [53] software. The coherent scattering region (CSR) sizes d_{CSR} were calculated by the Sherrer equation.

3.2.2. ζ-potential measurement. ζ-potentials of the aqueous nanocomposite suspensions were measured using Zetasizer Nano ZS. Titania P25 suspension was adjusted to the required pH value (pH of 3–9 range) by the drop-wise addition of 2M HCl and NaOH solutions and then 1 ml of obtained suspension was transferred into the Malvern Instruments DTS1070 cell. Measurement was performed in the transmission geometry using standard 633 nm laser and 17° scattering measurement angle.

3.2.3. Total reflectance spectroscopy. The total reflectance spectra (TRS; both diffuse and specular reflectance) of synthesized nanocomposites were registered in UVvisible-NIR range using Lambda 950 (Perkin Elmer) spectrophotometer (wavelength range of 300–1000 nm, with 1 nm step). The spectra were collected using Spectralon-coated integrating sphere (150 mm diameter). The samples were placed to the reflectance port of the sphere. White Spectralon standard was used to collect 100% total reflectance reference. The registered TRS were recalculated to the absorbance using the standard software of the spectrophotometer.

3.2.4. Electron Microscopy. The Scanning Electron Microscopy (SEM) images and energy-dispersive X-ray spectra (EDX) were recorded on a Supra 50VP (Leo), equipped with EDX X-MAX 80 detector and INCA software (Oxford Instruments Inc.). Transmission Electron Microscopy (TEM) Bright Field (BF) images and the corresponding EDX maps were obtained on the Libra 200MC (Zeiss) microscope operating at 200 kV and equipped with EDX X-MAX 80T detector and the AZtec software (Oxford Instruments Inc.). The TEM images were analyzed with the Gwyddion software [54] to calculate the size and shape distributions of NPs. Observed NPs were approximated as elliptical particles, so the lengths of a and b pair axes for each ellipse were measured (see the scheme on Fig. 2).

(a) (b)
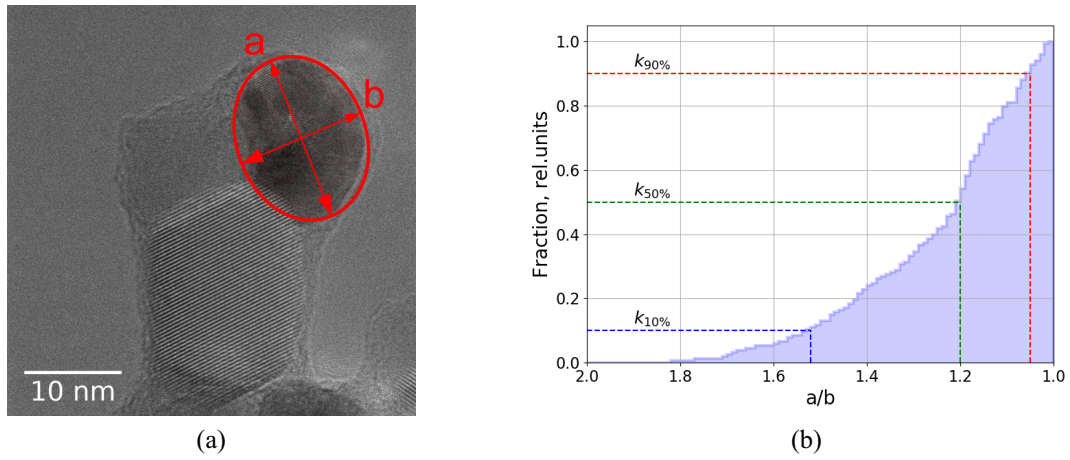
FIG. 2. (a) Au/TiO$_2$ (cit) TEM BF image with scheme of the particle size measurements, a and b — elliptical axes. (b) Normalized negative cumulative distribution

For each particle the effective size d_{eff} was calculated as a diameter of the sphere with the same volume:

$$d_{eff} = \sqrt[3]{a \cdot b^2}. \tag{7}$$

After that the d_{eff} distributions were calculated with the step of 1 nm using *scipy* and *Matplotlib* software [55, 56]. The parameters of Gauss fits for the obtained size distributions are presented in Table 2.

TABLE 2. Statistical parameters of the nanocomposites

Sample	CSR, nm	d_{eff},nm	ω_{eff}	k$_{90\%}$	k$_{50\%}$	k$_{10\%}$	λ_{SPR}
Au/TiO$_2$ (imp)	25	30	4	1.02	1.11	1.28	557
Au/TiO$_2$ (b)	7	11	6	1.01	1.12	1.33	544
Au/TiO$_2$ (cit)	17	22	7	1.04	1.17	1.37	537
Au/TiO$_2$ (UV)	15	17	5	1.03	1.16	1.43	550
Ag/TiO$_2$ (imp)	20	16	6	1.02	1.11	1.30	440
Ag/TiO$_2$ (b)	7	13	4	1.01	1.10	1.30	438
Ag/TiO$_2$ (cit)	14	20	11	1.05	1.20	1.52	447
Ag/TiO$_2$ (UV)	23	21	8	1.05	1.22	1.46	453

To reveals the observable anisotropy of metal NPs, the negative cumulative distribution of $k = a/b$ value was calculated with the step of 0.01. Based on this distribution, there were calculated the k_{10}, k_{50} and k_{90} values, which corresponds to the 10%, 50% and 90% amount of NPs with anisotropy higher than k.

3.3. PCA measurements

The photocatalytic activity of the samples was measured by the decolorization of a methyl orange (MO) dye solution. For that, 2–3 mg of the sample were dispersed in 8 ml of DW by the ultrasonic treatment and placed into the thermostated (40°C) AceGlass reactor. Part of measurements were repeated with the use of phosphate buffer (pH 6.9) instead of DW. The 7 ml of 0.3 mM MO solution was added after 10 minutes. The concentrations in the suspension was of 0.14 mM/l of MO and 130–200 mg/l of catalyst. After the next 10 min, the suspension was irradiated by 5W high pressure Hg lamp. The photocatalytic experiments were performed for 3 hours. During the experiment, the reaction mixture was pumped through Malvern Instruments DTS1070 cell, where the absorption spectra was acquired every 3 s using the xenon HRX-2000 lamp and Ocean Optics QE65000 spectrometer. The details of experimental setup and data processing are described in our previous articles [15,57]. In the work [57], we demonstrated, that in the case of this set up the obtained data of the MO decoloration corresponds to the oxidative photodegradation of MO. The initial titania (Aeroxide P25) was used as a reference in all the measurements. The PCA value PCA_S for the sample S was calculated from the MO decolorization rate r_S in the normalization on the sample weight m_S as follows:

$$PCA_S = \frac{r_S/m_S}{r_{P25}/m_{P25}} \cdot 100\%. \tag{8}$$

The value of r_{P25}/m_{P25} for the used setup was of 0.09 mg^{-1}·h^{-1} for the buffer solution and of 0.14 mg^{-1}·h^{-1} for the DW. The use of inorganic buffer solution for PCA measurements allows one to reach the stability of pH value during the photodegradation process, which is preferrable in the case of the decolorization rate measurements for the pH-sensitive dyes. Moreover, for the PCA measurements of titania and titania-based nanocomposites, the phosphate buffer solution significantly improve the suspension stability.

Such effect is not too obvious: it is well-known, that the point of zero charge (PZC) for titania is about of the pH 6–7, and the pH of phosphate buffer solution is pH 6.9. Besides, due to the adsorption of phosphate anions on the titania surface and the following changes in ζ-potential, the aggregation ability in the case of DW is more than in the case of buffer solution. Measured values of ζ-potential for P25 titania suspension with different pH, compared to the same for phosphate buffer solution are shown in Fig. 3. However, due to the phosphate anions absorbtion, measured PCA value significantly decrease and it should be taken into the account during the measurements [58–60].

(a)   (b)
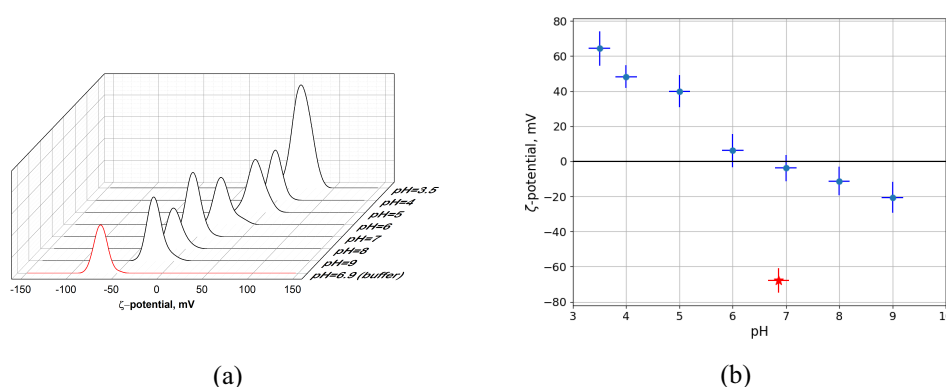
FIG. 3. (a) ζ-potential distributions and (b) pH dependency of ζ-potential for the titania suspension in DW and phosphate buffer solution (red curve). The red dot corresponds to the ζ-potential value in the buffer solution

4. Results and discussion

Wet chemistry techniques are widely used for silver and gold NPs decorization of titania [8, 27, 35, 41] and other semiconductors [61]. Among these techniques, the most popular are impregnation of semiconductor powder by previously synthesized metal NP sols and *in situ* growth of NPs on the semiconductors surface. The latter is usually based on reduction of dissolved Au(III) and Ag(I) compounds. The rate of reduction has a strong impact on the morphology of obtained metal NPs. Additionally, it may determine the type of nucleation (homogeneous or heterogeneous) and, hence, the contact quality between metal and semiconductor counterparts in

final nanocomposites, affecting their properties. Therefore, here, we used different rates of $HAuCl_4$ and $AgNO_3$ reduction in the presence of titania suspension. For the rapid reduction we employed sodium borohydride, whereas slower reduction was provided by sodium citrate and UV irradiation. Moreover, to tune the reduction rate using citrate anions, the reaction mixture additionally was heated to increase the rate of reduction, whereas in the case of a borohydride anions in this work used an ice-cold solution to slow it down. The reduction by photogenerated charge carriers [62] was used to increase the contact effect on the nanocomposites properties via directly NPs formation on the semiconductor surface. Photoexcited electrons reduce the metal ions adsorbed on the semiconductor surface, and hence this reduction method leads to heterogeneous nucleation. In the case of the rapid reduction, which we can observe using borohydride anions, we can expect a homogeneous nucleation and the formation of a weak metal/semiconductor contact. Therefore, in this case metal NPs have a lower effect on the properties of the obtained nanocomposites. Using citrate anions and UV irradiation the rate of reduction is low, and hence the heterogeneous nucleation and a better contact formation should be expected. Au/TiO_2 and Ag/TiO_2 nanocomposites prepared by impregnation technique were used as reference samples.

4.1. Size and morphology

The TEM BF images of the synthesized nanocomposites are shown on Fig. 4 and Fig. 5. All the employed techniques resulted in appearance of gold or silver NPs distributed on the surface of titania NPs (40 nm for both anatase and rutile phases). The results for Au/TiO_2 and Ag/TiO_2 nanocomposites obtained by the impregnation of titania powder with previously synthesized NPs demonstrate that this method results in a narrow distribution of NPs sizes, but generally, the nanocomposites include aggregated NPs as at Fig. 4a and Fig. 5a. The presence of suspended titania particles may initiate the aggregation process of the initially stable metal NPs aqueous colloid suspension. Generally, to prevent the NPs aggregation, it may be reasonable to use well-stabilized water redispersible metal NPs, stabilized by humate polyanions [50], but the use of stabilizing agents affects on the metal/semiconductor contact due to the organic interlayer, and hence obtained materials are not applicable in photocatalysis.

(a)   (b)   (c)   (d)
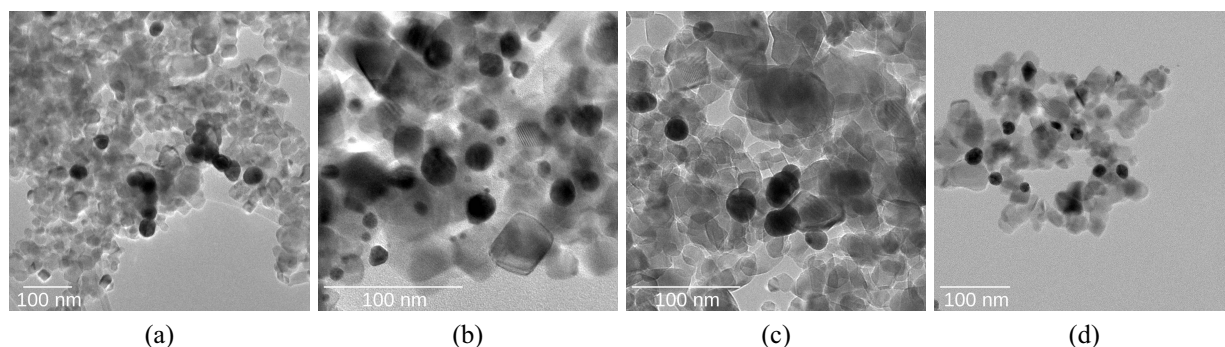
FIG. 4. TEM BF images of the nanocomposites: (a) Au/TiO_2 (imp), (b) Au/TiO_2 (b), (c) Au/TiO_2 (cit), (d) Au/TiO_2 (UV)

(a)   (b)   (c)   (d)
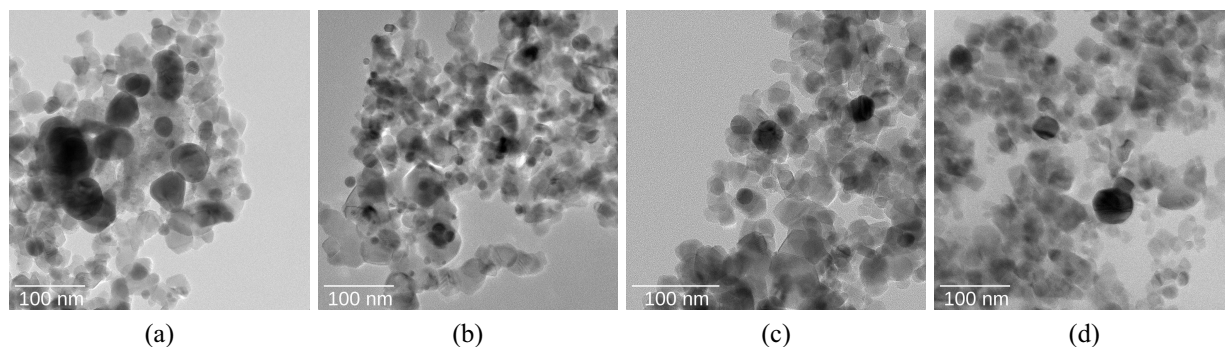
FIG. 5. TEM BF images of the nanocomposites: (a) Ag/TiO_2 (imp), (b) Ag/TiO_2 (b), (c) Ag/TiO_2 (cit), (d) Ag/TiO_2 (UV)

To quantify the particles size and compare the anisotropy of NPs, a statistical analysis was performed. The average effective diameters of metal NPs were calculated for all samples and are presented in the Table 2. In the case of nanocomposites obtained with the reduction by borohydride the averaged diameter of the metal NPs is significantly smaller both for gold and silver (11–13 nm) that in the case of reduction by citrate and UV (20–22 nm). According to the calculated cumulative anisotropy distributions $k_{10\%}$, $k_{50\%}$, and $k_{90\%}$ values were determinated and are presented in the Table 2. In the case of reduction with sodium borohydride and deposited by impregnation metal NPs anisotropies are smaller that in the case of the citrate and UV irradiation syntheses methods. These differences may be caused by the reduction rate differences. Rapid reduction with the borohydride results in the high probability of the homogeneous nucleation, but in the case of slow reduction with the citrate and especially UV irradiation it leads to the heterogeneous nucleation on the surface of titania particles. Therefore, such anisotropy may indicates the contact quality. The differences in the anisotropies of metal NPs, obtained by a citrate reduction with and without titania presence may serve as an additional evidence of the heterogeneous nucleation. In the case of the titania presence, the anisotropy of metal NPs is higher, that in the case of reduction without the titania, and the size of AuNPs is lower. Ag NPs in the sample Ag/TiO$_2$ (cit) have the size distribution too wide for such comparison (see Figs. 6, 7 and Table 2). It seems to be caused by the secondary nucleation in these conditions [63].

(a)   (b)   (c)   (d)
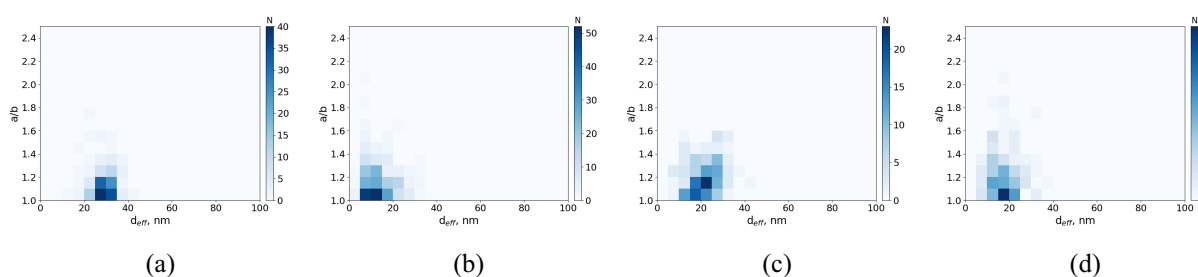
FIG. 6. 2D distributions of gold NPs in the Au/TiO$_2$ nanocomposites: (a) Au/TiO$_2$ (imp), (b) Au/TiO$_2$ (b), (c) Au/TiO$_2$ (cit), (d) Au/TiO$_2$ (UV)

(a)   (b)   (c)   (d)
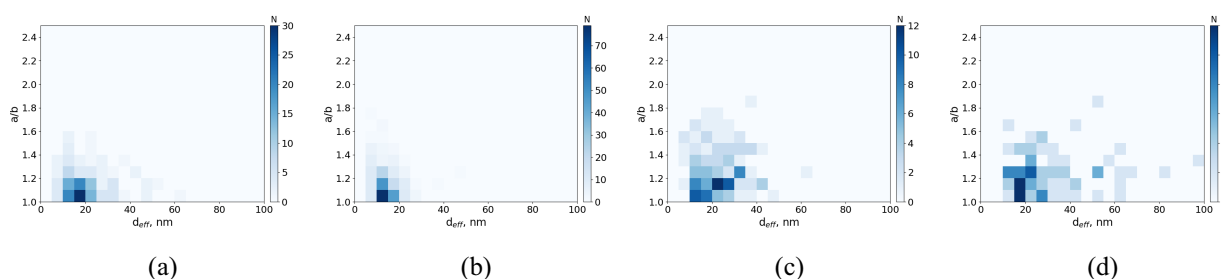
FIG. 7. 2D distributions of silver NPs in the Ag/TiO$_2$ nanocomposites: (a) Ag/TiO$_2$ (imp), (b) Ag/TiO$_2$ (b), (c) Ag/TiO$_2$ (cit), (d) Ag/TiO$_2$ (UV)

In the case of samples, obtained using UV irradiation, high anisotropy were expected due to a reduction of metal ions directly on the surface of titania, and, hence, the heterogeneous nucleation. According to the obtained data, NPs size and anisotropy distributions are similar to the particles, obtained by the citrate reduction. The number of particles of ≥ 75 nm in the Ag/TiO$_2$ (UV) and the corresponding value of $k_{10\%}$ higher, that in the case of all the other samples, seems to be caused by the direct AgNO$_3$ decomposition in the solution under the UV irradiation. The metal NPs size and anisotropy distributions are presented on Figs. 7, and 6. Summarizing the TEM statistics results we conclude that the k-values, presented in the Table 2 may be used as an anisotropy descriptors, and according to the synthesis methods, allows one to estimate the quality of contact between titania and metal NPs.

4.2. X-ray diffraction

The XRD demonstrates that all samples posses titania with initial anatase-rutile ratio, whereas gold and silver included in nanocomposites correspond only to fcc phases(Anatase (JCPDS Card no. 21-1272), Rutile (JCPDS Card no. 21-1276), Gold (JCPDS Card no. 4-784), Silver (JCPDS Card no. 4-783)). Using EDX analysis it

was confirmed that the metal content corresponds to the 5%w.p. Based on results of the XRD profile analysis, the coherent scattering regions (CSR) were calculated and shown in the Table 2. Being in the 10–25 nm range the calculated CSR sizes consistent with with the TEM data: samples, obtained by the borohydride reduction demonstrate the smaller CSR size of 7 nm in comparison with the case of reduction by citrate (14–17 nm). The CSR size for impregnated sample Au/TiO_2 (imp) is less that the same value for the Au/TiO_2 (cit) sample, obtained by the similar value in the presence of titania. Generally, the XRD results confirm the TEM data and hence we can consider the TEM statistics sufficient. For the NPs size relations for the samples Ag/TiO_2 (imp) and Ag/TiO_2 (cit) there are the difference between TEM data and the CSR sizes. These differences potentially caused by the significant anisotropy of the particles for the Ag/TiO_2 (cit) sample (see Fig. 7). Insufficient number of fcc metals peaks on the XRD patterns and overlapping of reflexes does not allow to resolve the anisotropy of CSR in this case (Fig. 8), therefore, the TEM data seems to be more informative here.
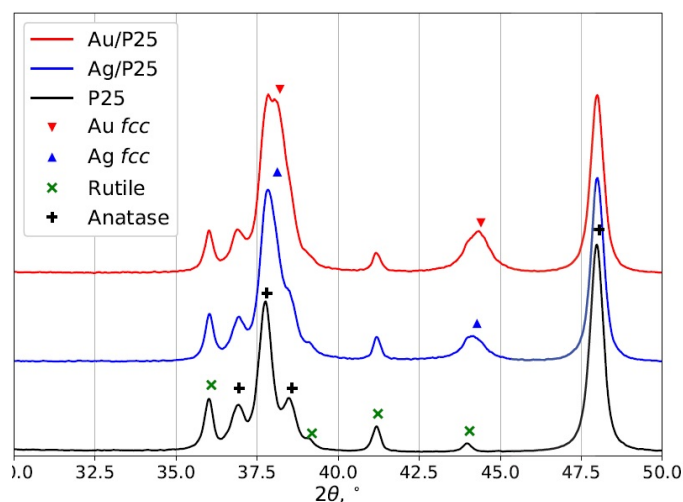
FIG. 8. XRD patterns of Au/TiO_2 (cit), Ag/TiO_2 (cit) nanocomposites and the initial Aeroxide P25

4.3. Optical properties

According to the eq. (1) the SPR peak position should be expected to shift to the higher wavelength range with the increase of the medium permittivity up to the value, corresponding to the core-shell metal@TiO_2 NPs. The results of DDA calculations are exemplified on the Fig. 9. Range of d_{eff} and anisotropy values were taken of 5–100 nm and 1–1.25 correspondingly to be representative for the previously calculated distributions (Figs. 6,7). It was shown that in the selected range of parameters, there are no significant changes of the SPR peak position, associated with the size and anisotropy effects. Meanwhile, broadening of the SPR peak increases with the anisotropy, which may indicates the contact formation analyzing optical absorption spectra. It should be noted, that the mean value of refractive index varies from one particle to another due to different quantity of neighboring titania particles. Therefore, the red shift of the SPR peak may be interpreted as a descriptor of the contact properties.
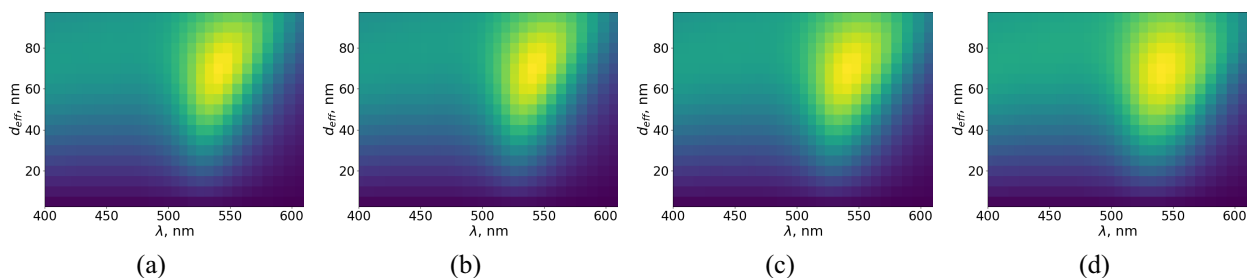
FIG. 9. Simulated absorption spectra for Au NPs with the d_{eff} value vary from 5 to 100 nm and the asymmetry coefficient of (a) 1, (b) 1.05, (c) 1.15 and (d) 1.25

UV-vis TRS allowed collection of optical absorption spectra, which are presented on the Fig. 10 and Fig. 11. According to this spectra, we can observe the presence of absorption edge at *ca.* 400 nm, which corresponds to the titania band gap. Since there are not shift of absorption edge position, initial titania matrix have not changed in the nanocomposites syntheses. In the range of 535–560 nm for the Au/TiO$_2$ nanocomposites and 435–455 nm for Au/TiO$_2$ nanocomposites we can find an intense SPR peak. The position of the SPR peaks are between the extinction maximums for metal NPs in air and in titania media, therefore, changing of the medium permittivity particularly effect on the spectra.

(a)   (b)
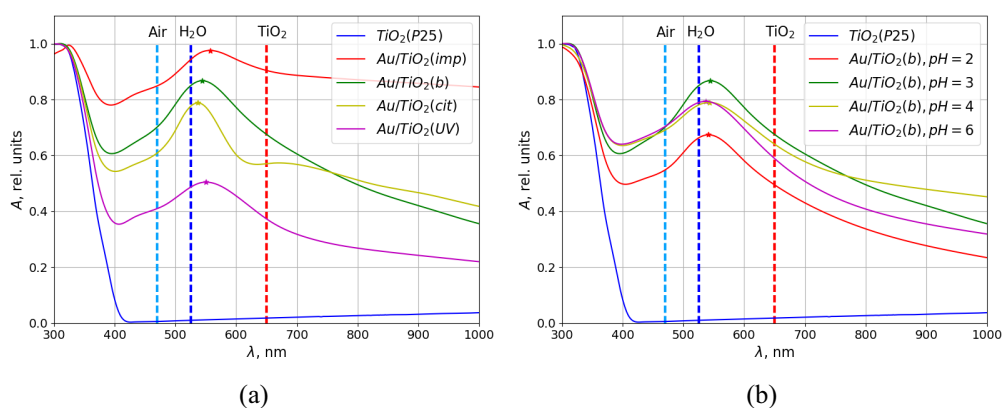
FIG. 10. Experimental absorption spectra for Au/TiO$_2$ nanocomposites: (a) synthesized by different reduction methods and (b) synthesized with borohydride reduction at different pH values. The vertical lines correspond to the simulated SPR peak positions at the different media

(a)   (b)
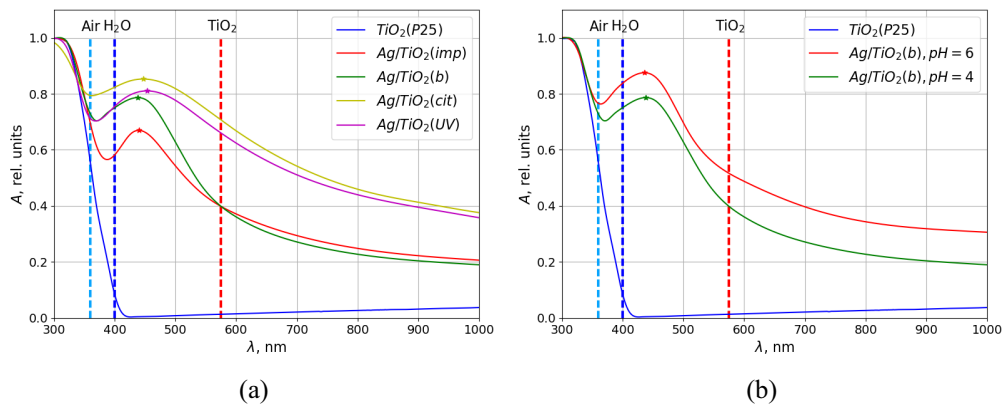
FIG. 11. Experimental absorption spectra for Ag/TiO$_2$ nanocomposites: (a) synthesized by different reduction methods and (b) synthesized with borohydride reduction at different pH values. The vertical lines correspond to the simulated SPR peak positions at the different media

According to the maximum of absorption presented in the Table 2 in the case of Ag/TiO$_2$ there is red shift of SPR peaks positions associated with slow reduction in UV and citrate assistance syntheses. As it was shown on the TEM data, the reduction rate affects on the anisotropy of metal NPs, and the quality of the contact with titania. According to the results of simulations for the measured range of sizes and anisotropy values, the red shift primarily caused by the formation of contact between titania and metal NPs. In the case of Au/TiO$_2$ nanocomposites, we also can observe similar behavior, however in the case of Au/TiO$_2$ (cit) nanocomposite the SPR peak position is lower than peak position of other nanocomposites. It may be caused by the side process of homogeneously nucleation in this case.The presence of a minor absorption peak at the 680–700 nm range may be interpreted as the evidence of the two different reduction processes.

For the silver NPs, the broad peaks are observed in the case of wide size distributions of NPs (Ag/TiO$_2$ (cit), Ag/TiO$_2$ (UV)), and for the gold NPs SPR peaks has a similar width, except the case of Au/TiO$_2$ (imp) sample, where the NPs aggregation additionally affects on the optical properties.

Comparing the absorption spectra of the nanocomposites obtained at different pH values using borohydride reduction (Fig. 10b and Fig. 11b), it should be noted that the SPR peak position shifts insignificantly. Therefore, in this case, the pH value does not affect on the absorption spectra or the nanocomposite morphology.

4.4. Effect of synthesis method on the photocatalytic activity

The photocatalytic measurements were performed in phosphate buffer (pH 6.9) in the case of Au/TiO_2 nanocomposites, but in the case of Ag/TiO_2 nanocomposites the DW was used due the possibility of a silver phosphate formation during the photocatalytic process. The obtained PCA values are presented on the Table 3.

TABLE 3. The photocatalytic activity of nanocomposites

Sample	PCA*	Sample	PCA*
Au/TiO_2 (b)	190	Ag/TiO_2 (b)	200
Au/TiO_2 (cit)	270	Ag/TiO_2 (cit)	95
Au/TiO_2 (UV)	280	Ag/TiO_2 (UV)	100

*PCA values correspond to the MO decoloration rate, normalized using eq. (8)

It should be noted that in the case of Au/TiO_2 nanocomposites series (Au/TiO_2 (b), Au/TiO_2 (cit), Au/TiO_2 (UV)) there is the improvement of PCA. These results very closely correlates with the initial assumption that slow reaction methods like UV and citrate reduction results in better contact formation. According to the TEM statistics data, the grade of contact is also associated with increasing of the anisotropy k values.

In front of this, in the case of Ag/TiO_2 nanocomposites similar behavior is not detected. Slow reduction methods and demonstrated above increasing of anisotropy do not lead to PCA improvement. Besides, the $Ag/TiO_2(b)$ nanocomposite demonstrate the twice increasing of PCA compared with initial titania, that may be caused by size effect. As it was reported in articles review (Table 1) small silver NPs, which we can observe in this case, posses shifted Fermi level, and hence metal/semiconductor contact turns to Schottky type. Therefore, the size effect dominates in the case of PCA of Ag/TiO_2 nanocomposites.

5. Conclusion

In this work, we demonstrated that the various synthetic methods allow one to obtain the Au/TiO_2 and Ag/TiO_2 nanocomposites with different morphology and properties. The use of different reducing agents results in the various quality of the contact between metal NPs and titania, that significant effects on the PCA. Nevertheless the direct observation of the contact properties is complicated, therefore the metal NPs anisotropy were suggested as a contact quality descriptor. We proposed the TEM-based quantitative method of anisotropy measurements with the use of statistical analysis. It was shown that the increase of anisotropy is likely caused by the interaction of metal NPs and titania in the synthetic process. Thus, in the case of the low reduction rate the better contact formation and the high anisotropy are observed.

The results of the PCA measurement demonstrated the opposite effects in the case of the Au/TiO_2 and Ag/TiO_2 nanocomposites, associated with different work functions of gold and silver. For the Au/TiO_2 nanocomposites, the positive effect of the contact on the PCA value was confirmed, and it correlates with the NPs anisotropy. In the case of Ag/TiO_2 nanocomposites the PCA increasing was detected only in the case of small NPs formation.

Acknowledgements

References

[1] Chong M.N., Jin B., Chow C.W., Saint C. Recent developments in photocatalytic water treatment technology: A review. *Water Research*, 2010, **44**(10), P. 2997-3027.

[2] Turchi C.S., Ollis D.F. Photocatalytic degradation of organic water contaminants: Mechanisms involving hydroxyl radical attack. *Journal of Catalysis*, 1990, **122**(1), P. 178-192.

[3] Zaleska A., Hupka J., Wiergowski M., Biziuk M. Photocatalytic degradation of lindane, p,p-DDT and methoxychlor in an aqueous environment. *Journal of Photochemistry and Photobiology A: Chemistry*, 2000, **135**(23), P. 213-220.

[4] Karthikeyan N., Narayanan V., Stephen A. Visible light degradation of textile effluent using nanostructured TiO$_2$/Ag/CuO photocatalysts. *Nanosystems: Physics, Chemistry, Mathematics*, 2016, **7**(4), P. 695-698.

[5] Abe R. Recent progress on photocatalytic and photoelectrochemical water splitting under visible light irradiation. *Journal of Photochemistry and Photobiology C: Photochemistry Reviews*, 2010, **11**(4), P. 179-209.

[6] Habisreutinger S.N., Schmidt-Mende L., Stolarczyk J.K. Photocatalytic reduction of CO$_2$ on TiO$_2$ and other semiconductors. *Angewandte Chemie International Edition*, 2013, **52**(29), P. 7372-7408.

[7] Carp O., Huisman C., Reller A. Photoinduced reactivity of titanium dioxide. *Progress in Solid State Chemistry*, 2004, **32**(12), P. 33-177.

[8] Low J., Cheng B., Yu J. Surface modification and enhanced photocatalytic CO$_2$ reduction performance of TiO$_2$: a review. *Applied Surface Science*, 2017, **392**, P. 658-686.

[9] Kolesnik I.V., Chebotaeva G.S., Yashina L.V., Konstantinova E.A., Eliseev A.A., Lukashin A.V., Tretyakov Y.D. Preparation of Nanocrystalline Nitrogen-doped Mesoporous Titanium Dioxide. *Mendeleev Communications*, 2013, **23**(1), P. 11-13.

[10] Maksimov V.D., Shaporev A.S., Ivanov V.K., Churagulov B.R., Tretyakov Y.D. Hydrothermal synthesis of nanocrystalline anatase from aqueous solutions of titanyl sulfate for photocatalytic applications. *Theoretical Foundations of Chemical Engineering*, 2009, **43**(5), P. 713.

[11] Meskin P.E., Gavrilov A.I., Maksimov V.D., Ivanov V.K., Churagulov B.P. Hydrothermal/microwave and hydrothermal/ultrasonic synthesis of nanocrystalline titania, zirconia, and hafnia. *Russian Journal of Inorganic Chemistry*, 2007, **52**(11), P. 1648-1656.

[12] Trommer R.M., Bergmann C.P. et al. *Flame Spray Technology*. Springer-Verlag, Berlin, Heidelberg, 2015.

[13] Moiseev A., Qi F., Deubener J., Weber A. Photocatalytic activity of nanostructured titanium dioxide from diffusion flame synthesis. *Chemical Engineering Journal*, 2011, 170(1), P. 308-315.

[14] Saekow S., Maiakgree W., Jarernboon W., Pimanpang S., Amornkitbamrung V. High intensity UV radiation ozone treatment of nanocrystalline TiO$_2$ layers for high efficiency of dye-sensitized solar cells. *Journal of Non-Crystalline Solids*, 2012, **358**(17), P. 2496-2500. Proceedings of the 24-th International Conference on Amorphous and Nanocrystalline Semiconductors (ICANS 24) Nara, Japan August 21–26, 2011.

[15] Lebedev V.A., Sudin V.V., Kozlov D.A., Garshev A.V. Photocatalytic properties of nanocrystalline TiO$_2$ modified with CuO and WO$_3$. *Nanotechnologies in Russia*, 2016, **11**(1), P. 20-28.

[16] Han T., Zhou D., Wang H., Zheng X. The study on preparation and photocatalytic activities of Cu$_2$O/TiO$_2$ nanoparticles. *Journal of Environmental Chemical Engineering*, 2015, **3**(4), P. 24532462.

[17] Tseng I.-H., Wu J. C.-S. Chemical states of metal-loaded titania in the photoreduction of CO$_2$. *Catalysis today*, 2004, **97**(2), P. 113-119.

[18] Koirala A.R., Docao S., Lee S.B., Yoon K.B. Fate of methanol under one-pot artificial photosynthesis condition with metal-loaded TiO$_2$ as photocatalysts. *Catalysis Today*, 2015, **243**, P. 235-250.

[19] Logar M., Jančar B., Šturm S., Suvorov D. Weak polyion multilayer-assisted in situ synthesis as a route toward a plasmonic Ag/TiO$_2$ photocatalyst. *Langmuir*, 2010, **26**(14), P. 12215-12224.

[20] Evans J.E., Springer K.W., Zhang J.Z. Femtosecond studies of interparticle electron transfer in a coupled CdS-TiO$_2$ colloidal system. *The Journal of Chemical Physics*, 1994, **101**(7), P. 6222–6225.

[21] Cushing S.K., Li J., Meng F., Senty T.R., Suri S., Zhi M., Li M., Bristow A.D., Wu N. Photocatalytic activity enhanced by plasmonic resonant energy transfer from metal to semiconductor. *Journal of the American Chemical Society*, 2012, **134**(36), P. 15033-15041.

[22] Riviere J. The work function of gold. *Applied Physics Letters*, 1966, **8**(7), P. 172172.

[23] Imanishi A., Tsuji E., Nakato Y. Dependence of the work function of TiO$_2$ (Rutile) on crystal faces, studied by a scanning auger microprobe. *The Journal of Physical Chemistry C*, 2007, **111**(5), P. 2128-2132.

[24] Dweydari A., Mee C. Work function measurements on (100) and (110) surfaces of silver. *Physica Status Solidi (A)*, 1975, **27**(1), P. 223-230.

[25] Schnippering M., Carrara M., Foelske A., Kötz R., Fermín D.J. Electronic properties of Ag nanoparticle arrays. A Kelvin probe and high resolution XPS study. *Physical Chemistry Chemical Physics*, 2007, **9**(6), P. 725-730.

[26] Cozzoli P.D., Fanizza E., Comparelli R., Curri M.L., Agostiano A., Laub D. Role of metal nanoparticles in TiO$_2$/Ag nanocomposite-based microheterogeneous photocatalysis. *The Journal of Physical Chemistry B*, 2004, **108**(28), P. 9623-9630.

[27] Subramanian V., Wolf E.E., Kamat P.V. Catalysis with TiO$_2$/gold nanocomposites. Effect of metal particle size on the Fermi level equilibration. *Journal of the American Chemical Society*, 2004, **126**(15), P. 4943-4950.

[28] Liang Y.-C., Wang C.-C., Kei C.-C., Hsueh Y.-C., Cho W.-H., Perng T.-P. Photocatalysis of Ag-loaded TiO$_2$ nanotube arrays formed by atomic layer deposition. *The Journal of Physical Chemistry C*, 2011, **115**(19), P. 9498-9502.

[29] Grabowska E., Zaleska A., Sorgues S., Kunst M., Etcheberry A., Colbeau-Justin C., Remita H. Modification of titanium (IV) dioxide with small silver nanoparticles: application in photocatalysis. *The Journal of Physical Chemistry C*, 2013, **117**(4), P. 1955-1962.

[30] Zhang L., Yu J.C., Yip H.Y., Li Q., Kwong K.W., Xu A.-W., Wong P.K. Ambient light reduction strategy to synthesize silver nanoparticles and silver-coated TiO$_2$ with enhanced photocatalytic and bactericidal activities. *Langmuir*, 2003, **19**(24), P. 10372-10380.

[31] Sung-Suh H.M., Choi J.R., Hah H.J., Koo S.M., Bae Y.C. Comparison of Ag deposition effects on the photocatalytic activity of nanoparticulate TiO$_2$ under visible and UV light irradiation. *Journal of Photochemistry and Photobiology A: Chemistry*, 2004, **163**(1), P. 37-44.

[32] El-Kemary M., Abdel-Moneam Y., Madkour M., El-Mehasseb I. Enhanced photocatalytic degradation of Safranin-O by heterogeneous nanoparticles for environmental applications. *Journal of Luminescence*, 2011, **131**(4), P. 570-576.

[33] Zhang H., Liang C., Liu J., Tian Z., Wang G., Cai W. Defect-mediated formation of Ag clusterdoped TiO$_2$ nanoparticles for efficient photodegradation of pentachlorophenol. *Langmuir*, 2012, **28**(8), P. 3938-3944.

[34] Ko S., Banerjee C. K., Sankar J. Photochemical synthesis and photocatalytic activity in simulated solar light of nanosized Ag doped TiO$_2$ nanoparticle composite. Composites Part B: Engineering, 2011, **42**(3), P. 579-583.

[35] Pan X., Xu Y.-J. Defect-mediated growth of noble-metal (Ag, Pt, and Pd) nanoparticles on TiO$_2$ with oxygen vacancies for photocatalytic redox reactions under visible light. *The Journal of Physical Chemistry C*, 2013, **117**(35), P. 17996-18005.

[36] Xiang Q., Yu J., Cheng B., Ong H. Microwave-Hydrothermal Preparation and Visible-Light Photoactivity of Plasmonic Photocatalyst Ag-TiO$_2$ Nanocomposite Hollow Spheres. *ChemistryAn Asian Journal*, 2010, **5**(6), P. 1466-1474.

[37] Wang Q., Yang X., Liu D., Zhao J. Fabrication, characterization and photocatalytic properties of Ag nanoparticles modified TiO$_2$ NTs. *Journal of Alloys and Compounds*, 2012, **527**, P. 106-111.

[38] He X., Cai Y., Zhang H., Liang C. Photocatalytic degradation of organic pollutants with Ag decorated free-standing TiO_2 nanotube arrays and interface electrochemical response. *Journal of Materials Chemistry*, 2011, **21**(2), P. 475-480.

[39] Zheng Z., Huang B., Qin X., Zhang X., Dai Y., Whangbo M.-H. Facile in situ synthesis of visible-light plasmonic photocatalysts $M@TiO_2$ (M= Au, Pt, Ag) and evaluation of their photocatalytic oxidation of benzene to phenol. *Journal of Materials Chemistry*, 2011, **21**(25), P. 9079-9087.

[40] Shan Z., Wu J., Xu F., Huang F.-Q., Ding H. Highly effective silver/semiconductor photocatalytic composites prepared by a silver mirror reaction. *The Journal of Physical Chemistry C*, 2008, **112**(39), P. 15423-15428.

[41] Liu C., Yang D., Jiao Y., Tian Y., Wang Y., Jiang Z. Biomimetic synthesis of TiO_2SiO_2Ag nanocomposites with enhanced visible-light photocatalytic activity. ACS applied materials & interfaces, 2013, **5**(9), P. 3824-3832.

[42] Njoki P.N., Lim I.-I. S., Mott D., Park H.-Y., Khan B., Mishra S., Sujakumar R., Luo J., Zhong C.-J. Size correlation of optical and spectroscopic properties for gold nanoparticles. *The Journal of Physical Chemistry C*, 2007, **111**(40), P. 14664-14669.

[43] Eustis S., El-Sayed M.A. Why gold nanoparticles are more precious than pretty gold: noble metal surface plasmon resonance and its enhancement of the radiative and nonradiative properties of nanocrystals of different shapes. *Chemical society reviews*, 2006, **35**(3), P. 209-217.

[44] Zhao J., Pinchuk A. O., McMahon J.M., Li S., Ausman L.K., Atkinson A.L., Schatz G.C. Methods for describing the electromagnetic properties of silver and gold nanoparticles. *Accounts of chemical research*, 2008, **41**(12), P. 1710-1720.

[45] Kelly K.L., Coronado E., Zhao L.L., Schatz G.C. The Optical Properties of Metal Nanoparticles: The Influence of Size, Shape, and Dielectric Environment. *The Journal of Physical Chemistry B*, 2003, **107**(3), P. 668–677.

[46] Draine B.T., Flatau P.J. Discrete-dipole approximation for scattering calculations. *Journal of the Optical Society of America A*, 1994, **11**(4), P. 1491-1499.

[47] Rakić A. D., Djurišić A. B., Elazar J. M., Majewski M.L. Optical properties of metallic films for vertical-cavity optoelectronic devices. *Applied optics*, 1998, **37**(22), P. 5271-5283.

[48] Zhou M., Wang B., Rozynek Z., Xie Z., Fossum J.O., Yu X., Raaen S. Minute synthesis of extremely stable gold nanoparticles. *Nanotechnology*, 2009, **20**(50), P. 505606.

[49] Chatenet M., Micoud F., Roche I., Chainet E. Kinetics of sodium borohydride direct oxidation and oxygen reduction in sodium hydroxide electrolyte: Part I. BH_4^- electro-oxidation on Au and Ag catalysts. *Electrochimica Acta*, 2006, **51**(25), P. 5459-5467.

[50] Polyakov A.Y., Lebedev V.A., Shirshin E.A., Rumyantsev A.M., Volikov A.B., Zherebker A., Garshev A.V., Goodilin E.A., Perminova I.V. Non-classical growth of water-redispersible spheroidal gold nanoparticles assisted by leonardite humate. *CrystEngComm*, 2017, **19**(5), P. 876-886.

[51] Ojea-Jiménez I., Campanera J. M. Molecular Modeling of the Reduction Mechanism in the Citrate- Mediated Synthesis of Gold Nanoparticles. *The Journal of Physical Chemistry C*, 2012, **116**(44), P. 23682–23691.

[52] Kumar S., Gandhi K.S., Kumar R. Modeling of Formation of Gold Nanoparticles by Citrate Method. *Industrial & Engineering Chemistry Research*, 2007, **46**(10), P. 3128–3136.

[53] Petříček V., Dušek M., Palatinus L. Crystallographic Computing System JANA2006: General features. *Zeitschrift für Kristallographie - Crystalline Materials*, 2014, **229**(5), P. 345-352.

[54] Nečas D., Klapetek P. Gwyddion: an open-source software for SPM data analysis. *Central European Journal of Physics*, 2012, **10**(1), P. 181-188.

[55] Jones E., Oliphant T., Peterson P. et al. SciPy: Open source scientific tools for Python. 2001. URL: http://www.scipy.org/.

[56] Hunter J. D. Matplotlib: A 2D graphics environment. *Computing In Science & Engineering*, 2007, **9**(3), P. 90-95.

[57] Lebedev V., Kozlov D., Kolesnik I., Poluboyarinov A., Becerikli A., Grünert W., Garshev A. The amorphous phase in titania and its influence on photocatalytic properties. *Applied Catalysis B: Environmental*, 2016, **195**, P. 39-47.

[58] Chen H.Y., Zahraa O., Bouchy M. Inhibition of the adsorption and photocatalytic degradation of an organic contaminant in an aqueous suspension of TiO_2 by inorganic ions. *Journal of Photochemistry and Photobiology A Chemistry*, 1997, **108**(1), P. 37-44.

[59] Chen F., Zhao J., Hidaka H. Adsorption factor and photocatalytic degradation of dye-constituent aromatics on the surface of TiO_2 in the presence of phosphate anions. *Research on chemical intermediates*, 2003, **29**(7-9), P. 733-748.

[60] Zhao D., Chen C., Wang Y., Ji H., Ma W., Zang L., Zhao J. Surface Modification of TiO_2 by Phosphate: Effect on Photocatalytic Activity and Mechanism Implication. *The Journal of Physical Chemistry C*, 2008, **112**(15), P. 5993–6001.

[61] Polyakov A.Y., Lebedev V., Yadgarov L., Goodilin E. Two facile routes for functionalization of WS_2 nanotubes with silver nanoparticles. *Nanosystems: Physics, Chemistry, Mathematics*, 2017, **8**(5), P. 628-634.

[62] Tian Y., Tatsuma T. Mechanisms and applications of plasmon-induced charge separation at TiO_2 films loaded with gold nanoparticles. *Journal of the American Chemical Society*, 2005, **127**(20), P. 7632-7637.

[63] Gorup L.F., Longo E., Leite E.R., Camargo E.R. Moderating effect of ammonia on particle growth and stability of quasi-monodisperse silver nanoparticles synthesized by the Turkevich method. *Journal of Colloid and Interface Science*, 2011, **360**(2), P. 355-358.

Experimental studies of impact on a critical heat flux the parameters of nanoparticle layer formed at nanofluid boiling

V. B. Khabensky[1], A. L. Sirotkina[2], V. I. Almjashev[1,3], E. D. Fedorovich[2], V. V. Sergeev[2], V. V. Gusarov[4]

[1]A. P. Alexandrov Research Institute of Technology "NITI",
188540, Leningrad Region, Sosnovy Bor, Koporskoe shosse, 72, Russia

[2]Peter the Great St. Petersburg Polytechnic University,
195251, St. Petersburg, Politekhnicheskaya str., 29, Russia

[3]Saint Petersburg Electrotechnical University "LETI",
197376, St. Petersburg, Prof. Popov str., 5, Russia

[4]Ioffe Institute, 194021, St. Petersburg, Politekhnicheskaya str., 28, Russia

sashulena991@inbox.ru, vac@mail.ru

The paper presents experimental studies of nanoparticle layer, which is established on the heated surface during the boiling of nanofluid, and the influence of the process and resulting nanoparticle layer on the magnitude of critical heat flux. The examined nanofluid is distilled water (distillate) with dispersed ZrO_2 nanoparticles. A nichrome wire is used as heater. The varied parameters are: volumetric concentration of particles (C_0); exposition time in the nucleate boiling regime (τ); initial heat flux at exposition (q_0). Critical heat flux (CHF) was measured in each case. The morphology of nanoparticle layer produced in different conditions is analyzed using the method of scanning electron microscopy. The experiments have determined the influence of boiling parameters on the nanoparticle layer formation on the heated surface and sensitivity of the CHF magnitude to the properties of established nanoparticle layer in the experimental conditions.

Keywords: nanofluid, ZrO_2 nanoparticles, nanostructured surface, microstructure, departure from nucleate boiling (DNB), critical heat flux (CHF).

Received: 10 March 2018

Revised: 20 March 2018

1. Introduction

One of the main indicators of improved efficiency of heat transfer from the heated surfaces is the increased critical heat flux (CHF). Higher CHF increases thermal strength of the surface, reduces its dimensions, provides better coolant performance and improves operating reliability and safety of heat exchange equipment.

There are several ways to increase CHF: by changing the surface relief and wetting, adding surface-active agents into the coolant, though each method has inherent limitations.

Over the last 15 years, different research teams have been active in CHF studies; they examine CHF behavior at the boiling of nanoparticle (NP) water-dispersions and study their thermophysical characteristics (thermal conductivity, heat capacity, viscosity, surface tension). Main results of the studies can be found in papers and surveys (e.g. [1] and [2], respectively).

Along with the studies of CHF effects influenced by nanoparticles of different chemical composition, their concentration in the boiling coolant, heated surface geometry, NP layer morphology and other parameters, the completed research has put forward new technical solutions for the application of NP technologies for increasing CHF in the nuclear power engineering (e.g. severe accident source term mitigation in LWR); solar and space technologies, microelectronics for increasing the thermal strength and reducing dimensions of heated surfaces [3–8]. This shows the inherent utility of this technology for industrial applications.

Nanoparticles used in the fabrication of nanofluids (NF) in the CHF experimental studies were mostly based on oxides (e.g., ZrO_2, Al_2O_3, SiO_2, CuO, TiO_2 and others), different carbon formations (e.g. diamond, graphite, carbon nanotubes), carbides, also oxidation-resistant metals (e.g., gold, silver, copper).

All experiments on nanofluid boiling have registered a NP layer formation on the heated surface and, to a certain degree, the CHF increase (up to 200%) in comparison with the same at distilled water boiling.

It should be noted that the formation of a porous layer on a heater surface can take place not only upon nanofluid boiling, but also when different chemical and technological methods are applied. For example, in [9], a porous layer was synthesized, which was similar to the one produced on the heat generation components of

operating nuclear reactors. The layer was produced by the layer-on-layer deposition of particles on a substrate. The electrophoresis deposition (EPD) [10] can also be used for producing a layer having such structure.

Surface layers produced by similar methods are less heat-exchange efficient in comparison with the NP layer produced at nanofluid boiling. This is probably due to the fact that the morphology and physicochemical characteristics of the surface show the most optimal parameters only if the layer is formed during nanofluid boiling.

The following essential results have been provided by the completed experimental studies [2, 11–18]:

- Small volumetric NP concentrations in the water dispersion (0.001 – 0.1 vol. %) can cause a sufficient CHF increase.
- Thermophysical and thermodynamical properties of nanofluid, which contains small volumetric NP concentrations (heat capacity, thermal conductivity, viscosity, surface tension, density, angle of wetting on a clean surface) are practically the same as similar properties of the base liquid (for water dispersion – distilled water), and they cannot cause the CHF increase.
- At the boiling of water containing nanoparticles, the layer of these particles is established on the heated surface. It has a regular microporous structure, and its thickness grows versus the time of nucleate boiling at the rate, which increases with the growth of volumetric concentration of nanoparticles in the liquid and heat flux.
- Porous layer on the heater surface improves the wettability – reduces the wetting angle at boiling more than three-fold in comparison with the smooth steel surface, the main condition for CHF increase. This correlates to a high CHF at the distillate boiling on the surface covered by the NP layer.
- Different models have been developed to take into account the CHF sensitivity to the wetting effect; most well-known were put forward by T. G. Theofanous, T. N. Dinh [19] and S. G. Kandlikar [1]. These models give close to actual values of CHF increase at the experimental studies of nanofluid boiling, but they require the evaluated wetting angle of the NP layer, which can be determined only by experiments.

In spite of the large inventory of experimental data, the available results are ambiguous. E.g. the following is known about the influence of NP concentration on CHF: CHF increase vs. concentration growth; CHF increase vs. concentration growth to 0.01 vol.% followed by saturation; with the concentration increase a CHF grows up to a certain value, reaches its maximum and goes down. The following is known concerning the effect of NP size on CHF: the larger particle size – the smaller CHF; the correlation of CHF vs. particle size is nonmonotonic and has a maximum.

A possible reason for mentioned differences is the kinetic peculiarities of the NP layer formation, which depend on three parameters, the NP size being the same, they are: concentration of dispersed particles, magnitude of heat flux during nucleate boiling and the time of steady boiling regime. Kinetic peculiarities of the NP layer formation at the set value of these parameters determine the relief structure, its thickness and eventually the wetting angle and CHF growth.

The first experimental results on the influence of regime parameters on CHF are given in [15]: the longer period of steady nucleate boiling is accompanied by a linear growth of both NP layer thickness and CHF magnitude until saturation at the steady heat flux and different levels of NP concentration. But in [15] the inventory of experimental data is limited; the reciprocal influence of regime parameters of the NP layer thickness and relief structure, also the aggregate influence of regime parameters on the optimal characteristics of the nanoparticle layer, which provides the maximum CHF increase, is not determined.

Therefore, the objective of current work is integrated study of the effect of NF boiling regime parameters on the formation kinetics and structure of NP layer and CHF.

2. Experiments, materials and methods

At the first stage the nanofluid boiling experiments were conducted at the experimental setup having a novel design. In the experiments the nanofluid was heated to the saturation temperature in the free convection conditions. The principal schematic of the setup is shown in Fig. 1.

The setup consists of the following basic parts (Fig. 1):

- 170 ml work cell (1) – thick-walled hollow horizontal cylinder with clamp flange and glass windows to monitor the boiling process and current leads (4) having collet clamps to fix the studied heater;
- steam volume above the work cell with a thermocouple channel designed to avoid the work cell overpressurization during the experiments and for steam temperature measurements (5);
- condenser (7), in which the steam coming from the steam volume during boiling is condensed and returns into the work cell (7);

1 – work cell; 2 – preheater; 3 – drainage tank; 4 – electrodes;
5 – thermocouple channel; 6 – video camera; 7 – condenser;
8,9 – automation and measurements unit; 10 – PC; 11 – power supply
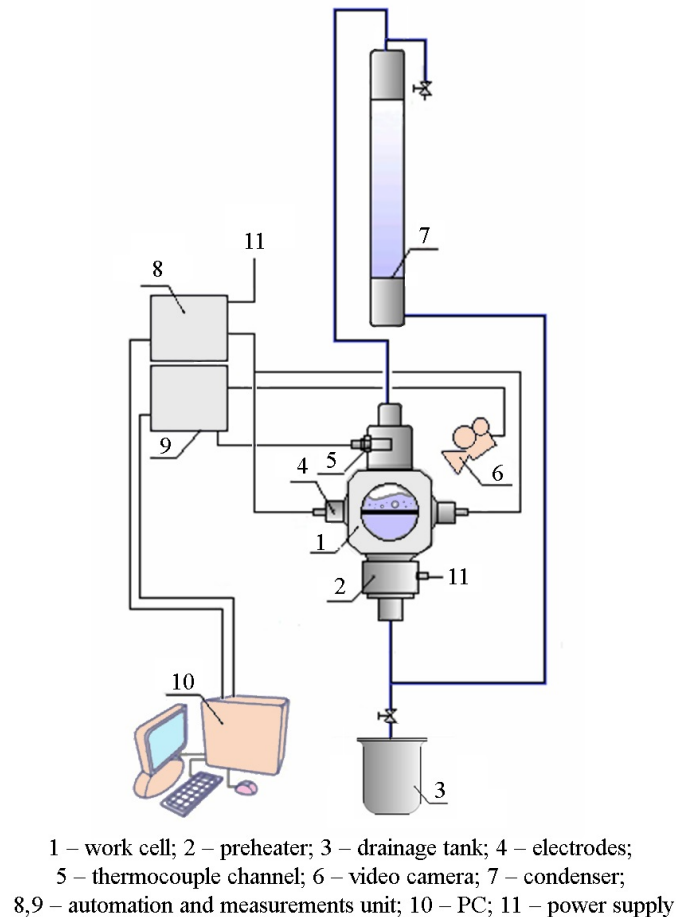
FIG. 1. Principal schematics of experimental setup

- heater (2) for the preheating of the studied fluid to the saturation temperature and its maintaining at the work cell entrance during the experiment;
- pipes and fittings for filling the work cell with a fluid and its drainage from the experimental setup;
- direct current power supply (11);
- automation and measurement unit (8, 9);
- video camera (6);
- computer (10);
- drainage tank (3).

The examined heater was a nichrome (Kh15N60 GOST 12766.1-90) wire (0.17 mm diameter).

To monitor experimental conditions, the setup included the online measurement, data acquisition and processing system. Beside that, the boiling was video-recorded through the work cell window.

The studied substance is nanofluid based on distilled water with ZrO_2 100 nm nanoparticles (manufacturer HWNANO, Hong Kong). The nanoparticle concentration in the liquid ranged from 0.001 to 0.1 vol.%. After addition of predetermined mass of nanoparticles into distilled water, the resulting dispersion was treated in an ultrasonic bath. The time of ultrasonic treatment was chosen to ensure the maximum dispersion stability. Once the dispersion was prepared, the volumetric concentration and size distribution of particles were kept under control. The period of ultrasonic exposure being optimal, if after seven days of exposition in the ambient conditions, also after several hours of boiling the nanofluid remained stable. Practically no coagulation or precipitation was observed.

The nanofluid was prepared immediately prior to each experiment. To evaluate CHF in the experimentally modelled conditions a series of calibration experiments with the distillate was conducted. At boiling on the distillate or clean surface, also at the boiling of water nanoparticle dispersions the CHF was evaluated from electric parameters at the moment of wire burnout, which was registered by the system of experimental measurements and

indicated by the data collected and processed online. Both CHF and NP layer thickness were measured in series (each combination of parameters was repeated several times).

The experiment procedure is as follows: after the experimental setup cell is filled with nanofluid, which has the preset volumetric nanoparticle concentration (from 0.001 to 0.1 vol.%), it is heated to the close to saturation temperature level; the heater is connected to power, its load corresponds to the preset initial HF level (varies in the range of 0.5 – 1.2 MW/m^2). This load level is maintained for a certain period of time – exposition time (between 1.5 – 30 min). After this, the heat flux is gradually increased in small steps up to the DNB crisis. The procedure was repeated three times in each regime; heat flux step was made shorter as the CHF was approached. The crisis is registered as the burnout of heater (wire). Corresponding value of the heat flux density is calculated as $q_{CHF} = \dfrac{U \cdot I}{\pi dL}$ (where U – voltage, V; I – current, A; d – wire diameter, m; L – length of the studied wire section, m).

This is followed by the post-test analysis of the NP layer morphology, resulting from the NF boiling on the heater in changed conditions. Nanoparticle layer thickness was evaluated in several sections along the wire length and in the two projections in the cross section close to the place of burnout. Scanning electron microscopy (SEM) was made using microscope Supra 55VP-25-78. Morphology and NP layer thickness were analyzed in the regime of secondary electrons.

Using photos provided by Supra 55VP-25-78 microscope the NP layer thickness was evaluated as the average value, to which the heater (wire) diameter increases in several locations.

3. Results and discussion

3.1. Experimental data on the CHF evaluation

Figures 2–5 provide experimental results on the evaluation of relative CHF changes in NF, when different parameters in the $q_{cr}^{nf}/q_{cr}^{dist} = f(q_0, C_0, \tau)$ coordinates were changed, where q_{cr}^{nf} – CHF in NF; q_{cr}^{dist} – CHF in the distilled water; C_0 – volumetric concentration of NP, vol.%; τ – exposition time in the boiling regime at q_0 heat flux; q_0 – initial heat flux value, MW/m^2.

The error given in Figs. 2–5 was calculated as the standard uncertainty (standard deviation) in the measurement series for each combination of parameters.
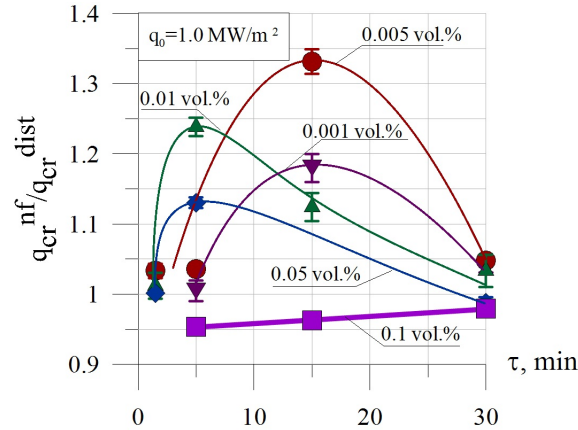
FIG. 2. $q_{cr}^{nf}/q_{cr}^{dist}$ versus exposition τ for different volumetric concentrations of nanoparticles C_0 at initial heat flux $q_0 = 1.0$ MW/m^2

Experimental data on the evaluation of $q_{cr}^{nf}/q_{cr}^{dist}$ given in Figs. 2–5 show the following:

1. Increase in the value of one of the above-given parameters, others kept the same, first leads to the growth of relative critical heat flux ($q_{cr}^{nf}/q_{cr}^{dist}$), it goes down after the maximum CHF level is reached.

2. At this, when one of the three parameters (q_0, C_0, τ) is varied and two others are kept constant, $q_{cr}^{nf}/q_{cr}^{dist}$ gets the maximum value, which corresponds to practically same values of ($q_0^{\max}$, $C_0^{\max}$, $\tau^{\max}$).

3. E.g. at $q_0 = 1.0$ MW/m^2, $C_0 = 0.01$ vol.% and $\tau = 5$ min we have:

- in Fig. 2 and Fig. 5 at fixed values of $q_0 = 1.0$ MW/m^2, $C_0 = 0.01$ vol.% and τ varying, the maximum $q_{cr}^{nf}/q_{cr}^{dist} = 1.25$ is reached at $\tau = 5$ min;
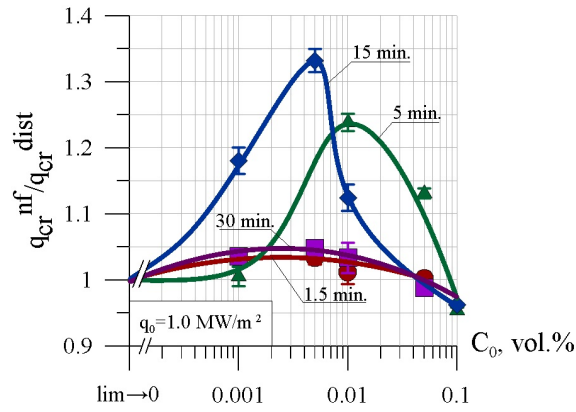
FIG. 3. $q_{cr}^{nf}/q_{cr}^{dist}$ versus volumetric concentration NP C_0 for different expositions τ at initial heat flux $q_0 = 1.0$ MW/m^2
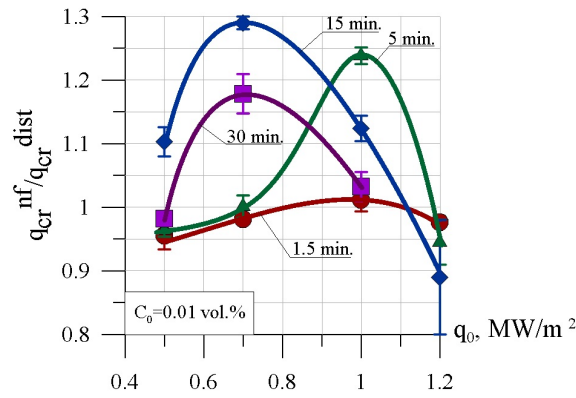
FIG. 4. $q_{cr}^{nf}/q_{cr}^{dist}$ versus initial heat flux q_0 for different expositions τ at the volumetric nanoparticle concentration $C_0 = 0.01$ vol.%
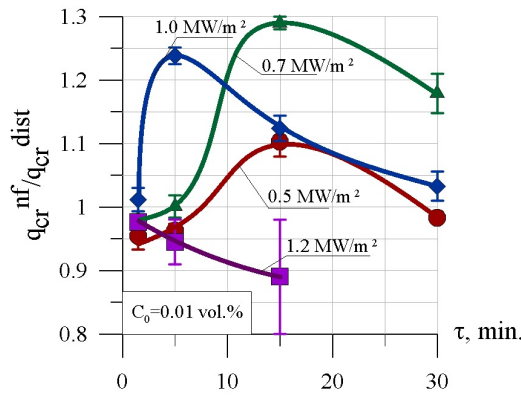
FIG. 5. $q_{cr}^{nf}/q_{cr}^{dist}$ versus exposition τ for different initial heat flux values q_0 at the volumetric nanoparticle concentration $C_0 = 0.01$ vol.%

- in Fig. 3 at fixed values of $q_0 = 1.0$ MW/m^2, $\tau = 5$ min and C_0 varying the maximum value of $q_{cr}^{nf}/q_{cr}^{dist} = 1.25$ is reached at $C_0 = 0.01$ vol.%;
- in Fig. 4 at fixed values of $C_0 = 0.01$ vol.%, $\tau = 5$ min and q_0 varying the maximum value of $q_{cr}^{nf}/q_{cr}^{dist} = 1.25$ is reached at $q_0 = 1.0$ MW/m^2.

Therefore, as the increase of any parameter leads to the NP layer thickness growth, the $q_{cr}^{nf}/q_{cr}^{dist}$ maximum value reached at the same parameter values can indicate the following: first, close to linear influence of each parameter on the NP layer thickness; and second, maximum value of $q_{cr}^{nf}/q_{cr}^{dist}$, with a high probability, corresponds to the determined optimal thickness and morphology of ZrO$_2$ nanoparticle layer, which ensures the smallest wetting angle, insignificant thermal resistance and open porosity, which is sufficient for the capillary water supply.

3.2. Morphology of nanoparticle layer

To analyze the morphology of NP layer, which was produced on the boiling surface at different regimes and parameters, and to determine its influence on CHF the following SEM studies of samples were conducted.

Analysis of the X-ray diffraction data and SEM images has shown that the size of the main fraction of ZrO$_2$ nanoparticles used in the experiment is about 100 nm, but there is a finer-grain fraction present, which has <100 nm particles. Analysis of the nanopowder's elemental composition made by EDX analysis gives the following: 76.7 mass % zirconium, 21.6 mass % oxygen; the sample also contains 1.7 mass % hafnium, which corresponds to the solid solution of hafnium dioxide in zirconia. The X-ray diffractometry of nanopowder also provides evidence that the main phase of the examined powder is the monoclinic modification of ZrO$_2$.

In order to analyze the influence of NP layer relief on CHF, let us consider the relief changes vs. its thickness. As an example, we consider surface relief versus the exposition time extension at the same NF concentration and unchanged initial heat flux. Fig. 6 shows images of the NP layer relief, which was produced by changing the exposition time at nanofluid concentration $C_0 = 0.01$ vol.% and initial heat flux $q_0 = 1.0$ MW/m^2. In this case the maximum CHF occurs at the exposition time $\tau = 5$ min (Fig. 6b). The ZrO$_2$ nanoparticle layer has a rather regular roughness with a distance between the neighboring nanoparticle aggregate peaks of 1.5–2.5 μm.

IIt is evident from Fig. 6 that as the exposition time increases, the surface relief changes. After the 1.5 min exposition, it is homogeneous, microregular with a relatively uniform combination of peaks and hollows. At the 5 min exposition the relief continues to be homogeneous and microregular, but, as a result of grown thickness of NP layer the hollow is deeper, which can make the wetting angle smaller. As is evident from Figs. 2–5, at the 5 min exposure, the maximum value of $q_{cr}^{nf}/q_{cr}^{dist}$ is reached. Further exposition to 15 min and 30 min makes the relief of NP layer irregular; it has different thicknesses and microstructure. The growth of NP layer thickness increases its thermal resistance. Both factors contribute to the considerable CHF decrease, up to $q_{cr}^{nf}/q_{cr}^{dist} \approx 1$.

Therefore, it can be assumed that there exists an optimal NP layer thickness, which corresponds to the highest CHF.

The completed SEM analysis of the wire samples after the CHF was reached also confirmed the assumption given in Section 3: close to linear correlation between the NP layer thickness growth character at changes in one of the given parameters (q_0, C_0, τ), the other two kept steady. Fig. 7 gives the NP layer thickness versus changing one of the three parameters.

It can be seen from Fig. 7a,b,c that at changing one of the parameters and getting in each case values of $q_0 = 1.0$ MW/m^2, $C_0 = 0.01$ vol.% and $\tau = 5$ min, the NP layer thickness stays unchanged and corresponds to ≈ 2 μm. At this, Figs. 2 and 5 show that in the mentioned parameter values the $q_{cr}^{nf}/q_{cr}^{dist}$ gets its maximum. This is an indirect proof of an optimal thickness of NP layer, at which the CHF is at its maximum.

Statistical analysis of experimental data (71 measurements) is represented on Fig. 8. Residual dispersion is 0.0315, standard uncertainty is 0.0214. Therefore, we can conclude that data scattering is less than 5 %. High values of scattering for measurements with low heat flux levels could be due to sufficient irregularity of nanoparticles layer thickness with high nanofluid concentration and long boiling time.

The limited inventory of experimental data and inherent properties of experimental facility (small volume of work cell, small diameter of heater – 0.17 mm-diameter wire) and a rather big size of nanoparticles (~ 100 nm) does not allow a detailed study of the changed nanoparticle layer morphology and geometric parameters of the cells – steam generation centers – versus the thickness of NP layer and CHF sensitivity to them. These data are critical for the numerical model development. However, the provided qualitative relationships provide well-grounded conclusions.
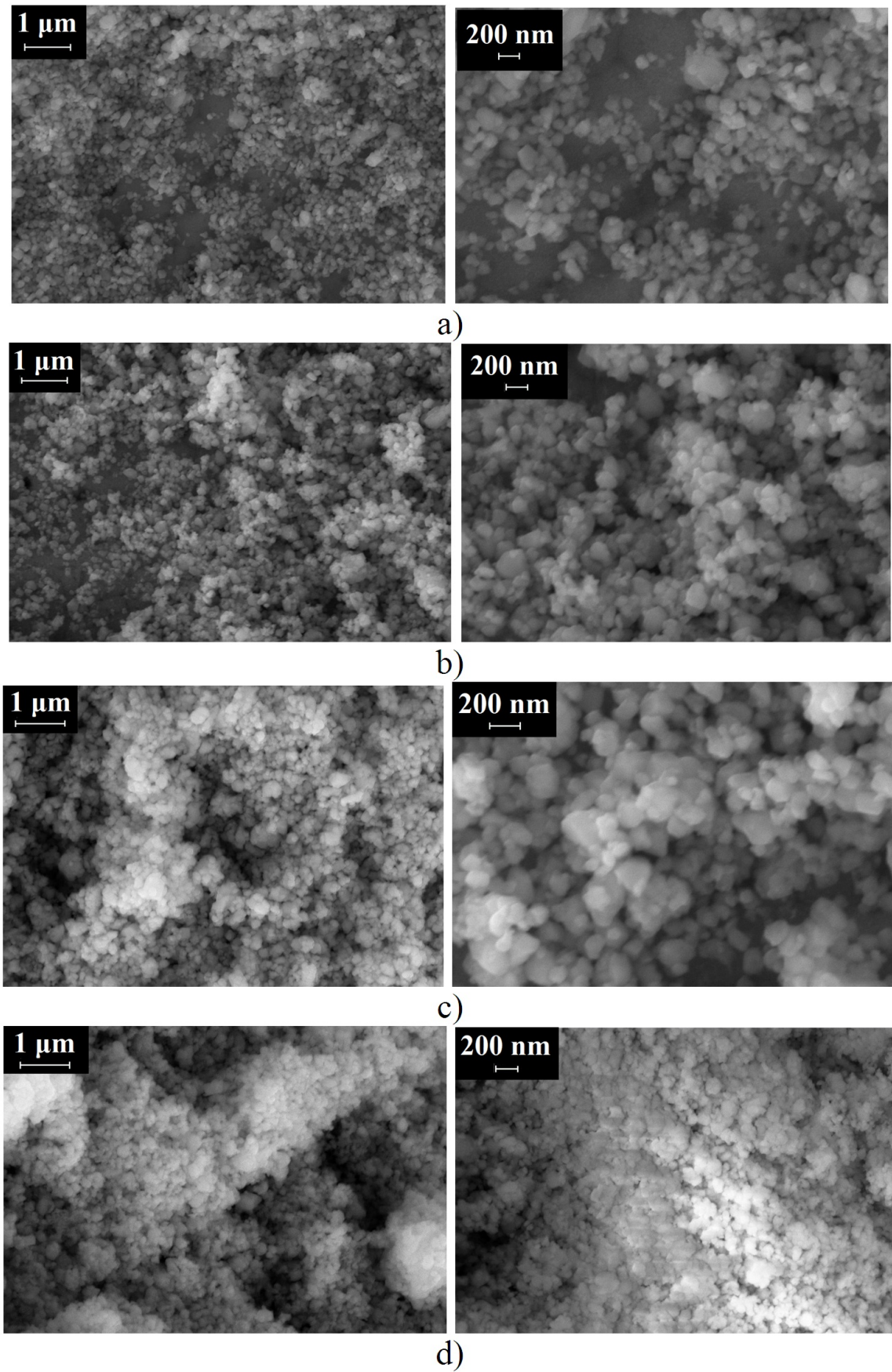
FIG. 6. Surface relief changes versus the longer exposition time (concentration 0.01 vol.%, initial heat flux 1.0 MW/m^2) a) $\tau = 1.5$ min; b) $\tau = 5$ min; c) $\tau = 15$ min; d) $\tau = 30$ min
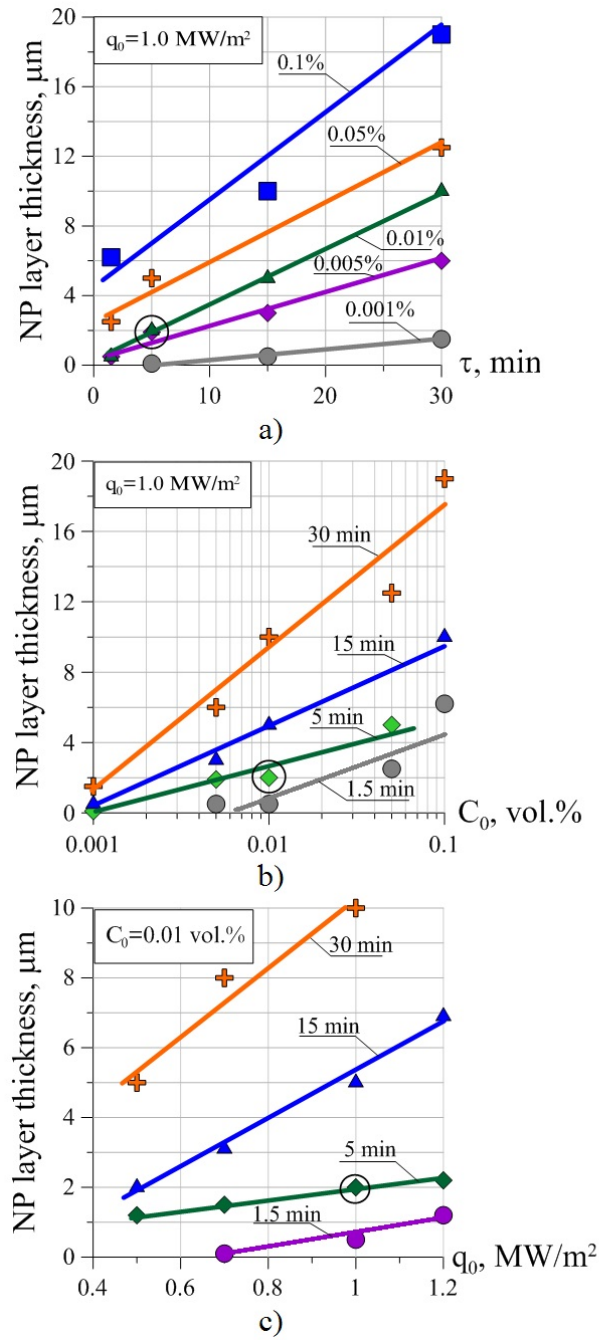
FIG. 7. NP layer thickness (μm) versus boiling parameters: a) at $q_0 = 1.0$ MW/m^2, changed τ (min) for different C_0 (vol.%); b) at $q_0 = 1.0$ MW/m^2, changed C_0 (vol.%) for different τ (min); c) at $C_0 = 0.01$ vol.%, changed q_0 (MW/m^2) for different τ (min). Black circle indicates points with coordinates $C_0 = 0.01$ vol.%, $q_0 = 1.0$ MW/m^2, $\tau = 5$ min, which corresponds to the maximum CHF value
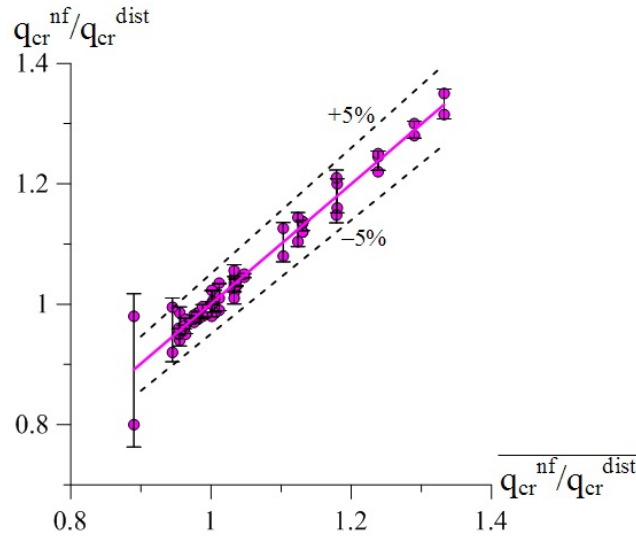
FIG. 8. $q_{cr}^{nf}/q_{cr}^{dist}$ variation against average value of this parameter in all experimental data

4. Result discussion

Completed experimental studies have determined the following qualitative relationships for the relevant conditions and parameter ranges:

1. If one of the three parameters (q_0, C_0, τ) is increased, and two others stay fixed, the critical heat flux ($q_{cr}^{nf}/q_{cr}^{dist}$) on the heated surface covered with a layer of ZrO_2 nanoparticles grows, gets its maximum value and decreases.

2. Each combination of (q_0, C_0, τ) parameter values has its maximum value of ($q_{cr}^{nf}/q_{cr}^{dist}$), which is fixed irrespective of the varied specific parameter.

3. Thickness of nanoparticle layer on the heated surface grows following the close to linear curve with an increase of any parameter (q_0, C_0, τ).

4. For each combination of (q_0, C_0, τ) parameter values the ($q_{cr}^{nf}/q_{cr}^{dist}$) maximum is reached at an approximately the same optimal thickness of NP layer (2 μm), irrespective of the varied parameter.

We can assume that the experimentally observed pattern of CHF dynamics (initial growth to maximum followed by decrease) at the increased NP layer thickness was caused by the changes in geometric characteristics of the cells – steam generation centers, and in the NP layer morphology.

In the publication [2] discuss the dependence of wetting angle, the nanolayer morphology being regular, on geometrical characteristics of cells (distance between the vertices and pits) formed at boiling. The cells are steam generation centers, which make a critical contribution into the wetting angle magnitude and, consequently, determine the tear-off diameter of the bubble and CHF.

We can propose the following mechanism of changing wetting angle and CHF. If one of the parameters (C_0, q_0 and τ) changes at nanofluid boiling, the NP layer thickness grows linearly. In the early period of the NP layer growth the surface continues to keep regular morphology and the ratio between the mentioned geometric characteristics of cells (steam generation centers) changes. This results in the decrease of wetting angle and tear-off diameter of the bubble and to the growth of CHF. When the NP layer grows to a certain thickness, the ratio of cell geometric parameters reaches an optimal value, which corresponds to maximum CHF. With further growth of the NP layer thickness the ratio between geometric parameters of the cell – steam generation center reduces. At this, the regularity of the NP layer morphology starts to decay. These factors cause the wetting angle increase and CHF reduction. It is evident that the NP layer thickness is the integral parameter, which determines the character of CHF changes, when any of the regime parameters is changed.

We should mention another important experimental result produced within this work. In all situations, when one of the regime parameters was varied (C_0, q_0 and τ), the maximum CHF occurred at the same NP layer thickness, which was ~ 2 μm. If the detailed examination proves that the same NP layer thickness corresponds to the maximum CHF, and the known linear speed of NP layer thickness growth when one of the regime parameters

is changed, we can get the optimal NP layer morphology (in terms of heat transfer characteristics). We also can model the optimal morphology using other methods.

The mentioned relationship patterns bring a number of conclusions for practical application. Here are some examples.

When nanofluids are used as coolants in the boiling type systems, as recommended in some publications, the NP layer thickness increases and, with time, the heat transfer efficiency is lost both for the CHF and heat exchange at boiling. For this reason, a positive effect of the NP layer is possible only in case of distilled water boiling.

A number of works studying the influence of volumetric concentration of nanoparticles on CHF gave different sensitivity of CHF vs. C_0 for nanoparticles of the same type. This can be a consequence of the methodology and experimental specifications. For example, if we set constant values of the initial heat flux (q_0) and exposition time (τ), when the volumetric NP concentration (C_0) is varied, the CHF is evaluated at different NP layer thicknesses, which, in the end, determines the different character of CHF versus C_0 correlations. But, in accordance with experimental data given in the paper, there should be no influence of volumetric NP concentration on the CHF, if we consider the CHF dependence on the NP layer thickness. These considerations also show low efficiency of a high volumetric concentration of nanoparticles in the dispersion (> 0.5 vol.%) on the CHF, as a fast growth of the NP layer thickness to the beyond optimal value cannot ensure a significant CHF increase.

Heat exchange at nanofluid boiling was beyond the presented research study. Anyway, the provided correlations and patterns can be used for qualitative estimate of the possible ambiguous behavior of heat transfer coefficient at boiling on the surface covered with NP layer, depending on the layer thickness. We can assume that at the NP layer corresponding to the increased CHF, the heat transfer coefficient will increase in comparison with the boiling on the clean surface, because the wetting angle is smaller (tear-off diameter of the bubble) and low thermal resistance (as the NP layer thickness is less than 2 μm, at $q = 1$ MW/m^2, $\Delta t \leq 1$ °C). It will get the highest value at maximum CHF. When the NP layer grows to ~ 8 μm the heat transfer coefficient can decrease sufficiently in comparison with the heat exchange at boiling on a clean surface because of the wetting angle increase (larger tear-off diameter of the bubble) and considerable increase of thermal resistance (NP layer thickness 8 μm, at $q = 1$ MW/m^2, $\Delta t \approx 4$–5 °C).

5. Conclusions

The completed experimental studies of nanoparticle layer formation in a boiling nanofluid have identified a number of patterns and correlations related to the influence of nanolayer thickness on the critical heat flux. Using the provided patterns, a qualitative analysis has been made. It examined peculiarities of the CHF behavior versus the NP layer thickness; influence of regime parameters (C_0, q_0 and τ) on the CHF value; restrictions of the experimental methodology and specifications in the studies of the CHF sensitivity to regime parameters; characteristic NP layer thickness at the maximum CHF; influence of the NP layer thickness on the heat transfer coefficient at the nanofluid boiling in comparison with the heat transfer coefficient at the boiling of distilled water on the smooth surface.

Unfortunately, a rather small volume of the work cell, small diameter of the heating element and a rather big size of nanoparticles restrict the possibilities for obtaining detailed quantitative information on the structure and geometric characteristics of the nanoparticle layer, also understanding of the influence of these parameters on the wetting angle and thermal characteristics (CHF and heat transfer coefficient) versus the NP layer thickness.

In order to analyze the possibility of extrapolatory scaling of the experimental data, it is necessary to make dedicated experiments on a series of experimental facilities with different heated surfaces and nanoparticles of different size and composition. In the context of determining heat transfer characteristics and CHF, of highest importance are the studies of the wetting angle and geometric parameters of cells – steam generation centers versus the nanoparticle layer thickness, especially in the vicinity of maximum CHF.

References

[1] Kandlikar S.G. A theoretical model to predict pool boiling CHF incorporating. *International Journal of Heat and Mass Transfer*, 2001, **123**, P. 1071–1079.
[2] Truong B., Hu L.-W., Buongiorno J. Optimizing Critical Heat Flux Enhancement Through Nanoparticle-Based Surface Modifications. *Proceedings of ICAPP'08*: Paper 8209, Anaheim, CA USA, 2008, P. 1699–1706.

[3] Kim H., Buongiorno J., Hu L.-W. [et al]. Experimental study on quenching of small metal sphere in nanofluids. *Proceedings of IMECE 2008*. Paper 67788, Boston, MA USA, 2008.

[4] Kim H., Buongiorno J., Hu L.-W., McKrell T. Nanoparticle deposition effects on the minimum heat flux point and quench front speed during quenching in water-based alumina nanofluids. *International Journal of Heat and Mass Transfer*, 2010, **53**, P. 1542–1553.

[5] Chinchole A.S., Kulkarni P.P., Nayak A.K. Experimental investigation of quenching behavior of heated zircaloy rod in accidental condition of nuclear reactor with water and water based nanofluids. *Nanosystems: Physics, Chemistry, Mathematics*, 2016, **7**(3), P. 528–533.

[6] Chupin A., Hu L.-W., Buongiorno J. Applications of nanofluids to enhance LWR accidents management in in-vessel retention and emergency cooling systems. *Proceedings of ICAPP'08*. Paper 8043, Anaheim, CA USA, 2008, P. 1707–1714.

[7] Bang I.Ch., Jeong J.H. Nanotechnology for advanced nuclear thermal-hydraulics and safety: boiling and condensation. Nuclear engineering and technology, 2011, **43**(3), P. 217–242.

[8] Barrett T.R. Investigation the use of nanofluids to improve high heat flux cooling systems. *Fusion Engineering and Design*, 2013, **88**(9-10), P. 2594–2597.

[9] Buongiorno J. et al. *Synthesis of CRUD and its Effect On Pool and Subcooled Flow Boiling*. CASL L3 Milestone Report. US Department of Energy, 2015.

[10] Corradini M., Marschman S., Goldner F. *Improved LWR cladding performance by EPD surface modification technique*. Final report of NEUP project 09-766. Madison: University of Wisconsin, 2012.

[11] Bang I.C., Chang S.H. Boiling heat transfer performance and phenomena of Al_2O_3 – water nano-fluids from a plane surface in a pool. *International Journal of Heat and Mass Transfer*, 2005, **48**, P. 2407–2419.

[12] Vassalo P., Kumar R., D'Amigo S. Pool boiling heat transfer experiments in silica-water nano-fluids. *International Journal of Heat and Mass Transfer*, 2004, **47**, P. 407–411.

[13] Kim S.J., Bang I.C., Buongiorno J., Hu L.-W. Surface wettability change during pool boiling of nanofluids and its effect on critical heat flux. *International Journal of Heat and Mass Transfer*, 2007, **50**, P. 4105–4116.

[14] B.S. Fokin, M.Ya. Belenkiy, V.I. Almjashev, V.B. Khabensky, O.V. Almjasheva, V.V. Gusarov, Critical heat flux in a boiling aqueous dispersion of nanoparticles. *Technical Physics Letters*, 2009, **35**(5), P. 440–442.

[15] Kwark S.M., Moreno G., Kumar R. [et al]. Nanocoating characterization in pool boiling heat transfer of pure water. *International Journal of Heat and Mass Transfer*, 2010, **53**, P. 4579–4587.

[16] Kleinstreuer C., Feng Yu. Experimental and theoretical studies of nanofluid thermal conductivity enhancement: a review. *Nanoscale Research Letters*, 2011, **6**(229), P. 1–13.

[17] Rudyak V.Ya., Belkin A.A.. Tomilina E.A. On the thermal conductivity of nanofluids. *Technical Physics Letters*, 2010, **36**(7), P. 660–662.

[18] Surtaev A.S., Serdyukov V.S., Pavlenko A.N. Nanotechnologies for thermophysics: Heat transfer and crisis phenomena at boiling. Nanotechnologies in Russia, 2016, **11**(11-12), P. 696–715.

[19] Theofanous T.G., Dinh T.N. High heat flux boiling and burnout as microphysical phenomena: mounting evidence and opportunities. *Multiphase Science Tech*, 2006, **18**(1), P. 361–364.

Particle size analysis of niosomes as a function of temperature

E. I. Diskaeva[1], O. V. Vecher[1], I. A. Bazikov[1], D. S. Vakalov[2]

[1]Stavropol State Medical University, Mira, 310, Stavropol, 355017, Russia

[2]North Caucasus Federal University, Pushkina, 1, Stavropol, 355000, Russia

vecher.olga@mail.ru

The aim of the present investigation is to study and evaluate influence of temperature factor on the size of niosomes and particle size distribution. Particle size was defined with analysis electronic microscopy images. By the analysis of the probability density functions and cumulative distribution functions for particle size was confirmed influence temperature on their equivalent diameter. On the basis of the statistical analysis, we proved possibility of management niosomes size using the change temperature on the niosomes dispersion.

Keywords: niosomes dispersion, nonionic surfactant vesicles, particle size distribution.

1. Introduction

One of the more promising directions for the development of modern pharmacology is perfection of methods which have already confirmed the efficiency of drug delivery. There are vesicular drug delivery system such as liposomes and niosomes [1–4]. Niosomal drug delivery systems have great advantage for poorly soluble drug by increasing its solubility, controlling its release and prolong its activity over period of time.

Niosomes are stable nonionic microscopic vesicles consisting of one or several membrane of various structures. Wide application of nonionic surfactants and lipids in designing of such systems is caused by their biocompability, ability, ability for biodegradation and also low toxicity.

Advantages noisome-delivered drugs include an in increase bioavailability of medical products by increased penetration through biological membrane, in propagation of pharmalogical action and selective accumulation in a place of entered [5–8]. Niosomes can be used for excipient biological active products, pharmaceuticals and non-pharmaceutical drugs.

Principles of a target drug delivery system used possibility management in wide range of niosomes size. For example, at oral – less than 1000000 nm, at a local entered – less than 300 nm, at enter in a circulation blood – 10 nm [9].

Many methods, developed now give us possibility to change and controlled diameter niosomes, their physical and chemical properties, surface structure in a preparation process [10–12]. The particle size and particle distribution of niosomes have an important role on their biodistribution. A narrow particle size distribution is desired for drug carriers [13]. At the same time, there has been keen interest to change the size of already-prepared solutions using the temperature. Temperature change of niosomal system affects assembly of surfactants into vesicles and also induced vesicle shape transformations [14].

2. Experimental

In the present study niosomes were used that consisted of a shell in the form of a water-insoluble double layer of a nonionic surfactant, which is a group of dimethiconecopolyol substances that are esters of polyethylene glycol and polydimethylsiloxane (PDMS) backbone [15–17].

To obtain the silicone-based capsules, we used physico-chemical methods for the synthesis of molecules. The shell of the obtained niosome vesicles were generated from PEG-12 Dimethicone. In the hydrophilic part of dimethicone there are functional groups of silicon oxide. The length of the Si-O bond was 1.6 Å, which is much longer than the C-C bond of 1.4 Å. Due to this, the functional groups of the molecules are able to rotate with respect to each other. This provided niosomes with greater elasticity than liposomes made up of phospholipids. The use of PEG-12 Dimethicone promoted the formation of vesicles without significant energy effort. The Si-O-Si bond angle was 130°, in contrast to the 109° of the C-C-C bond, which increased the elasticity and stability [18]. The stage of vesicle formation occurred with intensive mechanical mixing of the mixture using an automatic reclosure homogenizer. The dispersion was then placed in a vessel for ultrasonic treatment. Ultrasonic irradiation

was carried out at a frequency of 20 kHz; power – 200 W, exposure time – 10 minutes. Monolamellar niosomes were formed. Then, samples were diluted with ultrapure water (C=0.01%) and heating on the water bath (Ulab, China) on temperature interval 303–333 K.

The dispersion of nanoparticles was studied using scanning electron microscopic method (SEM Tescan Mira 3 Im). The particle size determined using computer program Image J.Excel statistical package program was used to perform the analysis. The measurements were carried out after 1.5 hours and after 7 and 14 days.

The image in Fig. 1 presents come series of microscopy pictures. Apparently the water solution of niosomes consists of particles with various diameters.
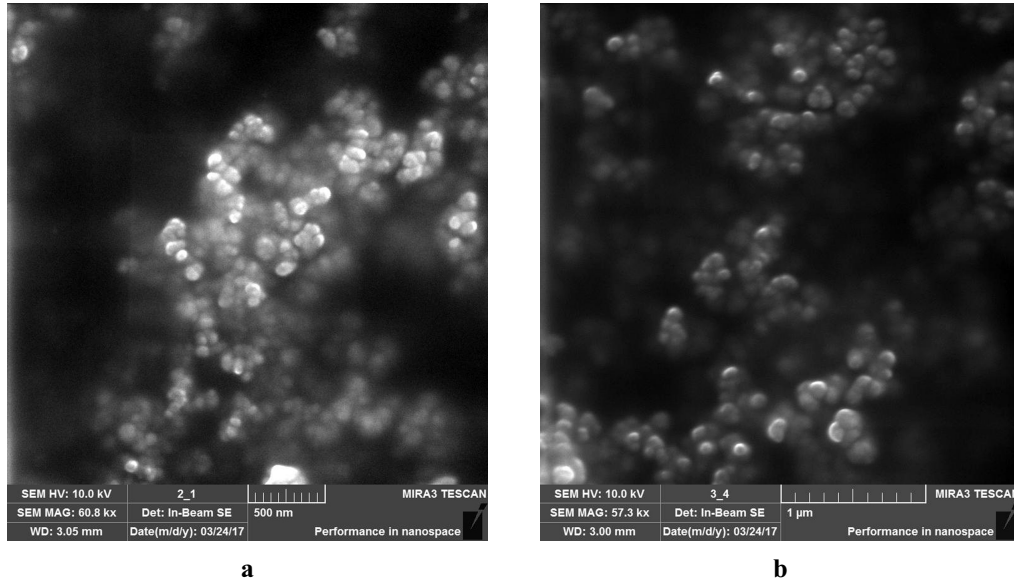
FIG. 1. Scanning electron microscopy (SEM) micrographs of niosomes (a – after 1.5 h; b – after 14 days)

As can be seen from the presented microphotographs, niosomes, for the most part, are spherical particles. This means that to determine the equivalent diameter of particles, we can use the projected diameter. The area of the projected diameter is equal to the area of the image of the projection of the particle.

Since the area of the projection of a spherical particle is:

$$S_P = \frac{\pi \delta_P^2}{4},\qquad(1)$$

Then, the average projection diameter calculation is:

$$\delta_P = \sqrt{\frac{4 S_P}{\pi}}.\qquad(2)$$

To obtain information on the particle size for each temperature regime, fractions with a total number of a part of 500 was investigated. This procedure was done in triplicate for each sample.

The cumulative distribution function, $D(\delta)$, was used to evaluate the average particle size. This function is equal to the ratio of all particles, whose diameter does not exceed the value δ, to the total number of particles expressed in fractions or percentages (Fig. 2).

For a more detailed analysis, can use the function obtained by differentiating the cumulative distribution function, i.e. distribution density:

$$f(\delta) = \frac{dD(\delta)}{d\delta}.\qquad(3)$$

In this case, the following equation must be true:

$$\int_{\delta_{\min}}^{\delta_{\max}} f(\delta)d\delta = D(\delta_{\max}) - D(\delta_{\min}).\qquad(4)$$
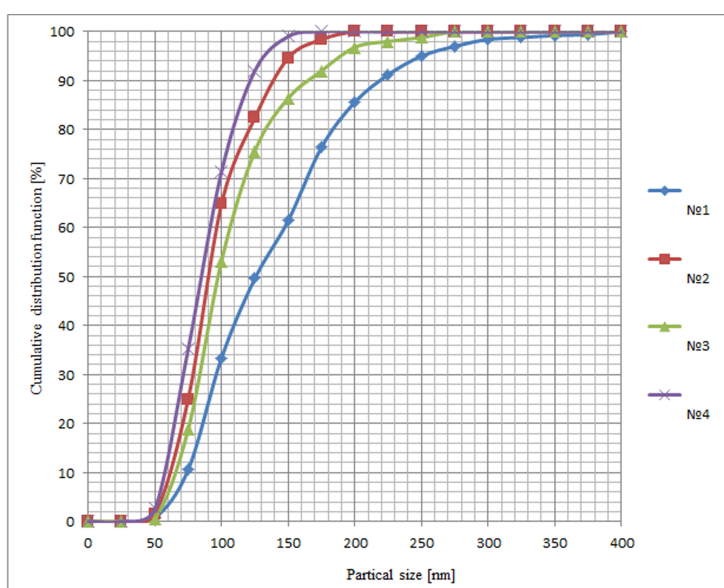
FIG. 2. Cumulative distribution function of particle size in niosomal dispersions after heating to temperatures of 303 K (No 1), 313 K (No 2), 323 K (No 3) and 333 K (No 4)
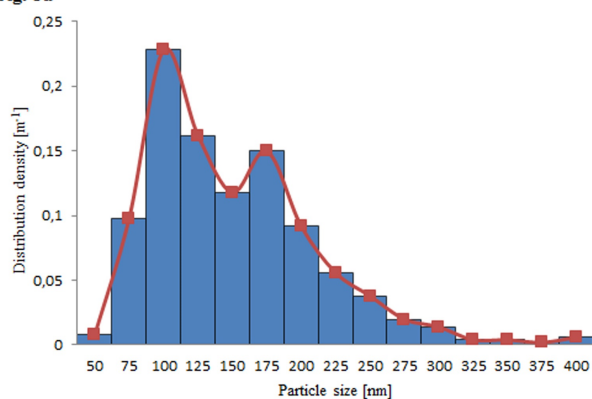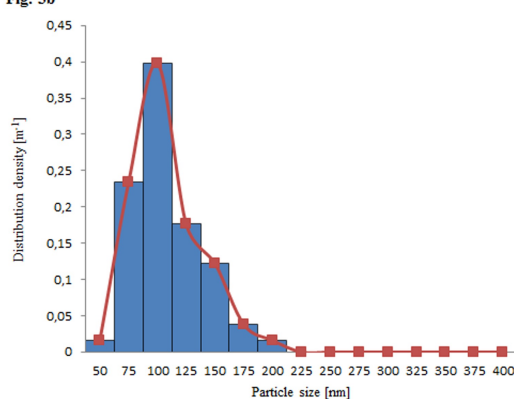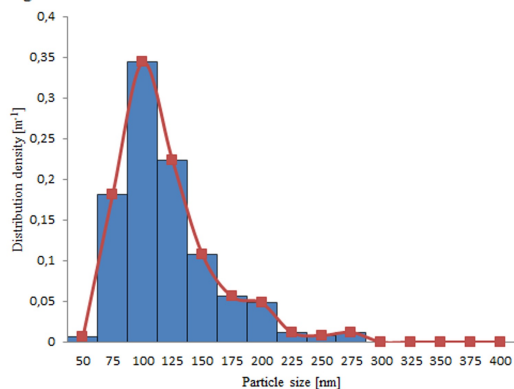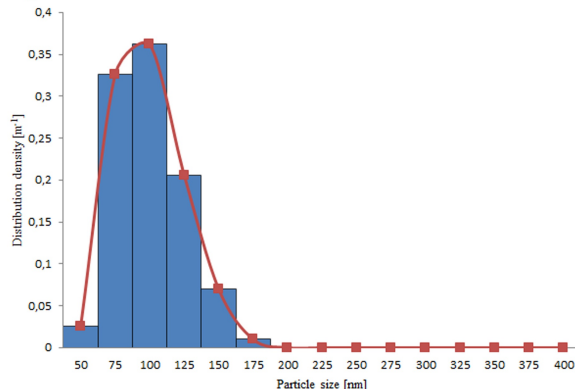
FIG. 3. Column charts of particle size distribution in niosomal dispersions subjected to heating to temperatures of 303 K (a), 313 K (b), 323 K (c), and 333 K (d)

Experimental studies of the composition of niosomal dispersion were accompanied by the construction of the function in the form of a column charts and completed with mathematical approximation. The column charts of the particle size distribution for different temperature regimes are shown on Fig. 3.

The area of each rectangle is the percentage of the fraction with a defined particle size interval. The correctness of the approximation was controlled by the equality:

$$\sum_{i=1}^{k} f_i \Delta \delta_i = \int_{0}^{\infty} f(\delta)\, d\delta = 1. \tag{5}$$

Probability density function of particles by the size subjected to heating the different temperatures 303–333 K accordingly are shown on Fig. 4.
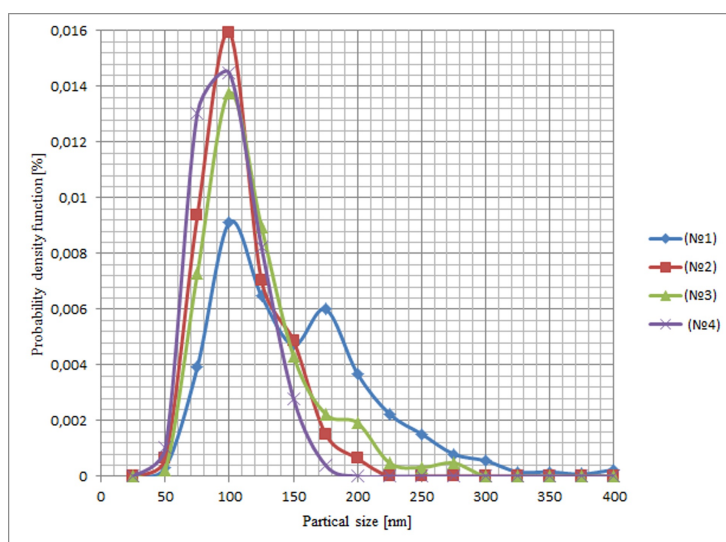
FIG. 4. Probability density function of particle size distribution in niosomal dispersions subjected to heating to temperatures of 303 K (No 1), 313 K (No 2), 323 K (No 3) and 333 K (No 4)

3. Results and discussion

Figure 4 shows that the probability density functions presented monomodal distribution and bimodal particle size distribution. Using these curves, we can determine possible value of the equivalent diameter corresponding to the maximum number of particles in niosomal dispersion, i.e. the most likely size of vesicles. Comparison of these values for different temperature regimes demonstrates homogenization with respect to particle size of niosomes dispersion.

The size of niosomes is of enormous importance for transporting drugs and their therapeutic effectiveness. So, if the niosomes diameter decreases, then the efficiency of penetration into deep layers of a skin is increased. Therefore, the most interesting are monolamellar niosomes, with diameter approximately 80–100 nm, having a thin flexible shell. These niosomes move more efficiently through intercellular spaces, lymphatic and blood capillaries. Dimethicone, which forms a bilayer structure in an aqueous medium, made it possible to obtain a hyperfine and elastic membrane niosomes.

Considering the interval of values of the vesicles diameter in the range from 75 nm to 125 nm, it can be seen that the effect of temperature increase has a direct effect on the decrease of particle size: from 48.8 % at 303 K to 89.4 % at 333 K. Thus, on the basis of the statistical analysis, we have proved the possibility of controlling niosome size using the temperature regimes, acted on the niosomes dispersion. Heat energy, in this case, is expended an endothermic phase transitions and the process destruction of conglomerates or temporary associates of niosomes.

The aqueous suspension of niosome is a colloidal system, and the interaction between the particles can lead to the formation of either stable aggregates or temporary associates due to coagulation and flocculation. As a result of these processes, niosomal dispersion is a combination of structures of the following types: small individual vesicles, flocculated vesicles, aggregated vesicles and fused vesicles.

Niosomes of small dimensions are thermodynamically unstable, so their content is detected only after a short time after the preparation of the suspension, provided it has a small concentration. The distance between niosomes

in the aggregates is so small that a strong intervesicular interaction arises between them. This is accompanied by a curvature of the contacting surfaces and further leads to the formation of more profitable energetically large niosomes, i.e. they are merged. With the rise in temperature, the fusion of niosomes in aggregates slows down under the influence of the forces of repulsion of the structuredness of water in the space between them and the increase in Brownian motion.

4. Conclusions

Thus, an analysis of the effect of heating niosomal dispersion on the average particle size reveals a tendency to decrease the diameter of niosomes with increasing temperature. Niosomes subjected to heat treatment become more stable in time and retain an average particle size of about 100 nm. This approach can be recommended for further improvement of methods of preparation and storage of stable drug forms.

References

[1]   Growi R., Balaji P., Vijayalakshmi P., Preethy Mol.G., Karthik Raja P. Niosomes – a vesicular drug delivery system. *International Journal of Current Research*. 2013, **5**(08), P. 2239–2244.

[2]   Viviane F. Naggar, Safaa S. Elgamal, Ahmed N. Allam Formulation and Physicochemical Characterization. *Journal of American Science*, 2012, **8**(9), P. 417–428.

[3]   Abhinav Kumar, Pal Jogender Lal, Jaiswal Amit, Singh Vishwabban. Review of niosomes as novel druid delivery system. Int. Research Journal of Pharmacy, **2**(5) 2011, P. 61–65.

[4]   Zerrin Sezgin Bayindir, Nilufer Yuksel. Characterization of niosomes Prepared with various Nonionic Surfactants for paclitaxel Oral delivery. *Journal of Pharmaceutical sciences*, 2010, **99**(4), P. 2049–2060.

[5]   Bazikov I.A. A method for transdermal transfer of active substances using niosomes on the basis of PEG-12 dimethicone. RF patent 2539396, 2014.

[6]   Bazikov I.A., Zelensky V.A., Gukasyan A.L. *Nanobiotechnologies of the use of niosomes in dentistry*, Maikop: Quality, 2015, 112 p.

[7]   Malay K. Das, Narahari N. Palei. Sorbitan ester niosomes for topical delivery of rofecoxib. *Indian Journal of Experimental Biology*, 2011, **49**, P. 438–445.

[8]   Sakthivel M., Kannan K., Manavalan R., Senthamarai R. Non Ionic Surfactant Vesicles. *A Review. Research Journal Pharmaceutical, Biological and Chemical*, 2012, **3**(01), P. 604–614.

[9]   *Handbook of nanostructured materials and nanotechnology*. Ed. H.S. Nalwa. Boston: Academic Press, 2000, 3461 p.

[10] Gannu P. Kumar, Pogaku Rajieshwarrao. Nonionic Surfactants vesicular system for effective druid delivery – an overview. *Acta Pharmaceutica Simca B*, 2011, **1**(4), P. 208–219.

[11] Apeora Agarwal, Weha Jugal, Gauree Kukreti, Sachdew Yadav. Niosomes of targeted druid delivery systems. *International Journal of Pharmaceutical Science Review and Research*, 2012, **12**(1), P. 53–60.

[12] Ahuja N., Saini V., Bishnoi V.K., Garg A., Hisoria M., Sharma J., et al. Formulation and evaluation of lansoprazol noisome. *Rasayan J. Chem.*, 2008, **1**, P. 561–564.

[13] Zerrin Sezgin Bayindir, Nilufer Yuksel. Investigation of formulation variables and excipient interaction on the production of niosomes. *Pharm. Sci. Tech.*, 2012, **13**, P. 826–835.

[14] Arunothayanum P. et al. Extrusion of niosomes from capillaries approaches to a pulsed delivery device. *J. Cont Release*, 1999, **60**, P. 1999.

[15] Bazikov I.A., Beyer E.V., Maltsev A.N., et al. Investigation of the cardiotoxicity of the niosomal form of doxorubicin. *Medical Gazette of the North Caucasus*, 2016, **11**(3), P. 421–424.

[16] Bazikov I.A., Lukinova V.V., Maltsev A.N., et al. The interaction of niosomal doxorubicin with cell membranes. *Medical Gazette of the North Caucasus*, 2016, **11**(1), P. 108–110.

[17] Bazikov I.A., Lukinova V.V., Malinina N.I., Maltsev A.N. Study of the mechanisms of intercellular interaction of the niosomal form of the antitumor drug doxorubicin with plasma membranes. *The Eurasian Union of Scientists*, 2016, **3**(24), P. 34.

[18] Bazikov I.A., Omelyanchuk P.A. The method of delivery of biologically active substances with the help of niosomes RF patent 2320323, 2008.

Spontaneous growth of petal crystals in fullerite films

L. V. Baran

Belarusian State University, Nezavisimosti ave., 4, Minsk, 220030, Belarus

baran@bsu.by

Changes in the structure, elemental and phase compositions of fullerite films after their storage in air are investigated by scanning electronic microscopy, atomic force microscopy, X-ray spectroscopic microanalysis, X-ray diffraction, and Raman spectroscopy. The formation of the petal and flower-like fullerite crystals under the action of internal stress is established.

1. Introduction

Fullerenes are unique objects with interesting physical and chemical properties. In the condensed condition, fullerenes form a molecular crystal – fullerite, whose crystallographic symmetry depends on many factors: method of production, type and substrate temperature of heating on which molecules are adsorbed, deposition rate, etc. C_{60} fullerite crystals, grown at room temperature from a solution by the salting-out method, usually have face-centered lattice [1], in which molecules rotate, as interaction forces between molecules are small, and the symmetry degree is very high [2]. At 260 K the transition into a primitive cubic lattice occurs with simultaneous partial freezing of the molecular motion, owing to increased intermolecular interaction. During the process of the fullerite films producing, the crystal structure with a hexagonal close-packed lattice [3] can be formed from a gas phase.

In previous works [4–8] research was presented for the structure dependence of deposited fullerite C_{60} layer from a substrate type, where monocrystal silicon, metals, highly oriented pyrolytic graphite, substrate heating temperatures were usually used. The structure of the fullerite films is determined both by the technological spraying parameters, including vacuum level, sublimation speed, distance of the evaporator to substrate holder, heating temperature and type of the substrate on which the film is to be deposited. To use this structure in actual practice, the time properties stability of the received films is important, which is to a great extent determined by the stability of structure. However, there are, virtually, no facts in the literature about the structure evolution of the fullerite films over time.

The purpose of work is research of the changes of the crystal fullerite films C_{60} structure grown onto silicon substrates that occur after storing samples in air.

2. Experimental

Fullerite films were prepared by successive chemical vapor deposition in a VUP-5M system in vacuum no worse than $1.3 \cdot 10^{-3}$ Pa. As a feedstock, C_{60} powder with purity greater than 99.98 % was used. C_{60} molecules were deposited onto the oxidized single-crystal Si (111) wafers. Fullerenes were sublimated from a tantalum crucible, whose temperature was maintained at $T = 770$ K. This value ensured a high deposition rate for the films (2 nm/s).

The synthesized films had a thickness 350 nm. The surface morphology was analyzed using a Solver PRO-P47 atomic force microscope in contact mode. We used ultrasharp silicon cantilever probes with a tip radius in the range 1 – 3 nm.

The phase composition of the films was determined by X-ray diffraction on a Rigaku Ultima IV multipurpose X-ray diffractometer with $CuK_{\alpha 1}$ radiation in Bragg–Brentano geometry (intensity data were collected using a Rigaku ultrasensitive, highspeed, multichannel detector, which allowed us to obtain X-ray diffraction patterns of thin layers). The film structure was investigated under an LEO-1455 VP scanning electron microscope at accelerating voltages of 15 kV. Distribution of elements in the films was obtained by X-ray microanalysis using an Aztec Energy Advanced X-Max 80 nitrogen-free energy dispersive microanalyzer (123-eV energy resolution for MnK_{α}) during electron beam scanning along the linear direction. Spectra of combination scattering at a fixed resolution (1 cm^{-1}) were registered at room temperature using a Nanofinder High End (Lotis TII, Belarus–Japan)

confocal-microscope-based setup. To start excitation of a sample, the laser radiation with a $\lambda = 473$ nm was applied. The laser capacity was weakened through the use of filters to values less than 0.5 W/cm^2. The choice of low capacity laser energy is required in order to avoid photoinduced changes or heating of the samples.

3. Results and discussion

The structure and phase composition of C_{60} powder used for spraying are illustrated in Fig. 1. The powder appears as crystallites with an average size 150 μm, possessing face-centered cubic lattice ($a = 1.4115$ nm), sp. gr. Fm3m. It was established by atomic-force microscopy that the as-prepared fullerite films onto the substrates of the oxidized monocrystal silicon have homogeneous granulated structure at an average granular size of 80 nm (Fig. 2a).
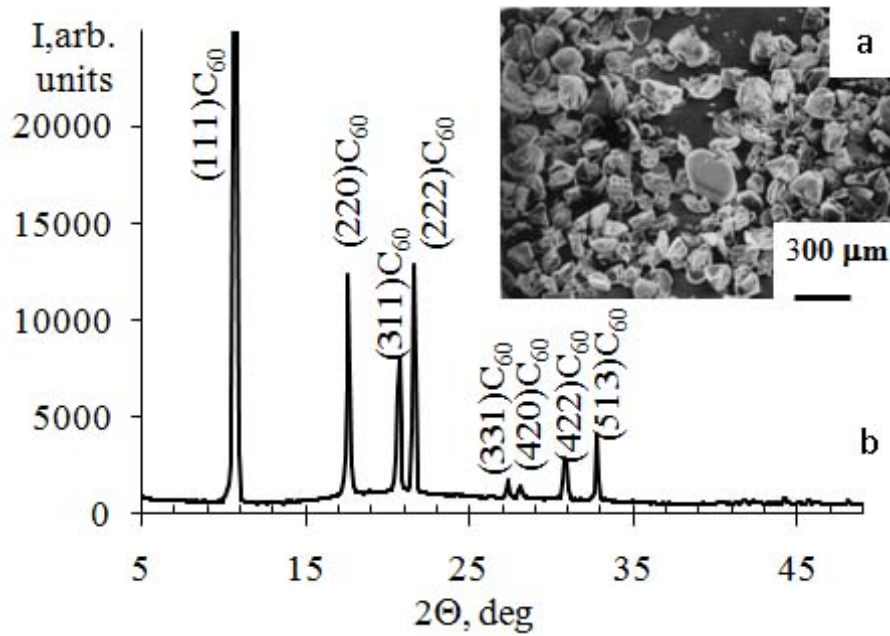
FIG. 1. The structure (a) and X-ray diffraction pattern (b) of C_{60} powder
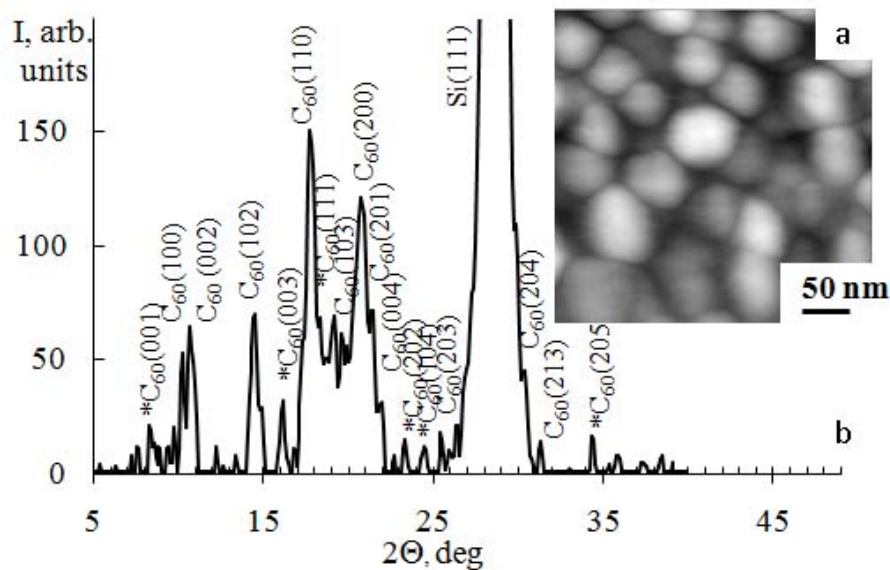
FIG. 2. The AFM-image (a) and X-ray diffraction pattern (b) as-prepared C_{60} fullerite films

By the method of X-ray diffraction, it was established that during the process of condensation onto the silicon substrate of C_{60} molecule one is forming the crystal structure with hexagonal close-packed lattice ($a = 1.0020$ nm, $c = 1.6381$ nm), sp. gr. $P6_3$/mmc (Fig. 2b). There are a number of lines of low intensity in the XRD patterns, which are also visually displayed on the theory of the hexagonal system ($a = 1.0020$ nm, $c = 1.6162$ nm), sp. gr. P6/mmm. The transformation of the fcc into an hcc lattice occurred as a result of the high deposition rate of C_{60} molecules (2 nm/s) onto the non-heated substrate, as a result of which the nanocrystal film was formed. Halo presence in the angles area of 17 – 22 degrees is caused by X-ray amorphous clusters of C_{60} molecules in size of up to 10 nm that are present in the films, which have been found out in the work [9].

Figure 3 shows Raman spectra of C_{60} film. The spectrum contains all the 10 vibration modes (the pentagonal pinch $A_g(2)$ mode, two "breathing" A_g – the modes conformed to symmetric fluctuations of entire molecule (492.3 cm^{-1}) and pentagons (1464.2 cm^{-1}) and 8 H_g-mode), active in Raman spectroscopy, which testifies the purity and uniformity of the film.
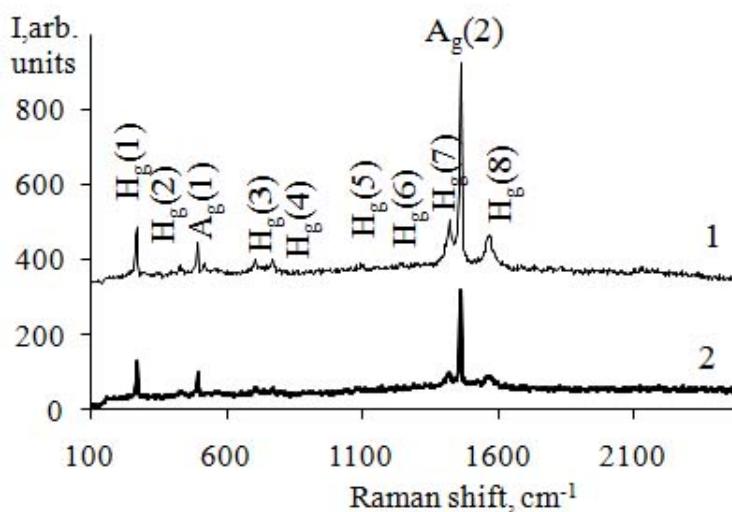
FIG. 3. Raman spectra of C_{60} films: 1 – as-prepared; 2 – after storage in air within 30 months

After long-term aerobic storage in the desiccator (30 months), petal and flowerlike formations were found on the surface of fullerite films (Fig. 4). By the method of atomic-force microscopy it was established that petal formations have thickness of 50 – 500 nanometers, with that their length changes from units to several tens micrometers. For the element structure specification of petal formations X-ray spectroscopic microanalysis was carried out. Electronic beam scanning of the lined AB-direction showed that this formation consists of carbon (Fig. 5).

Due to the developed surface morphology, the fullerite phase line's intensity decreases fractionally on X-ray pattern of the films; new phases are not revealed. There are vibration modes C_{60} on the Raman light dispersion spectrum in the flower-like formation.

It is known that whisker crystals of metals with low melting temperature (Sn, Cd, Zn, Sb, In, etc.) can grow on thin metal layers without any foreign action at room temperature. Fullerite is a crystal with a low sublimation temperature (650 K); therefore, spontaneous growth of whisker fullerite crystals may occur at room temperature.

Spontaneous growth of whisker crystals is characterized by the existence of a long-term incubation period. Under ordinary conditions, the growth depends on the sublayer on which a coating was deposited.

Spontaneous growth of whisker crystals is based on the dislocation mechanism. Internal stress is the energy source. This energy source is internal stresses, which arise in the fullerite films as consequence of parameters discrepancy of the contacting materials lattice and structural defects. Growth in the form of thin petal crystals can be caused by helical sources, emerging to two mutually perpendicular surfaces. Petals crystals develop either through overgrowth of bridges between neighboring parallel whisker crystals or via expansion of prismatic faces to opposite sides.

Unintentional atomic or molecular impurities adsorbed on the end faces of whisker crystals can also stimulate the expansion of faces, as a result of which, the layer-by-layer or chain formation of faces occurs without hindrances. Thus, petal microcrystals are formed through anisotropic lateral growth of whisker crystals playing a leading role. Interaction between petal crystals leads to the development of flowerlike formations.
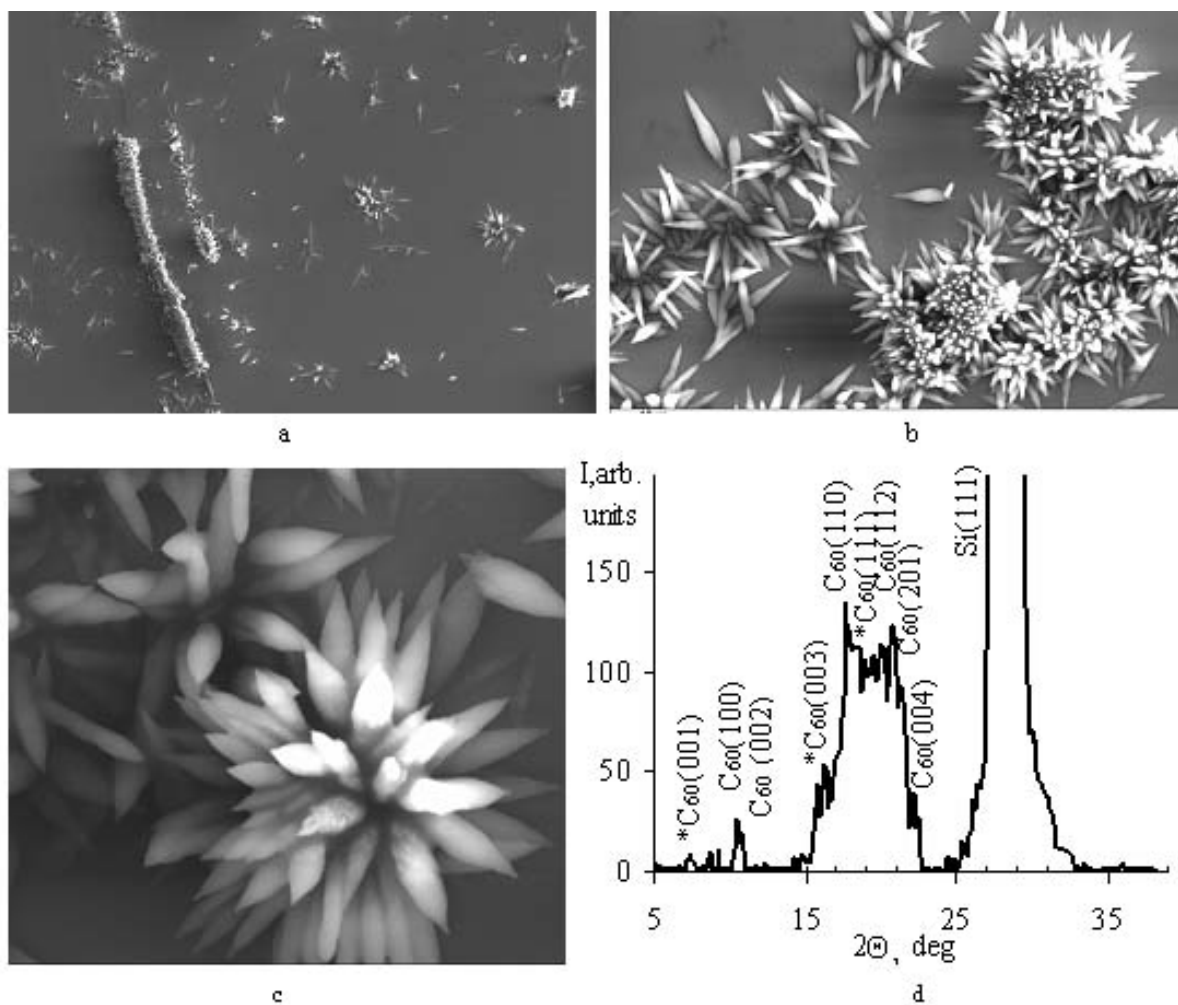
FIG. 4. The structure (a) and X-ray diffraction pattern (b) fullerite films after the in-air storage
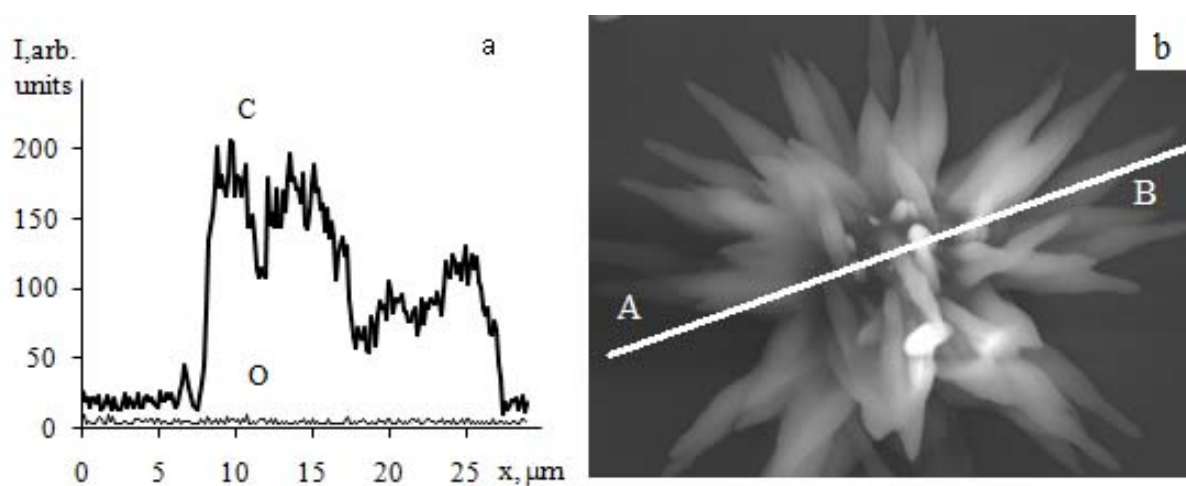
FIG. 5. Distribution of elements (a), obtained by the method of X-ray microanalysis in the electronic beam scanning along the indicated line (shown in panel b) of fullerite films after the in-air storage

4. Conclusions

Thus, as a result of the conducted research, it is established that under condition of aerobic storage over a protracted period (30 months), the spontaneous growth of petal crystals occurs on the surfaces of fullerite films.

Acknowledgements

References

[1] Fischer J.E. Structure and dynamics of solid C_{60} and its intercalation compounds. *Mat. Sci. Eng.*, 1999, **B19**, P. 90–99.

[2] Eklund P.C., Rao Apparao M. (Eds.) *Fullerene polymers and fullerene polymer composites*. Springer series in materials science, 2002, 394 p.

[3] Skokan E.V., Arkhangelskii I.V., et al. Stability of hexagonal modification of fullerite C_{60}. *Carbon*, 2005, **43**, P. 803–808.

[4] El-Nahass M.M., Ali1 H.A.M., et al. Analysis of structural and optical properties of annealed fullerene thin films. *Eur. Phys. J. D*, 2015, **69**, P. 200–207.

[5] Hyeon Suk Shin, Seok Min Yoon, et al. Highly Selective Synthesis of C_{60} Disks on Graphite Substrate by a VaporSolid Process. *Angew. Chem. Int. Ed.*, 2007, **46**, P. 1–5.

[6] Wen-Rong Cheng, Shiow-Jing Tang, et al. Effects of substrate temperature on the growth of C_{60} polycrystalline films by physical vapor deposition. *Journal of Crystal Growth*, 2003, **247**, P. 401–407.

[7] Singh Th. Birendra, Yang H., et al. Characterization of highly crystalline C_{60} thin films and their field-effect mobility. *Phys. Stat. Sol. B*, 2007, **244** (11), P. 3845–3848.

[8] Solonin Yu.M., Graivoronskaya E.A., Galii O.Z. Structure and electrochemical activity of C_{60} fullerite films. *Powder Metallurgy and Metal Ceramics*, 2001, **40**, P. 618–624.

[9] Korolev Yu.M., Kozlov V.V., Polikarpov V.M., Antipov E.M. X-Ray Powder Diffraction and Phase Composition of Fullerene C_{60}. *Doklady Physical Chemistry*, 2000, **374** (1–3), P. 167–171.

NANOSYSTEMS:

PHYSICS, CHEMISTRY, MATHEMATICS

INFORMATION FOR AUTHORS

The journal publishes research articles and reviews, and also short scientific papers (letters) which are unpublished and have not been accepted for publication in other magazines. Articles should be submitted in English. All articles are reviewed, then if necessary come back to the author to completion.

The journal is indexed in Web of Science Core Collection (Emerging Sources Citation Index), Chemical Abstract Service of the American Chemical Society, Zentralblatt MATH and in Russian Scientific Citation Index.

Author should submit the following materials:

1. Article file in English, containing article title, the initials and the surname of the authors, Institute (University), postal address, the electronic address, the summary, keywords, MSC or PACS index, article text, the list of references.
2. Files with illustrations, files with tables.
3. The covering letter in English containing the article information (article name, MSC or PACS index, keywords, the summary, the literature) and about all authors (the surname, names, the full name of places of work, the mailing address with the postal code, contact phone number with a city code, the electronic address).
4. The expert judgement on possibility of publication of the article in open press (for authors from Russia).

Authors can submit a paper and the corresponding files to the following addresses: nanojournal.ifmo@gmail.com, popov1955@gmail.com.

Text requirements

Articles should be prepared with using of text editors MS Word or LaTex (preferable). It is necessary to submit source file (LaTex) and a pdf copy. In the name of files the English alphabet is used. The recommended size of short communications (letters) is 4-6 pages, research articles– 6-15 pages, reviews – 30 pages.

Recommendations for text in MS Word:

Formulas should be written using Math Type. Figures and tables with captions should be inserted in the text. Additionally, authors present separate files for all figures and Word files of tables.

Recommendations for text in LaTex:

Please, use standard LaTex without macros and additional style files. The list of references should be included in the main LaTex file. Source LaTex file of the paper with the corresponding pdf file and files of figures should be submitted.

References in the article text are given in square brackets. The list of references should be prepared in accordance with the following samples:

[1]   Surname N. *Book Title*. Nauka Publishing House, Saint Petersburg, 2000, 281 pp.
[2]   Surname N., Surname N. Paper title. *Journal Name*, 2010, **1** (5), P. 17-23.
[3]   Surname N., Surname N. Lecture title. In: Abstracts/Proceedings of the Conference, Place and Date, 2000, P. 17-23.
[4]   Surname N., Surname N. Paper title, 2000, URL: http://books.ifmo.ru/ntv.
[5]   Surname N., Surname N. Patent Name. Patent No. 11111, 2010, Bul. No. 33, 5 pp.
[6]   Surname N., Surname N. Thesis Title. Thesis for full doctor degree in math. and physics, Saint Petersburg, 2000, 105 pp.

Requirements to illustrations

Illustrations should be submitted as separate black-and-white files. Formats of files – jpeg, eps, tiff.